

**Group 4 Ureate Complexes: Synthesis, Reactivity, and
Catalytic Carbon-Element Bond Formation**

by

David Charles Leitch

B. Sc., The University of British Columbia, 2004

A THESIS SUBMITTED IN PARTIAL FULFILLMENT OF
THE REQUIREMENTS FOR THE DEGREE OF

DOCTOR OF PHILOSOPHY

in

The Faculty of Graduate Studies

(Chemistry)

THE UNIVERSITY OF BRITISH COLUMBIA
(Vancouver)

September 2010

© David Charles Leitch, 2010

ABSTRACT

The synthesis, characterization, and reactivity patterns of three new classes of ureate-supported group 4 compounds are described, constituting the first comprehensive examination of the use of these electron-rich ligands. Four ureates with varying steric and electronic properties are included here: two mono(ureate)s and two tethered bis(ureate)s.

Synthesis of dichlorobis(ureato) titanium and zirconium derivatives can be accomplished using several methods, with direct protonolysis between the urea prolignand and $M(NMe_2)_2Cl_2$ precursors giving the highest yield. Solid-state and solution-phase characterization indicates the distal dialkylamino substituent on the ureate donates electron density into the chelate. While use of non-tethered ligands results in zirconium complexes that are fluxional in solution, tethered bis(ureato) ligands support well-defined species. These complexes retain neutral ligands, which are not easily removed. Ureate-supported zirconium dialkyl complexes can also be prepared by protonolysis between a urea and tetraalkyl zirconium compounds. The electron-rich nature of the ureate ligands allows the isolation of coordinatively unsaturated dialkyl complexes.

Ureate-supported bis(amido) compounds of titanium and zirconium have been developed as precatalysts for hydroamination. A comprehensive structural comparison between related amidate and ureate complexes reveals that the ureate ligands bind tighter to their metal centers than amidates. As a consequence of this, and the electron-rich nature of the ureate ligands, amidate precatalysts are generally more effective for

intramolecular hydroamination of alkenes than ureate precatalysts. In contrast, precatalysts with tethered ureate ligands are more effective than analogous amidates. The most active system identified through catalytic screening exhibits broad substrate scope and functional group tolerance. Most importantly, this is the first group 4 system that is highly effective with both primary and secondary amines.

Mechanistic investigations have revealed that catalysis with the tethered bis(ureate) precatalyst does not proceed through an imido-mediated [2+2] cycloaddition-type mechanism. Instead, the key bond forming step is proposed to occur through concerted insertion of the alkene into a Zr–N bond and protonation of the terminal alkene carbon by a coordinated amine ligand. This proposal is supported by stoichiometric and kinetic investigations, which indicate that a proton-source accelerates alkene insertion, and a primary kinetic isotope effect when using an *N*-deuterated aminoalkene.

PREFACE

Parts of the research conducted for this thesis were carried out collaboratively with other members of the Schafer research group. I, in consultation with my supervisor Dr. Laurel Schafer, designed all of the experiments described herein. Furthermore, I carried out nearly all of these experiments; however, others collected the following specific pieces of data. As described in the text, all DFT calculations were performed by Jean Michel P. Lauzon. Courtney S. Turner, Philippa R. Payne, and Christine R. Dunbar contributed to catalyst screening experiments involving amidate-supported precatalysts (Chapter Three, Table 3.6). These individuals also assisted with substrate scope exploration, being responsible for the synthesis and characterization of compounds **178**, **179**, **186**, and **193**. Finally, the reaction represented in equation 4.4 (Chapter Four) was carried out by Courtney S. Turner. The following is a list of publications stemming from this work. I wrote each of these papers, with editorial assistance from the co-authors listed. Any work from these papers that I did not directly carry out, with the exceptions listed previously, does not appear in this thesis, or is appropriately referenced.

- Leitch, D. C.; Beard, J. D.; Thomson, R. K.; Wright, V. A.; Patrick, B. O.; Schafer, L. L. *Eur. J. Inorg. Chem.* **2009**, 2691. (Chapter Two)
- Leitch, D. C.; Payne, P. R.; Dunbar, C. R.; Schafer, L. L. *J. Am. Chem. Soc.* **2009**, *131*, 18246. (Chapter Three)
- Leitch, D. C.; Turner, C. S.; Schafer, L. L. *Angew. Chem. Int. Ed.* **2010**, *in press*. (Chapter Four)
- Leitch, D. C.; Schafer, L. L. *Organometallics* **2010**, *in press*. (Chapter Two and Chapter Four)

TABLE OF CONTENTS

Abstract	ii
Preface	iv
Table of Contents	v
List of Tables	x
List of Figures	xii
List of Schemes	xx
List of Abbreviations and Acronyms.....	xxii
Acknowledgements	xxvii
Dedication	xxviii
 CHAPTER 1. Ureates as Modular Supporting Ligands for Group 4 Chemistry.....	 1
1.1 The “Post-Metallocene” Era.....	1
1.2 The Ureate Ligand Set	6
1.3 Synthesis of Ureate Complexes by Isocyanate Insertion	9
1.3.1 Groups 6-10.....	9
1.3.2 Group 4	12
1.4 Alternate Synthetic Approaches.....	16
1.5 Scope of This Thesis.....	21

CHAPTER 2. Synthesis, Bonding, and Reactivity of Dichloro and Dialkyl Complexes.....	24
2.1 Introduction.....	24
2.1.1 Post-Metallocene Polymerization	25
2.1.2 Potential Advantages of Ureate Ligands.....	32
2.2 Results and Discussion.....	34
2.2.1 Efficient and Modular Synthesis of Urea Proligands.....	34
2.2.2 Synthesis of Dichlorobis(ureato) Complexes	37
2.2.3 Synthesis of Ureate-Supported Dialkyl Complexes	49
2.2.4 Formation of Pyridine Adducts.....	58
2.2.5 Preliminary Screening of Olefin Polymerization Precatalysts	61
2.3 Conclusions	64
CHAPTER 3. Catalytic Hydroamination, Part I: Catalyst Development.....	66
3.1 Introduction.....	66
3.1.1 The Hydroamination Reaction.....	66
3.1.2 Rare-Earth Metal Catalysts.....	69
3.1.3 Late Transition Metal Catalysts	73
3.1.4 Group 4 Systems.....	76
3.1.5 Two Major Challenges	78
3.2 Results and Discussion.....	82
3.2.1 Synthesis and Characterization of Non-Tethered Precatalysts	82
3.2.2 Precatalysts with Tethered Ureate Ligands	91
3.2.3 Metal–Ureate Bonding Model.....	95

3.2.4	Steric and Electronic Effects on Hydroamination Catalysis	97
3.2.5	Hydroamination Scope of Tethered Precatalyst.....	101
3.3	Conclusions	106
CHAPTER 4. Catalytic Hydroamination, Part II: Mechanistic Elucidation.....		107
4.1	Introduction	107
4.1.1	General Hydroamination Catalytic Cycles.....	107
4.1.2	Hydroamination <i>via</i> Imido Intermediates.....	109
4.1.3	Hydroamination <i>via</i> Insertion.....	113
4.1.4	Proposed Hydroaminoalkylation Mechanism.....	116
4.2	Results and Discussion	119
4.2.1	Precatalyst Reactivity I: Effect of Neutral Donors	119
4.2.2	Precatalyst Reactivity II: Thermal Stability.....	122
4.2.3	Precatalyst Reactivity III: Synthesis of Imido Compounds	124
4.2.4	Precatalyst Reactivity IV: Insertion of Alkynes	133
4.2.5	Precatalyst Reactivity V: Insertion of Alkenes.....	139
4.2.6	Kinetic Analysis of Aminoalkene Cyclization	141
4.2.7	Summary of Pertinent Details and Mechanistic Proposal	153
4.3	Conclusions	163
CHAPTER 5. Synopsis, Future Directions.....		165
5.1	Conclusions Drawn.....	165
5.2	Further Research Avenues	168
5.2.1	Mechanistic Elucidation	168

5.2.2	Enantioselective Hydroamination	170
5.2.3	Toward Intermolecular Alkene Hydroamination.....	173
5.2.4	Hydrophosphination, Dehydrocoupling of Phosphines.....	175
5.2.5	Alkyne Coupling	177
5.3	Concluding Statements	179
REFERENCES		180
APPENDIX A. Experimental Details		197
A.1	General Considerations	197
A.2	Materials	198
A.3	Synthesis of Urea Proligands	199
A.4	Synthesis of Metal Complexes.....	203
A.4.1	Dichlorides (Chapter Two)	203
A.4.2	Dialkyls (Chapter Two)	206
A.4.3	Bis(amido)s (Chapter Three, Chapter Five)	213
A.4.4	Catalytic Model Compounds (Chapter Four)	218
A.5	Procedure for Polymerization Reactions (Chapter Two).....	224
A.5.1	Dichloride Precatalysts (90 , 91).....	224
A.5.2	Dibenzyl Precatalysts (94 , 96 , 98)	224
A.6	Procedure for Hydroamination Catalysis (Chapter Three).....	224
A.6.1	Intramolecular Reactions	225
A.6.2	Intermolecular Reactions	226
A.6.3	Aminoalkene Substrate Synthesis	227

A.6.4 Product Characterization.....	231
A.7 Procedure for Kinetics Experiments (Chapter Four)	233
A.8 Derivation of the Catalytic Rate Law (Chapter Four)	234
APPENDIX B. Tabulated Crystallographic Parameters	236
APPENDIX C. Selected NMR Spectra	244
REFERENCES FOR APPENDICES	260

LIST OF TABLES

Table 3.1. Rare-earth metallocene catalyst activities for the cyclization of 113 and 115	70
Table 3.2. A comparison of late transition metal catalyst systems for primary and secondary aminoalkene hydroamination.....	74
Table 3.3. Group 4 catalysts for the cyclization of 113	78
Table 3.4. Hydroamination versus hydroaminoalkylation with group 4 precatalysts...	79
Table 3.5. NBO charges from preliminary computational investigations.....	96
Table 3.6. Precatalyst screening for primary aminoalkene hydroamination.....	98
Table 3.7. Precatalyst screening for secondary aminoalkene hydroamination.....	100
Table 4.1. Effect of added 2-methylpiperidine on reaction rate.....	145
Table 4.2. Aminoalkene cyclization at varying precatalyst concentrations.....	150
Table 4.3. Observed rate constants for aminoalkene cyclization at varying reaction temperatures; parameters for Eyring analysis.....	152
Table 4.4. Temperature dependence of K_{eq} values for the cyclization of 131 ; parameters for van't Hoff analysis.....	160
Table B.1. Crystallographic parameters for tethered proligand (Chapter Two).....	236
Table B.2. Crystallographic parameters for dichloride compounds (Chapter Two) ...	237
Table B.3. Crystallographic parameters for dialkyl compounds (Chapter Two)	238
Table B.4. Crystallographic parameters for non-tethered bis(amido) compounds (Chapter Three).....	239
Table B.5. Crystallographic parameters for tethered bis(amido) compounds (Chapter Three)	240

Table B.6. Crystallographic parameters for catalytic model compounds (Chapter Four)	241
Table B.7. Crystallographic parameters for alkyne insertion products (Chapter Four)	242
Table B.8. Crystallographic parameters for chiral bis(amido) complex (Chapter Five)	243

LIST OF FIGURES

Figure 1.1. Prototypical group 4 metallocene compounds.....	2
Figure 1.2. Examples of non-Cp ligand classes used in group 4 chemistry; names and years reflect first report of use as ligand on titanium, zirconium, or hafnium.....	3
Figure 1.3. Small molecule activation by non-metallocene group 4 complexes.....	4
Figure 1.4. Stereoelectronic forms of ureate anions.....	7
Figure 1.5. Steric attenuation of guanidinate electron donation.....	8
Figure 1.6. Several potential coordination modes of monoanionic ureate ligands.....	8
Figure 1.7. Geometric isomers of octahedral L_2MX_2 complexes ($L = \kappa^2\text{-}N,O\text{-ureate}$)...	9
Figure 1.8. Structural diversity in first row transition metal ureate complexes prepared <i>via</i> salt metathesis (counterions omitted for clarity).....	19
Figure 2.1. Bis(amidato) complexes that exhibit fluxional behaviour, neutral ligand retention, and/or multinuclearity.....	25
Figure 2.2. Examples of group 4 amido complexes that exhibit very high activity ($A > 1,000$) for the polymerization of olefins.....	29
Figure 2.3. (<i>N,O</i>)-Chelating phenoxyimine- and β -ketoiminate-supported precatalysts for ethylene polymerization, with activities indicated. Complexes 77 and 78 produce polymer in a living manner.....	30
Figure 2.4. Amidinate ethylene polymerization precatalysts, with activities indicated.....	31
Figure 2.5. Guanidinate precatalysts, with ethylene polymerization activities indicated.....	32

Figure 2.6. ORTEP representation of the molecular structure of **87** (top left) (ellipsoids plotted at 50% probability, hydrogens except those on N2 and N3 omitted for clarity, displayed hydrogen atoms located from unassigned electron density and their positions refined); view approximately down the crystallographic *a* axis (top right); illustration of linear hydrogen bonding network (bottom) (H-bonds in red). Selected bond lengths (Å), bond and torsion angles (°): N1–C7, 1.368(3); N2–C7, 1.350(3); O1–C7, 1.235(3); N3–C13, 1.364(3); N4–C13, 1.361(3); O2–C13, 1.244(3); O2–H100, 2.00(3); sum of angles about N1, 359.6(6); sum of angles about C7, 360.0(6); sum of angles about N2, 358(4); average torsion angle through N1–C7: 13.2(4).....37

Figure 2.7. ¹H NMR spectra (300 MHz, C₇D₈) showing C–N(*i*-Pr)₂ bond rotation dynamic behaviour for complex **90** with coalescence at 348.1 K. Proligand constitutes <5% of the composition. Performing the above calculation using signal ‘a’ gives an identical ΔG^\ddagger value.....40

Figure 2.8. ORTEP representation of the molecular structure of **90** (ellipsoids plotted at 50% probability, disordered toluene molecule removed with SQUEEZE routine,¹⁷³ hydrogens omitted for clarity) with selected bond lengths (Å), bond and torsion angles (°): Ti–N1, 2.044(9); Ti–O1, 2.006(7); Ti–Cl1, 2.271(3); C1–N1, 1.35(1); C1–O1, 1.30(1); C1–N2, 1.37(2); N1–Ti–O1, 64.8(3); N1–Ti–N1*, 151.4(4); sum of angles about N2, 360(2); N1–C1–N2–C13, 7(1).....41

Figure 2.9. ORTEP representation of the molecular structure of **91**•THF (ellipsoids plotted at 50% probability, carbons of the THF ring, disordered pentane, and hydrogens omitted for clarity, one conformation of the N4 piperidine ring shown) with selected bond lengths (Å), bond and torsion angles (°): Zr–N1, 2.285(2); Zr–O1, 2.092(2); Zr–Cl1, 2.437(1); Zr–O3, 2.297(2); C1–N1, 1.316(3); C1–O1, 1.300(3); C1–N2, 1.337(3); N1–Zr–O1, 59.63(6); Cl1–Zr–Cl2, 165.24(2); sum of angles about N2, 357.6(6); O1–C1–N2–C2, 8.8(3).....43

Figure 2.10. Selected ¹H NMR spectra (300 MHz, C₇D₈) showing C–N(*i*-Pr)₂ bond rotation dynamic behaviour for complex **92** with coalescence at 201.0 K. Performing the above calculation using signal c gives an identical ΔG^\ddagger value.....45

Figure 2.11. ORTEP representation of the molecular structure of **92** (ellipsoids plotted at 50% probability, benzene molecule and hydrogens except H999 not shown, H999 located from unassigned electron density and its position refined) with selected bond lengths (Å), bond and torsion angles (°): Ti–N1, 2.0345(9); Ti–O1, 2.0583(8); Ti–N3, 2.0709(9); Ti–O2, 2.0190(7); Ti–N5, 2.2889(9); Ti–Cl1: 2.3751(3); C1–N1, 1.334(1); C1–O1, 1.297(1); C1–N2, 1.343(1); N1–Ti–O1, 63.63(3); Cl1–Ti–Cl2, 172.46(1); sum of angles about N2, 359.8(3); O1–C1–N2–C5, 13.8(2).....46

Figure 2.12. ORTEP representation of the molecular structure of **93** (ellipsoids plotted at 50% probability, hydrogens except H999 not shown, H999 located from unassigned electron density and its position refined) with selected bond lengths (Å), bond and torsion angles (°): Zr–N1, 2.170(1); Zr–O1, 2.176(1); Zr–N5, 2.445(2); Zr–Cl1: 2.4846(5); C1–N1, 1.332(2); C1–O1, 1.310(2); C1–N2, 1.345(2); N1–Zr–O1, 60.19(3); Cl1–Zr–Cl2, 162.98(2); sum of angles about N2, 359.9(3); O1–C1–N2–C5, 12.0(2).....48

Figure 2.13. ORTEP representation of the molecular structure of **95** (ellipsoids plotted at 50% probability, hydrogens and all but *ipso*-carbons of aromatic groups removed for clarity, disordered pentane solvent removed with SQUEEZE routine¹⁷³) with selected bond lengths (Å), bond and torsion angles (°): Zr–N1, 2.401(2); Zr–N3, 2.276(3); Zr–N5, 2.359(2); Zr–O1, 2.134(1); Zr–O2, 2.199(2); Zr–O3, 2.136(2); Zr–C55, 2.279(3); C1–N1, 1.325(3); C1–O1, 1.309(3); C1–N2, 1.354(2); average ureate bite angle, 58.13(8); average angle between C–Zr–C', 109.2(9); sum of angles about N2, N4, N6: 359.9(6), 354.4(6), 355.6(9); N1–C1–N2–C14: 19.7(4).....51

Figure 2.14. ORTEP representation of the molecular structure of **97** (ellipsoids plotted at 50% probability, hydrogens removed for clarity) with selected bond lengths (Å), bond and torsion angles (°): Zr–N1, 2.193(2); Zr–N3, 2.183(1); Zr–O1, 2.208(1); Zr–O2, 2.240(1); Zr–C20, 2.266(2); Zr–C25, 2.259(2); C1–N1, 1.331(2); C1–O1, 1.295(2); C1–N2, 1.351(2); N1–Zr–O1, 59.32(4); N1–Zr–N3, 76.33(5); average angle between C–Zr–C', 109.3(6); Zr–C20–C21, 123.8(1); Zr–C25–C26, 130.7(1); sum of angles about N2, N4: 359.5(3), 359.2(3); N1–C1–N2–C5: 14.7(3).....55

Figure 2.15. ORTEP representation of the molecular structure of **98** (left) and abbreviated structure showing η^2 -benzyl interaction (right) (ellipsoids plotted at 50% probability, hydrogens removed for clarity) with selected bond lengths (Å), bond and torsion angles (°): Zr–N1, 2.195(1); Zr–N3, 2.183(1); Zr–O1, 2.221(1); Zr–O2, 2.257(1); Zr–C25, 2.265(2); Zr–C29, 2.282(2); C1–N1, 1.334(2); C1–O1, 1.294(2); C1–N2, 1.346(2); N1–Zr–O1, 59.31(5); N1–Zr–N3, 75.34(5); average angle between C–Zr–C', 109.8(6); Zr–C29–C230, 109.8(1); Zr–C36–C37, 92.6(1); sum of angles about N2, N4: 359.6(3), 359.2(3); N1–C1–N2–C5: 14.3(3).....57

Figure 2.16. ORTEP representation of the molecular structure of **96•py** (ellipsoids plotted at 50% probability, hydrogens and pentane solvent removed for clarity) with selected bond lengths (Å), bond and torsion angles (°): Zr–N1, 2.177(2); Zr–N3, 2.186(1); Zr–N5, 2.397(2); Zr–O1, 2.216(1); Zr–O2, 2.197(2); Zr–C20, 2.365(2); Zr–C27, 2.373(2); C1–N1, 1.326(2); C1–O1, 1.300(2); C1–N2, 1.360(3); N1–Zr–O1, 59.49(6); N1–Zr–N3, 77.56(6); C20–Zr–C27, 156.54(8); C20–Zr–N5, 80.02(7); C27–Zr–N5, 76.59(7); Zr–C20–C21, 126.7(2); Zr–C27–C28, 108.2(1); sum of angles about N2, N4: 359.8(6), 360.0(6); N1–C1–N2–C2: 22.9(3).....59

Figure 2.17. ORTEP representation of the molecular structure of **98**•py (ellipsoids plotted at 50% probability, hydrogens removed for clarity) with selected bond lengths (Å), bond and torsion angles (°): Zr–N1, 2.200(1); Zr–N3, 2.378(1); Zr–O1, 2.1965(9); Zr–C8, 2.350(1); C1–N1, 1.356(2); C1–O1, 1.283(2); C1–N2, 1.337(2); N1–Zr–O1, 60.06(4); N1–Zr–N1*, 79.13(4); C8–Zr–C8*, 154.83(5); C8–Zr–N3, 77.42(5); Zr–C8–C9, 117.3(1); sum of angles about N2: 359.4(3); N1–C1–N2–C5: 20.4(2); C18–C23–C23*–C18*, 68.5(2).....60

Figure 2.18. *Top:* bis(amidato) complexes with high activity (>100) in the polymerization of ethylene. *Bottom:* complexes exhibiting low to no activity (<10)....61

Figure 3.1. Representative intra- and intermolecular hydroamination reactions of alkynes and alkenes; new bonds formed indicated in red, new stereogenic centers with asterisks.....67

Figure 3.2. Metallocene-based rare-earth hydroamination precatalysts.....69

Figure 3.3. Challenging transformations achieved with rare-earth metallocene catalysts71

Figure 3.4. Post-metallocene rare-earth catalysts.....72

Figure 3.5. Effective ligands for late metal catalyzed hydroamination.....74

Figure 3.6. Successful group 4 precatalysts for the hydroamination of alkenes.....77

Figure 3.7. Cationic (left) and neutral (right) group 4 precatalysts capable of hydroamination with secondary amines.....80

Figure 3.8. Non-tethered bis(ureato) precatalysts with bis(amidato) analogues.....83

Figure 3.9. ORTEP representation of the molecular structure of **89** (ellipsoids plotted at 50% probability, hydrogens omitted for clarity, one orientation of NMe₂ ligands shown) with selected bond lengths (Å), bond and torsion angles (°): Ti–N1, 2.102(2); Ti–O1, 2.125(2); Ti–N3, 1.910(2); C1–N1, 1.327(2); C1–O1, 1.292(3); C1–N2, 1.355(3); N1–Ti–O1, 61.92(6); N1–Ti–N1*, 149.92(7); sum of angles about N2, 359.6(6); N1–C1–N2–C5, 18.1(3).....84

Figure 3.10. ORTEP representation of the molecular structure of **159** (ellipsoids plotted at 50% probability, hydrogens omitted for clarity) with selected bond lengths (Å), bond and torsion angles (°): Zr–N1, 2.253(2); Zr–O1, 2.222(1); Zr–N3, 2.059(2); C1–N1, 1.335(2); C1–O1, 1.301(2); C1–N2, 1.348(2); N1–Zr–O1, 58.61(5); N1–Zr–N1*, 149.38(8); sum of angles about N2, 359.8(5); sum of angles about N3, 355.6(5); N1–C1–N2–C3, 16.8(3).....85

Figure 3.11. ORTEP representation of the molecular structure of **160** (ellipsoids plotted at 50% probability, hydrogens omitted for clarity) with selected bond lengths (Å), bond and torsion angles (°): Ti–N1, 2.086(1); Ti–O1, 2.141(1); Ti–N5, 1.913(1); C1–N1, 1.337(2); C1–O1, 1.284(2); C1–N2, 1.347(2); N1–Ti–O1, 62.36(5); N1–Ti–N3, 141.63(6); sum of angles about N2, 358.3(6); sum of angles about N5, 359.7(4); O2–C19–N4–C36, 0.9(2).....86

Figure 3.12. ORTEP representation of the molecular structure of **161** (ellipsoids plotted at 50% probability, hydrogens omitted for clarity) with selected bond lengths (Å), bond and torsion angles (°): Zr–N1, 2.244(2); Zr–O1, 2.240(2); Zr–N3, 2.051(3); C1–N1, 1.336(3); C1–O1, 1.292(3); C1–N2, 1.353(3); N1–Zr–O1, 58.70(8); N1–Zr–N4, 141.03(8); sum of angles about N2, 357.4(7); sum of angles about N3, 359.5(6); O1–C1–N2–C18, 2.8(4); N1–C1–N2–C14, 22.0(4).....87

Figure 3.13. Structural comparison of non-tethered precatalysts.....88

Figure 3.14. Tethered bis(ureato) and bis(amidato) precatalysts under investigation...91

Figure 3.15. ORTEP representation of the molecular structure of **166** (ellipsoids plotted at 50% probability, hydrogens omitted for clarity) with selected bond lengths (Å), bond and torsion angles (°): Ti–N1, 2.071(3); Ti–O1, 2.156(2); Ti–N5, 1.928(3); Ti–N6, 1.917(3); C1–N1, 1.338(4); C1–O1, 1.279(6); C1–N2, 1.352(5); N1–Ti–O1, 61.7(1); N1–Ti–N3, 78.8(1); N5–Ti–N6, 122.4(1); sum of angles about N2, 359.5(9); sum of angles about N3, 358.1(7); N1–C1–N2–C2, 25.7(6).....93

Figure 3.16. ORTEP representation of the molecular structure of **167** (ellipsoids plotted at 50% probability, hydrogens omitted for clarity) with selected bond lengths (Å), bond and torsion angles (°): Zr–N1, 2.280(1); Zr–O1, 2.240(1); Zr–N5, 2.092(2); Zr–N6, 2.135(1); Zr–N7, 2.503(2); C1–N1, 1.320(2); C1–O1, 1.308(2); C1–N2, 1.371(2); N1–Zr–O1, 57.91(5); N1–Zr–N3, 74.45(5); N5–Zr–N7, 175.19(6); sum of angles about N2, 359.7(6); sum of angles about N3, 355.6(5); N1–C1–N2–C3, 16.8(3).....94

Figure 3.17. Hydroamination of alkynes using precatalyst **167**.....102

Figure 3.18. Cyclization of aminoalkenes using precatalyst **167**.....104

Figure 4.1. Azametallacyclobutenes of the group 4 metals formed by formal [2+2] cycloaddition between metal-imido bonds and alkynes.....111

Figure 4.2. Azametallacyclobutanes of the group 4 metals formed by formal [2+2] cycloaddition between metal-imido bonds and allenes (top) or alkenes (bottom).....112

Figure 4.3. ORTEP representation of the molecular structure of **274** (ellipsoids plotted at 50% probability, hydrogens omitted) with selected bond lengths (Å), bond and torsion angles (°): Zr–N1, 2.224(3); Zr–O1, 2.248(3); Zr–N5, 2.067(3); Zr–N6, 2.097(3); Zr–N7, 2.508(3); C1–N1, 1.299(5); C1–O1, 1.288(4); C1–N2, 1.362(5); N1–Zr–O1, 57.7(1); N5–Zr–N7, 173.8(1); N3–C8–N4–C9: 24.0(6).....120

Figure 4.4. ORTEP representation of the molecular structure of **275** (ellipsoids plotted at 50% probability, hydrogens omitted) with selected bond lengths (Å), bond and torsion angles (°): Zr–N1, 2.241(1); Zr–O1, 2.226(1); Zr–N5, 2.108(1); Zr–N6, 2.323(1); Zr–N6*, 2.374(1); C1–N1, 1.312(2); C1–O2, 1.296(2); C1–N3, 1.373(2); N1–Zr–O2, 58.37(4); N1–Zr–N2, 74.43(4); N5–Zr–N6, 93.69(4); N5–Zr–N6*, 170.01(4); N6–Zr–N6*, 76.34(4); Zr–N6–Zr*, 103.66(4); N1–C1–N3–C8, 44.1(2).....121

Figure 4.5. Thermally induced ligand disproportionation of zirconium hydroamination precatalysts supported by tethered ligands.....122

Figure 4.6. ORTEP representation of the molecular structure of **285** (ellipsoids plotted at 50% probability, hydrogens omitted) with selected bond lengths (Å), bond and torsion angles (°): Zr–N1, 1.891(3); Zr–N2, 2.245(3); Zr–O1, 2.244(2); Zr–N6, 2.579(3); Zr–N7, 2.375(3); C13–N2, 1.322(4); C13–O1, 1.290(4); C13–N4, 1.369(4); N2–Zr–O1, 58.44(9); Zr–N1–C1, 177.6(3); O1–C13–N4–C14, 20.2(5).....127

Figure 4.7. ORTEP representation of the molecular structure of **286** (ellipsoids plotted at 50% probability, hydrogens and NiPr₂ groups omitted) with selected bond lengths (Å), bond and torsion angles (°): Zr1–N1, 2.279(1); Zr1–N3, 2.243(1); Zr1–O1, 2.147(1); Zr1–O2, 2.192(1); Zr1–N9, 2.073(1); Zr2–N9, 2.125(1); Zr1–N10, 2.080(1); Zr2–N10, 2.089(1); C1–N1, 1.312(2); C1–O1, 1.314(2); C1–N2, 1.360(2); N1–Zr1–O1, 59.25(5); N1–Zr1–N3, 78.46(5); C1–Zr1–C13, 105.31(5); C1–Zr1–N9, 122.89(5); C1–Zr1–N10, 107.50(5); N9–Zr1–N10, 80.36(5); Zr1–N9–Zr2, 97.97(6).....129

Figure 4.8. ORTEP representation of the molecular structure of **287** (ellipsoids plotted at 50% probability, hydrogens omitted) with selected bond lengths (Å), bond and torsion angles (°): Zr–N1, 2.2455(9); Zr–O1, 2.2373(8); Zr–N5, 2.1653(9); Zr–N5*, 2.0338(9); Zr–N6, 2.557(1); C1–N1, 1.321(1); C1–O1, 1.291(1); C1–N2, 1.361(1); N1–Zr–O1, 57.91(3); N1–Zr–N3, 74.21(4); N5–Zr–N6, 87.17(4); N5–Zr–N6*, 166.70(4); N5–Zr–N5*, 79.84(4); Zr–N6–Zr*, 100.16(4); N1–C1–N2–C5, 15.2(2); N3–C8–N4–C12, 42.6(2).....131

Figure 4.9. ORTEP representation of the molecular structure of **288** (ellipsoids plotted at 50% probability, hydrogens and methyls from isopropyl groups omitted) with selected bond lengths (Å), bond and torsion angles (°): Zr–N1, 2.208(1); Zr–N2, 2.188(2); Zr–N5, 2.443(1); Zr–N6, 2.087(2); Zr–C20, 2.324(2); Zr–O1, 2.200(1); Zr–O2, 2.227(1); C1–N1, 1.330(2); C1–O1, 1.296(2); C1–N3, 1.371(2); C20–C27, 1.326(2); C27–N5, 1.477(3); N1–Zr–O1, 59.28(5); N1–Zr–N2, 77.28(5); N5–Zr–C20, 58.25(6); N6–Zr–C20, 148.10(6); N1–C1–N3–C2, 20.4(3).....136

Figure 4.10. ORTEP representation of the asymmetric unit of **289** (left) and of one of three independent molecules (right) (ellipsoids plotted at 50% probability, hydrogens and methyls from isopropyl groups omitted) with selected bond lengths (Å), bond and torsion angles (°) averaged over three molecules: Zr–N1, 2.191(2); Zr–N2, 2.203(2); Zr–N5, 2.440(2); Zr–N6, 2.099(2); Zr–C20, 2.333(2); Zr–O1, 2.214(2); Zr–O2, 2.204(2); C1–N1, 1.327(3); C1–O1, 1.302(3); C1–N3, 1.352(3); C20–C27, 1.332(3); C27–N5, 1.488(3); N1–Zr–O1, 59.24(6); N1–Zr–N2, 77.69(7); N5–Zr–C20, 58.44(7); N6–Zr–C20, 149.00(8); N1–C1–N3–C2, 20.2(4).....137

Figure 4.11. Plot of the consumption of aminoalkene substrates (c/c_0) versus time (min) through three (top) or five (bottom) half-lives. Red data points indicate exponential decay regime (not included in linear regression analysis). Error bars indicate $\pm 5\%$142

Figure 4.12. *Top:* Plot of the consumption of **131** (c/c_0) versus time (min) with added 2-methylpiperidine (0.750 to 4.50 M), error bars indicate $\pm 5\%$. *Bottom:* Plot of $\ln(c/c_0)$ versus time (min) for same reactions.....144

Figure 4.13. Plot of k_{obs} versus concentration of 2-methylpiperidine (M) showing zero-order dependence over a six-fold concentration range. Error bars represent standard errors from Table 4.1.....146

Figure 4.14. Effect of *N*-substitution on cyclization rate: statistically identical rates for primary and secondary aminoalkenes (top); primary kinetic isotope effect (bottom). Error bars indicate $\pm 5\%$148

Figure 4.15. Plot of k_{obs} (min^{-1}) versus [precatalyst] (M), showing first-order dependence up to ~ 0.15 M. Error bars from estimated errors tabulated in Table 4.2.....150

Figure 4.16. Eyring plot in the temperature range 90–105 °C; activation parameters as indicated. Error bars from estimated errors tabulated in Table 4.3; error on activation parameters estimated from regression analysis.....152

Figure 4.17. Possible active (*A*) and inactive (*C*) catalytic intermediates in the cyclization of **131**.....158

Figure 4.18. Determination of ΔH° and ΔS° values for the pictured equilibrium by van't Hoff analysis.....161

Figure 5.1. Two views of the ORTEP representation of the molecular structure of (\pm)-**307** (ellipsoids plotted at 50% probability, hydrogens omitted for clarity) with selected bond lengths (Å), bond and torsion angles (°): Zr–N1, 2.320(2); Zr–O1, 2.235(2); Zr–N5, 2.054(2); Zr–N7, 2.464(2); C1–N1, 1.336(3); C1–O1, 1.280(3); C1–N2, 1.346(3); N1–Zr–O1, 57.54(6); N1–Zr–N3, 77.71(6); N5–Zr–N7, 173.60(7); N1–C1–N2–C5, 15.9(3); C24–C29–C31–C32, 74.9(3).....171

Figure 5.2. Enantioselective hydroamination with homochiral precatalyst 306 (derived from (-)-enantiomer of 2,2'-diamino-6,6'-dimethylbiphenyl).....	171
Figure 5.3. Potential urea proligands incorporating chirality in secondary amino group.....	173
Figure A.1. Proposed catalytic cycle (reproduced from Scheme 4.11, Chapter Four)	234

LIST OF SCHEMES

Scheme 1.1. Comparison of resonance forms of monoanionic amidates and ureates.....	6
Scheme 1.2. Group 6 ureate complexes formed <i>via</i> isocyanate insertion.....	10
Scheme 1.3. Formation of unexpected chromium complex 26	11
Scheme 1.4. Isocyanate insertion into rhenium– and platinum–amido bonds.....	12
Scheme 1.5. Preparation of the first ureate-supported group 4 metal complexes.....	13
Scheme 1.6. Multiple isocyanate insertions at a single zirconium center; catalytic cyclotrimerization of phenylisocyanate.....	14
Scheme 1.7. Synthesis of ureate-supported hafnium complexes <i>via</i> isocyanate insertion.....	15
Scheme 1.8. Salt metathesis and protonolysis routes to ureate complexes.....	16
Scheme 1.9. Synthesis of a manganese ureate complex by transmetallation with a tin reagent.....	17
Scheme 1.10. Stabilization of mononuclear iron(oxo) and iron(hydroxo) species by ureate ligands (potassium counterions omitted for clarity).....	18
Scheme 1.11. Formation of an ytterbium ureate (64) by protonolysis and subsequent reaction with arylisocyanates; comparison to isocyanate insertion.....	20
Scheme 2.1. Simplified coordination-insertion mechanism for olefin polymerization..	26
Scheme 2.2. Synthesis of 90 <i>via</i> two routes.....	39
Scheme 2.3. Synthesis of dibenzyl complex 94 and unexpected formation of tris(ureato) 95	50
Scheme 4.1. Simplified pathways for metal-catalyzed hydroamination; top two routes common for early transition metals, bottom two for late transition metals.....	108

Scheme 4.2. Proposed mechanisms for the hydroamination of alkynes with zirconocene (198 , left) and titanocene (3 , right) precatalysts; formation of imido species.....	109
Scheme 4.3. Originally proposed concerted insertion/protonolysis transition-state, accounting for primary KIE in lanthanide-catalyzed aminoalkene hydroamination....	113
Scheme 4.4. Proposed σ -bond insertion mechanism for the hydroamination of primary or secondary aminoalkenes for constrained geometry zirconium precatalysts 156 and 157	114
Scheme 4.5. Characterized alkyne (top) and alkene (bottom) insertion products.....	115
Scheme 4.6. Proposed mechanism for the hydroaminoalkylation of primary aminoalkenes by zirconium precatalyst 143 ; synthesis and solid-state molecular structure of dinuclear titanaaziridine 273	117
Scheme 4.7. Replacement and removal of neutral donors from complex 167	119
Scheme 4.8. Synthesis of mononuclear (285) and dimeric (286) imido complexes through aminolysis of dibenzyl compound 96	126
Scheme 4.9. Chelate effect rationale for hydroamination chemoselectivity by tethered precatalyst 167	132
Scheme 4.10. Attempted intramolecular alkene insertion reactions; evidence for proton-assisted insertion.....	140
Scheme 4.11. Simplified proposed catalytic cycle for intramolecular alkene hydroamination using 167 , with derived differential rate law (steady-state approximation for $[A]$, $[B]$, and $[C]$).....	156
Scheme 5.1. Synthesis of biaryl tethered hydroamination precatalysts.....	170
Scheme 5.2. Proposed synthesis of chiral tethered hydroamination precatalysts.....	172
Scheme 5.3. Proposed synthesis of axially substituted hydroamination precatalysts..	174
Scheme 5.4. Observation of phenylacetylene homocoupling with precatalyst 167	177

LIST OF ABBREVIATIONS AND ACRONYMS

<i>A</i>	olefin polymerization activity ($\text{g mmol}^{-1} \text{ bar}^{-1} \text{ h}^{-1}$)
Å	angstrom (10^{-10} m)
Ac	acetyl
anal.	analysis
Ar	aryl
Bn	benzyl
Boc	<i>tert</i> -butoxycarbonyl
br	broad
<i>c</i>	concentration
cal	calorie
calcd.	calculated
COD	cyclooctadiene
conv.	conversion
Cp	cyclopentadienyl
Cp*	pentamethylcyclopentadienyl
Cy	cyclohexyl
d	doublet
<i>d</i>	deuterium
δ	chemical shift
Da	dalton

DCM	dichloromethane
DFT	density functional theory
ΔG^\ddagger	Gibbs free energy of activation
ΔH°	standard enthalpy change
ΔH^\ddagger	enthalpy of activation
DEPT	distortionless enhancement by polarization transfer
DIPEA	diisopropylethylamine
DMA	dimethylacetamide
DME	1,2-dimethoxyethane
DMSO	dimethylsulfoxide
dr	diastereomeric ratio
ΔS°	standard entropy change
ΔS^\ddagger	entropy of activation
e	electronic charge
ee	enantiomeric excess
EI	electron impact
equiv.	equivalent(s)
ESI	electrospray ionization
Et	ethyl
e.u.	entropy units ($\text{cal K}^{-1} \text{mol}^{-1}$)
F_w	formula weight
<i>gem</i>	geminal
HSAB	hard/soft acid/base

HMDS	hexamethyldisilazane ($\text{N}(\text{SiMe}_3)_2$)
HRMS	high resolution mass spectrometry
<i>i</i> -Bu	isobutyl
<i>i</i> -Pr	isopropyl
IR	infrared
<i>J</i>	coupling constant
K_a	acid dissociation constant
K_{eq}	equilibrium constant
KIE	kinetic isotope effect
k_n	rate constant
L	supporting ligand
L_n	ligand set
Ln	rare-earth metal
M	multiplet
M	metal
M^+	molecular ion
μ	absorption coefficient (X-ray crystallography)
MAO	methylaluminumoxane
Me	methyl
Mes	mesityl
M_n	number average molecular weight
MOCVD	metal organic chemical vapour deposition
MS	mass spectrometry

M_w	weight average molecular weight
m/z	mass-to-charge ratio
ν	frequency
NBO	natural bonding orbital
NMR	nuclear magnetic resonance
no.	number
ORTEP	Oak Ridge thermal ellipsoid plot
p	$-\log$ (as in pK_a)
PDI	polydispersity index (M_w / M_n)
Ph	phenyl
ppm	parts per million
precat.	precatalyst
psi	pounds per square inch
p -tol	<i>para</i> -tolyl
Py, py	pyridine / pyridyl
q	quartet
R	organic substituent
ρ	density
reflns	reflections
rpm	rotations per minute
rt	room temperature
s	singlet
sept	septet

t	triplet
<i>t</i> -Bu	<i>tert</i> -butyl
T_c	coalescence temperature
<i>tert</i>	tertiary
TFA	trifluoroacetic acid
THF	tetrahydrofuran
TOF	turnover frequency
Tp	tris(pyrazolyl)borate
Tp*	tris(3,5-dimethylpyrazolyl)borate
Ts	tosyl, <i>para</i> -toluenesulfonyl
UHMWPE	ultra-high molecular weight polyethylene
v/v	volume per volume
w/w	weight per weight
X	halide
xyl	xylyl, 3,5-dimethylphenyl

ACKNOWLEDGEMENTS

I am deeply indebted to many people and organizations that have contributed to the assembly of this work. First, I would like to thank Dr. Michael Wolf, Dr. Peter Legzdins, and Courtney Turner for taking the time to read this thesis prior to submission. Their comments have certainly improved the quality of this document. Second, I would like to acknowledge the various funding agencies that have supported my research: the University of British Columbia, the Natural Sciences and Engineering Research Council of Canada, Imperial Oil Ltd., Boehringer Ingelheim Ltd, and the American Chemical Society.

I would also like to thank the many collaborators that have assisted with my research. Dr. Douglas Stephan and the Stephan research group at the University of Toronto generously provided laboratory space, equipment use, and expertise that enabled me to carry out ethylene polymerization reactions. The entire Schafer research group, past to present, deserves particular distinction for sharing space, ideas, and mishaps with me over the past five years: Chun-Yu, Dave Beard, Kevin, Rob, Ali, Frank, Leon, Rashidat, Louisa, Jason, Mark, Johanna, Charles, Wen, Courtney, Neal, Scott, JM, Jakie, Patrick, Chin, Andrey, Philippa, Chris, Christine, Rémy, Hope, Patri, Rachel, Eugene, and Jacky. It has been a privilege and a pleasure to have worked alongside all of you.

Finally, and most importantly, I would like to thank my supervisor, Dr. Laurel Schafer, for leading one of the best research groups in the world. I hope that our research approaches the “great things” you felt we should accomplish.

DEDICATION

This thesis is dedicated
To someone who has filled my life with love
Someone who has infinite patience
Someone who has shared with me all of the highest points
And stuck with me through all of the lowest depths.

This thesis is dedicated
To my beautiful wife
Tamsin Elizabeth Mulvogue.

You change all the lead
Sleeping in my head
To gold.

CHAPTER 1. Ureates as Modular Supporting Ligands for Group 4 Chemistry

1.1 The “Post-Metallocene” Era

Since the serendipitous synthesis^{1,2} and subsequent structural elucidation^{3,4} of ferrocene in the early 1950s,⁵ metal complexes containing cyclopentadienyl (Cp) ligands, and derivatives thereof, have dominated the field of organometallic chemistry.⁶ This is particularly true for the group 4 metals, with bis(cyclopentadienyl) titanium, zirconium, and hafnium fragments representing enduring structural motifs (Figure 1.1).⁷⁻¹³ Synthesis of the first group 4 “metallocene,” the prototypical Cp_2ZrBr_2 (**1**), was reported in 1953 by Wilkinson, Pauson, Birmingham, and Cotton.⁷ Unfortunately, the synthetic potential of these compounds remained largely unrealized until the discovery of the hydrozirconation reaction using $\text{Cp}_2\text{Zr(H)(Cl)}$ (**4**). Hydrozirconation, first reported by Wailes¹⁴ and subsequently popularized by Schwartz,¹⁵ transforms alkynes and alkenes into organozirconium compounds that are versatile synthetic intermediates.¹⁶ This development sparked wide interest into the use of group 4 metallocenes in organic synthesis.¹⁷ Many other reactions have since been developed, including carboalumination using catalytic zirconocene dichloride (**2**),¹⁸ olefination using the Tebbe (**5**)¹¹ or Petasis (**3**)¹⁹ reagents, and reductive coupling using the Rosenthal reagent (**6**).^{12,20} Perhaps the most significant use of group 4 metallocenes is in the production of polyolefins, a multi-billion dollar global industry; this facet of group 4 based catalysis will be reviewed in Chapter Two.

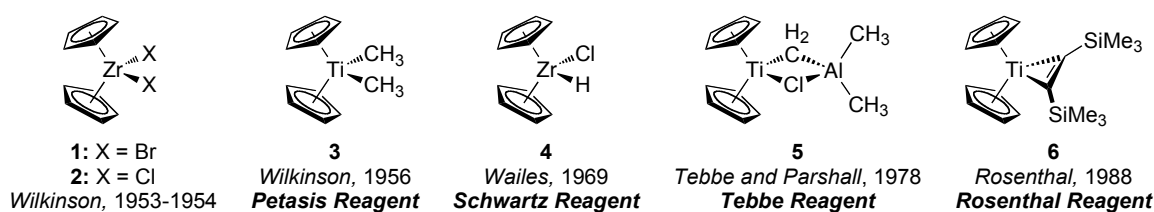


Figure 1.1. Prototypical group 4 metallocene compounds.

Despite the richness of group 4 metallocene chemistry,^{13,21,22} a reliance on Cp as a ligand framework limits the scope of developing new reactivity. Therefore, many researchers have shifted focus to other anionic supporting ligands, taking advantage of flexible organic structural moieties that offer a more modular approach to ligand design. In this sense, adjustment of metal center reactivity is simply a matter of changing one ligand substituent for another, something that can be laborious to accomplish with Cp.^{21,23} This “post-metallocene” trend is particularly prevalent with regard to early transition metals.²⁴⁻²⁷ Several common anion classes are portrayed below in Figure 1.2;²⁸⁻⁴³ this list is not exhaustive. Nearly all non-Cp ligands used for group 4 metals are based on oxygen and/or nitrogen as donor atoms. These hard bases form strong bonds with the hard metal centers, resulting in robust metal–ligand interactions.⁴⁴

While structurally simple, these ligand classes have been incorporated into diverse and complicated architectures. Common design motifs include linking individual anions together to form chelating structures,^{27,45-56} the addition of neutral donors to augment the metal–ligand interaction,^{27,45-47,49, 53,54,57,58} the introduction of chirality through choice of organic substituents,^{48,49,55,59} and the combination of several anion classes into a single ligand framework.^{27,60} These multiple permutations lead to literally endless structural possibilities. As a result, the depth of reactivity exhibited by non-metallocene compounds is immense.

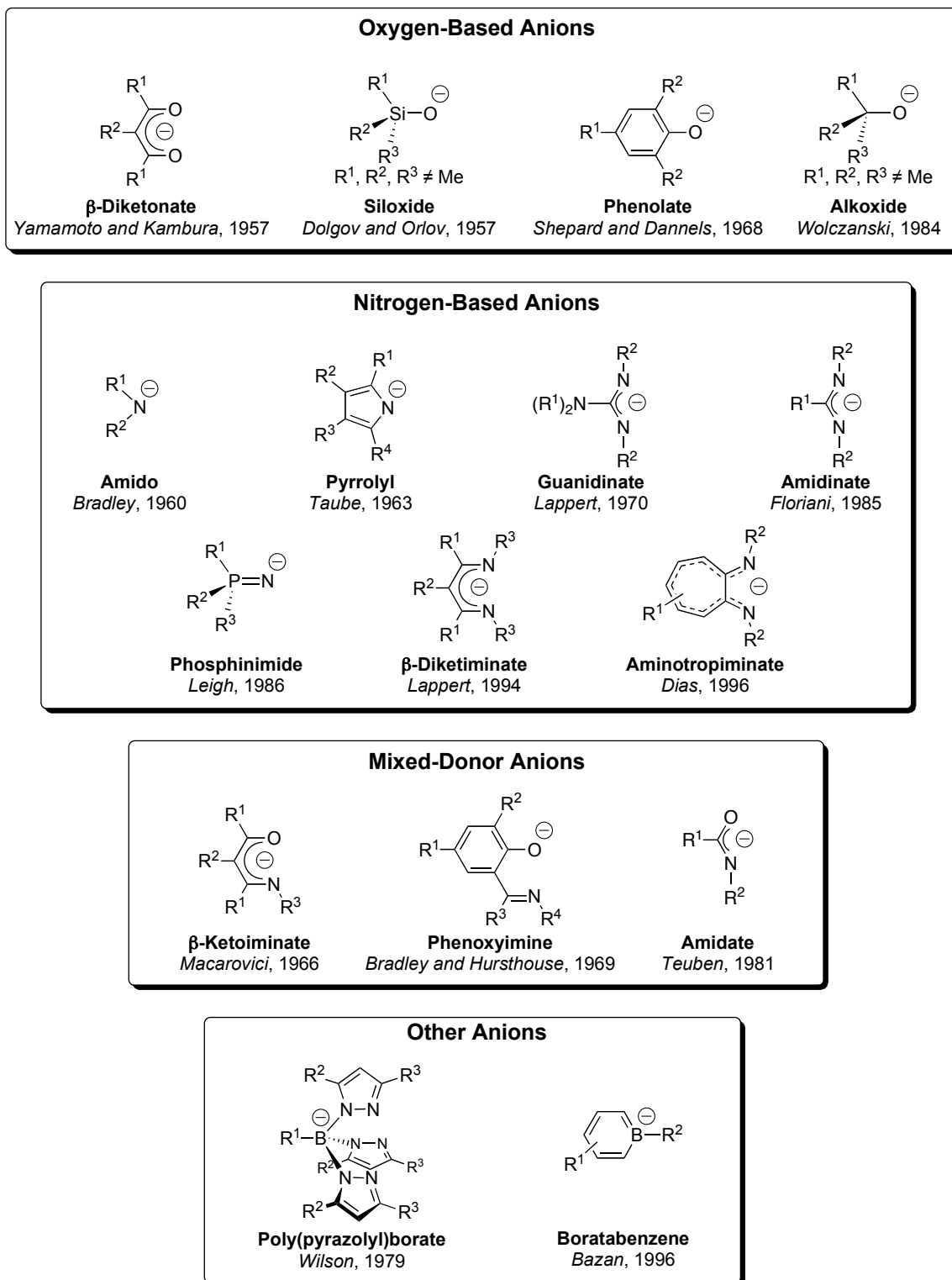


Figure 1.2. Examples of non-Cp ligand classes used in group 4 chemistry; names and years reflect first report of use as ligand on titanium, zirconium, or hafnium.

Figure 1.3 illustrates some of the remarkable feats accomplished by non-Cp group 4 complexes. A landmark contribution, published in 1997 by Fryzuk and co-workers, describes the use of macrocyclic amido ligands to support a zirconium dinitrogen complex (**7**).⁶¹ This compound reacts with dihydrogen to form **8**, enabling the functionalization of one of the most inert molecules known. More recently, Mindiola and co-workers reported evidence for the first and thus far only example of a group 4 alkylidyne (**10**), generated from an alkylidene precursor (**9**).⁶² This highly reactive species induces a ring-opening dearomatization of pyridine *via* C–H activation (**11**).⁶³ Matsuo and Kawaguchi have developed a bis(phenolate) zirconium catalyst (**12**) for the reduction of carbon dioxide to methane.⁶⁴ Finally, Abu-Omar and co-workers, through the use of redox-active enediamido ligands, were able to effect a *pseudo*-oxidative addition of dioxygen to a d^0 -zirconium center (**13**) to form a bis(peroxide) complex (**14**).⁶⁵

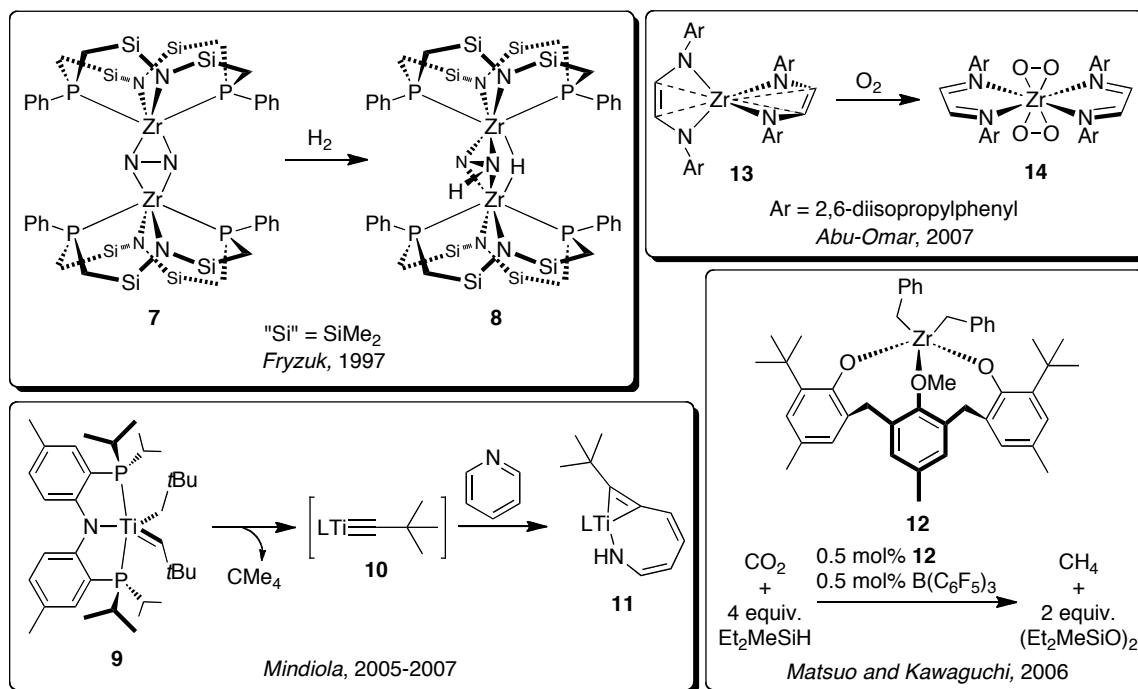


Figure 1.3. Small molecule activation by non-metallocene group 4 complexes.

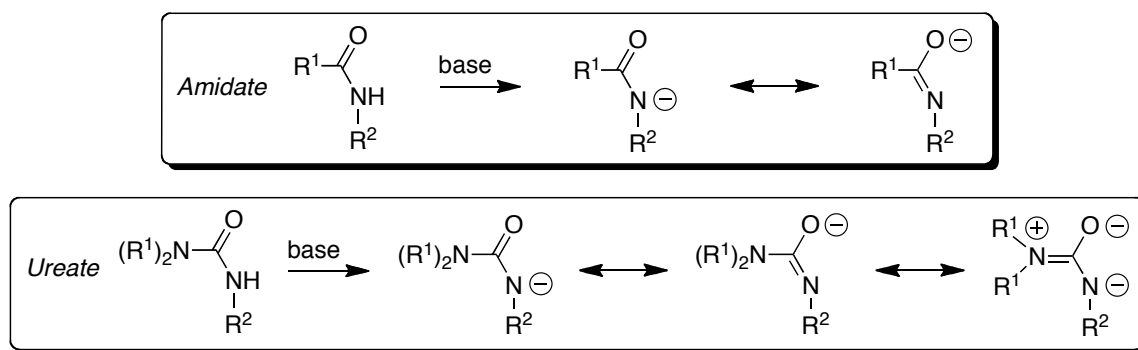
Due to the large body of literature concerning the use of non-Cp supporting ligands for group 4 complexes, an extended discussion of these widely varied systems is beyond the scope of this thesis. The interested reader is instead directed to a plethora of excellent review articles that cover all aspects of this chemistry.^{24-27,45-60,66-80} The following sections will instead focus on the ureate ligand set, and evaluate its potential as a robust and modular support for group 4 organometallic complexes. Section 1.2 will introduce ureate ligands through a general overview of their steric and electronic properties, and a comparison with structurally similar amidate ligands. Section 1.3 will discuss previous work to prepare ureate complexes by the insertion of isocyanates into metal–amido bonds, and demonstrate the need for an alternate synthetic approach. Section 1.4 will present precedent for two such alternatives, involving the use of ureas as proligands for ureate preparation. Finally, Section 1.5 will outline the scope of the research reported herein with regard to the synthesis, characterization, and reactivity of group 4 ureate complexes.

1.2 The Ureate Ligand Set

As many supporting ligands used in organometallic chemistry are anions generated from neutral organic precursors, ureates are formed through deprotonation of an appropriately substituted urea. Due to their structural diversity and ease of preparation, ureas are ideal as a modular class of proligands for application in organometallic chemistry. Furthermore, ureate anions can easily be either mono- or dibasic, depending on the substitution pattern and degree of deprotonation. The following discussion will deal exclusively with ureate monoanions, as these are the focus of later chapters.

Ureate ligands are closely related to amidates, another modular ligand class that is being used in group 4 chemistry.⁸¹ Both of these ligand sets are based on easily accessible organic precursors, and as a result can be made sterically analogous. However, there is one major difference between the two ligands. Scheme 1.1 illustrates generic amidate and ureate anions resulting from proligand deprotonation, and the possible resonance forms these anions can adopt. While amidates can delocalize negative charge between the two potential donor atoms, ureates have an amino group attached to the central carbon that can engage in resonance with the main N–C–O framework.

Scheme 1.1. Comparison of resonance forms of monoanionic amidates and ureates.



The consequences of the increased ureate delocalization are two-fold. First, these ligands are anticipated to be more electron-rich than their amidate counterparts, due to possible π -electron donation from the disubstituted amino group (Scheme 1.1, far right structure). In order for this donation to occur, the distal nitrogen atom must adopt a planar, sp^2 -hybridized geometry, and orient itself to be co-planar with the N–C–O plane (Figure 1.4). This feature of the ureate framework allows one, in principle, to modulate the degree of electron donation by altering the size of the R^1 -substituents. Small groups in this position will allow the required co-planar arrangement; however, large groups will inhibit such an orientation through steric repulsion, effectively preventing any electron donation.

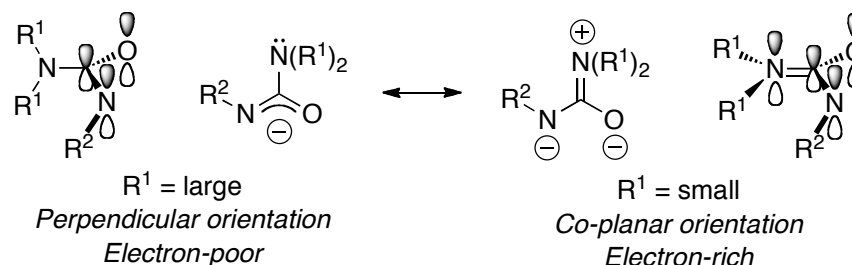


Figure 1.4. Stereoelectronic forms of ureate anions.

Steric control of this π -electron donation is known for related systems: group 4 complexes supported by guanidinate ligands exhibit this effect (**15** and **16**, Figure 1.5).^{82,83} X-ray crystallography indicates that the bulky amino groups of complex **15** sit perpendicular to the N–C–N chelate plane.⁸² In contrast, the dimethylamino substituents of complex **16** adopt co-planar orientations with shorter C–N bond lengths, indicating electron donation.⁸³ The differing electronic properties of the guanidinate ligands of **15** and **16** also influence metal–guanidinate bonding. The Zr–N distances of **15** are, on average, 0.036(7) Å longer than those of **16**; a small but statistically significant

difference. Furthermore, the average guanidinate bite angle of **15** is $1.1(2)^\circ$ smaller than that for **16**. These metrical data suggest that the guanidates of **16** are more tightly bound to zirconium, as anticipated for a more electron-rich ligand.

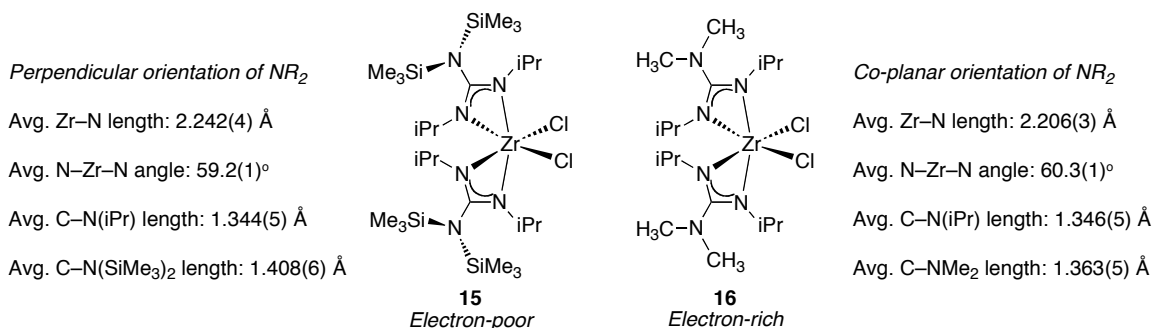


Figure 1.5. Steric attenuation of guanidinate electron donation.

The second consequence of ureate resonance is that the delocalization of negative charge enables these ligands to adopt a wide variety of coordination modes. Several of these modes, with the ureate bound to either one or two metal centers, are illustrated in Figure 1.6; the mononuclear κ^2 -*N,O* mode, commonly observed for group 4 amidate complexes,⁸¹ is highlighted. Due to the presence of an extra potential donor atom, there are more possible coordination isomers for ureates than for analogous amidates.

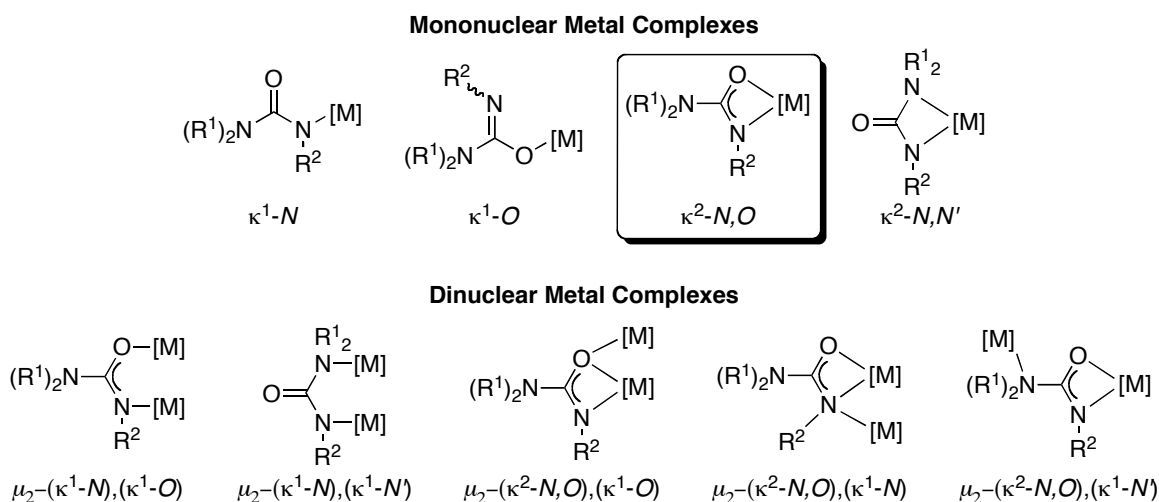


Figure 1.6. Several potential coordination modes of monoanionic ureate ligands.

In addition to coordination isomerism, each metal complex containing ligands of a given binding mode can exhibit geometric isomerism. The five possible stereoisomers for an octahedral complex of the form L_2MX_2 (L is a κ^2 - N,O ureate ligand), not including enantiomeric pairs, are shown in Figure 1.7. These myriad bonding permutations highlight both the potential richness of ureate chemistry, and the challenge in predictably accessing and characterizing discrete species.

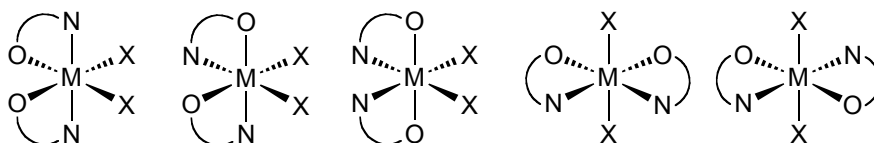


Figure 1.7. Geometric isomers of octahedral L_2MX_2 complexes ($L = \kappa^2$ - N,O -ureate).

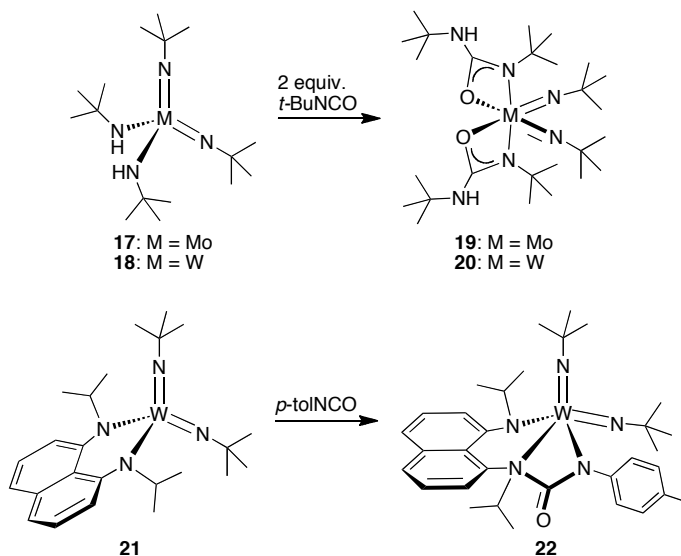
1.3 Synthesis of Ureate Complexes by Isocyanate Insertion

1.3.1 Groups 6-10

To date, the vast majority of metal complexes with monoanionic ureate ligands have been prepared *via* the insertion of an isocyanate into a metal–amido bond. In 1993, Hursthouse and Wilkinson reported the synthesis of group 6 ureate complexes **19** and **20** by the reaction of *tert*-butylisocyanate with bis(amido)bis(imido) derivatives **17** and **18** (Scheme 1.2).⁸⁴ Their results indicate that isocyanates react selectively with amido ligands, and do not undergo [2+2] cycloaddition with the imido moieties. This reactivity was unexpected, as the authors had asserted the opposite in an earlier report.⁸⁵ Similar behaviour has since been observed by Richeson and co-workers for a tungsten bis(imido) complex supported by a chelating diamido ligand (**21**).⁸⁶ The resulting complex (**22**) has the ureate ligand bound in a κ^2 - N,N manner, rather than κ^2 - N,O . This is likely due to the

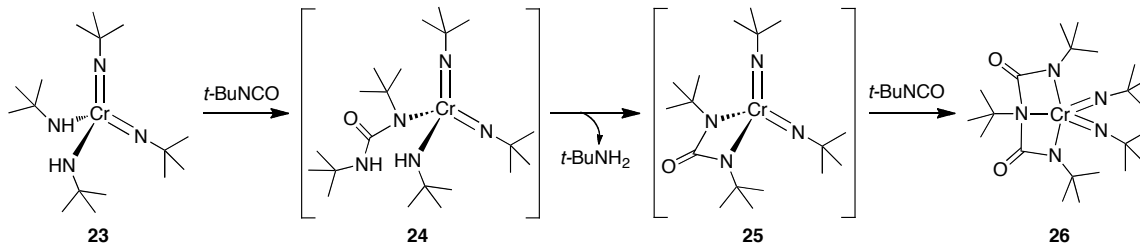
rigid nature of the tethered ligand, which forces coordination of the trisubstituted *N*-atom neutral donor *in lieu* of the carbonyl oxygen.

Scheme 1.2. Group 6 ureate complexes formed *via* isocyanate insertion.



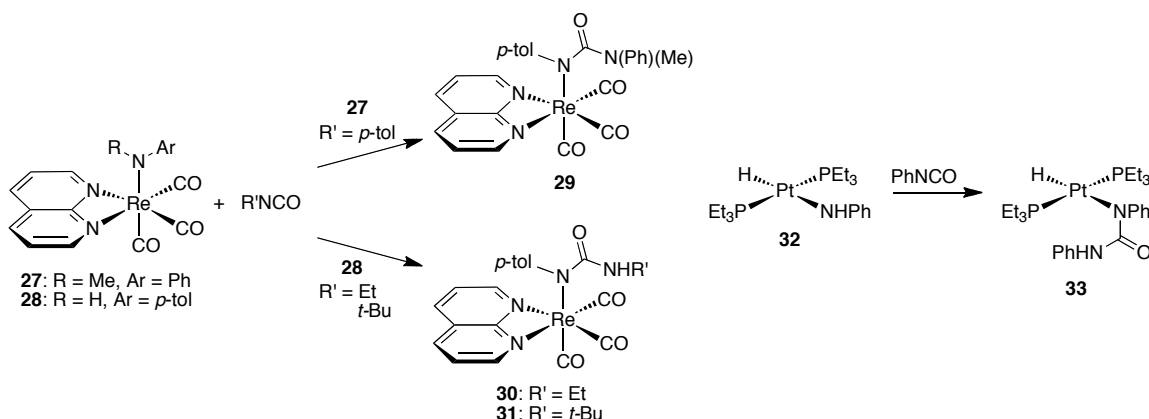
While molybdenum and tungsten compounds **17** and **18** undergo two successive isocyanate insertions to form bis(ureato) complexes, the analogous reaction with chromium congener **23** gives a different product (**26**, Scheme 1.3).⁸⁴ This complex contains a dianionic ligand derived from the coupling of two isocyanate units. A proposed mechanism for the formation of **26** is shown in Scheme 1.3. Once a κ^1 -*N*-ureate complex is generated by initial isocyanate insertion (**24**), an intramolecular proton abstraction can occur to liberate *tert*-butylamine, forming a transient dianionic ureate complex (**25**). A second equivalent of isocyanate can then insert into one of the Cr–N_{ureate} bonds to give the observed product (**26**). This result indicates that ureates are not always inert spectator ligands, and can undergo further transformations while attached to a metal center. Careful ligand design is therefore required to minimize the possibility of ureate decomposition through pathways such as that described above.

Scheme 1.3. Formation of unexpected chromium complex **26**.



Amido ligands attached to electron-rich low-valent transition metals will also undergo insertion reactions with isocyanates to form ureate derivatives (Scheme 1.4). Pérez and co-workers have examined the reactivity of Re(I) amido compounds **27** and **28** with aryl and alkyl isocyanates.^{87,88} These insertion reactions form monodentate $\kappa^1\text{-N}$ -ureate derivatives (**29-31**), rather than $\kappa^1\text{-O}$ or chelating ureates. This is likely due to coordinative saturation of the octahedral products, and hard/soft acid/base (HSAB) thermodynamic considerations.⁴⁴ Notably, the identity of the precursor amido ligand dictates the coordination mode of the resulting ureate. The secondary amido from **27** becomes detached from the metal center after insertion, giving **29**, while the primary amido nitrogen of **28** remains coordinated to rhenium in **30** and **31**. The authors propose that the ligand rearrangement in these latter cases results from the difference in pK_a between the two halves of the parent ureas. Proton transfer from the more acidic aryl-substituted nitrogen, originating from the Re-NHAr group, to the initially coordinated alkyl-substituted nitrogen from the inserted isocyanate forms the more stable coordination isomer. Late transition metal ureate complexes can also be generated *via* isocyanate insertion. Cowan and Troglér showed that phenylisocyanate preferentially inserts into the platinum–amido bond of complex **32**, rather than the platinum–hydride bond (Scheme 1.4).⁸⁹ The ureate ligand of complex **33** is also $\kappa^1\text{-N}$ -bound, analogous to rhenium complexes **29-31**.

Scheme 1.4. Isocyanate insertion into rhenium– and platinum–amido bonds.

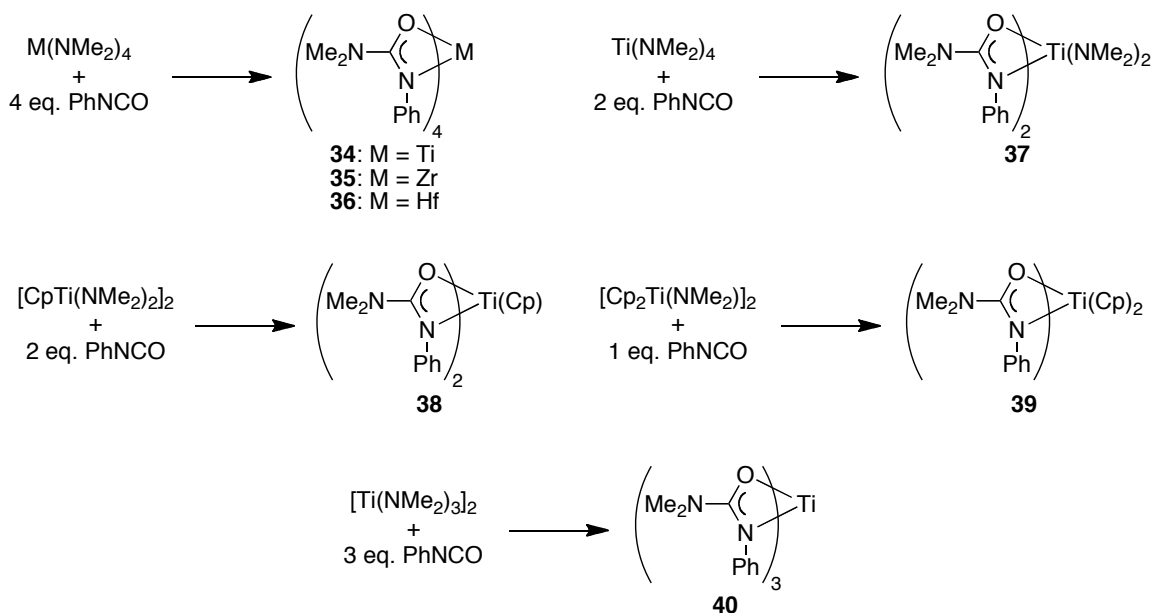


1.3.2 Group 4

The first group 4 ureate compounds, indeed the first ureate compounds of *any* metal, were reported by Lappert and co-workers in 1970.^{90,91} The authors demonstrate that, by reacting group 4 amido derivatives with phenylisocyanate, a number of ureate complexes can be synthesized (**34-40**, Scheme 1.5). These products were characterized by IR and NMR spectroscopy, the results of which suggest a κ^2 -*N,O* binding mode; however, no solid-state molecular structures, or reactivity of the resulting ureate complexes were reported.

While this work is very important from a fundamental perspective, it nonetheless highlights a significant limitation of the insertion method. Treatment of either Zr(NMe₂)₄ or Hf(NMe₂)₄ with two equivalents of phenylisocyanate does not give the intended bis(ureato) complex, but instead forms only **35** or **36**. Thus, the development of alternate synthetic routes is required to access zirconium or hafnium congeners of compound **37**. This is particularly relevant for the synthesis of catalytically applicable group 4 compounds, as these would require the presence of both supporting (i.e. ureate) and reactive (i.e. amido) ligands.

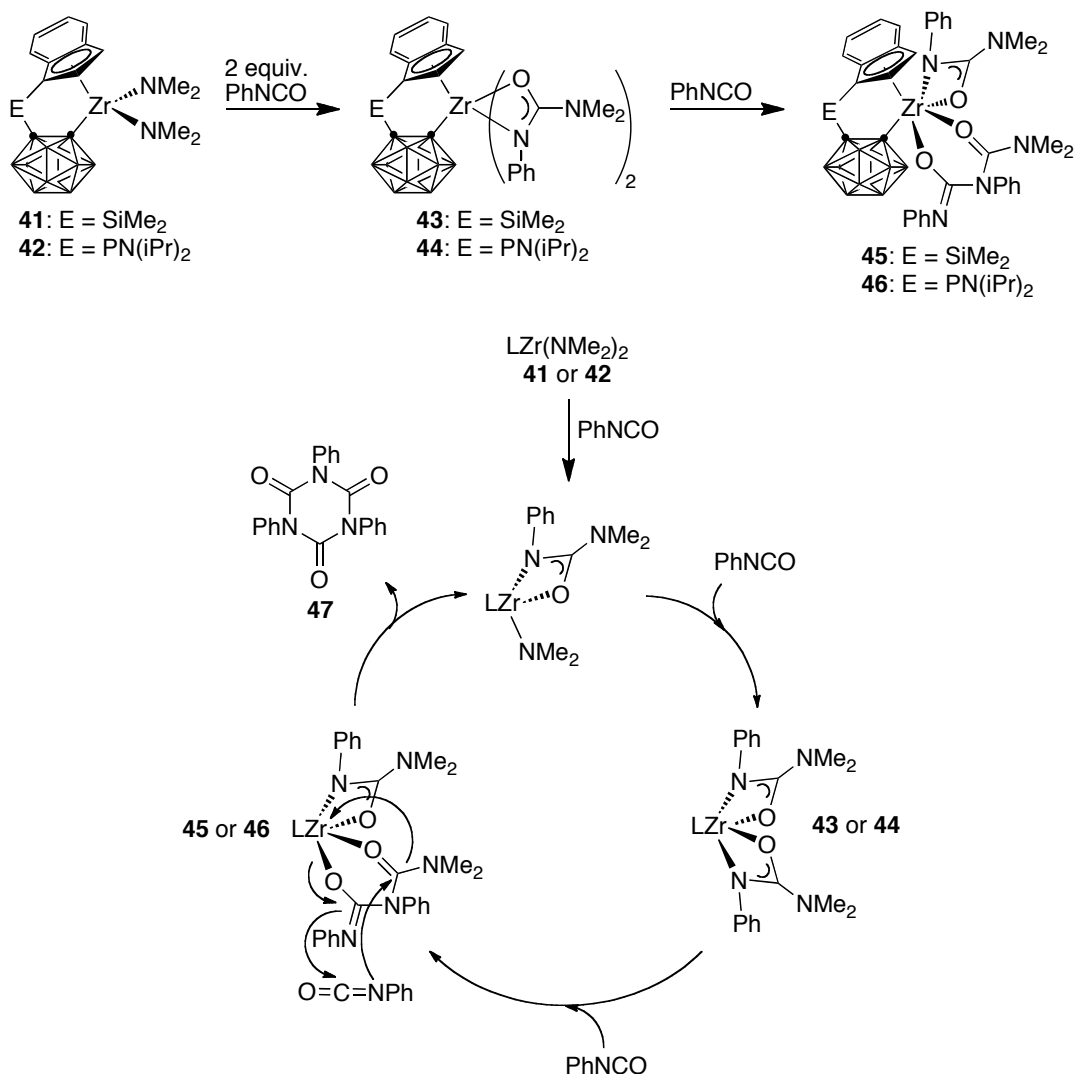
Scheme 1.5. Preparation of the first ureate-supported group 4 metal complexes.



After these pioneering studies, no monoanionic ureate derivatives of the group 4 metals were reported for more than thirty years. This fact is incredibly surprising, given the apparent suitability of modular, hard donor ligands for early transition metals. In 2003, Xie and co-workers disclosed an investigation on the insertion of unsaturated organic molecules into the zirconium–amido bonds of cyclopentadienyl-carboranyl supported complexes **41** and **42** (Scheme 1.6).^{92,93} The authors discovered that under stoichiometric conditions, two equivalents of phenylisocyanate react with **41** or **42** to form bis(ureato) complexes (**43**, **44**). Treating these ureate compounds with an additional equivalent of phenylisocyanate results in further insertion into the Zr–N_{ureate} bond, generating **45** or **46**; similar reactivity was previously proposed for the formation of chromium complex **33**. If the isocyanate is present in excess, compounds **41–46** catalyze a cyclotrimerization reaction to produce tris(urea) **47** in 50–65% yield. The authors propose that this reaction proceeds through multiple isocyanate insertions, akin to those observed under stoichiometric conditions. These results again highlight the propensity of ureates to act in

a noninnocent fashion, and the unsuitability of isocyanate insertion as a reliable synthetic protocol for the selective preparation of ureate complexes.

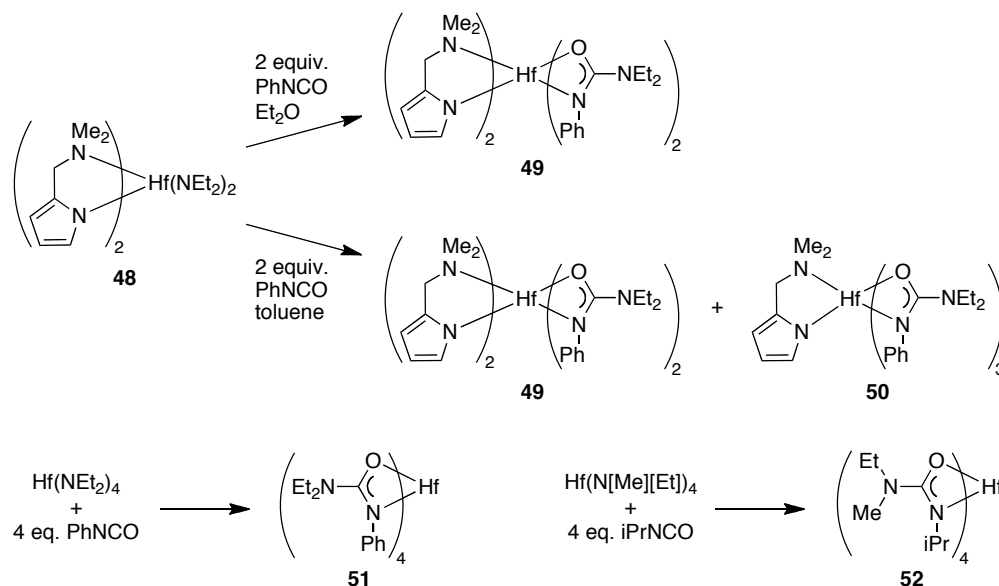
Scheme 1.6. Multiple isocyanate insertions at a single zirconium center; catalytic cyclotrimerization of phenylisocyanate.



Isocyanate insertion into group 4 metal–nitrogen bonds can also be accomplished with bulkier amido ligands (Scheme 1.7). Huang and co-workers demonstrated that treatment of the amino-pyrrolyl-supported hafnium complex **48** with phenylisocyanate in diethyl ether forms the expected bis(ureato) derivative (**49**); however, changing the

reaction solvent to toluene gives a mixture of **49** and a tris(ureato) byproduct (**50**).⁹⁴ This byproduct likely results from ligand disproportionation under the conditions employed. Homoleptic tetrakis(ureato) complexes have also been prepared by isocyanate insertion into bulky Hf–NR₂ bonds. Huang and co-workers synthesized **51** by the reaction of Hf(NEt₂)₄ with excess phenylisocyanate.⁹⁴ A similar complex, **52**, was prepared in an analogous manner by Devi and co-workers as a potential MOCVD precursor to hafnium nitride.⁹⁵ These latter two examples are reminiscent of compound **19** (Scheme 1.2).

Scheme 1.7. Synthesis of ureate-supported hafnium complexes *via* isocyanate insertion.



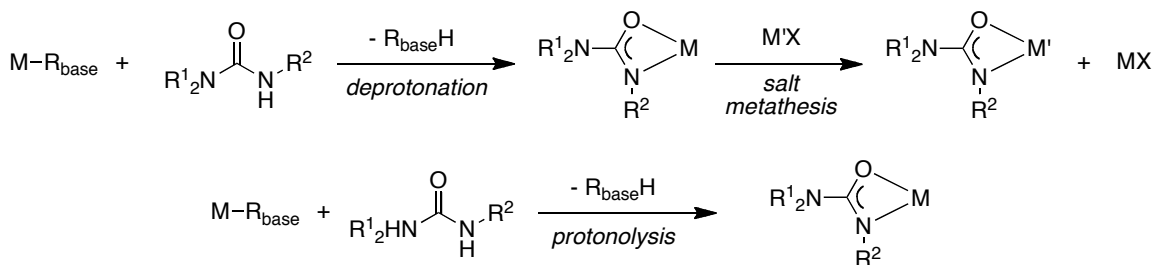
Using the above methods to synthesize a wide variety of group 4 ureate complexes has significant limitations. That ureate ligands are themselves susceptible to further isocyanate insertion has already been established; therefore, relying on the insertion protocol would necessitate tedious reaction optimization and product purification. In addition, the final ureate ligand structure is dependant on the identity of the amido ligand undergoing insertion. Accordingly, preparation of functionally varied ligands would require the synthesis of exotic metal–amido precursors. Finally, many organic

isocyanates are not commercially available, and can be difficult to synthesize, isolate, and purify. Organic ureas, on the other hand, can act as a convenient source of the ureate framework. Surprisingly, the use of urea proligands has rarely been applied to the synthesis of ureate compounds, despite widespread precedent for these protocols involving the preparation of many other metal complexes.

1.4 Alternate Synthetic Approaches

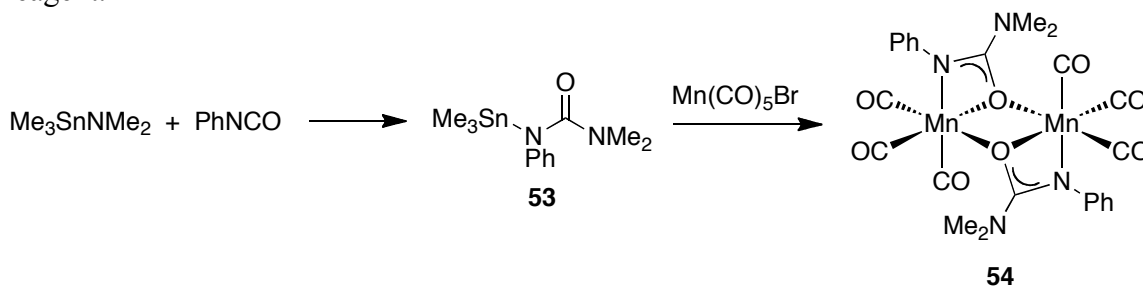
The two most common synthetic routes to install supporting ligands onto group 4 metals involve either salt metathesis or protonolysis reactions (Scheme 1.8). The former reaction is usually accomplished by deprotonating an organic proligand with a strong, alkali metal base. The intermediate lithium, sodium, or potassium complex can then undergo transmetalation with a transition metal halide species to form the desired complex, and eliminate MX (M = alkali metal). Protonolysis reactions, on the other hand, involve a direct reaction between the organic proligand and a transition metal starting material containing basic ligands, generally amidos or alkyls. Previous work in the Schafer research group has already established the viability of both routes to prepare amidate-supported group 4 complexes;⁸¹ therefore, these methods should be suitable for the installation of ureate ligands.

Scheme 1.8. Salt metathesis and protonolysis routes to ureate complexes.



An early example of a salt metathesis reaction to form a ureate complex was reported by Abel and Dunster in 1973 (Scheme 1.9).⁹⁶ In this case, a tin ureate compound (**53**) was prepared by the insertion of phenylisocyanate into the Sn–N bond of Me₃SnNMe₂. Transmetallation of **53** with Mn(CO)₅Br generates a dinuclear manganese complex (**54**) with concomitant liberation of Me₃SnBr. On the basis of IR spectroscopy, the ureate ligands of **54** are proposed to chelate one manganese center in a κ^2 -*N,O*-manner, while bridging to a second manganese through the ureate oxygen; however, the solid-state molecular structure was not determined. While this reaction demonstrates the feasibility of salt metathesis as a synthetic route to ureate complexes, the tin reactant **53** is still formed using isocyanate insertion methodology.

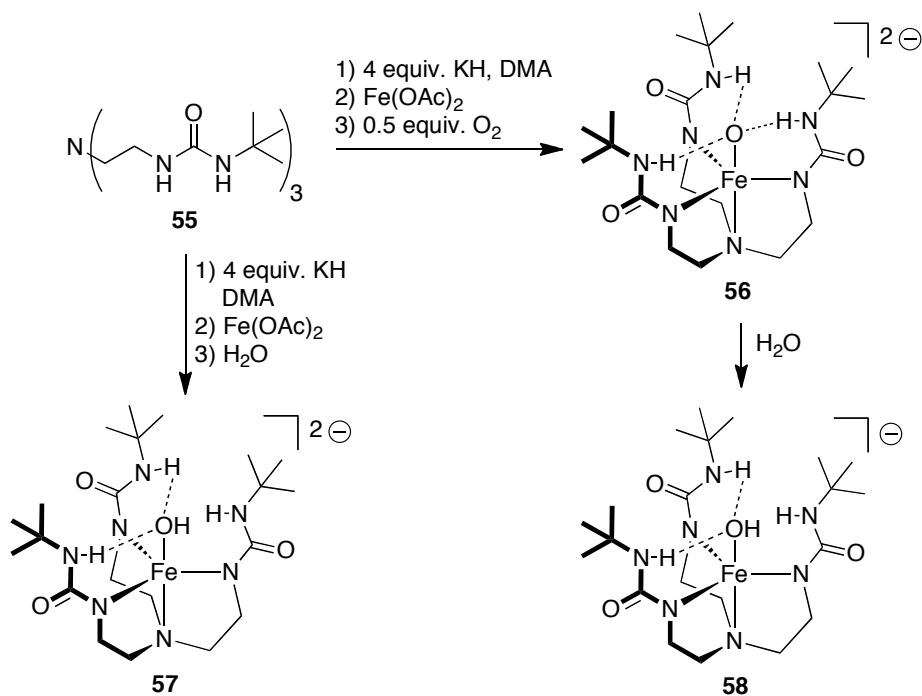
Scheme 1.9. Synthesis of a manganese ureate complex by transmetallation with a tin reagent.



More recently, Borovik and co-workers have beautifully demonstrated the synthetic power of salt metathesis reactions involving urea proligands.⁹⁷⁻⁹⁹ These researchers have prepared a wide variety of biologically inspired, multidentate ureate complexes of first row transition metals, many of which exhibit remarkable reactivity, particularly with regard to small molecule activation (Scheme 1.10).¹⁰⁰ The ureate-supported iron complex **56** represents one of the few examples of stable, characterized mononuclear iron(oxo) species resulting from O₂ activation.

The general synthetic route to these compounds involves the use of potassium ureate salts as transmetallating reagents. These salts are formed *in situ* by treating the desired urea proligand (for example, **55**) with an appropriate amount of potassium hydride. Addition of simple transition metal salts to potassium ureates forms the desired ureate complexes (for example, **56** and **57**). By using this synthetic strategy, many ureate ligand architectures that would be nigh impossible to assemble by isocyanate insertion are easily accessible; examples of structurally diverse complexes (**59-62**) are illustrated in Figure 1.8.¹⁰¹⁻¹⁰⁴ It should be noted that in nearly every complex prepared by the Borovik group, the ureates bind the transition metal center in an exclusively κ^1 -*N*-mode, and exhibit little electron delocalization through the [N₂CO] core. The lone exception is the dinuclear copper complex **60**, wherein the ureates bridge between two metal centers.

Scheme 1.10. Stabilization of mononuclear iron(oxo) and iron(hydroxo) species by ureate ligands (potassium counterions omitted for clarity).



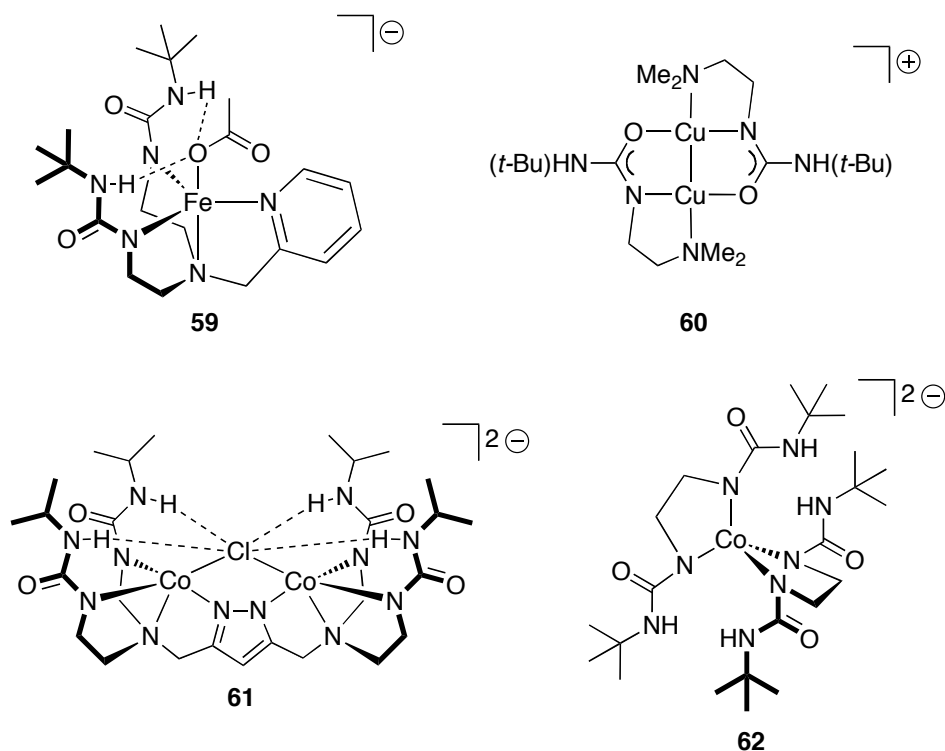
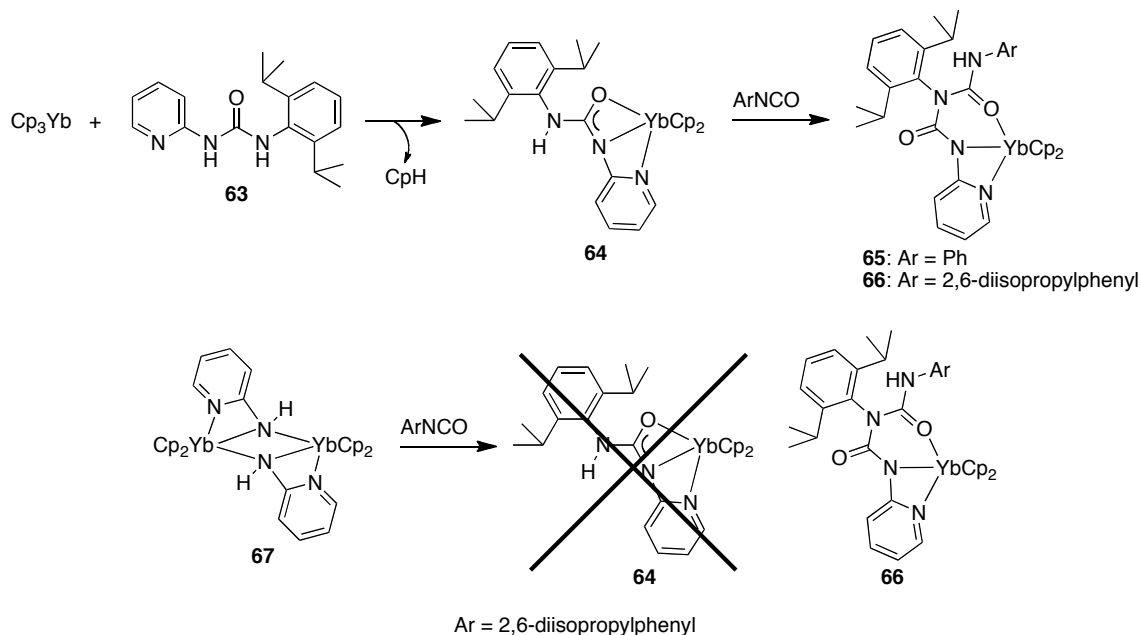


Figure 1.8. Structural diversity in first row transition metal ureate complexes prepared *via* salt metathesis (counterions omitted for clarity).

In addition to the synthesis of ureate compounds *via* salt metathesis, there is one reported example of a urea proligand being used in a protonolysis reaction. Zhou and co-workers developed a pyridyl-substituted urea (**63**) for the preparation of an ytterbium ureate complex (**64**) from Cp_3Yb (Scheme 1.11).¹⁰⁵ Treatment of ureate complex **64** with one equivalent of either phenylisocyanate or 2,6-diisopropylphenylisocyanate forms compounds **65** or **66** through reaction at the distal amino group. The use of protonolysis involving urea **63** is therefore required for the successful isolation of the ureate complex **64**: treating $[\text{Cp}_2\text{Yb}(\text{NHPy})_2]$ (**67**) with 2,6-diisopropylphenylisocyanate results in the exclusive formation of compound **66**. This reaction demonstrates the potential of urea protonolysis as a selective means to generate ureate complexes that are otherwise inaccessible by isocyanate insertion.

Scheme 1.11. Formation of an ytterbium ureate (**64**) by protonolysis and subsequent reaction with arylisocyanates; comparison to isocyanate insertion.



Despite the potential of salt metathesis and protonolysis as general routes to transition metal ureate compounds, the above examples constitute the only reported instances of these reactions being used. Notably, no group 4 ureate compounds have been assembled in this manner. Given the remarkable reactivity promoted by related amidinate,⁵⁵ guanidinate,⁵⁵ and amidate ligands,⁸¹ the striking lack of literature on ureate complexes affords an excellent opportunity to explore these little known group 4 compounds.

1.5 Scope of this Thesis

The major research question unifying this thesis concerns an elucidation of the similarities and differences between group 4 amidate and ureate complexes, specifically with regard to structure, bonding, and reactivity trends. The connection between these two ligand sets was established above in Section 1.2. The central facet of this relationship is that, while structurally similar, ureates have the ability to be more electron-rich than their amidate counterparts. Intuitively, this should result in tighter metal–ligand binding; such an effect has been observed previously for guanidinate complexes **15** and **16**.^{82,83} However, at the outset of this research project, the full effect of this electron donation on the synthesis, structure, and reactivity of group 4 complexes was unknown.

Two main areas were targeted for a systematic comparison of the amidate and ureate ligand sets. Both of these projects centered on the use of ureate ligands as a supporting framework for group 4 mediated catalysis. As outlined above in Section 1.3, every previously reported group 4 compound containing monoanionic ureate ligands has been prepared by isocyanate insertion into an existing metal–nitrogen bond. In order to synthesize the structurally varied complexes required for comprehensive catalytic investigations, this insertion-based methodology must be abandoned in favour of a more modular approach. The use of preformed ureas as proligands, as outlined above in Section 1.4, was therefore targeted as a synthetic strategy. These ureas can be easily assembled from inexpensive, readily obtained materials, enabling the preparation of sterically and electronically diverse ligand architectures, thus aiding catalyst development.

Chapter Two describes the synthesis and characterization of dichlorobis(ureato) and dialkylbis(ureato) derivatives of titanium and zirconium. These compound classes were targeted in order to establish viable synthetic routes of the type described above in Section 1.4. Furthermore, there are hundreds of examples of group 4 dichloro and dialkyl fragments supported by all manner of ligand systems. An examination of the structural features of ureate derivatives can therefore provide multiple points of comparison to known complexes. It has been established that amidate ligands have a tendency to be unreliable supports for these types of compounds, resulting in fluxional species that can be difficult to characterize.^{106,107} One possible reason for this is that the bis(amidato) complexes are highly electron deficient. These species may be prone to fluxional behaviour, such as ligand disproportionation and/or aggregation, to increase electron density at the electron-poor metal centers. The use of electron-rich ureate analogues should therefore help in generating well-defined molecular species. Finally, group 4 complexes of the type L_2MX_2 , where X is a halide or alkyl ligand, are very often used as olefin polymerization precatalysts;^{24,25,108} therefore, establishing a reliable synthetic protocol to access a wide variety of ureate derivatives will provide the groundwork necessary for catalyst optimization.

Chapter Three is focused on the second major point of comparison between group 4 amidates and ureates: their suitability for hydroamination catalysis. The Schafer group has published a solid body of work on the remarkable activity of bis(amidato)bis(amido)-titanium and zirconium precatalysts for hydroamination.¹⁰⁹⁻¹¹⁸ Specifically, it has been observed that catalysts supported by ligands containing electron-withdrawing substituents tend to be more active for these reactions;^{109,114} it therefore stands to reason that electron-

rich ureate compounds should be less active. However, the effects responsible for this trend are unclear. A detailed investigation regarding steric and electronic effects on hydroamination catalysis by amidate and ureate complexes was therefore undertaken, with the goal of enabling the design of more efficient catalytic systems.

As a result of these studies, a highly effective ureate-supported hydroamination catalyst has been identified. In an effort to better understand the factors responsible for the reactivity exhibited by this catalyst, an in-depth mechanistic study was initiated. The details of this study are the subject of Chapter Four. Through a combination of stoichiometric synthetic chemistry and kinetic analyses, a stereoelectronic rationale for the catalytic activity observed and a feasible catalytic cycle have been constructed.

Finally, the major findings of these research projects are summarized in Chapter Five, along with the presentation of preliminary results that warrant further investigation. As this thesis constitutes the first systematic evaluation of ureate-supported group 4 complexes, there are myriad conceivable projects stemming from this work. The discussion will focus on the further development of ureate-supported hydroamination catalysts, and potential applications of these compounds to other bond forming reactions. The simple yet highly modular nature of ureate ligands, and the unique reactivity resulting from their use, renders this topic deserving of extensive future research. The work contained herein represents a seminal contribution to this on-going area of investigation, providing reliable synthetic protocols, accurate and informative structural details, reactivity profiles, and catalytic applications for this new and promising class of group 4 compounds.

CHAPTER 2. Synthesis, Bonding, and Reactivity of Dichloro and Dialkyl Complexes

2.1 Introduction

Two of the most common structural motifs for group 4 compounds involve metal dichloride or dialkyl fragments, predominantly due to their suitability for polymerization catalysis.^{24,25,108} However, there are no known examples of ureate-supported complexes of this type, and only select examples of related amidate compounds have been reported.^{106,107,119,120} The majority of these are difficult to characterize, due to complicating factors such as neutral ligand retention (**67-69**),^{107,119} solution-phase fluxionality and geometric isomerization (**67**),¹⁰⁷ and aggregation (**70** and **71**)¹⁰⁶ (Figure 2.1). In addition, many synthetic attempts have been reported as unsuccessful, leading to product mixtures. Reliable access to these and related compounds is particularly relevant, given their potential as olefin polymerization precatalysts.^{120,121}

In pursuit of this goal, the ureate ligand set, described previously in Chapter One, was chosen as an alternative to amidates for the preparation these compounds. The electron-rich nature of the ureate framework should allow for the isolation of stable molecular species that are amenable to characterization. As there are no previous examples of such compounds, the major focus of this initial investigation is to elucidate the fundamental chemistry of group 4 ureate complexes for comparison with known amidate derivatives, with a secondary goal of evaluating their use in ethylene polymerization. The following sections will review the olefin polymerization reaction, specifically with regard to the use of non-Cp based catalysts.

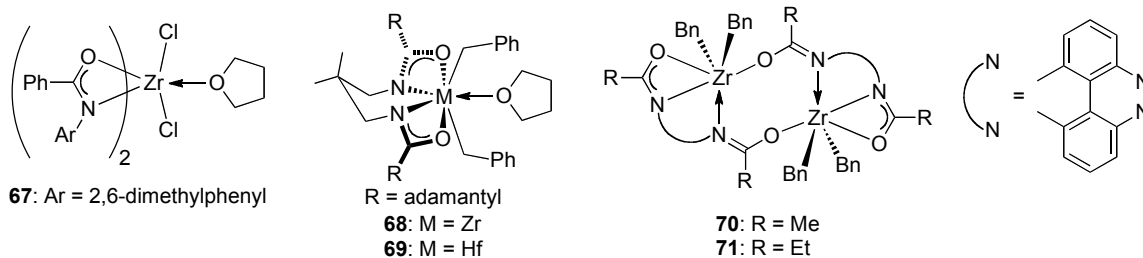


Figure 2.1. Bis(amidato) complexes that exhibit fluxional behaviour, neutral ligand retention, and/or multinuclearity.

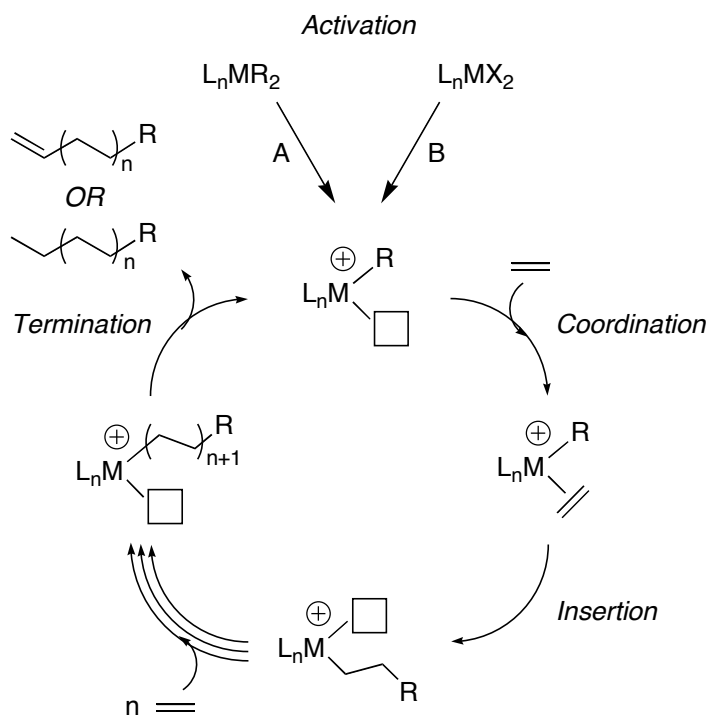
2.1.1 Post-Metallocene Polymerization

The production of polyolefins is a multi-billion dollar global industry, representing arguably the most important application of organometallic chemistry in the world.¹²²⁻¹²⁴ Since the discovery of transition-metal-based polymerization catalysts in the early 1950s,^{125,126} an immense amount of research has been applied to the development of efficient catalytic systems.¹²⁴ Even though currently employed catalysts are extremely active, novel technologies are still being sought to control the molecular structure, and therefore material properties, of polymer products. Particularly attractive in this regard are homogeneous, single-site catalysts of the group 4 metals.¹²⁷ These systems offer the ability to tune the polymerization behaviour of the metal center through modification of the surrounding ligands, allowing access to new polymer architectures and monomer combinations.^{128,129}

One of the major advantages of homogeneous, single-site polymerization catalysts is that mechanistic investigations are generally more feasible than those involving surface-based, heterogeneous catalysts.¹³⁰ A detailed knowledge of the polymerization process is key to the development and optimization of new reaction strategies.¹³¹ Not surprisingly, there has been extensive work undertaken to elucidate the underlying chemistry of olefin

polymerization.^{130,132-137} While a detailed discussion of this intricate process is beyond the scope of this thesis, a simplified reaction scheme describing the salient features of the proposed catalytic cycle is outlined in Scheme 2.1.

Scheme 2.1. Simplified coordination-insertion mechanism for olefin polymerization.



The active species is generally accepted to be a coordinatively unsaturated, cationic alkyl complex.¹³⁸⁻¹⁴⁰ Generation of this species is commonly achieved in two ways:¹⁴¹ first, abstraction of an alkyl anion (R^-) from a precatalyst of the form L_nMR_2 (pathway A);¹⁴⁰ second, combined alkylation and abstraction of a dihalide precatalyst (pathway B).¹⁴² This latter process can be accomplished through use of a two-component co-catalyst (alkylating agent and abstracting agent), or a single co-catalyst that effects both transformations. Once generated, the highly reactive cationic species undergoes a series of olefin coordination and insertion steps in a chain growth process. Termination can occur through several mechanisms,¹⁴³ such as β -hydride elimination, giving

unsaturated end groups, chain transfer to a co-catalyst metal center, or protonolytic cleavage upon reaction quenching, both giving saturated chain ends. In the first two cases, the resulting transition-metal species can undergo further olefin coordination/insertion to generate a new polymer chain. One key aspect of the above mechanism is that the metal complex is not a “catalyst” in the strictest sense. While present in sub-stoichiometric amounts (olefin to metal concentration ratio usually 1 : $\sim 10^{-5}$), it does not necessarily regain its original composition at the completion of a cycle, and generally cannot be reused for subsequent polymerizations; however, the term “catalyst” will be used throughout to describe these species, in accordance with the plethora of literature on the subject.^{122,124}

Group 4 metallocene complexes (Cp_2MX_2), when appropriately activated, have long been known as olefin polymerization catalysts.¹⁴⁴ Their utility was somewhat limited until the serendipitous discovery of a potent single-component aluminum activator, methylaluminoxane (MAO), formed by partial hydrolysis of trimethylaluminum.^{142,145,146} Using MAO as a co-catalyst increases the polymerization activity of Cp_2ZrCl_2 by a factor of $\sim 10^4$ relative to simple alkyl aluminum activators, such as Et_2AlCl .¹⁴⁶ This realization spurred widespread research on group 4 metallocene-based catalysts, leading to the development of highly successful systems for the production of a multitude of materials.¹⁴⁷ While modification of the cyclopentadienyl ligand framework has enabled a range of structural diversity in metallocene catalysts,^{21,148} alternative ligand systems afford greater flexibility with respect to tuning steric and electronic properties. These post-metallocene systems show great promise in the ongoing effort for greater control over polymer structure and material properties.²⁴⁻²⁶ Remaining challenges in the field of

olefin polymerization include precise control over polymer stereochemistry,^{127,148} molecular weight (magnitude and distribution),¹³¹ and efficient co-monomer incorporation, particularly with regard to polar co-monomers.¹⁴⁹

In order to effectively compare the vast number of catalysts that have been developed, a consistent “activity” metric must be applied. For the remainder of this chapter, an ethylene polymerization catalyst’s activity (*A*) will be quantified using the following formula (eqn. 2.1):²⁵

$$A = [\text{grams of polymer produced}][\text{mmol catalyst}]^{-1}[\text{bars of ethylene}]^{-1}[\text{h}]^{-1} \quad (2.1)$$

The classification “very high” in this regard is defined as an activity that exceeds 1,000 g mmol⁻¹ bar⁻¹ h⁻¹; as a benchmark, the metallocene precatalyst Cp₂ZrCl₂ attains activities on the order of 20,000-60,000 g mmol⁻¹ bar⁻¹ h⁻¹.[†] As polymerization activity is highly dependent on the reaction conditions, these numbers are not absolutes; often, a catalyst’s activity can range over an order of magnitude or more. In addition, activities reported in the literature give no indication of catalyst lifetime, leading to “inflated” activity figures for short-lived systems. In all of the following examples, an effort has been made to relate the highest activity reported for each system.

Among post-metallocene group 4 precatalysts, those with chelating amido ligands deserve particular distinction.^{60,150-152} Figure 2.2 illustrates several examples of these amido-based complexes with very high polymerization activities. For the series **72-74**, bulky aryl substituents on the amido donors are a key feature of the catalyst design, incorporated to provide steric protection of the low-coordinate active catalyst.

[†] Due to the cumbersome nature of the activity units, these values will henceforth be written as unitless quantities, with the understanding that the above units (g mmol⁻¹ bar⁻¹ h⁻¹) apply in all cases.

Complexes of the form illustrated by **75** represent what are known as the “constrained-geometry catalysts,” which have shown enough promise to be developed for commercial applications.⁶⁰

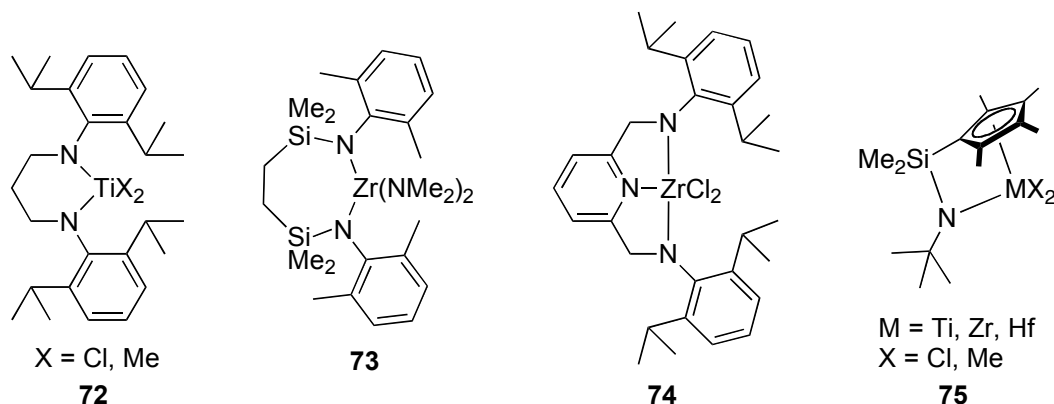


Figure 2.2. Examples of group 4 amido complexes that exhibit very high activity ($A > 1,000$) for the polymerization of olefins.

In addition to the success achieved with amido ligands, mixed donor chelates have also demonstrated remarkable polymerization reactivity.^{75,153,154} Figure 2.3 illustrates representative examples of (*N,O*)-chelating phenoxyimine- and β -ketoiminate-supported complexes and their corresponding activities. Clearly, this type of precatalyst is extremely active; complex **76** not only exhibits the highest activity ever reported for an ethylene polymerization catalyst, but the highest turnover frequency (TOF), $65,000 \text{ s}^{-1}$, of *any* non-biological catalyst for *any* reaction. By way of comparison, acetylcholinesterases exhibit rates (k_{cat}) on the order of $14,000 \text{ s}^{-1}$, and human carbonic anhydrase has a k_{cat} of $\sim 1,000,000 \text{ s}^{-1}$. These are two of the fastest enzymes known.¹⁵⁵

Replacing the *N*-substituents with polyfluorinated aromatics, as in the case of **77** and **78**, dramatically reduces the activity; however, these systems are still highly active, and possess characteristics that more than compensate for the rate reduction. When activated,

77 and **78** show “living” polymerization behaviour.^{156,157} A living catalyst displays highly controlled chain growth, giving polymers with extremely narrow and predictable molecular weight distributions.^{158,159} One measure of the molecular weight distribution of a polymer is the ratio between the *weight* average molecular weight (M_w) and the *number* average molecular weight (M_n); this ratio is termed the polydispersity index (PDI). Typical metallocene catalysts yield polymers with PDI values near 2; “living” catalysts, on the other hand, give PDIs approaching unity. This is achieved due to a lack of chain termination or chain transfer processes, and a rate of initiation much greater than propagation. In addition to producing polyolefins with predictable average molecular weight, these catalysts are useful in the synthesis of block co-polymers, and polymers with functionalized end-groups.^{158,159}

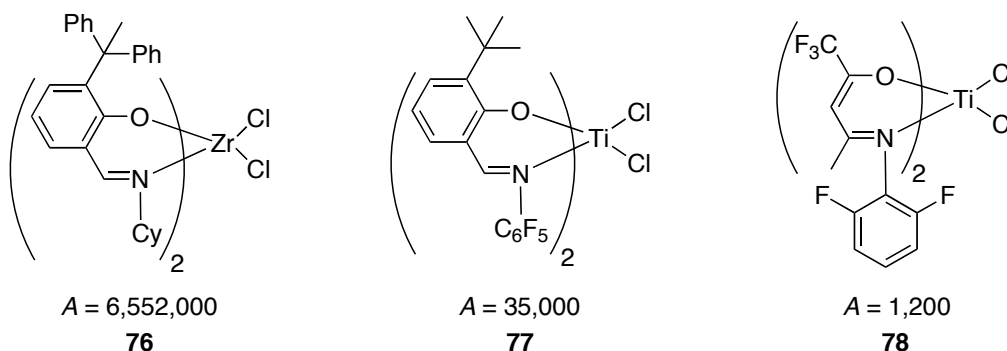


Figure 2.3. (*N,O*)-Chelating phenoxyimine- and β -ketoiminato-supported precatalysts for ethylene polymerization, with activities indicated. Complexes **77** and **78** produce polymer in a living manner.

Amidinate ligands, which form tight bite angle chelates similar to ureates, have also been investigated as supports for olefin polymerization catalysts; representative examples are shown in Figure 2.4.¹⁶⁰⁻¹⁶³ With the exception of **79**, these compounds generally exhibit low to moderate activity, and produce polymers with very broad molecular weight distributions: precatalyst **80** gives polyethylene with a PDI of nearly 90. A modification

of the catalyst architecture to replace one amidinate with a C_5Me_5 ligand (Cp^*) dramatically increases the catalyst utility.¹⁶⁴ These mixed Cp^* -amidinate catalysts, developed by Sita and co-workers, polymerize propylene and 1-hexene in a both a stereospecific and a living fashion, giving polymers with highly uniform isotacticity.

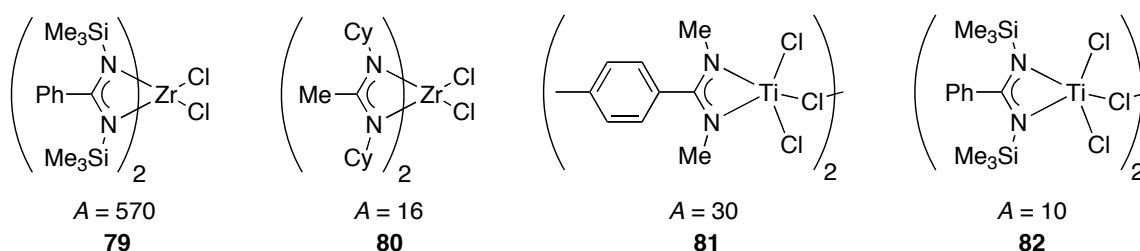


Figure 2.4. Amidinate ethylene polymerization precatalysts, with activities indicated.

One final class of post-metallocene polymerization catalyst that is relevant in the context of this thesis is that of group 4 guanidines. Arnold and co-workers prepared and investigated a series of guanidine-supported dichloro (**16**) and dialkyl (**83**) zirconium complexes, as well as remarkably stable cationic derivatives (**84**) (Figure 2.5).⁸³ The authors postulated that the loose ion-pairing and thermal stability observed for **84** were due to electron-donation by the NMe_2 group on the guanidine ligand. Solid-state structural evidence for this donation was previously described in Chapter One for complex **16**. Solution-phase spectroscopy of **16** and **83**, however, does not reveal any indicators consistent with hindered rotation about the $C-NMe_2$ bond. This is unexpected, given the proposed multiple-bond character of this linkage. Similar to their amidinate counterparts, complexes **16**, **83**, and **84** are only moderately active for ethylene polymerization, and also yield polymer chains with extremely broad PDIs (~ 25 -50). Here, the authors postulate that the action of multiple active species may be responsible

for the high PDIs, possibly resulting from abstraction of the supporting guanidinate ligands by excess aluminum activator.

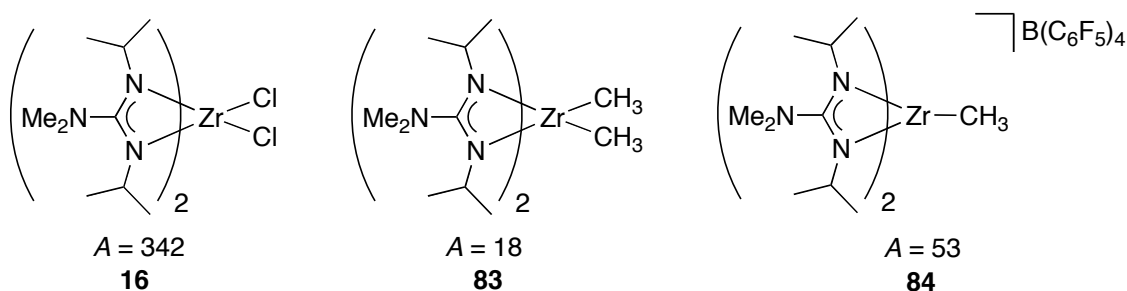


Figure 2.5. Guanidinate precatalysts, with ethylene polymerization activities indicated.

2.1.2 Potential Advantages of Ureate Ligands

The impetus for exploring the use of ureate ligands as supports for olefin polymerization precatalysts is two-fold. First, as described at the beginning of this chapter, the synthesis of amidate-supported polymerization precatalysts is generally unreliable, often leading to intractable product mixtures. One possible rationale is that the resulting bis(amidato) complexes are inherently unstable, and prone to isomerization and/or decomposition.¹⁰⁷ Amidate-supported hydroamination precatalysts of the general formula $\text{L}_2\text{M}(\text{NMe}_2)_2$ are known to be very electropositive; it is therefore reasonable to expect the corresponding dichloro and dialkyl derivatives to be even more electron-deficient, possibly to the point of instability. The electron donating ability of ureate ligands can potentially stabilize these electron deficient metal centers, enabling isolation and characterization of the desired precatalysts. In addition, amidate complexes **67-69** each retain a neutral THF ligand from the reaction solvent, which could interfere with polymerization catalysis.^{107,119} Use of an electron-rich ureate ligand may enable the isolation of base-free analogues.

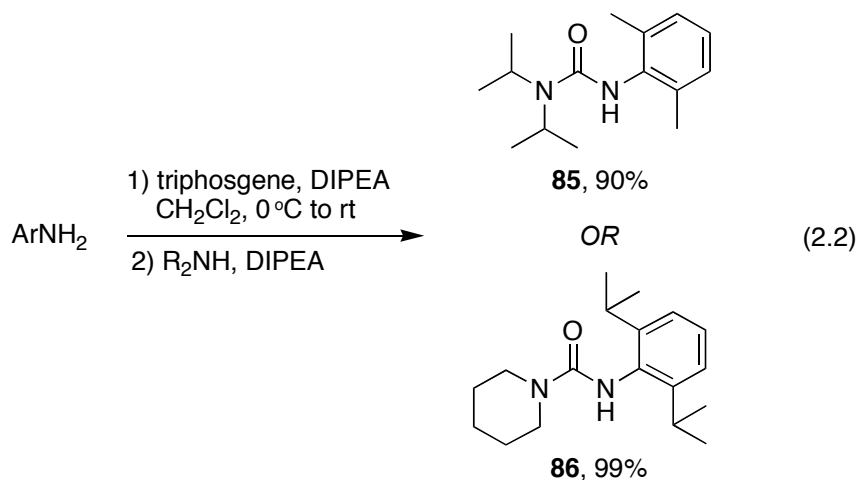
A second potential advantage of ureates is also related to electron donation. As outlined in Scheme 2.1, the proposed active site of olefin polymerization is a coordinatively unsaturated, cationic metal center. These reactive cationic complexes are also highly unstable, resulting in decreased catalytic performance over time. While many olefin polymerization catalysts boast high activities and turnover frequencies, a catalyst lifetime on the order of minutes or seconds drastically diminishes overall productivity. In addition to stabilizing the electropositive metal center of the precatalyst, ureate ligands could also stabilize the cationic active species, increasing catalyst lifetimes and therefore polymer yield. This effect has precedent in the stabilization of guanidinate-supported zirconium cations, as described by Arnold.⁸³

The remainder of this chapter will detail research undertaken toward the synthesis, characterization, and reactivity of the first group 4 dichlorobis(ureato) and dialkylbis(ureato) derivatives. As these represent novel compound classes, substantial effort has been directed toward fundamental structural characterization, with a focus on comparison with analogous amidate complexes. A major point of comparison lies with electronic effects stemming from the higher donating potential of the ureate ligand. This electron donation appears to exert influence on the feasibility of certain synthetic routes to these compounds, as well as solid-state and solution-phase structural aspects. Finally, preliminary screening of the prepared ureate complexes as ethylene polymerization precatalysts has been carried out. Unfortunately, all of the ureate-supported derivatives tested exhibit very low polymerization activity under the conditions employed.

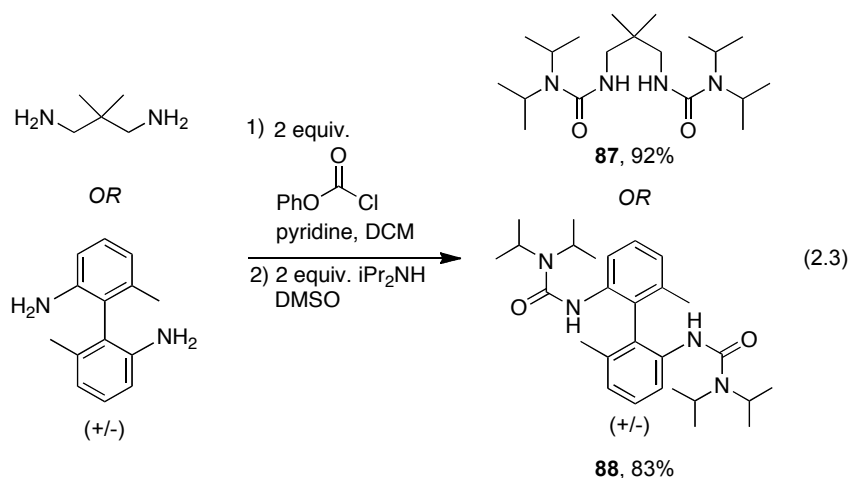
2.2 Results and Discussion

2.2.1 Efficient and Modular Synthesis of Urea Proligands

In order to enable the preparation of structurally and electronically varied metal complexes, a modular synthetic route to a variety of proligand architectures is required. The previous use of urea proligands to synthesize corresponding ureate complexes was outlined in Chapter One (Section 1.2.3); however, in each of those cases, the ureas were themselves generated using commercially available isocyanates.⁹⁷ An alternate synthetic route is desirable, as this would enable the preparation of ligand architectures beyond those accessible from commercial isocyanates. Fortunately, due to the ubiquity of the urea functionality in organic chemistry, a wide variety of synthetic methods are available.^{165,166-169} Particularly attractive is a one-pot protocol that avoids the isolation of reactive isocyanate intermediates. Reaction of a primary amine with one third of an equivalent of triphosgene in the presence of a sterically demanding tertiary amine base generates an isocyanate *in situ*.^{166,168} This isocyanate is then reacted directly with a secondary amine to give an *N,N,N'*-trisubstituted urea in excellent yield (eqn. 2.2). Two such urea proligands, which will be used throughout this thesis (**85** and **86**), are shown below. These compounds are crystalline and easily handled. Purification can be achieved by flash chromatography, recrystallization, or vacuum sublimation as required. Both **85** and **86** exhibit NMR spectral features consistent with the structures illustrated. A broad signal between δ 5.5-5.7 in the ^1H NMR spectra of both compounds corresponds to the *NH* proton, while a signal near δ 156 in the ^{13}C NMR spectra corresponds to the carbonyl carbon. For compound **85**, all of the isopropyl methyl protons are equivalent, as are the isopropyl methine protons.



Unfortunately, this urea synthesis cannot be applied to the preparation of tethered bis(urea) proligands. Reaction of a suitable diamine with triphosgene would instead lead to the formation of a cyclic urea as the major, if not the sole product. In order to circumvent this problem, a strategy involving activated carbamate intermediates was employed.¹⁶⁹ Addition of two equivalents of phenyl chloroformate to either 2,2-dimethyl-1,3-diaminopropane or 2,2'-diamino-6,6'-dimethylbiphenyl in the presence of pyridine leads to the quantitative formation of the bis(phenylcarbamate). These compounds react with two equivalents of diisopropylamine in DMSO at room temperature to give the bis(urea)s **87** and **88** in 92% and 83% overall yield (eqn. 2.3). As observed for **85** and **86**, diagnostic signals in the ¹H and ¹³C NMR spectra are present. The NH protons resonate at δ 5.31 (broad triplet) for **87** and δ 6.01 (broad singlet) for **88**. This difference in chemical shift is likely due to the differing electronic structures of the alkyl and aryl tethers. The NH protons of **87** are coupled to the adjacent methylene protons, which appear as a doublet at δ 2.99, further supporting the proposed structure. Similar to the above non-tethered ureas, the C=O signal appears between δ 153.0-159.0. Finally, as for urea **85**, the isopropyl groups are equivalent.



Recrystallization of anhydrous **87** results in the deposition of large crystals, which were used to determine the solid-state structure by X-ray crystallography. The molecular structure and illustrations of crystal packing are shown below in Figure 2.6. The molecule exhibits the expected connectivity, confirming the structural assignment from solution-phase spectroscopy. Each atom of the urea N–C–N moiety is sp^2 -hybridized, as indicated by the planarity of the $[N_2CO]$ core and the corresponding substituents. Furthermore, each urea moiety adopts a *transoid* conformation with respect to the NH and the carbonyl oxygen. In terms of extended solid-state structure, the bis(urea) engages in both intra- and intermolecular hydrogen bonding between the NH protons and the carbonyl oxygens. This hydrogen bonding results in the formation of linear supramolecular helices along the crystallographic *a* axis. The observed propensity of **87** toward hydrogen bonding brings up an important practical consideration regarding the use of these urea proligands. After isolation, these compounds must be rigorously dried (with heat, *in vacuo*, for 24 hours) to remove water that is retained after workup and purification. Several early attempts to prepare group 4 ureate complexes using incompletely dried bis(urea) **87** led to impure compounds, likely resulting from partial hydrolysis of the intended products by residual water.

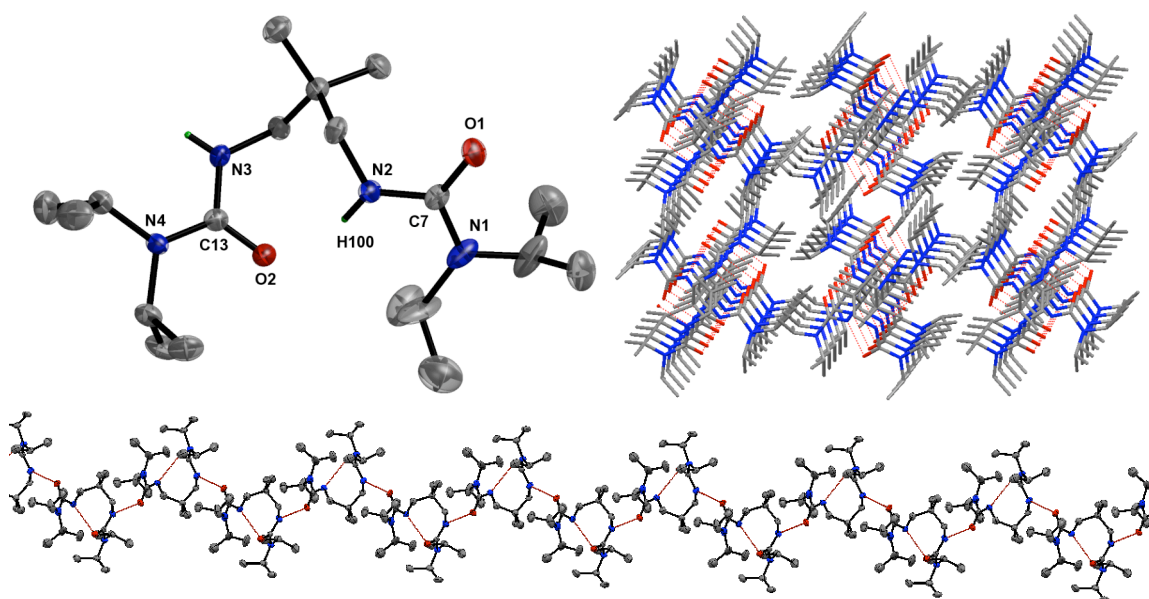


Figure 2.6. ORTEP representation of the molecular structure of **87** (top left) (ellipsoids plotted at 50% probability, hydrogens except those on N2 and N3 omitted for clarity, displayed hydrogen atoms located from unassigned electron density and their positions refined); view approximately down the crystallographic *a* axis (top right); illustration of linear hydrogen bonding network (bottom) (H-bonds in red). Selected bond lengths (Å), bond and torsion angles (°): N1–C7, 1.368(3); N2–C7, 1.350(3); O1–C7, 1.235(3); N3–C13, 1.364(3); N4–C13, 1.361(3); O2–C13, 1.244(3); O2–H100, 2.00(3); sum of angles about N1, 359.6(6); sum of angles about C7, 360.0(6); sum of angles about N2, 358(4); average torsion angle through N1–C7: 13.2(4).

While only four examples are given here, the synthetic routes outlined in equations 2.2 and 2.3 can be used to prepare a range of structurally varied urea proligands. This will allow future researchers to access a variety of ligand architectures, enabling the formation of diverse ureate-supported metal complexes.

2.2.2 Synthesis of Dichlorobis(ureato) Complexes

Using the urea proligands described above, various synthetic routes to metal dichlorides were initially considered. Attempted reactions of TiCl_4 with the sodium ureate derived from **85** and $\text{Na}[\text{N}(\text{SiMe}_3)_2]$ resulted in an impure solid after workup.

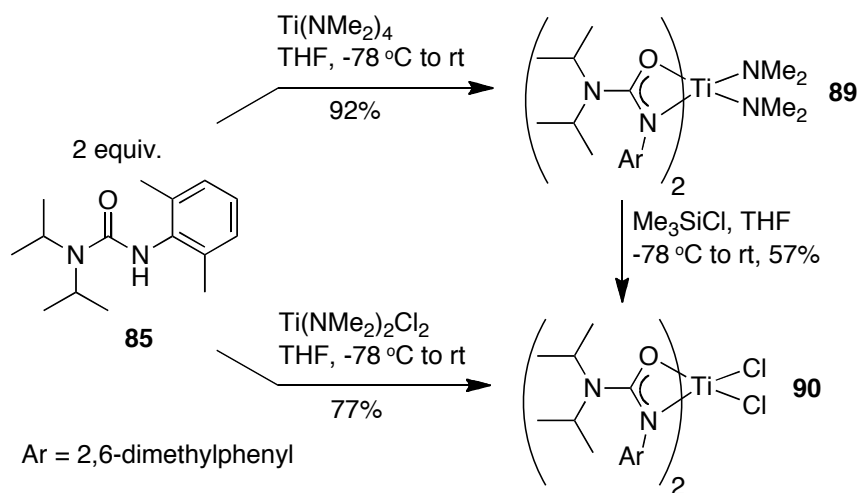
Unfortunately, the low solubility of the resulting titanium dichloride compound (**90**) in many common hydrocarbon solvents makes removal of the NaCl byproduct very difficult. Therefore, a synthetic protocol that avoids the use of transmetallation was sought. Direct protonolysis of known precursors of the type $M(\text{NMe}_2)_2\text{Cl}_2$ is attractive in this regard, as the only byproduct is a volatile amine. While $\text{Ti}(\text{NMe}_2)_2\text{Cl}_2$ was prepared according to a published procedure,¹⁷⁰ $\text{Zr}(\text{NMe}_2)_2\text{Cl}_2(\text{DME})$ (DME = 1,2-dimethoxyethane) was synthesized *via* a conproportionation reaction between $\text{Zr}(\text{NMe}_2)_4$ and $\text{ZrCl}_4(\text{THF})_2$ in the presence of an excess of DME, giving the product in 86% yield without the need for recrystallization. This route is both more convenient and more economical than the previously reported synthesis.¹⁷¹

The synthesis of L_2TiCl_2 complex **90** using proligand **85** can be accomplished in two ways: directly, involving protonolysis of $\text{Ti}(\text{NMe}_2)_2\text{Cl}_2$ in THF, and *via* the reaction of intermediate bis(amido) complex **89** with excess chlorotrimethylsilane (Scheme 2.2). Both of these routes are feasible, with the direct protonolysis method giving a higher overall yield (77% versus 52%). It should be noted that attempted syntheses of bis(amidato)dichloro compounds using either of these methods was unsuccessful. The reactions result in crude mixtures that contain multiple products, each exhibiting incomplete protonolysis or chlorination.

^1H NMR spectroscopy of **90** indicates that the two isopropyl groups on the distal nitrogen are inequivalent, as two distinct resonances for the methyl protons are observed at δ 0.54 and 1.38. This is in contrast to the corresponding signal for the bis(dimethylamido) complex **89**, which appears as a very broad peak between δ 0.6 and 1.7. In addition, two distinct signals at δ 2.90 and 3.59 are observed for the isopropyl

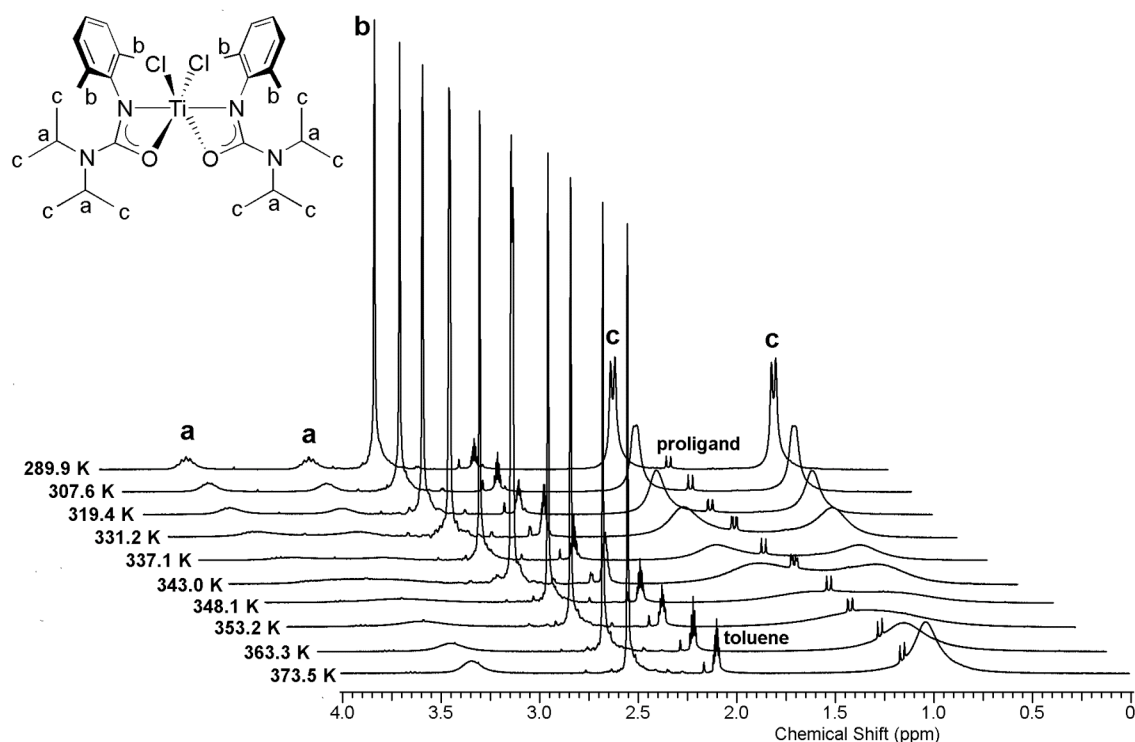
methine protons of **90**, while this resonance is broadened almost into the baseline between δ 3.5 and 3.7 for complex **89**. Notably, both isopropyl groups are equivalent in the proligand **85**. These observations are consistent with a greater degree of restricted C–N bond rotation in **90** relative to both **85** and **89**. This is likely due to increased electron donation from the backbone nitrogen in the dichloride complex than for the bis(amido), resulting in appreciable double bond character. This hindered rotation must be an electronic effect, since the isopropyl groups in both **89** and **90** are distal to the metal center, and **90** is less sterically crowded than **89**. The hindered rotation indicated by ^1H NMR spectroscopy for these ureate complexes stands in contrast to the solution-phase behaviour noted by Arnold and co-workers, who did not observe similar spectroscopic features for guanidinate complexes **16** and **83**.⁸³

Scheme 2.2. Synthesis of **90** *via* two routes.



The nature of the C–N bond rotation in complex **90** was investigated using variable temperature ^1H NMR spectroscopy. Figure 2.7 shows a series of spectra collected between 298.9 and 373.5 K. As described above, there are two sets of isopropyl signals evident at room temperature (top spectrum). As the temperature is increased, these

signals broaden and coalesce near 345 K. At the high temperature limit, the methyl (c) and methine (a) protons resonate as single but broad signals. These data were used to calculate the ΔG^\ddagger of this bond rotation process at the coalescence temperature.¹⁷² The value obtained in this manner, $\Delta G^\ddagger(348 \text{ K}) = 16.1 \pm 0.5 \text{ kcal mol}^{-1}$, is an indirect measure of the degree of electron-donation by the distal $\text{N}(i\text{-Pr})_2$ group; performing a similar analysis on the bis(amido) complex **89**, whose signals coalesce at room temperature, gives $\Delta G^\ddagger(298 \text{ K}) = 13.7 \pm 0.8 \text{ kcal mol}^{-1}$.



$$\Delta G^\ddagger(T_c) = RT_c[22.96 + \ln(T_c/\Delta\nu)], \text{ where } \Delta\nu = 246.0 \text{ Hz, } T_c = 348.1 \text{ K (signal c)}$$

$$\Delta G^\ddagger(348 \text{ K}) = 16.1 \pm 0.5 \text{ kcal mol}^{-1} \text{ (error estimated by determining } \Delta G^\ddagger \text{ at } T_c \pm 10 \text{ K)}$$

Figure 2.7. ^1H NMR spectra (300 MHz, C_7D_8) showing C–N(*i*-Pr)₂ bond rotation dynamic behaviour for complex **90** with coalescence at 348.1 K. Proligand constitutes <5% of the composition. Performing the above calculation using signal ‘a’ gives an identical ΔG^\ddagger value.

Compound **90** was recrystallized from a hot toluene solution for an X-ray crystallographic study; the solid-state molecular structure is shown in Figure 2.8. The complex exhibits distorted octahedral geometry and rigorous C_2 symmetry, with the two chloride ligands oriented *cis* to one another. Evidence of electron donation from the disubstituted nitrogen is apparent from the metrical parameters, consistent with the aforementioned NMR spectroscopic evidence. The sum of the bond angles about N2 is $360(2)^\circ$, indicating sp^2 -hybridization, the C1–N1 and C1–N2 bond lengths are similar ($1.35(1)$ Å versus $1.37(2)$ Å), indicating electron-delocalization, and there is a high degree of coplanarity between the chelate ring and the trigonal plane about N2 (torsion angle $7(1)^\circ$), necessary for π -donation to occur. These structural features are analogous to those noted by Arnold and co-workers for guanidinate complexes **16**, **83**, and **84**.⁸³ Unfortunately, the low quality of the diffraction data obtained eliminates the possibility of a more detailed structural analysis.

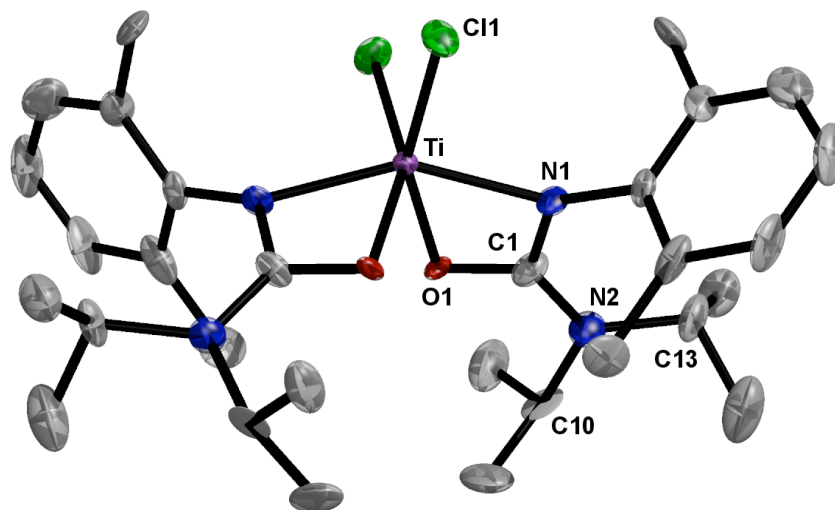
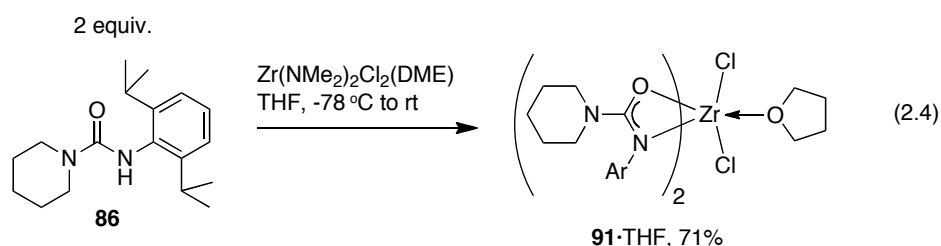


Figure 2.8. ORTEP representation of the molecular structure of **90** (ellipsoids plotted at 50% probability, disordered toluene molecule removed with SQUEEZE routine,¹⁷³ hydrogens omitted for clarity) with selected bond lengths (Å), bond and torsion angles ($^\circ$): Ti–N1, 2.044(9); Ti–O1, 2.006(7); Ti–Cl1, 2.271(3); C1–N1, 1.35(1); C1–O1, 1.30(1); C1–N2, 1.37(2); N1–Ti–O1, 64.8(3); N1–Ti–N1*, 151.4(4); sum of angles about N2, 360(2); N1–C1–N2–C13, 7(1).

Formation of a dichlorobis(ureato)zirconium complex through a reaction between proligand **86** and $\text{Zr}(\text{NMe}_2)_2\text{Cl}_2(\text{DME})$ in THF gives adduct **91**•THF (eqn. 2.4). The ^1H NMR spectrum of **91**•THF reveals a high degree of fluxional behaviour in solution, likely due to exchange of the labile THF ligand and conversion between coordination isomers. Similar behaviour was noted previously for bis(amidato) complex **67**. At higher temperature (345 K), the spectrum simplifies considerably, consistent with a time-averaged C_2 symmetric coordination isomer.



Crystals for X-ray diffraction were obtained from a cold pentane solution of **91**•THF; the solid-state molecular structure is shown in Figure 2.9. The geometry is distorted pentagonal bipyramidal, with the ureate ligands and the THF molecule in equatorial positions. The chlorides occupy the apical sites and are slightly canted toward the THF ligand, with a Cl1-Zr-Cl2 angle of $165.24(2)^\circ$. The ureates are arranged to give a molecule with C_1 symmetry. As for the solid-state structure of complex **90**, there is evidence of electron delocalization between the tertiary amino substituent and the chelate ring (C1-N1 1.316(3) Å versus C1-N2 1.337(3) Å, sum of angles about N2 is $357.6(6)^\circ$, torsion angle between O1-C1-N2-C2 is $8.8(3)^\circ$). Subjecting **91**•THF to high vacuum for 48 hours results in removal of the THF ligand to give **91**. The ^1H NMR spectrum of this compound is consistent with C_1 symmetry. Unfortunately, **91** is a poorly soluble microcrystalline solid; attempts to obtain single crystals of this compound for X-ray diffraction have failed.

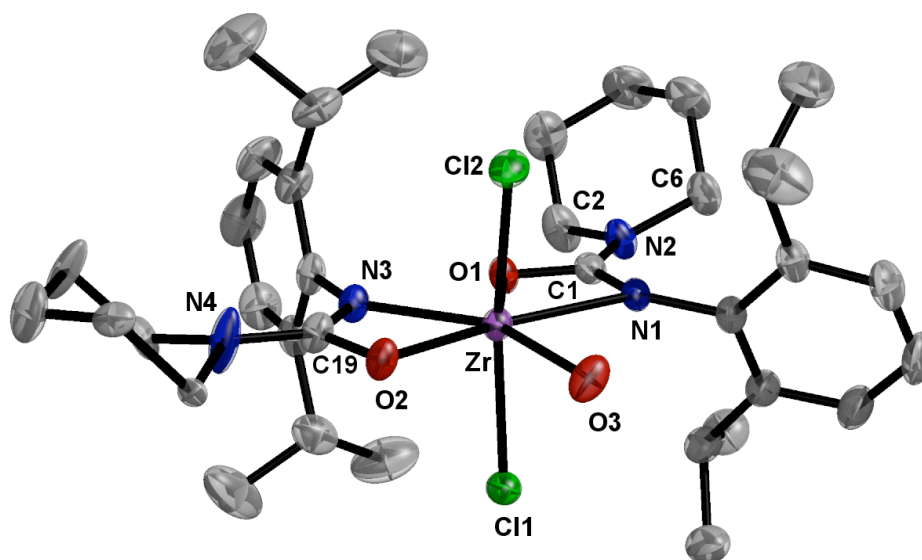
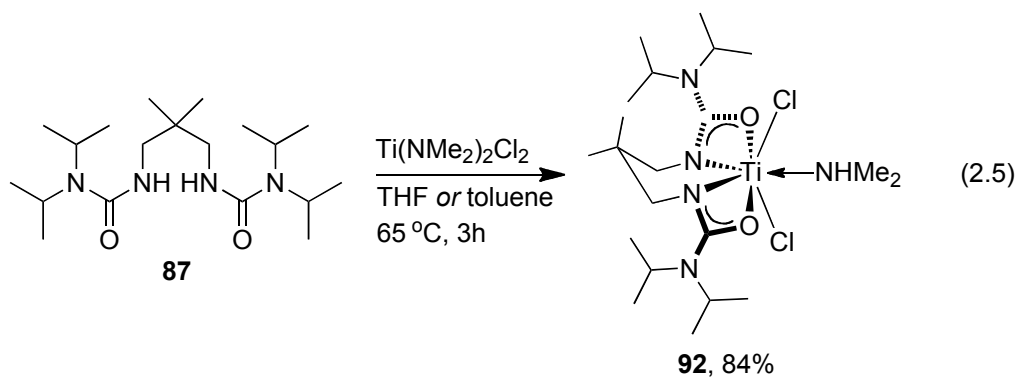
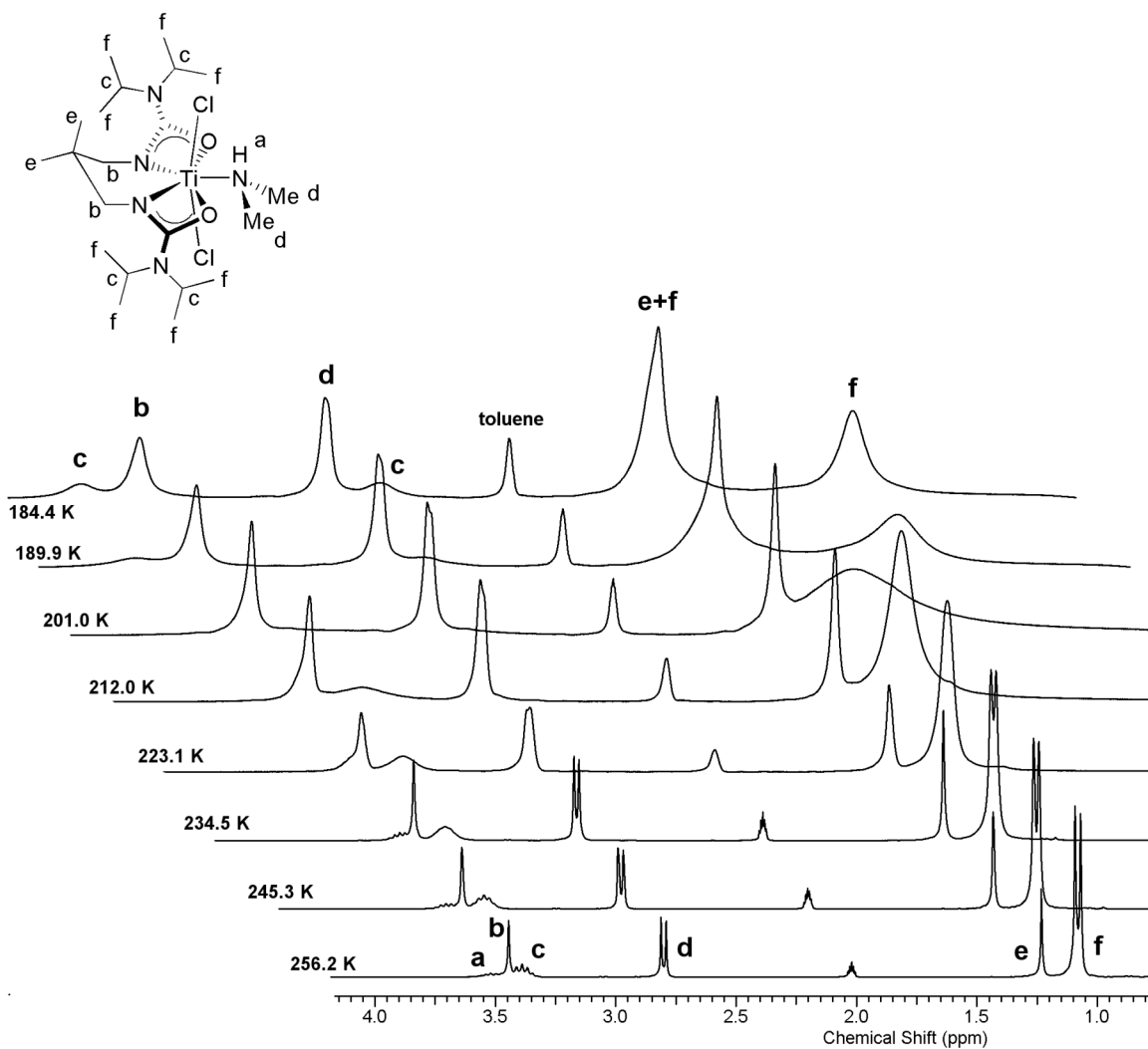


Figure 2.9. ORTEP representation of the molecular structure of **91**•THF (ellipsoids plotted at 50% probability, carbons of the THF ring, disordered pentane, and hydrogens omitted for clarity, one conformation of the N4 piperidine ring shown) with selected bond lengths (Å), bond and torsion angles (°): Zr–N1, 2.285(2); Zr–O1, 2.092(2); Zr–Cl1, 2.437(1); Zr–O3, 2.297(2); C1–N1, 1.316(3); C1–O1, 1.300(3); C1–N2, 1.337(3); N1–Zr–O1, 59.63(6); Cl1–Zr–Cl2, 165.24(2); sum of angles about N2, 357.6(6); O1–C1–N2–C2, 8.8(3).

Zirconium bis(amidato) complex **67** and bis(ureato) **91**•THF are both observed to undergo fluxional processes in solution. In order to minimize this behaviour, a tethered ureate ligand was envisioned to form discrete, well-defined dichloride complexes. A previous researcher in the Schafer group used a tethered bis(amidato) ligand to synthesize seven-coordinate, pentagonal bipyramidal zirconium and hafnium dibenzyl complexes (**68** and **69**) that exhibit the same coordination geometry observed for **91**•THF.¹⁷⁴ Preparation of a tethered bis(ureato)titanium dichloride can be accomplished by heating one equivalent of proligand **87** with $\text{Ti}(\text{NMe}_2)_2\text{Cl}_2$ in THF or toluene. This reaction leads to the exclusive formation of **92** (eqn. 2.5) in good yield, with no formation of side-products or bridging oligomers.



The ^1H NMR spectrum of **92** contains one set of resonances for the bis(ureato) ligand protons, indicating a high degree of magnetic equivalence. In addition, there is evidence that one equivalent of dimethylamine is present as a neutral donor, even when using THF as the reaction solvent. A doublet at δ 2.91 and a broadened multiplet at δ 3.64 correspond to the methyl groups and the NH proton respectively. Unlike titanium bis(ureato) **90**, there is only one signal corresponding to the methyl protons of the isopropyl groups, a doublet at δ 1.17, indicative of a lower barrier to rotation about the C–N bond. Variable temperature NMR spectroscopy reveals that low temperatures (~ 200 K) are required to observe signal coalescence. Determination of the ΔG^\ddagger of rotation gives a value of 9.1 ± 0.5 kcal mol $^{-1}$ at 201 K (Figure 2.10). This barrier is significantly lower than that for complex **90** (16.1 ± 0.5 kcal mol $^{-1}$ at 348 K), or even bis(amido) **89** (13.7 ± 0.8 kcal mol $^{-1}$ at 298 K). In the case of **92**, the presence of the neutral dimethylamine ligand results in a fourteen-electron, rather than twelve-electron, titanium center. This would presumably lower the amount of electron density donated from the backbone diisopropylamino substituents. Subjecting **92** to high vacuum at 65 °C for sixteen hours results in no change in composition. Evidently, the dimethylamino ligand is tightly bound to the titanium center.



$$\Delta G^\ddagger(T_c) = RT_c[22.96 + \ln(T_c/\Delta\nu)], \text{ where } \Delta\nu = 242.8 \text{ Hz, } T_c = 201.0 \text{ K (signal f)}$$

$$\Delta G^\ddagger(201 \text{ K}) = 9.1 \pm 0.5 \text{ kcal mol}^{-1} \text{ (error estimated by determining } \Delta G^\ddagger \text{ at } T_c \pm 10 \text{ K)}$$

Figure 2.10. Selected ^1H NMR spectra (300 MHz, C_7D_8) showing C–N(*i*-Pr) $_2$ bond rotation dynamic behaviour for complex **92** with coalescence at 201.0 K. Performing the above calculation using signal c gives an identical ΔG^\ddagger value.

The solid-state molecular structure of **92** is shown in Figure 2.11. The titanium center has distorted pentagonal bipyramidal geometry, with the chlorides in apical positions, and the ureate ligand donor atoms in the equatorial plane. The observed coordination geometry is entirely analogous to that of zirconium complex **91**•THF. This also

represents the first example of a seven-coordinate titanium complex supported by amidate or ureate ligands. The solid-state structure confirms that dimethylamine is in fact bound as a neutral ligand. The Ti–N5 length is much longer than the Ti–N1 length (2.2889(9) Å versus 2.0345(9) Å); furthermore, N5 is pyramidalized, as expected for an sp^3 -hybridized center. The Ti–Cl bond lengths in **92** are also considerably longer than those of the non-tethered bis(ureato) **90** (2.3751(3) Å versus 2.271(3) Å), due to the increased coordination number and electron count of the titanium center in **92**.

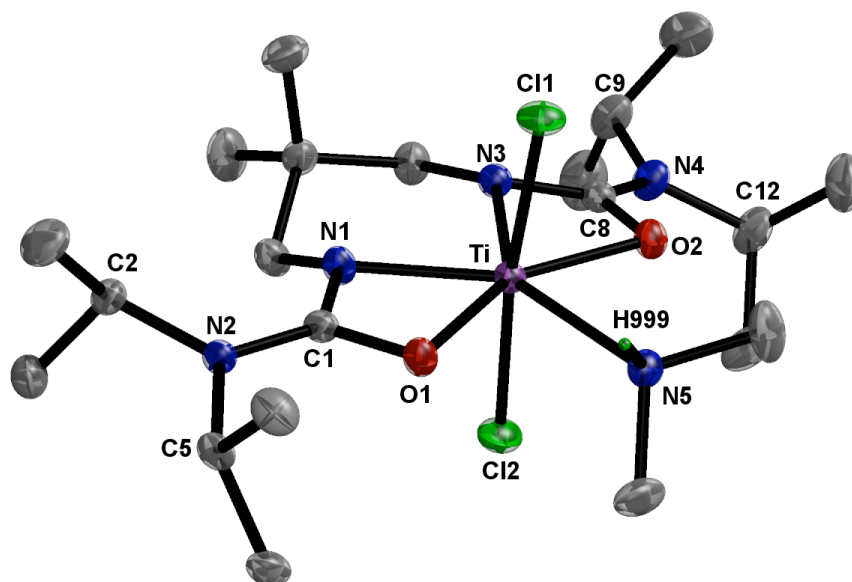


Figure 2.11. ORTEP representation of the molecular structure of **92** (ellipsoids plotted at 50% probability, benzene molecule and hydrogens except H999 not shown, H999 located from unassigned electron density and its position refined) with selected bond lengths (Å), bond and torsion angles (°): Ti–N1, 2.0345(9); Ti–O1, 2.0583(8); Ti–N3, 2.0709(9); Ti–O2, 2.0190(7); Ti–N5, 2.2889(9); Ti–Cl1: 2.3751(3); C1–N1, 1.334(1); C1–O1, 1.297(1); C1–N2, 1.343(1); N1–Ti–O1, 63.63(3); Cl1–Ti–Cl2, 172.46(1); sum of angles about N2, 359.8(3); O1–C1–N2–C5, 13.8(2).

An examination of the metrical parameters again reveals evidence of electron-donation from the diisopropylamino substituents: C1–N1, 1.334(1) Å versus C1–N2, 1.343(1) Å, the sum of angles about N2 is 359.8(3)°, and the torsion angle between O1–C1–N2–C5 is 13.8(2)°. This is in stark contrast to the aforementioned spectroscopic

results, which suggest a lesser degree of electron-donation from the amino groups at room temperature in solution. The discrepancy between these two sets of data highlights an important point regarding these complexes: that solid-state evidence is necessary, but not sufficient to characterize a ureate ligand as strongly electron-donating. Solution-phase data are more reliable indicators in this regard, as solid-state molecular structures are generally determined by X-ray diffraction at low temperature. Such solid-state characterization can be deceptive, especially when even small amounts of thermal energy can affect the dynamic, solution-phase behaviour of a compound.

Synthesis of the corresponding zirconium complex (**93**) was accomplished in the same manner as for **92**. Performing the reaction in THF leads to a mixture of two products in a 1:1 ratio, as indicated by ^1H NMR spectroscopy. One product is the dimethylamine adduct, analogous to **92**, while the other is assigned as the THF adduct. Performing the reaction in toluene leads to the exclusive formation of the dimethylamine adduct **93** in 89% yield. The spectroscopic data are nearly identical to the titanium congener, with the only major difference being an upfield shift for the *NH* proton to δ 2.97. The solid-state molecular structure of **93** is shown in Figure 2.12. Unlike the molecular structure for **92**, there is a mirror plane that bisects the zirconium complex through the Zr–N5 bond, rendering both halves of the molecule equivalent. The Zr–Cl bond distances are slightly longer than for **91**•THF (2.4846(5) Å versus 2.437(1) Å), possibly due to tighter binding by the tethered ligand: the Zr–N_{ureate} bond length is considerably shorter in **93** (2.170(1) Å) than in **91**•THF (average Zr–N_{ureate}: 2.231(1) Å). This is likely due to the differing electronic natures of the *N*-aryl versus *N*-alkyl substituents in **91**•THF and **93** respectively.

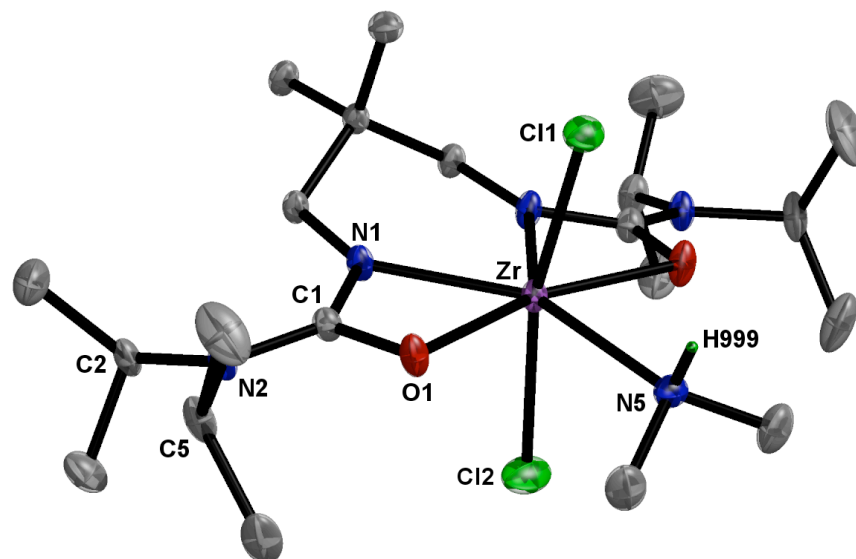


Figure 2.12. ORTEP representation of the molecular structure of **93** (ellipsoids plotted at 50% probability, hydrogens except H999 not shown, H999 located from unassigned electron density and its position refined) with selected bond lengths (Å), bond and torsion angles (°): Zr–N1, 2.170(1); Zr–O1, 2.176(1); Zr–N5, 2.445(2); Zr–Cl1: 2.4846(5); C1–N1, 1.332(2); C1–O1, 1.310(2); C1–N2, 1.345(2); N1–Zr–O1, 60.19(3); Cl1–Zr–Cl2, 162.98(2); sum of angles about N2, 359.9(3); O1–C1–N2–C5, 12.0(2).

With the exception of titanium complex **90**, each of the dichloride compounds described above retain neutral ligands from either the reaction solvent, or the evolved dimethylamine byproduct. This is likely due to the poor electron-donating capabilities of the chloride ligands, and mirrors the situation observed for amidate-supported dichloride **67**. It seems that the increased electron-donation afforded by the ureate ligand is insufficient to prevent adduct formation under these conditions. Easy access to donor-free bis(ureato) complexes would be desirable in the context of olefin polymerization, as the presence of neutral donors may inhibit catalysis. Group 4 dialkyl compounds are also commonly employed as olefin polymerization precatalysts. The larger alkyl ligands can afford greater steric protection than chlorides, which may enable the synthesis of donor-free complexes.

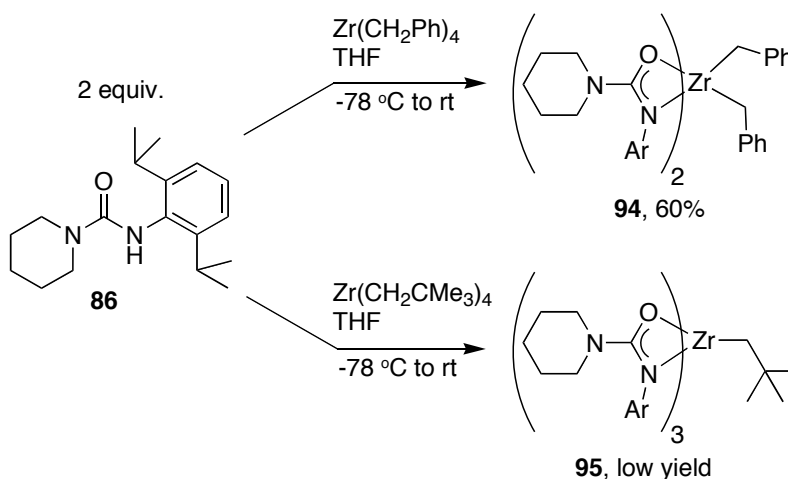
2.2.3 Synthesis of Ureate-Supported Dialkyl Complexes

The most common synthetic route used to prepare group 4 dialkyl compounds is through salt metathesis between dichloride compounds with alkyl lithium or Grignard reagents. Given previously observed difficulties with this reaction when using amidate supporting ligands, and the success in using protonolysis with urea prolignands, direct reactions between ureas and tetraalkyl zirconium compounds were explored. Treatment of $\text{Zr}(\text{CH}_2\text{Ph})_4$ with two equivalents of prolignand **86** at $-78\text{ }^\circ\text{C}$ in THF results in the formation of dibenzyl complex **94** in moderate recrystallized yield (Scheme 2.3, top pathway). ^1H NMR spectroscopy of the purified compound confirms the formulation as L_2ZrBn_2 : relative integration of the isopropyl methine multiplet and the benzyl methylene singlet gives a 1:1 ratio. The NMR spectra also give an indication of the solution-phase coordination geometry. There are two inequivalent signals for the isopropyl methyl groups, resonating as doublets at δ 1.11 and 1.38, while there is a single multiplet for the methine protons at δ 3.16. In addition, one singlet at δ 2.39 is observed for the methylene protons of the benzyl ligands. The ^{13}C NMR spectrum contains signals for seven aliphatic carbons, including one at δ 75.4 for the carbons attached to zirconium, and a diagnostic signal at δ 166.8 for the central carbon of a κ^2 -chelating ureate. No evidence of THF coordination is observed by NMR spectroscopy, in contrast to a previously reported bis(amidato)dibenzylhafnium complex.¹¹⁹

These spectral features are indicative of a C_2 -symmetric coordination geometry, with two equivalent κ^2 -(*N,O*) ureate ligands and two equivalent benzyl groups. The inequivalence of the isopropyl methyl groups is due to hindered rotation about the *i*-Pr–Ar bond, as hindered rotation about N–Ar or inequivalent ligand environments

would similarly split the methine protons into two groups. All of this is consistent with **94** as a six-coordinate, distorted octahedral complex. The likely coordination mode has the benzyl ligands in a *cis*-disposition, and the ureate nitrogens oriented *trans*, proposed by analogy to amidate complexes with a sterically similar ligand. Unfortunately, attempts to grow single crystals of **94** for definitive assignment by X-ray crystallography have thus far been unsuccessful.

Scheme 2.3. Synthesis of dibenzyl complex **94** and unexpected formation of tris(ureato) **95**.



Performing an analogous reaction with $\text{Zr}(\text{CH}_2\text{CMe}_3)_4$ and **86** leads to a mixture of products, from which can be isolated an unexpected tris(ureato) neopentyl complex **95** in low yield (Scheme 2.3, bottom pathway). Careful control of reaction stoichiometry and use of alternate solvents (toluene, hexanes) does not improve the reaction outcome. Furthermore, increasing the proligand-to-zirconium ratio to 3:1 also leads to a mixture of products, and a similar low yield of **95**. ^1H NMR spectroscopy and mass spectrometry of this compound are not consistent with the intended bis(ureato) complex, and instead indicate its composition as $\text{L}_3\text{Zr}(\text{CH}_2\text{CMe}_3)$. Fortunately, cooling a pentane solution of

the crude product mixture to -35 °C led to the deposition of a few single crystals; the solid-state molecular structure as determined by X-ray crystallography is shown in Figure 2.13. All NMR spectroscopy of **95** was performed on this crystalline sample in order to ensure consistency between the two methods of characterization.

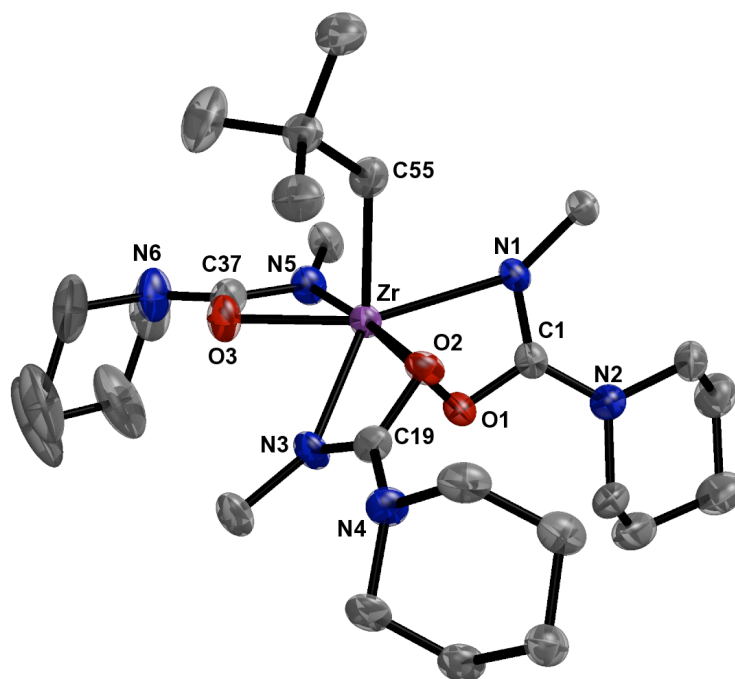
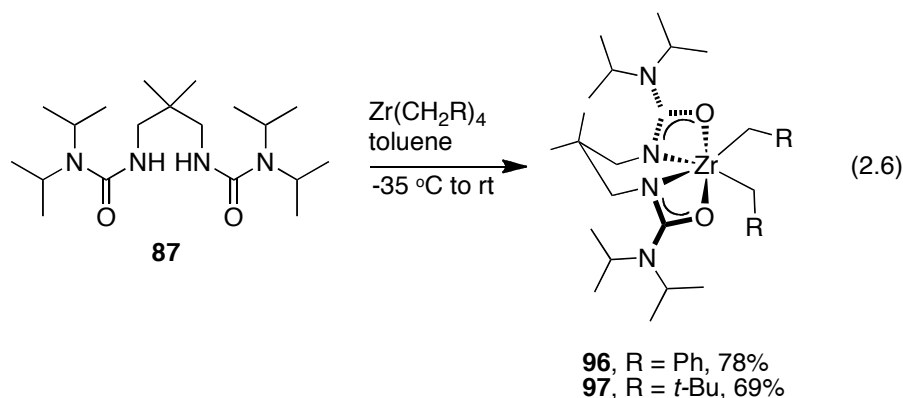


Figure 2.13. ORTEP representation of the molecular structure of **95** (ellipsoids plotted at 50% probability, hydrogens and all but *ipso*-carbons of aromatic groups removed for clarity, disordered pentane solvent removed with SQUEEZE routine¹⁷³) with selected bond lengths (Å), bond and torsion angles (°): Zr–N1, 2.401(2); Zr–N3, 2.276(3); Zr–N5, 2.359(2); Zr–O1, 2.134(1); Zr–O2, 2.199(2); Zr–O3, 2.136(2); Zr–C55, 2.279(3); C1–N1, 1.325(3); C1–O1, 1.309(3); C1–N2, 1.354(2); average ureate bite angle, 58.13(8); average angle between C–Zr–C', 109.2(9); sum of angles about N2, N4, N6: 359.9(6), 354.4(6), 355.6(9); N1–C1–N2–C14: 19.7(4).

The complex is seven-coordinate, with three κ^2 -ureate ligands; however, the ligand arrangement about zirconium does not conform to the typical pentagonal bipyramidal or mono-capped octahedral geometries. If the ureate ligands are instead viewed as occupying only *one* coordination site, the geometry can be assigned as distorted tetrahedral: the average angle between any two carbons, either as the central atom in the

ureate chelate or as the neopentyl methylene, through zirconium is $109.20(9)^\circ$ (average deviation, 10.49°). Each of the three ureate ligands adopts a non-symmetric binding mode, where the Zr–O lengths (2.134(1)–2.199(1) Å) are markedly shorter than the Zr–N lengths (2.276(3)–2.401(2) Å). This is likely due to steric crowding between the three bulky 2,6-diisopropylphenyl groups attached to the nitrogen atoms. As in previously characterized ureate complexes, the disubstituted amino group attached to the chelate shows evidence of electron donation. The sum of the angles about N2, N4, and N6 are all approximately 360° , the C–N lengths in the $[N_2CO]$ core are all between 1.320(3) Å and 1.361(4) Å, and the torsion angles between the NR_2 plane and the N–C–O plane average to $15.8(4)^\circ$.

The inability to reliably isolate **95**, even with proper stoichiometry, suggests that disproportionation reactions through ligand redistribution could be responsible for its formation, possibly through alkylidene intermediates.¹⁷⁵ In order to reduce the likelihood of ligand redistribution and/or alkylidene formation, the sterically open tethered prolignand **87** was tested for the synthesis of dialkyl derivatives. Equation 2.6 outlines the preparation of both benzyl (**96**) and neopentyl (**97**) derivatives from **87** and $Zr(CH_2R)_4$ in 78% and 69% yield respectively. Unlike the situation outlined above with prolignand **86**, the formation of bis(neopentyl) complex **97** is accomplished with minimal contamination by other compounds. A 1H NMR spectrum of the crude reaction mixture from the synthesis of **97** indicates the presence of a byproduct, which is tentatively assigned as the homoleptic tetrakis(ureato) complex; however, the byproduct is insoluble in pentane, and therefore easily removed by filtration. Lowering the reaction temperature to $-78^\circ C$ further reduces the amount of this byproduct, but does not prevent its formation.



The NMR spectral characteristics of compounds **96** and **97** are very similar, differing only in the signals associated with the alkyl ligands, and minor chemical shift changes for the ureate signals. The ^1H NMR spectra contain single resonances for each type of proton, including those of the isopropyl groups attached to the distal ureate nitrogen; ^{13}C NMR spectroscopy reveals a similar high degree of magnetic equivalence. This does not only indicate high molecular symmetry, but also fast rotation about the *i*-Pr₂N–C bonds, suggesting reduced π -donation by the distal nitrogen atoms.

In order to compare this solution phase behaviour with solid-state structural parameters, X-ray crystallographic characterization was undertaken. Repeated attempts to grow single crystals of compound **96** resulted in microcrystalline material that gave weak diffraction patterns; however, single crystals of compound **97** were obtained from a cold pentane solution. The solid-state molecular structure of **97** is shown in Figure 2.14, confirming the ligand arrangement about zirconium. The complex is six-coordinate, with the four donor atoms of the bis(ureate) ligand in a planar arrangement. As for **95**, there is no immediately obvious six-coordinate geometry to which this complex conforms; it is therefore best described as a distorted tetrahedron, with each ureate occupying one coordination site (average C–Zr–C' angle: 109.33(6) $^\circ$, deviation: 9.71 $^\circ$). An examination of the metrical parameters of complex **97** reveals evidence of π -electron donation by the

ureate diisopropylamino groups (sp^2 -hybridized nitrogens, electron delocalization, co-planar arrangement), in contrast to the solution-phase behaviour noted above. A similar discrepancy was observed for the dichloride complexes **92** and **93** supported by the same ligand. In those cases, it was postulated that the increased electron count of the metal center, due to the presence of an additional neutral ligand, is responsible for the diminished electron-donation by the ureate in solution. Complex **97** contains no such neutral donor; therefore, an alternate explanation for this behaviour is required. It is plausible that the structure of the ureate ligand is somehow responsible. In order to investigate this possibility, analogous dialkyl complexes were prepared using proligand **88**. This framework retains the diisopropylamino substituents, but replaces the electron-rich alkyl-tether with an electron-withdrawing biaryl-tether.

Treatment of $Zr(CH_2R)_4$ with proligand **88** results in the facile formation of complexes **98** and **99** in 75% and 54% recrystallized yield respectively (eqn. 2.7). 1H NMR spectroscopy of the purified compounds indicates the ligand binds in a C_2 -symmetric fashion, as the methyl groups attached to the biaryl tether are equivalent. The methylene protons of the $Zr-CH_2R$ group resonate as an AB quartet in both cases, due to the axial chirality of the ureate ligand. ^{13}C NMR spectra of **98** and **99** contain a single resonance for the ureate carbon at ~ 168 ppm, diagnostic of a κ^2 -chelating binding mode. All of these spectral features are in striking contrast to those observed previously for biaryl-tethered bis(amidato) benzyl compounds.¹⁰⁶

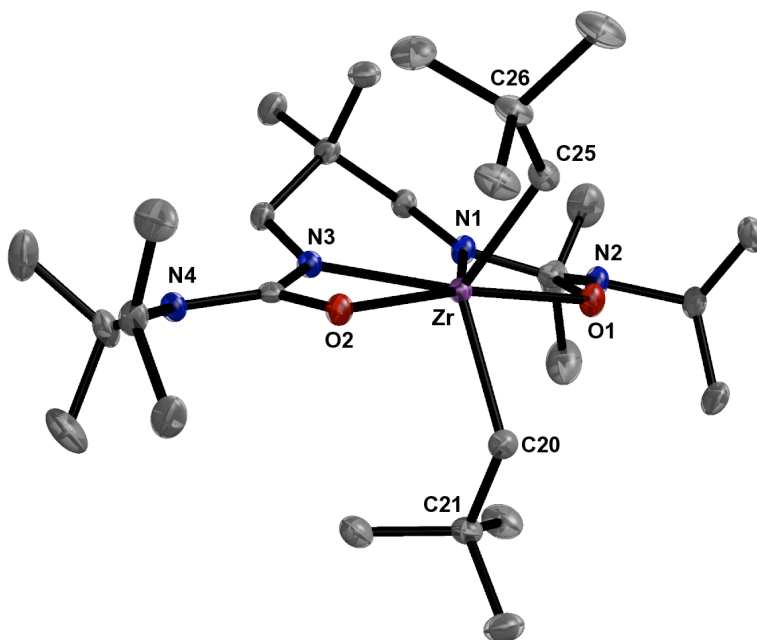
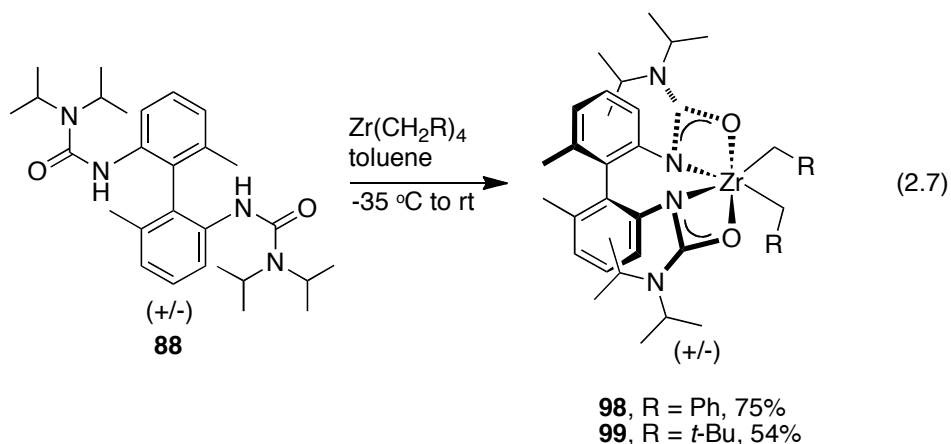


Figure 2.14. ORTEP representation of the molecular structure of **97** (ellipsoids plotted at 50% probability, hydrogens removed for clarity) with selected bond lengths (Å), bond and torsion angles (°): Zr–N1, 2.193(2); Zr–N3, 2.183(1); Zr–O1, 2.208(1); Zr–O2, 2.240(1); Zr–C20, 2.266(2); Zr–C25, 2.259(2); C1–N1, 1.331(2); C1–O1, 1.295(2); C1–N2, 1.351(2); N1–Zr–O1, 59.32(4); N1–Zr–N3, 76.33(5); average angle between C–Zr–C', 109.3(6); Zr–C20–C21, 123.8(1); Zr–C25–C26, 130.7(1); sum of angles about N2, N4: 359.5(3), 359.2(3); N1–C1–N2–C5: 14.7(3).



A major difference in the solution-phase behaviour between the alkyl-tethered complexes (**96**, **97**) and the biaryl-tethered complexes (**98**, **99**) is in the disposition of NMR signals corresponding to the diisopropylamino substituents on the ureate chelate. As noted above, fast rotation about the *i*-Pr₂N–C bond on the NMR timescale was

observed for **96** and **97**, resulting in equivalent methyl and methine protons. The ^1H NMR signals for isopropyl groups in **98** and **99**, however, are inequivalent and broad. The two sets of methine resonances are separated by ~ 1 ppm. The methyl signals are similarly separated, with the upfield resonance (centered around δ 0.75) further split into two broad, overlapping signals. This splitting is presumably due to the chiral environment about the metal center, rendering these methyl groups diastereotopic. The isopropyl carbons appear as very broad resonances in the ^{13}C NMR spectra, preventing a reliable chemical shift assignment in the case of **98**. This behaviour is indicative of slow rotation about the *i*-Pr₂N–C bond, in stark contrast to the situation for **96** and **97**. There are two possible explanations for this difference: first, greater steric compression by the biaryl-tether relative to the alkyl-tether hinders rotation about this bond; and second, the π -withdrawing aromatic substituents of the biaryl-tether induce a greater degree of π -donation by the diisopropylamino lone pair. As the distal nitrogen of the ureate ligand is spatially removed from the tether, the latter rationale is the most reasonable.

Single crystals of **98** were deposited from a cold pentane solution; the solid-state molecular structure is shown in Figure 2.15 (left). The complex adopts a coordination geometry analogous to that of the alkyl-tethered complex **97** described above, best described as distorted tetrahedral. Metrical evidence for π -donation from the *i*-Pr₂N group is also apparent. One other noteworthy aspect of the structure of **98** is that one of the benzyl ligands adopts an η^2 -bonding mode (Figure 2.15, right).¹⁷⁶ The Zr–C36–C37 angle ($92.6(1)^\circ$) and Zr–C37 distance ($2.759(2)$ Å) are in the range of other reported η^2 -interactions.¹⁷⁷ The second benzyl ligand is, however, clearly η^1 -bound. Due to the lack of solution-phase NMR spectroscopic evidence for η^2 -benzyl ligands, this

interaction is presumably not maintained in solution; therefore, both benzyls should be considered as time-averaged η^1 -ligands.¹⁷⁷ This exchange between η^1 - and η^2 -binding modes may be responsible for the broad signals observed by NMR spectroscopy. Single crystals of complex **99** were also obtained; however, the crystal morphology (leaf) led to a weak diffraction pattern. Therefore, **99** is proposed to be structurally analogous to **98**, based on the similar solution-phase spectroscopic features.

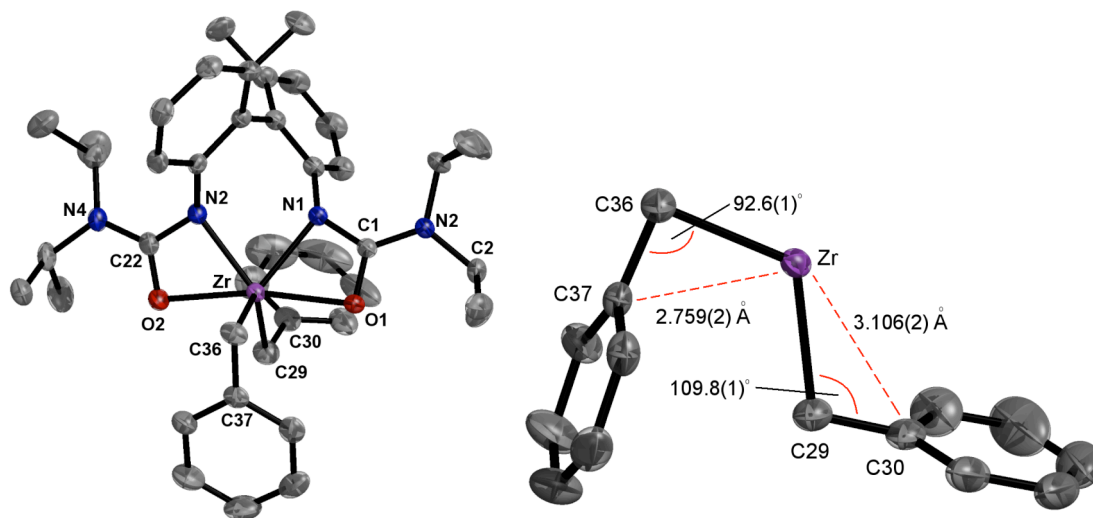


Figure 2.15. ORTEP representation of the molecular structure of **98** (left) and abbreviated structure showing η^2 -benzyl interaction (right) (ellipsoids plotted at 50% probability, hydrogens removed for clarity) with selected bond lengths (Å), bond and torsion angles (°): Zr–N1, 2.195(1); Zr–N3, 2.183(1); Zr–O1, 2.221(1); Zr–O2, 2.257(1); Zr–C25, 2.265(2); Zr–C29, 2.282(2); C1–N1, 1.334(2); C1–O1, 1.294(2); C1–N2, 1.346(2); N1–Zr–O1, 59.31(5); N1–Zr–N3, 75.34(5); average angle between C–Zr–C', 109.8(6); Zr–C29–C230, 109.8(1); Zr–C36–C37, 92.6(1); sum of angles about N2, N4: 359.6(3), 359.2(3); N1–C1–N2–C5: 14.3(3).

The isolation of tethered bis(ureato) zirconium complexes **96–99** as stable, monometallic, donor-free dialkyls is remarkable given the tendency of related dichloride complexes **92** and **93** to retain neutral ligands. The steric protection afforded by the benzyl and neopentyl groups likely assists in stabilizing these six-coordinate metal centers.

2.2.4 Formation of Pyridine Adducts

Given the steric accessibility of the zirconium centers in **96-99**, the coordinative saturation of these complexes was tested. Addition of excess pyridine (>2 equivalents) to C₆D₆ solutions of **96-99** results in an immediate colour change to bright orange, suggesting the formation of new products. In each case, the ¹H NMR spectra contain broad signals for the *ortho*-protons of the pyridine centered at δ 8.65, which is close to that of free pyridine (δ 8.53). For biaryl-tethered ureate complexes **98** and **99**, the resonances corresponding to the isopropyl protons become sharp and well resolved after pyridine addition, in contrast to the signals observed for the parent complexes. In particular, the broad signals for the isopropyl methyl groups resolve into two sets of nearly overlapping doublets, which integrate for twelve protons each. This further splitting occurs due to the chiral environment about zirconium, as proposed above for the parent complexes **98** and **99**. The pyridine adducts formed in this manner are surprisingly thermally robust: heating a solution of **99** in the presence of 5 equivalents of pyridine to 110 °C for several hours results in no detectable decomposition.

While the above spectroscopic experiments strongly suggest the formation of seven-coordinate, pyridine-stabilized complexes, they do not give an indication of the exact nature of these species. Therefore, complexes **96**•py and **98**•py were prepared on a larger scale by the reaction of **87** or **88** with Zr(CH₂Ph)₄ in the presence of a slight excess of pyridine; the compounds were recrystallized in 70% and 49% yield respectively. These pyridine-stabilized alkyls are stable to ambient heat and light under an inert atmosphere for months. NMR spectra of **96**•py and **98**•py contain similar features to those observed in the aforementioned small-scale reactions; however, the pyridine *ortho*-proton signal is

shifted downfield to δ 9.38 for **96**•py and δ 8.94 for **98**•py. Signals for free pyridine were not observed, suggesting that in the absence of excess pyridine, ligand exchange and/or loss does not occur, or that the equilibrium heavily favours the seven-coordinate species. Furthermore, subjecting solid **96**•py and **98**•py to high vacuum for 24 hours at room temperature does not remove the pyridine.

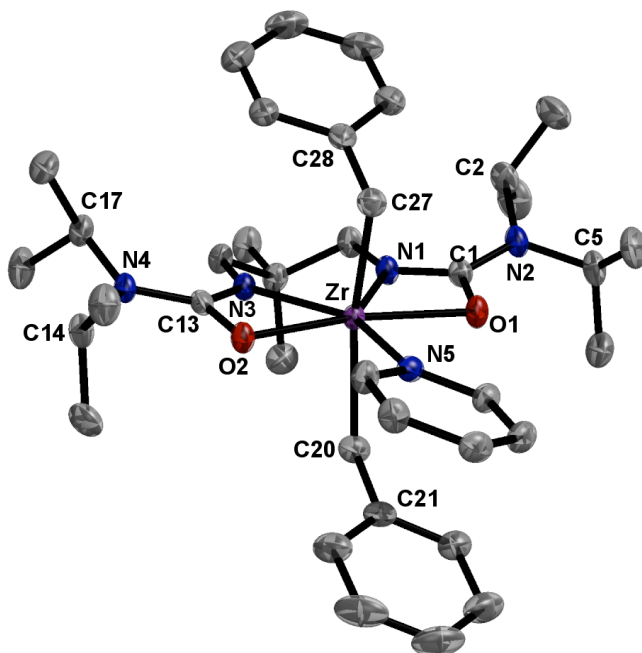


Figure 2.16. ORTEP representation of the molecular structure of **96**•py (ellipsoids plotted at 50% probability, hydrogens and pentane solvent removed for clarity) with selected bond lengths (Å), bond and torsion angles (°): Zr–N1, 2.177(2); Zr–N3, 2.186(1); Zr–N5, 2.397(2); Zr–O1, 2.216(1); Zr–O2, 2.197(2); Zr–C20, 2.365(2); Zr–C27, 2.373(2); C1–N1, 1.326(2); C1–O1, 1.300(2); C1–N2, 1.360(3); N1–Zr–O1, 59.49(6); N1–Zr–N3, 77.56(6); C20–Zr–C27, 156.54(8); C20–Zr–N5, 80.02(7); C27–Zr–N5, 76.59(7); Zr–C20–C21, 126.7(2); Zr–C27–C28, 108.2(1); sum of angles about N2, N4: 359.8(6), 360.0(6); N1–C1–N2–C2: 22.9(3).

The molecular structures of both **96**•py and **98**•py as determined by X-ray crystallography are shown in Figures 2.16 and 2.17 respectively. In each case, the complex is a seven-coordinate, C_2 -symmetric, distorted pentagonal bipyramid, with the benzyl ligands in a *trans*-disposition about the metal center; the equatorial plane is

comprised of the ureate ligand and the pyridine donor. For **98**•py, the ureate has undergone little structural reorganization from the parent six-coordinate complex; the Zr–N and Zr–O bond distances are statistically equal. The Zr–N_{py} distances are fairly short (2.378(1) and 2.397(2) Å), on the same order as the Zr–C lengths (2.350(1)-2.373(2) Å). Comparing the Zr–C distances between **98** and **98**•py reveals a significant lengthening (0.068-0.085 Å), due to the increased electron count of the pyridine adduct. Neither solid-state structure shows any evidence of η^2 -benzyl interactions.

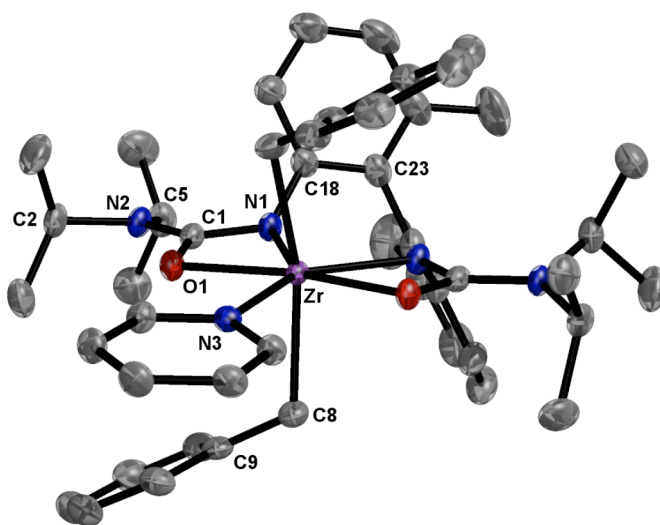


Figure 2.17. ORTEP representation of the molecular structure of **98**•py (ellipsoids plotted at 50% probability, hydrogens removed for clarity) with selected bond lengths (Å), bond and torsion angles (°): Zr–N1, 2.200(1); Zr–N3, 2.378(1); Zr–O1, 2.1965(9); Zr–C8, 2.350(1); C1–N1, 1.356(2); C1–O1, 1.283(2); C1–N2, 1.337(2); N1–Zr–O1, 60.06(4); N1–Zr–N1*, 79.13(4); C8–Zr–C8*, 154.83(5); C8–Zr–N3, 77.42(5); Zr–C8–C9, 117.3(1); sum of angles about N2: 359.4(3); N1–C1–N2–C5: 20.4(2); C18–C23–C23*–C18*, 68.5(2).

The propensity of **96-99** to bind pyridine speaks to the coordinative unsaturation of these six-coordinate complexes. The steric accessibility afforded by the tethered bis(ureato) ligands evidently allows for increased coordination numbers, which may have a dramatic effect on the reactivity of compounds supported by these ligands.

2.2.5 Preliminary Screening of Olefin Polymerization Precatalysts

After the establishment of reliable synthetic routes to well-defined, donor free bis(ureato) compounds of the form L_2MX_2 , preliminary screening for olefin polymerization activity was carried out. Previously, as part of an industrial collaboration with Exxon-Mobil Inc., several related bis(amidato) compounds were tested as precatalysts for ethylene polymerization (**67-69**, **100-104**, Figure 2.18).¹⁷⁸ Preliminary high-throughput screening revealed varying degrees of activity, ranging from completely inactive (Figure 2.18, bottom) to highly active (Figure 2.18, top). Compound **102** exhibits the highest activity, reaching a value of 450.

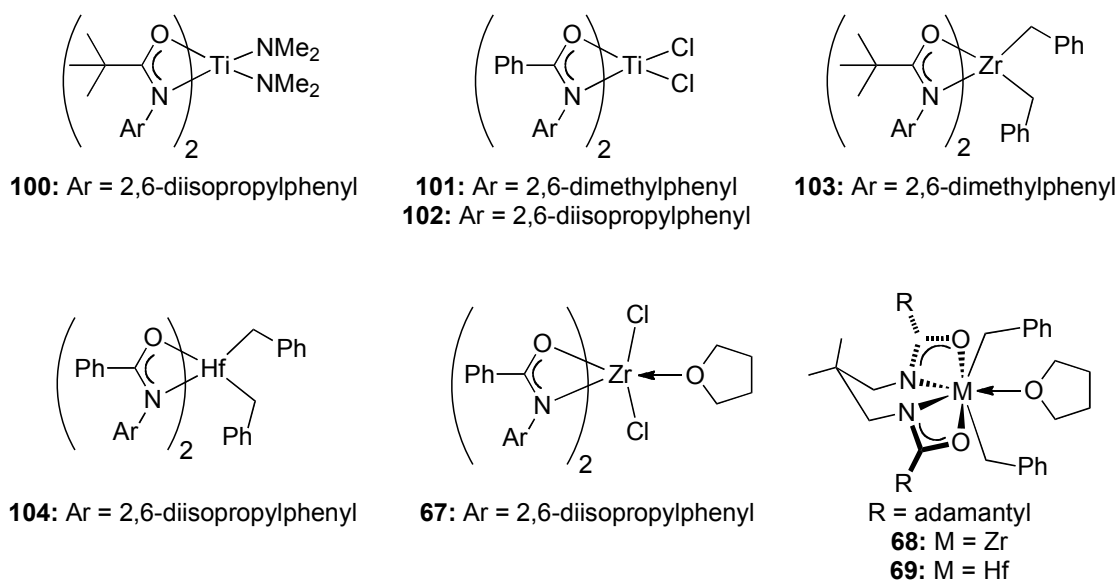


Figure 2.18. *Top:* bis(amidato) complexes with high activity (>100) in the polymerization of ethylene. *Bottom:* complexes exhibiting low to no activity (<10).

The activities attained by the best catalysts compare well to related amidinate¹⁶⁰⁻¹⁶³ and guanidinate⁸³ complexes. In addition, the PDIs of the resulting polymers are much lower, ranging between 1.3 and 6, with the majority near 2. This could be due to the greater stability of the metal-amidate interaction imparted by the oxygen-donor,

preventing amidate abstraction by excess MAO. Significantly, the polymer molecular weights attained are very high, on the order of 4×10^6 Da. This is in the range of Ultra-High Molecular Weight Polyethylene (UHMWPE), a material with an impact-strength higher than that of Kevlar.¹⁷⁹ While these particular amidate-supported complexes are in no danger of replacing current technology, the ease with which these precatalysts can be structurally and electronically tuned greatly assists in catalyst screening and further development. Based on this work, neutral, donor free ureate compounds **90**, **91**, **94**, **96**, and **98** were chosen for comparison.

Ethylene polymerization trials were carried out collaboratively with the research group of Dr. Douglas Stephan at the University of Toronto under the following conditions. In all cases, ethylene pressure was maintained at ~15 psi (atmospheric pressure) on a Schlenk line. The dichloride precatalysts **90** and **91** were activated with an approximately thousand-fold excess of MAO, while the dibenzyl precatalysts were activated with either $[\text{Ph}_3\text{C}][\text{B}(\text{C}_6\text{F}_5)_4]$ or $\text{B}(\text{C}_6\text{F}_5)_3$. Each reaction was left to proceed at either room temperature or 65 °C for twenty minutes before quenching. Unfortunately, in every case the observed activity was extremely low ($A < 5$); therefore, further characterization of the polyethylene produced was not undertaken. There are many factors that could contribute to this low activity, including rapid catalyst decomposition and/or inactivation.¹⁴¹ This is certainly possible, especially considering the sterically open nature common to many of the ureate complexes.

Notably, the amidate precatalysts pictured in Figure 2.18 were tested under very different reaction conditions, including the use of high ethylene pressure (200-350 psi), rather than the atmospheric pressure used for the ureate precatalyst screen. As explained

in the introduction, specific polymerization conditions can have a huge impact on catalyst performance. In this manner, the low activities observed may constitute a “false negative,” and therefore do not necessarily imply that the ureate precatalysts under consideration are inactive. Further catalyst screening under a broader range of conditions, especially at varied ethylene pressure, is required in order to draw meaningful comparisons to their amidate counterparts. However, the likelihood that these ureate precatalysts can reach productivities rivaling those of established highly active systems is doubtful.

2.3 Conclusions

The ureate-supported group 4 complexes described in the preceding sections constitute the first examples of these organometallic compounds. Efficient synthetic protocols have been established to access these derivatives in a variety of forms from readily available starting materials. During the course of synthetic and structural investigations, several key differences between the ureate ligand set and its amidate counterpart have been observed. In particular, unsuccessful synthetic routes to bis(amidato)dichloro compounds, namely protonolysis of $M(NMe_2)_2Cl_2$ precursors and chlorination of $L_2M(NMe_2)_2$ species with Me_3SiCl , are suitable for the preparation of analogous bis(ureato) compounds. Furthermore, complications previously encountered in the preparation of bis(amidato)dibenzyl compounds, such as the retention of neutral donor ligands, solution-phase isomerization, and dinuclear complex formation, are not observed in the case of ureate-supported derivatives.

The divergent properties between these two ligand sets stem directly from the electron-donating capability of the distal amino substituent on the ureate framework. For each ureate complex structurally characterized by X-ray crystallography, evidence for this electron-donation is apparent. Solution-phase NMR spectroscopy, however, provides a more accurate method for gauging the extent of this effect. Observation of hindered rotation about the pertinent C–N bond is an indicator of multiple bond character, a hallmark of π -electron-delocalization. Notably, some of the ureate complexes described do not exhibit hindered rotation about this bond, except at low temperature. These examples all contain the same ureate ligand, derived from bis(urea) **87**. These

observations indicate that the degree of electron-donation by the distal nitrogen is highly dependent on the overall electronic environment of the complex in question.

Preliminary reactivity data suggest that these compounds are ineffective for ethylene polymerization. While further experiments are no doubt needed to make this categorization definitive, alternate catalytic applications may prove more fruitful for this class of compound, and also provide more opportunities to compare and contrast the amidate and ureate ligand sets. The following chapter will detail the use of group 4 ureate complexes as precatalysts for catalytic C–N bond formation *via* hydroamination, a reaction for which amidate catalysts are known to be well-suited. The nature of the ureate ligand will be examined further, with an emphasis on both the electronic and steric effects exerted by π -donation, and the ensuing impact on reactivity.

CHAPTER 3. Catalytic Hydroamination, Part I: Catalyst Development

3.1 Introduction

3.1.1 The Hydroamination Reaction

The development of technologies that form carbon–element bonds in a completely atom-economic manner constitutes a fundamental challenge to synthetic chemists throughout the discipline.¹⁸⁰ Increasing public sensitivity toward environmental issues, and the resulting scientific and economic opportunities this represents, means that such atom-efficient technologies are being intensely investigated as alternatives to established chemical protocol. One of the major avenues currently being explored is the addition of element–hydrogen bonds across carbon–carbon unsaturations.^{181,182} These hydrofunctionalization reactions constitute an impressive family of transformations that can rapidly and efficiently increase chemical complexity directly from hydrocarbon feedstocks, without the formation of waste byproducts. One permutation thereof, the hydroamination reaction (Figure 3.1), has been the subject of research for over two decades.^{183,184} The products of hydroamination, including amines, enamines, and imines, are important compounds for a number of applications, including bulk and specialty chemical preparation, drug discovery and development, and natural product synthesis.

The intermolecular, anti-Markovnikov hydroamination of unactivated, terminal alkenes was named one of the “Ten Challenges for Catalysis” by *C&EN News* in 1993.¹⁸⁵ Notably, this challenge has not yet been met. A qualitative look at the kinetic and thermodynamic factors governing the reaction offers a convincing rationale for the

difficulty of this transformation. Coulombic repulsion between the electron-rich alkene π -bond and the nitrogen lone pair results in a significant activation energy, even when catalysis is employed. However, negative reaction entropy means that as temperature is increased to overcome this activation barrier, the process becomes less spontaneous.¹⁸⁶ Therefore, highly active catalysts are needed to maintain acceptable reaction rates at lower temperatures.

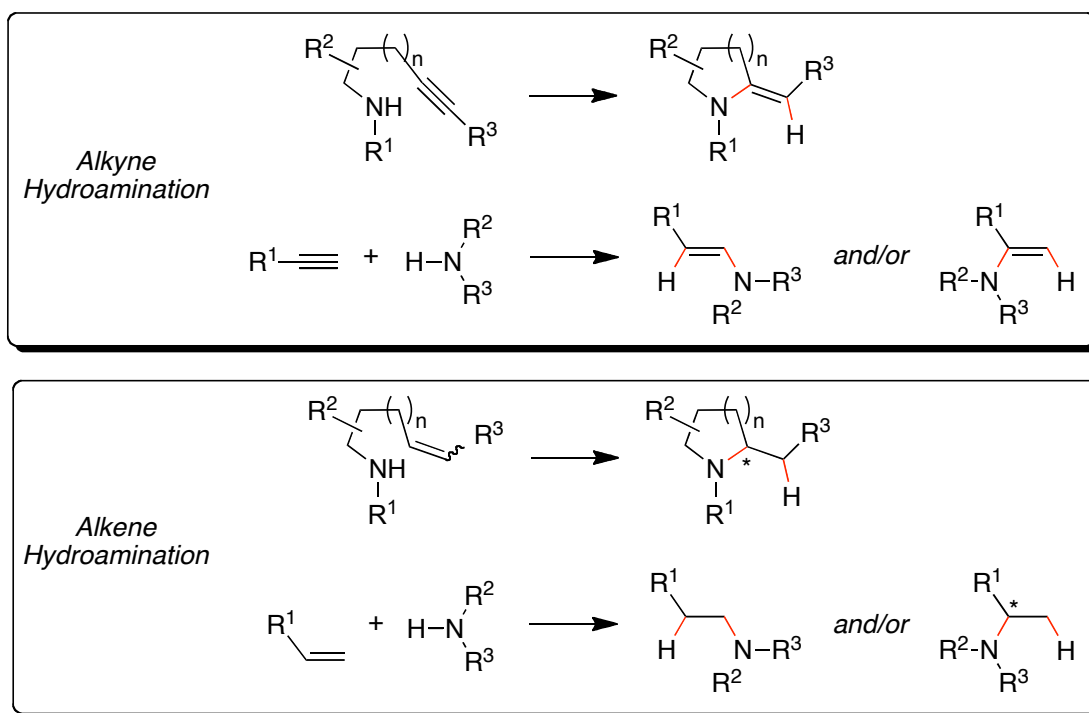


Figure 3.1. Representative intra- and intermolecular hydroamination reactions of alkynes and alkenes; new bonds formed indicated in red, new stereogenic centers with asterisks.

In response to this challenge, a great many catalytic systems for hydroamination have been developed. By far the most common approach involves the use of *d*- and *f*-block organometallic complexes, although other catalysts, including those based on *s*-block metals, main group elements, and organocatalysts have also been successfully employed.¹⁸³ However, only a handful of these systems are able to mediate the

intermolecular hydroamination of alkenes.¹⁸⁷⁻¹⁹³ Instead, the majority of research has been focused on catalyzing other, more facile hydroamination processes, such as alkyne hydroamination, and intramolecular alkene hydroamination. This latter reaction results in the formation of cyclic, α -chiral amines. These represent an ubiquitous structural motif in biologically active compounds, from simple amino acids, to synthetic pharmaceuticals, to complex naturally occurring alkaloids. In an effort to perform this reaction stereoselectively, many chiral catalysts have also been developed, although very few have achieved high enantioselectivities.^{59,194-197}

All of the catalytic systems developed to date have specific strengths with respect to substrate combinations. However, the necessity of employing vastly different catalysts for minor variations on the same transformation is a major obstacle to wider usage throughout the synthetic community. “General” catalyst systems, those that can operate with alkynes *and* alkenes, primary *and* secondary amines, and in an intra- *and* intermolecular fashion, are strikingly rare. The following sections will briefly review three major classes of hydroamination catalyst, in order to illustrate “state-of-the-art” catalyst activity, substrate scope, and selectivity. Accordingly, the discussion will focus on those systems that are able to employ the widest range of substrates, rather than those with the highest “activity.” Highly stereoselective systems that also exhibit good substrate scope will also be mentioned. A description of mechanistic details governing the relevant catalytic cycles will be deferred until Chapter Four.

3.1.2 Rare-Earth Metal Catalysts

The first main class of hydroamination catalyst encompasses compounds of the group 3 and lanthanide metals, henceforth referred to collectively as the rare-earth metals. Since a pioneering report in 1989 by Gagné and Marks,¹⁹⁸ involving the lanthanocene precatalyst $(\text{Cp}^*_2\text{LaH})_2$, rare-earth catalysts have remained among the most active, generally applicable, and selective hydroamination systems known.¹⁹⁹ Metallocene-based rare-earth catalysts and derivatives thereof (Figure 3.2) exhibit unsurpassed activity for the intramolecular hydroamination of alkenes, achieving these challenging transformations at or near room temperature, with turnover frequencies (TOF) of up to 200 h^{-1} . While this may not seem impressive relative to the efficiencies of olefin polymerization catalysts described in the previous Chapter, it far outstrips the activity of every other class of hydroamination catalyst.

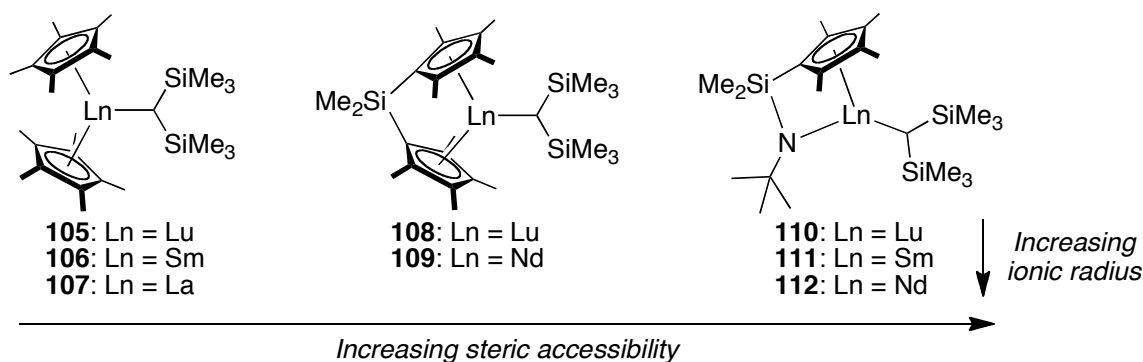
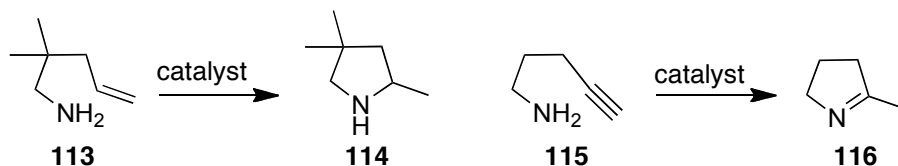


Figure 3.2. Metallocene-based rare-earth hydroamination precatalysts.

A key structural aspect governing catalytic activity of rare-earth systems is the steric accessibility of the metal center. This can be altered through ligand design, and also by using metals with varying ionic radii. In this sense, use of the rare-earths offers a unique opportunity for catalyst tuning, as they provide a gradual range of ionic radii from 0.88 Å for scandium to 1.16 Å for lanthanum.²⁰⁰ This steric influence on catalysis has

been well investigated, enabling a number of trends to be discerned.²⁰¹⁻²⁰³ First, greater steric accessibility has a positive effect on catalyst performance for the intramolecular hydroamination of alkenes (Table 3.1).^{201,202} Comparing catalyst TOF with metal ionic radius reveals that larger ions are dramatically more active for the conversion of aminoalkene **113**. Decreased ligand steric demand similarly leads to increased activity. The “constrained-geometry” neodymium precatalyst **112**, combining a large metal ion with a sterically open ligand, exhibits the highest activity for this transformation.²⁰²

Table 3.1. Rare-earth metallocene catalyst activities for the cyclization of **113** and **115**.



Entry	Precatalyst	Ionic radius (Å) ^a	Substrate	<i>T</i> (°C)	TOF (h ⁻¹)	Ref.
1	105 (Lu)	0.98	113	80	<1	201
2			115	21	711	203
3	106 (Sm)	1.08	113	60	48	201
4			115	21	580	203
5	107 (La)	1.16	113	25	95	201
6			115	21	135	203
7	108 (Lu)	0.98	113	80	75	201
8	109 (Nd)	1.11	115	21	78	203
9	110 (Lu)	0.98	113	25	90	202
10	111 (Sm)	1.08	113	25	181	202
11	112 (Nd)	1.11	113	25	200	202

^aEight-coordinate radius of M³⁺ ions, ref. 200.

Surprisingly, the exact opposite trend is observed for the intramolecular hydroamination of alkynes.²⁰³ In these reactions, a *more* sterically hindered metal center results in a more active catalyst. Comparing the precatalyst series **105-107** in the

cyclization of aminoalkyne **115** illustrates this effect, with the sterically congested lutetium complex **105** achieving the highest TOF. These diametrically opposed structure-activity relationships can be reconciled by considering the relative size of the alkene and alkyne substrates. Greater steric accessibility to the metal center accommodates approach of the alkene substrate, whereas steric effects are less important for the approach of an alkyne. In the latter case, the smaller lanthanide ions may enable a closer association of the amido nitrogen and the alkyne carbons, resulting in faster cyclization.²⁰⁴

As a result of their high catalytic activity, rare-earth metallocenes are able to catalyze a wide variety of very challenging hydroamination reactions (Figure 3.3), involving unactivated 1,2-disubstituted alkenes (**117** to **118**),²⁰⁵ formation of larger rings (**119** to **120**),²⁰⁶ and tandem cyclization (**121** to **122**).²⁰⁵ In each case, the products are formed in a highly diastereoselective manner (at least 10:1 in favour of the illustrated diastereomer). Particularly impressive is the hydroamination of 1-pentene by *n*-propylamine catalyzed by **109** to give the branched product **123**.^{188,207} This constitutes the only example of transition-metal catalyzed intermolecular hydroamination of an unactivated alkene by a strongly basic primary amine. Even though the activity is modest, the conditions employed are extremely mild relative to those used for alkali-metal catalyzed reactions ($T > 200\text{ }^{\circ}\text{C}$, $P > 800\text{ bar}$, yields $< 50\%$).¹⁸⁴

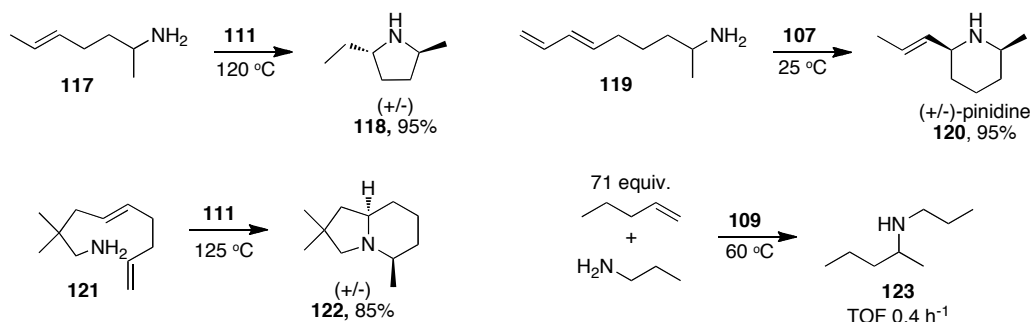


Figure 3.3. Challenging transformations achieved with rare-earth metallocene catalysts.

A major drawback of rare-earth metallocenes, largely preventing wider catalytic application, is their inherent instability. Due to the extremely basic nature of the reactive species and the oxophilicity of the metals involved, painstaking exclusion of air and moisture is a necessity. Further, the presence of many common functional groups results in catalyst deactivation. In addition, thermal instability prevents the use of higher reaction temperatures and longer reaction times to effect more difficult transformations.²⁰⁸ Finally, the precatalysts themselves are non-trivial to prepare, requiring several sensitive synthetic steps. In order to develop an alternative option, several researchers have introduced non-cyclopentadienyl supporting ligands (Figure 3.4).^{187,209-211} These post-metallocene catalysts have yet to attain the activities of metallocene systems; however, they possess other advantages. In general, these catalysts are relatively easy to use; for example, **124** and **125** are formed *in situ* from readily available materials. The wide variety of possible ligand frameworks leads to steric and electronic flexibility, simplifying catalyst design and development. Furthermore, these systems offer increased stereoselectivity. The scandium precatalyst **124**, while exhibiting somewhat low activity relative to other systems with larger metal ions, is highly diastereoselective.²⁰⁹ Finally, the chiral binaphtholate precatalyst **127** achieves the highest enantioselectivity ever reported for aminoalkene cyclization (95% *ee*).¹⁸⁷

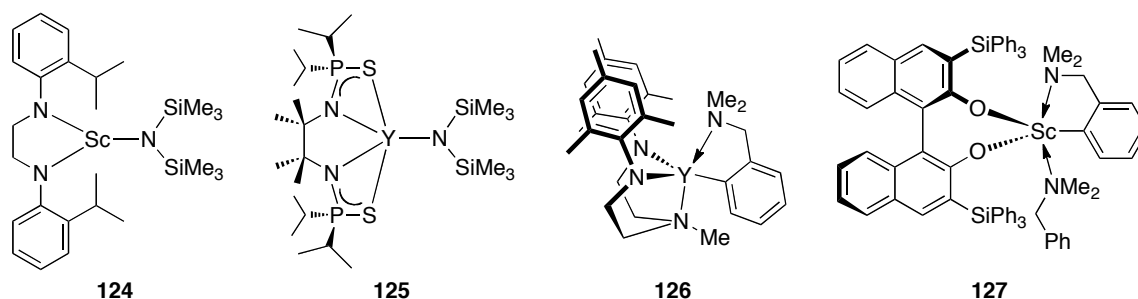


Figure 3.4. Post-metallocene rare-earth catalysts.

3.1.3 Late Transition Metal Catalysts

Despite the high catalytic activity of rare-earth metals, their use has remained limited outside of a few specialized laboratories. In contrast, late transition metal catalysts are heavily exploited in organic synthesis. Catalyst systems based on metals such as palladium, rhodium, iridium, and ruthenium have gained prominence for a wide range of revolutionary organic transformations, including cross-coupling,²¹² hydrogenation,²¹³ and olefin metathesis.²¹⁴ Their widespread use is due to several factors, including relative insensitivity to moisture, tolerance of many functional groups, well-understood redox chemistry, commercial availability, and ease of use. As a result, much recent hydroamination research has gone into developing effective late metal alternatives to organolanthanides. However, the vast majority of late metal hydroamination systems do not function with amines, instead requiring less nucleophilic substrates such as amides, sulfonamides, carbamates, and ureas.¹⁸³ Accordingly, there are very few reported catalysts able to use strongly basic primary and secondary amines.

In 2005, Bender and Widenhoefer reported the first late metal catalyst able to hydroaminate unactivated alkenes with basic amines, $[\text{PtCl}_2(\text{H}_2\text{C}=\text{CH}_2)]_2$ with added PPh_3 ; however, only secondary aminoalkenes can be cyclized.²¹⁵ Liu and Hartwig later disclosed that cationic rhodium complexes supported by bulky phosphine ligands are effective catalysts for primary and secondary aminoalkene cyclization.²¹⁶ The best system, $[\text{Rh}(\text{COD})_2]\text{BF}_4$ and ligand **128** (Figure 3.5), gives exclusive formation of the hydroamination product, with no side reactivity common to other catalysts (oxidative amination, alkene isomerization, alkene hydrogenation). Shortly thereafter, two other late metal systems were reported that work with both primary and secondary

amines.^{217,218} In all respects, the rhodium system outperforms its counterparts (Table 3.2, eq. 3.1). Particularly impressive is that both $[\text{Rh}(\text{COD})_2]\text{BF}_4 + \mathbf{128}$ and $[\text{Ir}(\text{COD})\text{Cl}]_2$ are able to hydroaminate 1,2-disubstituted alkenes (eq. 3.1). Note, however, the generally harsh conditions outlined in Table 3.2 relative to those used for rare-earth catalysts.

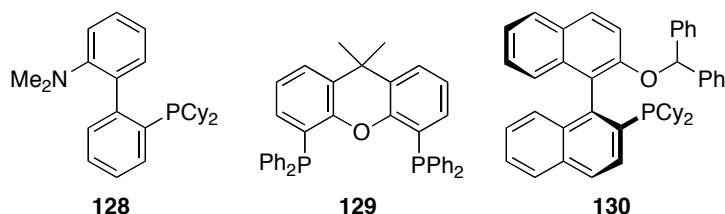
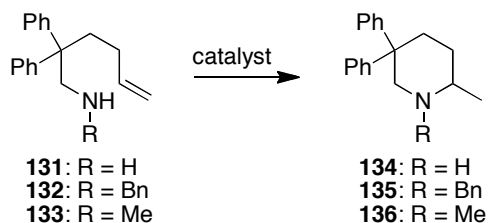


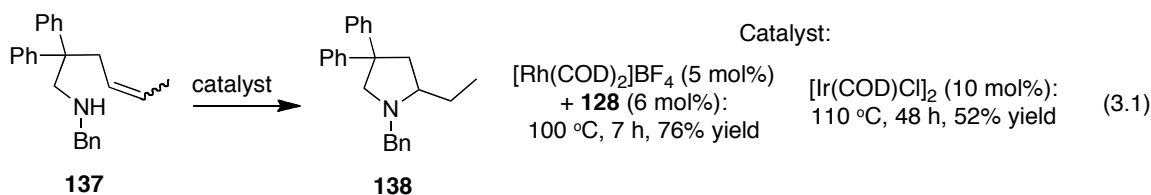
Figure 3.5. Effective ligands for late metal catalyzed hydroamination.

Table 3.2. A comparison of late transition metal catalyst systems for primary and secondary aminoalkene hydroamination.

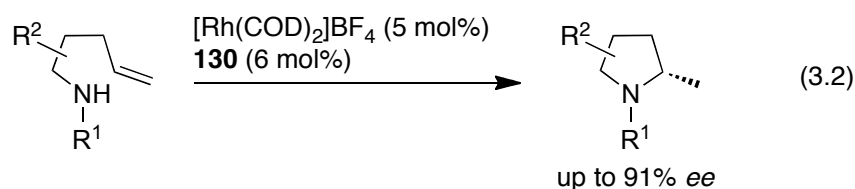


Entry	Substrate	Precatalyst (loading, mol%)	<i>T</i> (°C)	Time (h)	Isolated Yield (%)	Ref.
1	131	$[\text{Rh}(\text{COD})_2]\text{BF}_4$ (5) + 128 (6)	100	10	84	216
2	131	$[\text{Ir}(\text{COD})\text{Cl}]_2$ (5) + HNEt_3Cl (10)	110	24	84	218
3	131	$\text{Cu}(\text{OtBu})$ (15) + 129 (15)	100	72	87	217
4	132	$[\text{Rh}(\text{COD})_2]\text{BF}_4$ (2.5) + 128 (3)	70	7	86	216
5	132	$[\text{Ir}(\text{COD})\text{Cl}]_2$ (5)	80	24	72 ^a	218
6	133	$\text{Cu}(\text{OtBu})$ (15) + 129 (15)	100	24	92	217

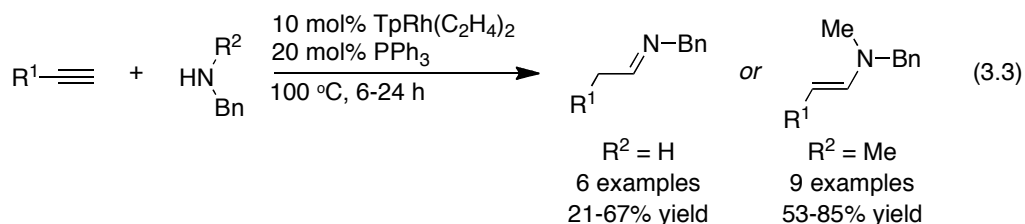
^a25% alkene isomerization byproduct also formed.



In 2010, Shen and Buchwald reported that a chiral phosphine ligand (**130**), similar to **128**, is effective for enantioselective rhodium catalyzed hydroamination (eq. 3.2).²¹⁹ This system offers largely the same substrate scope as the achiral variant, while imparting good to excellent enantioselectivities. Notably, the catalyst also works with both primary and secondary amines, although only one primary aminoalkene example was disclosed.



In terms of intermolecular hydroamination, there is only one late metal system that is able to use both primary and secondary amines, also based on rhodium. Fukumoto and co-workers used the neutral, tris(pyrazolyl)borate-supported complex $\text{TpRh}(\text{C}_2\text{H}_4)_2$ in the presence of PPh_3 to enable the anti-Markovnikov hydroamination of terminal alkynes bearing a variety of functional groups (eq. 3.3).²²⁰ For these reactions, it appears the use of the neutral Tp complex is essential. Catalyst screening revealed that a number of other rhodium sources, including $[\text{Rh}(\text{COD})_2]\text{BF}_4$, and ancillary ligands, including cyclopentadienyl and Tp^* (tris[3,5-dimethylpyrazolyl]borate) are ineffective, highlighting the challenge in identifying effective catalytic systems.



3.1.4 Group 4 Systems

The third major class of hydroamination catalyst, those containing group 4 metals, is the subject of the remainder of this thesis. Catalysts based on these metals possess distinct advantages over both organolanthanide and late metal systems. Titanium, zirconium, and hafnium are inexpensive, abundant, and environmentally and biologically benign metals, unlike many late transition metals.²²¹ Furthermore, their use in large-scale industrial processes and small-scale organic synthesis has been firmly established, unlike rare-earth catalysts. As described in Chapter Two, polymerization initiators based on group 4 metals are in heavy use for the production of polyolefin plastics.¹²⁴ Group 4 catalysts and reagents are also very common in organic chemistry.¹⁷

Group 4 hydroamination catalysts have been known for nearly as long as rare-earth systems. After landmark publications by Bergman²²² and Livinghouse²²³⁻²²⁴ in the early 1990s, myriad catalytic systems have been reported. As a result, titanium complexes are now among, if not the best catalysts for the regioselective hydroamination of alkynes with primary amines.¹¹⁶ Despite these efforts, neutral group 4 systems were long unsuitable for the hydroamination of alkenes. In 2005, our research group published a report that describes the use of commercially available $\text{Ti}(\text{NMe}_2)_4$ as a precatalyst for the intramolecular hydroamination of primary aminoalkenes.²²⁵ This reaction can now be carried out by many group 4 catalytic systems for select substrates,^{113,115,226-232} including examples with high diastereo-¹¹³ and enantioselectivity.^{115,228,232} An examination of hydroamination precatalysts capable of transforming more than three substrates (Figure 3.6) reveals several similarities. In particular, nearly every catalyst is supported by amidates (**139**, **142**, **146**, **148**, **149**), or related ligands (**143**, **144**, **147**).

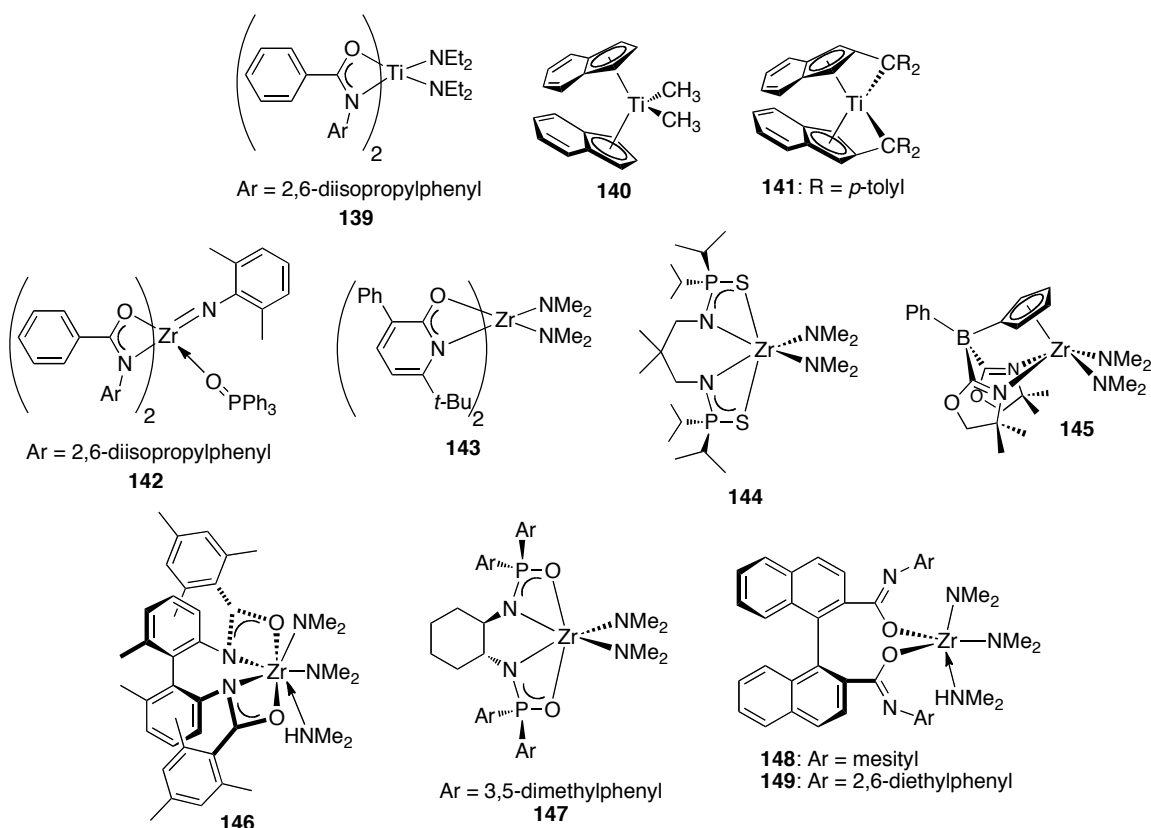
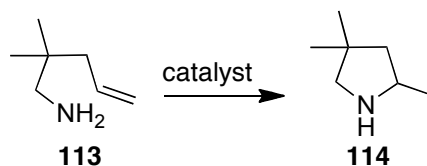


Figure 3.6. Successful group 4 precatalysts for the hydroamination of alkenes.

Comparing the activity of the above precatalysts offers further insight (Table 3.3). First, zirconium catalysts are clearly more active than their titanium counterparts (**139** versus **142**). Second, those catalysts with tethered, sterically open ligands provide the highest activities. This dramatic effect is illustrated by comparing complexes **142** and **146**. In both cases, the amidate ligands are electronically analogous; however, precatalyst **146** is approximately thirty times more active. These observations mirror the trends previously observed for rare-earth metal catalysts.²⁰¹ Further, amidate ligands are not required for high activity, as demonstrated by the zwitterionic zirconium precatalyst **145**, which cyclizes **113** at *room temperature*.²³¹ Unfortunately, the catalyst appears to be thermally unstable, as higher reaction temperatures do not improve reaction rate.

Table 3.3. Group 4 catalysts for the cyclization of **113**.

Entry	Precatalyst (loading, mol%)	<i>T</i> (°C)	Time (h)	Yield (%)	Ref.
1	Ti(NMe ₂) ₄ (5)	105	96	87 ^a	225
2	139 (5)	110	120	25 ^b	113
3	140 (5)	105	96	74 ^a	227
4	141 (5)	105	24	18 ^a	230
5	142 (10)	110	96	87 ^b	113
6	143 (10)	110	96	87 ^b	229
7	144 (5)	120	12	94 ^b	226
8	145 (10)	23	11	85 ^c	231
9	146 (10)	110	3	>95 ^c (93% <i>ee</i>)	115
10	147 (10)	115	48	91 ^a (80% <i>ee</i>)	228
11	148 (2)	100	26	>95 ^c (23% <i>ee</i>)	232
12	149 (2)	100	7	>95 ^c (42% <i>ee</i>)	232

^aUnless otherwise noted, isolated yield of **114**, or a derivative thereof. ^bDetermined by ¹H NMR spectroscopy relative to internal standard. ^cConversion as determined by ¹H NMR spectroscopy.

3.1.5 Two Major Challenges

Despite the encouraging catalytic activity displayed by the group 4 systems discussed thus far, all of these catalysts suffer from limited applicability. Often, a minor change to the substrate structure will result in undesired side-reactivity, or simply no reaction. Thus, the development of effective titanium or zirconium hydroamination catalysts must address specific challenges. Foremost among these challenges is the formation of larger heterocyclic rings *via* intramolecular hydroamination, and an expansion of reaction scope to include secondary amines in both intra- and intermolecular processes.

As outlined in Table 3.4, group 4 catalysts can efficiently form pyrrolidines from 1-amino-4-pentenes; however, many of these same systems suffer reduced activity when used for the synthesis of piperidines, and complete inactivity for the formation of azepanes. This latter point is a significant weakness from a practical standpoint, as six- and seven-membered nitrogen-containing heterocycles are common in biologically active compounds of both natural and synthetic origin. Furthermore, low catalyst activity is not the only concern with regard to the synthesis of larger *N*-heterocycles. Recently, select group 4 systems, namely $\text{Ti}(\text{NMe}_2)_4$, $\text{Ti}(\text{CH}_2\text{Ph})_4$, $\text{Zr}(\text{NMe}_2)_4$, **139**, **140**, and **143**, have been shown to promote an alternate, carbon–carbon bond forming process in addition to hydroamination.^{233–236} This reaction, dubbed hydroaminoalkylation,²³⁷ is particularly prevalent during the attempted synthesis of azepanes (Table 3.4), where amine-substituted cyclohexanes are often formed as the major product. While hydroaminoalkylation is a valuable transformation in its own right, developing systems that are chemoselective for hydroamination is critical for synthetically useful catalysis.

Table 3.4. Hydroamination versus hydroaminoalkylation with group 4 precatalysts.²³³

Reaction scheme: **150** (1-amino-4-(cyclopentylmethyl)pent-1-ene) reacts with a catalyst at 145 °C to form a mixture of **151** (1-(cyclopentylmethyl)pyrrolidine) and **152** (1-(cyclopentylmethyl)piperidine).

Entry	Precatalyst (loading, mol%)	Time (h)	Conv. (%) (Ratio of 151:152) ^a
1	$\text{Ti}(\text{NMe}_2)_4$ (20)	16	95 (1:18)
2	$\text{Zr}(\text{NMe}_2)_4$ (20)	21	87 (1:10)
3	142 (20)	115	55 (1:0)
4	143 (20)	22	92 (1:5)
5	144 (40)	6	96 (1:23)

^aConversion and product ratio determined by ^1H NMR spectroscopy.

A second drawback common to most group 4 hydroamination catalysts is their general inactivity toward hydroamination with secondary amines. There are very few reported systems that do not adhere to this trend (Figure 3.7). In 2004, the groups of Hultzs²³⁸ and Scott²³⁹ independently discovered that cationic titanium and zirconium precatalysts (**153-155**), which are isovalent with rare-earth complexes, are active for the intramolecular hydroamination of secondary aminoalkenes; however, these same systems are *inactive* with primary aminoalkenes. Later, in 2007 and 2008, the groups of Marks,²⁴⁰ Odom,²⁴¹ and Doye²⁴² disclosed the identity of a few neutral, group 4 complexes (**140**, **156-158**), including commercially available $\text{Zr}(\text{NMe}_2)_4$, capable of the hydroamination of both primary *and* secondary aminoalkenes. All of these examples, while impressive for their fundamental contribution to the advancement of group 4 catalyzed hydroamination, suffer from limited scope and low activity. In particular, precatalysts **140**, **156-158** and $\text{Zr}(\text{NMe}_2)_4$ were shown to be operative for only one secondary aminoalkene substrate. Development of a group 4 catalyst capable of hydroamination with a wide range of both primary and secondary amines would significantly expand the synthetic potential of the reaction.

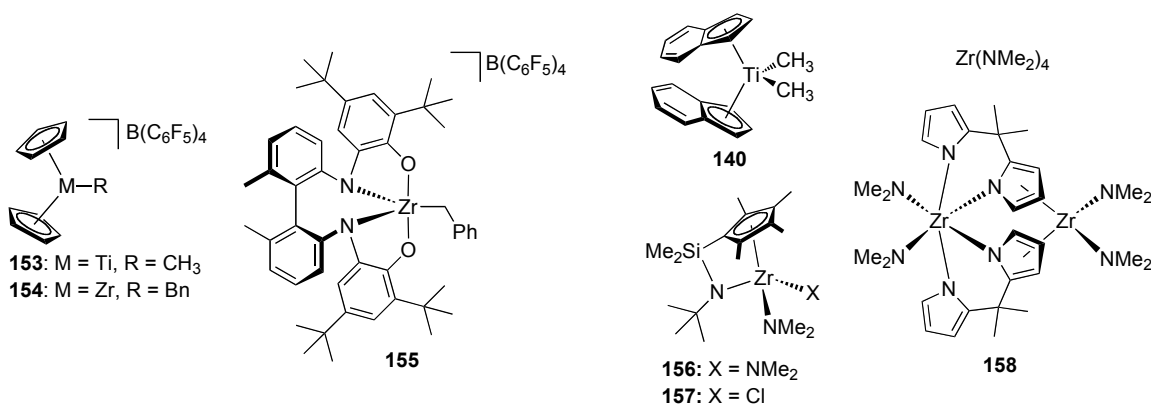


Figure 3.7. Cationic (left) and neutral (right) group 4 precatalysts capable of hydroamination with secondary amines.

Building upon the themes of Chapter Two, the remainder of this Chapter will compare and contrast the use of amidates and ureates as supporting ligands for group 4 bis(amido) compounds, with a particular focus on hydroamination catalysis. As mentioned previously, amidate-derived ligands appear to impart high catalytic activity (Figure 3.6). In an effort to determine the steric and electronic factors responsible for high hydroamination activity, a comprehensive catalyst screen of amidate and ureate complexes was undertaken. Based on the data generated, and an analysis of precatalyst structural details, it appears that complexes possessing sterically accessible, electron deficient zirconium centers constitute the most effective catalysts. As a result of these screening experiments, a highly active, broadly applicable zirconium hydroamination precatalyst has thus been identified. This bis(ureato) complex functions well with a variety of primary and secondary amines, and tolerates the presence of various functional groups. The substrate scope exhibited by this zirconium species is unprecedented for a group 4 catalyst, and even rivals that of previously discussed late metal systems.

3.2 Results and Discussion

3.2.1 Synthesis and Characterization of Non-Tethered Precatalysts

To establish a relationship between the steric and electronic properties of amidate- and ureate-supported bis(amido) complexes, and their corresponding catalytic activity for hydroamination, a variety of these compounds was targeted for investigation. Several bis(amidato)bis(amido)titanium and zirconium hydroamination precatalysts have been reported previously,^{109,110,113-115,243} however, there are no examples of analogous ureate compounds being used for hydroamination catalysis. The dichotomy between amidate and ureate ligands affords an opportunity to probe electronic effects on catalytic activity while keeping ligand steric features largely unchanged.

Given the success in using protonolysis for the synthesis of ureate-supported dichloro and dialkyl compounds, described previously in Chapter Two, a similar protocol was applied to prepare bis(amido)bis(ureato) precatalysts. Treatment of commercially available $M(NMe_2)_4$ ($M = Ti, Zr$) precursors with urea proligands **85** and **86** gives four non-tethered bis(ureato) complexes (**89**, **159-161**) in high recrystallized yield (Figure 3.8). These specific derivatives were chosen for comparison to previously reported bis(amidato) complexes (**100**, **139**, **162-165**).^{110,243} In this sense, the piperidinyl and diisopropylamino groups of the ureate ligands are steric analogues to the amidate phenyl and *tert*-butyl substituents respectively.

NMR spectroscopy of non-tethered bis(ureato) complexes **89** and **159-161** is consistent with the proposed molecular composition shown in Figure 3.8. The NMR spectroscopic features of **159** are very similar to that of titanium congener **89**, which were previously discussed in Chapter Two. ¹H NMR spectroscopy of **159** suggests fluxional

behaviour at ambient temperature in solution, as observed for **89**. The signals corresponding to the dimethylamido protons (singlet at δ 2.94), the Ar-CH₃ groups (singlet at δ 2.50), and the aromatic protons (triplet at δ 6.91, doublet at 7.06) are all well resolved and indicative of two equivalent ureate ligands. The remaining aliphatic signals, however, are broadened almost into the baseline; this signal broadening is also evident in the ¹³C NMR spectrum. These broad resonances correspond to the diisopropylamino substituents on the backbone of the ligand, and indicate slow rotation around the (*i*-Pr)₂N-C_{carbonyl} bond. This could be due to steric interactions, but is more likely due to electron donation, as previously proposed for **89**.

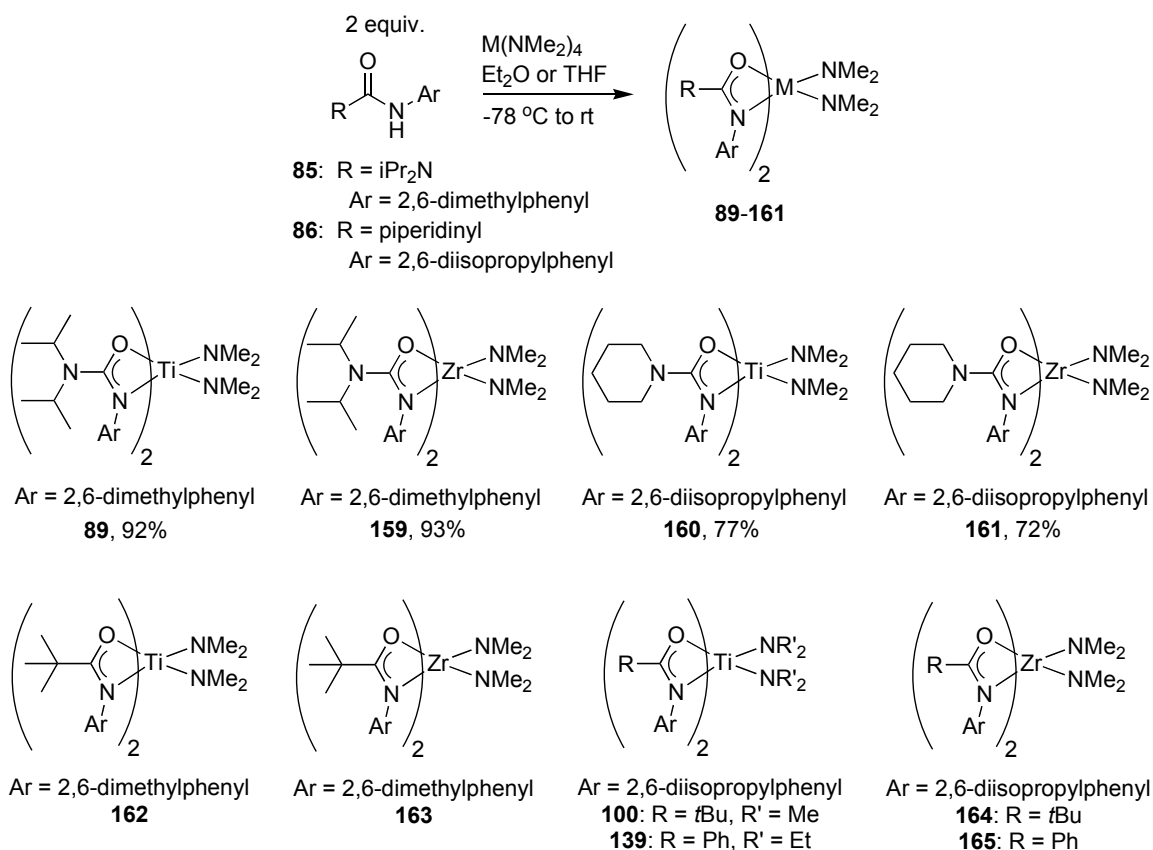


Figure 3.8. Non-tethered bis(ureato) precatalysts with bis(amidato) analogues.

The solid-state molecular structures of **89** and **159** are shown in Figures 3.9 and 3.10 respectively. Both complexes adopt distorted octahedral geometries, with the *N*-aryl groups situated *trans*. The molecules exhibit C_2 -symmetry in the solid state, consistent with the aforementioned NMR spectroscopic evidence. As observed for all ureate complexes discussed in Chapter Two, the metrical parameters provide evidence of electron donation by the distal nitrogen (N2): the bond lengths about C1 suggest a high degree of delocalization, the sum of the angles about the distal nitrogens approach 360° , and the torsion angles through the C–N bond indicate coplanarity between the chelate ring and the plane about the distal nitrogen. One notable feature of the structure of **89** is that the dimethylamido ligands are disordered between two orientations; only one of these is shown in Figure 3.9. Both orientations indicate an sp^2 -hybridized geometry about N3, typical for amido ligands attached to early transition metals.²⁷

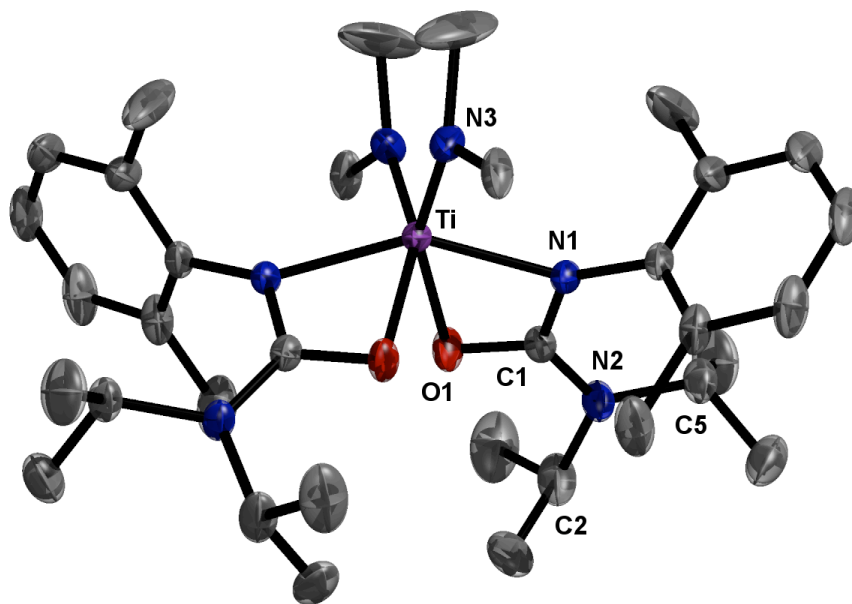


Figure 3.9. ORTEP representation of the molecular structure of **89** (ellipsoids plotted at 50% probability, hydrogens omitted for clarity, one orientation of NMe₂ ligands shown) with selected bond lengths (Å), bond and torsion angles (°): Ti–N1, 2.102(2); Ti–O1, 2.125(2); Ti–N3, 1.910(2); C1–N1, 1.327(2); C1–O1, 1.292(3); C1–N2, 1.355(3); N1–Ti–O1, 61.92(6); N1–Ti–N1*, 149.92(7); sum of angles about N2, 359.6(6); N1–C1–N2–C5, 18.1(3).

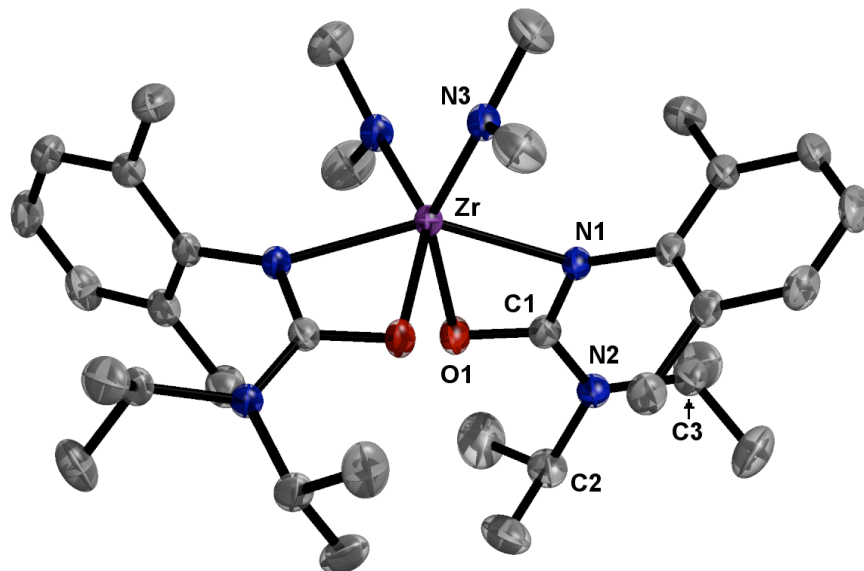


Figure 3.10. ORTEP representation of the molecular structure of **159** (ellipsoids plotted at 50% probability, hydrogens omitted for clarity) with selected bond lengths (Å), bond and torsion angles (°): Zr–N1, 2.253(2); Zr–O1, 2.222(1); Zr–N3, 2.059(2); C1–N1, 1.335(2); C1–O1, 1.301(2); C1–N2, 1.348(2); N1–Zr–O1, 58.61(5); N1–Zr–N1*, 149.38(8); sum of angles about N2, 359.8(5); sum of angles about N3, 355.6(5); N1–C1–N2–C3, 16.8(3).

Complexes **160** and **161**, which have the bulky 2,6-diisopropylphenyl substituents attached to the chelating nitrogen, also display very similar ^1H NMR spectral characteristics. A single septet around δ 3.7 (δ 3.69 for **160**, δ 3.72 for **161**) corresponds to the methine protons of the isopropyl substituents, while two doublets (δ 1.15, 1.36 for **160**; δ 1.35, 1.48 for **161**) indicate two inequivalent sets of methyl groups. These spectroscopic features suggest hindered rotation about the Ar–CH(CH₃)₂ bonds, which may be due to steric interactions between the aryl substituents and the dimethylamido ligands. In addition, one set of broad signals is observed for the piperidinyll protons (multiplets at δ 1.34, 3.02 for **160**; δ 1.07, 3.04 for **161**). This may indicate electron donation by the distal nitrogen, although a definitive statement to this effect cannot be made. These data suggest a structure that is C_2 -symmetric, with the bulky aryl groups

oriented *trans* to one another, analogous to that observed for the solid-state structures of **89** and **159**.

Fortunately, recrystallization of both **160** and **161** afforded single crystals for X-ray crystallography. The solid-state molecular structures of **160** and **161** are shown in Figures 3.11 and 3.12 respectively. Both complexes have distorted octahedral geometries, and are largely isostructural with **89** and **159**. Complex **161** is C_2 -symmetric, while **160** exhibits C_1 -symmetry due to differing ring conformations between the two ligands. As before, the metrical parameters are consistent with electron donation by the distal nitrogen atoms. The observed geometric isomers are in accord with the solution-phase spectroscopic data outlined above, confirming that the bulky aryl groups are proximal to the dimethylamido ligands.

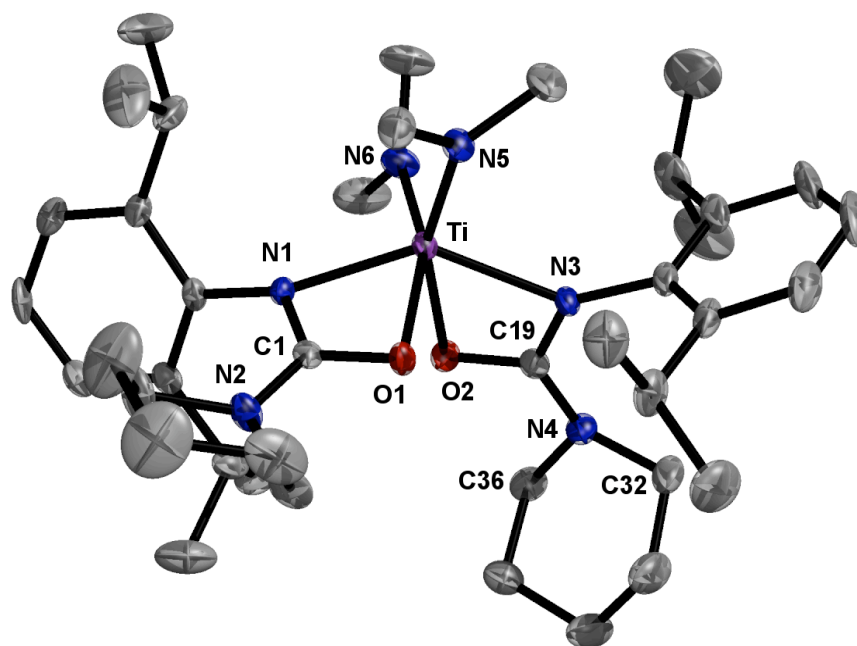


Figure 3.11. ORTEP representation of the molecular structure of **160** (ellipsoids plotted at 50% probability, hydrogens omitted for clarity) with selected bond lengths (Å), bond and torsion angles (°): Ti–N1, 2.086(1); Ti–O1, 2.141(1); Ti–N5, 1.913(1); C1–N1, 1.337(2); C1–O1, 1.284(2); C1–N2, 1.347(2); N1–Ti–O1, 62.36(5); N1–Ti–N3, 141.63(6); sum of angles about N2, 358.3(6); sum of angles about N5, 359.7(4); O2–C19–N4–C36, 0.9(2).

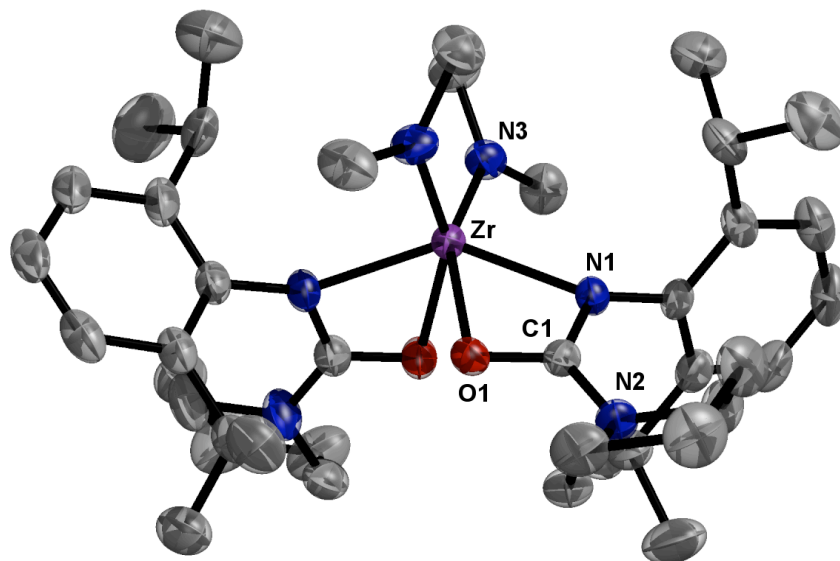


Figure 3.12. ORTEP representation of the molecular structure of **161** (ellipsoids plotted at 50% probability, hydrogens omitted for clarity) with selected bond lengths (Å), bond and torsion angles (°): Zr–N1, 2.244(2); Zr–O1, 2.240(2); Zr–N3, 2.051(3); C1–N1, 1.336(3); C1–O1, 1.292(3); C1–N2, 1.353(3); N1–Zr–O1, 58.70(8); N1–Zr–N4, 141.03(8); sum of angles about N2, 357.4(7); sum of angles about N3, 359.5(6); O1–C1–N2–C18, 2.8(4); N1–C1–N2–C14, 22.0(4).

In addition to the solid-state structural data collected for ureate compounds **89** and **159-161**, collaborators from within the Schafer research group have obtained X-ray crystallographic data for all of the amidate complexes from Figure 3.8 (**100**, **139**, **162-165**).^{110,243-245} Since all of the precatalysts under investigation here have been characterized by X-ray crystallography, a direct structural comparison between amidate- and ureate-supported complexes is possible. Comparing the metrical parameters of bis(ureato) complexes **89**, **159-161** to their bis(amidato) analogues reveals several consistent differences. Figure 3.13 illustrates the structural formulae of these complexes, and the average metal–ligand and metal–amido bond distances. Here, ‘ligand’ refers exclusively to the κ^2 -amidate or ureate; metrical parameters for κ^1 -bound amidates, as in **100** and **164**, are not included.

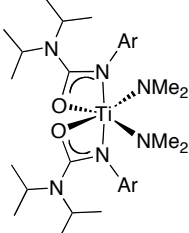
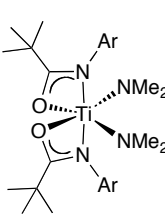
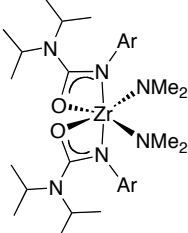
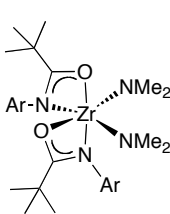
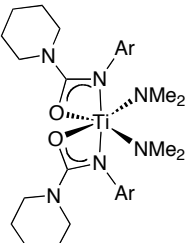
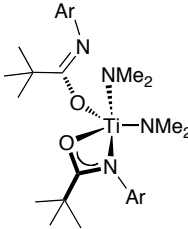
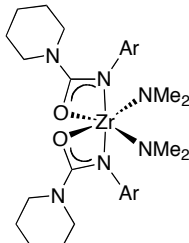
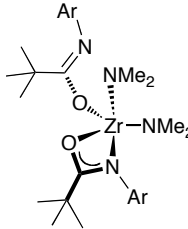
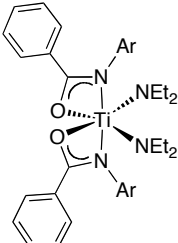
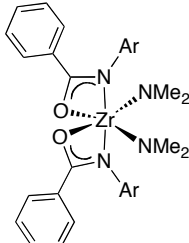
				
Ar = 2,6-dimethylphenyl 89	Ar = 2,6-dimethylphenyl 162	Ar = 2,6-dimethylphenyl 159	Ar = 2,6-dimethylphenyl 163	
Avg. M–N _{ligand} (Å)	2.102(2)	2.111(3)	2.253(2)	2.355(2)
Avg. M–O _{ligand} (Å)	2.125(2)	2.130(2)	2.222(1)	2.177(2)
Avg. M–N _{amido} (Å)	1.910(2)	1.906(3)	2.059(2)	2.041(3)
Avg. bite angle (°)	61.92(6)	61.5(1)	58.61(5)	57.39(8)
				
Ar = 2,6-diisopropylphenyl 160	Ar = 2,6-diisopropylphenyl 100	Ar = 2,6-diisopropylphenyl 161	Ar = 2,6-diisopropylphenyl 164	
Avg. M–N _{ligand} (Å)	2.115(1)	2.161(2)	2.241(2)	Quality of structural data does not allow for meaningful comparison
Avg. M–O _{ligand} (Å)	2.118(1)	2.072(2)	2.239(2)	
Avg. M–N _{amido} (Å)	1.920(2)	1.888(2)	2.054(2)	
Avg. bite angle (°)	62.18(5)	61.44(5)	58.82(7)	
				
Ar = 2,6-diisopropylphenyl 139		Ar = 2,6-diisopropylphenyl 165		
Avg. M–N _{ligand} (Å)	2.156(1)	2.264(2)		
Avg. M–O _{ligand} (Å)	2.146(1)	2.249(2)		
Avg. M–N _{amido} (Å)	1.899(2)	2.033(1)		
Avg. bite angle (°)	61.20(5)	58.09(5)		

Figure 3.13. Structural comparison of non-tethered precatalysts.

First, the structural data indicate that, in nearly every case, the electron-rich ureate ligands bind more tightly to the metal centers than the amidates. Only for titanium complexes **89** and **162** is there no discernable difference. One measure of the proximity

of ancillary ligands to a metal center is metal–ligand bond distance. Excluding complexes **89** and **162**, each pair of sterically similar ureate and amidate complexes has the ureate nitrogens closer to the metal center. The average difference ranges from 0.023(4) Å (**161/165**), to 0.102(4) Å (**159/163**). This means that for the ureate precatalysts, the bulky *N*-aryl substituents are closer to the reactive dimethylamido ligands. Conversely, the M–O_{ligand} distances show no consistent trend. However, another indicator of metal–ligand proximity is ligand bite angle (angle between N_{ligand}–M–O_{ligand}), with larger angles indicating tighter binding. Again, in every case except **89/162**, the average ureate bite angle is larger, from 0.73(12)° (**161/165**) to 1.22(13)° (**159/163**). This tighter binding by the ureate ligand also has an effect on the metal–amido bond distances. For every amidate/ureate pair except **89/162**, the M–N_{amido} distances are longer for the ureate derivatives.

Second, it is clear that ligand structure also has an impact on molecular geometry. Compare zirconium complexes **159** and **163**, which exhibit different coordination stereochemistry, despite the steric similarity of the ligands in question. Also compare titanium complexes **100**, **139**, and **160**, and zirconium complexes **161**, **164**, **165**. This series reveals that changing the substituent on the carbonyl group can also affect the binding mode of the ligand. Ureate complexes **160** and **161** adopt the same coordination geometry as the phenyl-substituted amidate complexes **139** and **165**, with both ligands bound in a κ^2 -fashion. However, *tert*-butyl substituted amidates **100** and **164** instead adopt a mixed κ^1, κ^2 -motif, resulting in five-coordinate complexes. Furthermore, the amidate ligands of **163** bind in a non-symmetric fashion, where the M–O_{amidate} lengths are markedly shorter than the M–N_{amidate} lengths. The bonding situation for amidate

complexes **163-165** can be described as arising from partial localization of the amidate negative charge on the oxygen donor. For **100** and **164**, steric hindrance likely disfavors coordination of both amidate nitrogens, resulting in the observed alkoxyimine tautomeric form. Non-symmetric amidate binding and ligand hemi-lability have been previously observed for other amidate complexes (for example, **148** and **149**).²³²

In contrast, this non-symmetric binding is not observed for ureate complexes **89** and **159-161**, or amidate complexes **139**, **162**, and **165**. The symmetric bonding in these complexes likely arises from a more delocalized negative charge between the nitrogen and oxygen donor atoms. Based on the present data, it appears that ligands containing substituents that can engage in π -conjugation favour this symmetric bonding: ureates have π -donating amino groups, while the amidates in **139** and **165** have π -withdrawing phenyl groups. Delocalization through the chelate may occur to increase the amount of π -conjugation with these substituents. Notably, none of the ureate complexes prepared as part of this thesis exhibit a monodentate binding mode.

The metrical analysis summarized above firmly establishes that ureate ligands are more electron-rich than analogous amidates, and that this increased electron donation influences metal–ligand bonding. Furthermore, the consequences of this stronger metal–ureate interaction are not only electronic in nature. Tighter ureate binding brings bulky ligand substituents closer to the metal center, reducing overall steric accessibility. These subtle effects can have a significant impact on reactivity. Understanding precatalyst structural details can therefore inform the design of improved catalysts. The following section will describe one such design modification, conceived to *increase* the steric accessibility of the metal center.

3.2.2 Precatalysts with Tethered Ureate Ligands

Given that most successful group 4 hydroamination systems have sterically accessible metal centers supported by multidentate ligands, the tethered bis(urea) proligand **87** was used to generate precatalysts **166** and **167** (Figure 3.14). Both of these compounds are crystalline, facilitating an easy and high yielding synthesis. Unfortunately, attempts to prepare analogous bis(amidato) complexes **168** and **169** from the appropriate diamide proligand led to the isolation of impure, amorphous material. Thus, a direct spectroscopic and structural comparison between amidates and ureates is not currently possible for this class of precatalyst.

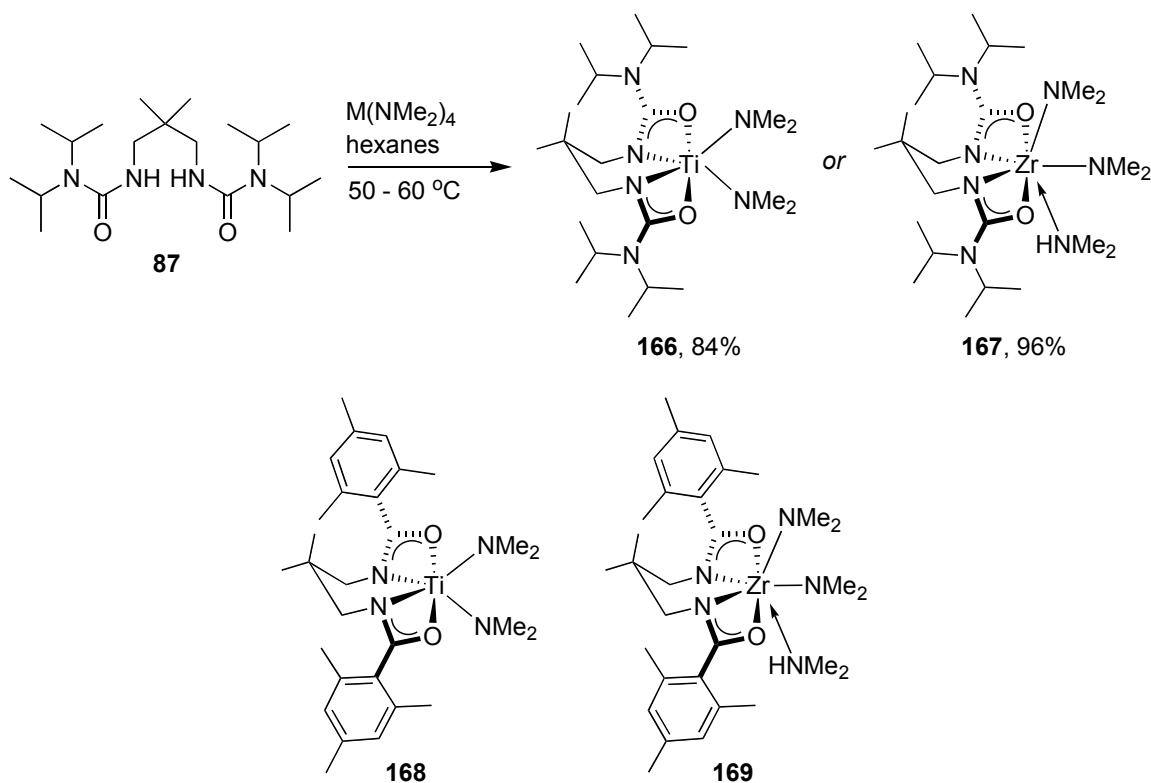


Figure 3.14. Tethered bis(ureato) and bis(amidato) precatalysts under investigation.

In contrast to the non-tethered complexes discussed above, the NMR spectra of tethered bis(ureato) complexes **166** and **167** reveal a high degree of magnetic

equivalence. The ^1H NMR spectra contain only one signal for each set of protons from the ureate ligand, including the potentially diastereotopic methylene protons of the alkyl tether. This is analogous to the solution-phase behaviour of related tethered bis(ureato) dichloride and dialkyl species from Chapter Two. Accordingly, these data suggest weaker electron donation by the distal nitrogen atoms of the ureate ligand: all of the isopropyl methine protons are equivalent, as are the methyl protons, indicating diminished multiple bond character in the $(i\text{-Pr})_2\text{N-C}$ linkage.

The ^1H NMR spectrum of **166** reveals that 30-40% of a contaminant is present in solution, even after recrystallization. This second compound gives broad NMR signals, all of which correspond to parts of the tethered bis(ureato) ligand. Heating the sample to 65 °C causes all of the resonances to broaden and coalesce into four large signals. A spectrum collected at 100 °C indicates only one compound is present. The room temperature spectrum is unchanged after heating. These data suggest that the mononuclear titanium complex reversibly dimerizes in solution, likely with the dimethylamido ligands bridging the two metal centers. This is not surprising, given the sterically open nature of the tethered ancillary ligand.

For zirconium complex **167**, only one component is present in solution; however, the signal corresponding to the dimethylamido groups is broad, and integrates to eighteen protons relative to the signals of the ureate ligand, rather than the expected twelve for a bis(amido) complex. This suggests the presence of one equivalent of dimethylamine acting as a neutral ligand. Analogous titanium and zirconium dichloride complexes from Chapter Two also contain a neutral dimethylamine. The signal broadening observed could be due to exchange between bound and unbound dimethylamine, and/or to proton

transfers between dimethylamine and dimethylamido ligands. The incorporation of a neutral ligand into the coordination sphere of **167** is another sign that metal centers supported by the tethered ureate ligand are sterically accessible. None of the non-tethered bis(ureato) complexes discussed previously display these structural features.

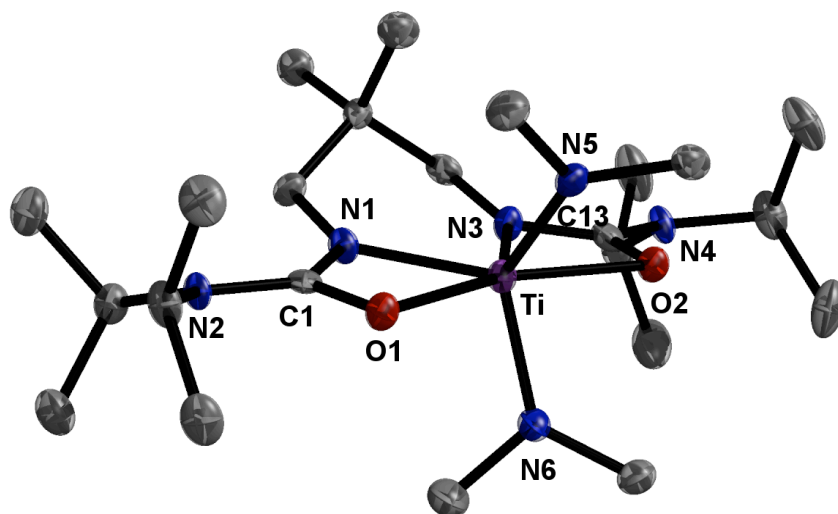


Figure 3.15. ORTEP representation of the molecular structure of **166** (ellipsoids plotted at 50% probability, hydrogens omitted for clarity) with selected bond lengths (Å), bond and torsion angles (°): Ti–N1, 2.071(3); Ti–O1, 2.156(2); Ti–N5, 1.928(3); Ti–N6, 1.917(3); C1–N1, 1.338(4); C1–O1, 1.279(6); C1–N2, 1.352(5); N1–Ti–O1, 61.7(1); N1–Ti–N3, 78.8(1); N5–Ti–N6, 122.4(1); sum of angles about N2, 359.5(9); sum of angles about N3, 358.1(7); N1–C1–N2–C2, 25.7(6).

The solid-state molecular structures of **166** and **167** are shown in Figures 3.15 and 3.16 respectively. The titanium congener is the mononuclear six-coordinate complex, with the bis(ureato) ligand coordinating in the previously observed planar arrangement. As for related base-free dialkyl complexes supported by tethered bis(ureato) ligands (**97**, **98**), the geometry about titanium is best described as distorted tetrahedral, with each *N,O*-chelate occupying one coordination site. In contrast, zirconium complex **167** is seven-coordinate, with the dimethylamido ligands oriented *cis* about the zirconium center, and the seventh coordination site occupied by a neutrally bound dimethylamine.

An examination of the metrical parameters reveals a remarkably long equatorial Zr–NMe₂ bond (2.135(1) Å). Structurally analogous seven-coordinate amidate and sulfonamidate complexes have Zr–NMe₂ lengths that range between 2.06–2.07 Å.^{115,246} The origin and consequences of this apparently weaker zirconium–nitrogen bond will be discussed in the following chapter

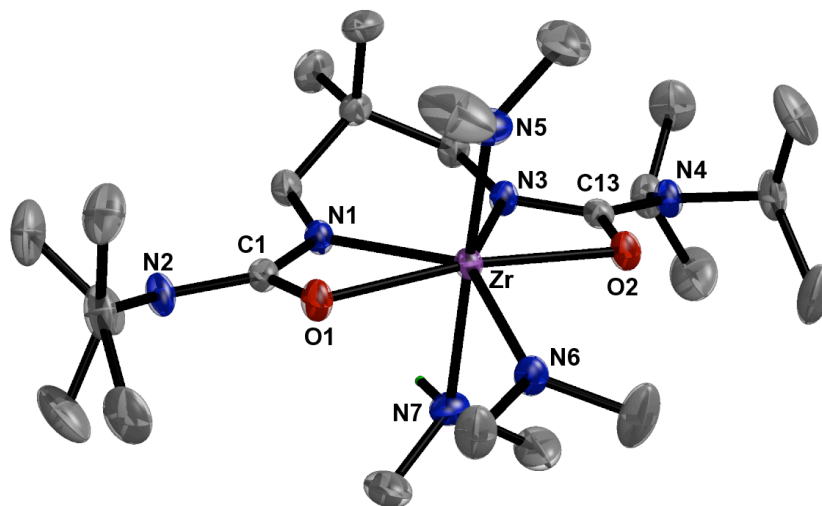


Figure 3.16. ORTEP representation of the molecular structure of **167** (ellipsoids plotted at 50% probability, hydrogens omitted for clarity) with selected bond lengths (Å), bond and torsion angles (°): Zr–N1, 2.280(1); Zr–O1, 2.240(1); Zr–N5, 2.092(2); Zr–N6, 2.135(1); Zr–N7, 2.503(2); C1–N1, 1.320(2); C1–O1, 1.308(2); C1–N2, 1.371(2); N1–Zr–O1, 57.91(5); N1–Zr–N3, 74.45(5); N5–Zr–N7, 175.19(6); sum of angles about N2, 359.7(6); sum of angles about N3, 355.6(5); N1–C1–N2–C3, 16.8(3).

As stated above, synthesis of the bis(amidato) analogues **168** and **169** was unsuccessful, negating the possibility of a direct structural comparison. The solution-phase behaviour of **166** and **167** suggests diminished electron donation from the distal amino groups, which would make these ureate derivatives less electron-rich than their non-tethered counterparts. It is therefore possible that the structural differences between tethered bis(amidato) and bis(ureato) complexes are less pronounced, which may affect the relative catalytic activities of these precatalysts.

3.2.3 Metal–Ureate Bonding Model

Up to this point, a wealth of structural evidence has been presented to support the notion that ureate ligands are more electron rich than corresponding amidate ligands. The prevailing hypothesis is that the distal nitrogen atom of the ureate ligand is the source of this extra electron density; however, exactly *how* this electron donation affects bonding is not immediately obvious. One possibility is that the increased π -electron density on the nitrogen and oxygen donor atoms results in stronger $p\pi$ - $d\pi$ bonding between the ligand and metal center. This is unlikely, as previous computational work has indicated that amidate ligands bind to group 4 metals in an exclusively σ -bonding fashion, with no $p\pi$ - $d\pi$ contribution.²⁴⁷ Preliminary Density Functional Theory (DFT) calculations, carried out in collaboration with J. M. P. Lauzon of the University of British Columbia, also reveal an exclusively σ -bonding metal–ligand interaction for ureate complexes **161** and **167**.²⁴⁸

Another possibility is that increased electron density affects the metal–ligand interaction in a purely electrostatic manner. In this sense, electron donation would increase the amount of negative charge on the donor atoms, resulting in a stronger anion/cation interaction. An analysis of Natural Bonding Orbital (NBO) charges for the nitrogen and oxygen donor atoms of computationally modeled ureates **161** and **167**, and analogous amidates **165** and **169**, supports this hypothesis (Table 3.5).²⁴⁸ In both cases, the ureate donor atoms carry a greater overall negative charge than those of the amidates. The effect is greater for non-tethered complexes **161** and **165**, with an average difference of $-0.071\ e$ in favour of the ureate nitrogen donors, and $-0.015\ e$ for the oxygen donors. In contrast, donor atom charges for the tethered ligands are closer, with those of the

oxygen atoms being effectively equal. This is consistent with aforementioned spectroscopic evidence suggesting diminished electron donation by the tethered ureate ligands of **167** relative to non-tethered ureates. Finally, the data indicate a greater degree of negative charge delocalization for the ureate ligands relative to the amidates. This is also consistent with experimental data, as evidenced by the metal–ligand bond lengths discussed previously.

Table 3.5. NBO charges from preliminary computational investigations.

Entry	Complex	Zr charge (<i>e</i>)	Average N _{ligand} charge (<i>e</i>)	Average O _{ligand} charge (<i>e</i>)
1	161 (ureato)	+2.003	-0.756	-0.742
2	165 (amidato)	+1.980	-0.685	-0.727
3	167 (ureato)	+1.883	-0.736	-0.748
4	169 (amidato)	+2.202	-0.713	-0.750

Based on the above structural analysis, ureate ligands are not just a more electron-rich version of amidates. Conjugation between the N–C–O chelate framework and the distal dialkylamino group also favours a symmetric κ^2 -*N,O* binding mode, and increases the amount of negative charge carried by the two donor atoms. It is this latter property that leads to a stronger metal–ureate interaction. Rather than arising from increased covalent π -bonding, this tighter ligand binding is the result of electrostatic forces between the ureate anion and the metal cation. All of these features serve to bring the ureate ligand substituents closer to the metal center, reducing steric accessibility. Notably, the ureate ligand containing the electron-rich alkyl tether exhibits less electron-donation from the distal nitrogen atoms. This may result in different reactivity for the complexes supported by this ligand (**166** and **167**) relative to non-tethered complexes (**89**, **159–161**).

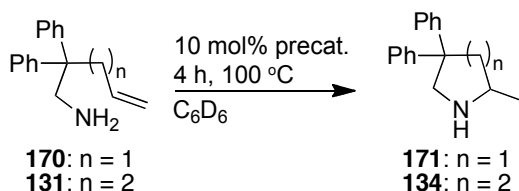
3.2.4 Steric and Electronic Effects on Hydroamination Catalysis

While the above analysis sought to correlate ligand electronics with structure and bonding, the following study focuses on determining the impact of steric and electronic effects on reactivity, specifically regarding hydroamination catalysis. To illuminate the relationship between precatalyst identity and catalytic activity, all of the compounds from Figure 3.8 and Figure 3.14 were subject to a series of catalytic screening experiments. Three aminoalkene substrates (**131**, **170** and **172**) were chosen in order to ensure that meaningful comparisons could be drawn between precatalysts. These represent common benchmark substrates used by other researchers to test catalytic activity.

The first set of experiments involves the cyclization of primary aminoalkenes **131** and **170** (Table 3.6). Each precatalyst was tested at least twice under identical conditions, with reaction progress determined after four hours by ^1H NMR spectroscopy. Several of the bis(amidato) precatalysts were formed *in situ* from the appropriate amide proligand and $\text{M}(\text{NMe}_2)_4$ ($\text{M} = \text{Ti}, \text{Zr}$). In particular, tethered bis(amidato) complexes **168** and **169** were not isolable as pure compounds, but were still included in catalytic screening experiments. This manner of *in situ* preparation is common for many hydroamination catalysts, including zirconium compounds **144** and **147**.^{226,228} There was no observed difference in activity between *in situ* generated and preformed catalysts.

An examination of the data in Table 3.6 reveals several trends regarding catalytic activity. Most striking is that the amidate precatalysts nearly always outperform their ureate counterparts, sometimes dramatically (for example, **161/165**). This is not surprising, given that previous work has indicated electron-withdrawing ligands tend to impart greater catalytic activity,^{109,114,246} conversely, electron-rich ureate ligands should

reduce activity. Similarly, amidates with π -withdrawing phenyl substituents (**139**, **165**) are more active than electron-rich amidates (**100**, **164**). Furthermore, it was established above that as a result of tighter metal–ureate binding, the bulky *N*-aryl groups on the ureate ligand are closer to the metal center, reducing overall steric accessibility. This may also contribute to lower catalytic activity for ureate precatalysts.



^a[precatalyst] = 0.075 M, [substrate] = 0.750 M. ^bConversion determined by ¹H NMR spectroscopy, number in brackets is isolated yield. ^cPrecatalyst formed *in situ*.

formation of **171**. The reason for the increased catalytic activity of **160** relative to **161** is unclear; especially considering **160** is *less* active for the formation of **134**.

Another method of altering metal center steric accessibility is through ligand design. Here, the data suggest that for zirconium precatalysts, use of less sterically hindered ligands results in higher activity (**159/161**, **163/164**), while for titanium complexes, the opposite appears to be true (**89/160**). While this does not seem to hold for precatalysts **100/162**, the solid-state structure of **100** reveals that one amidate ligand is κ^1 -bound, meaning this complex *less* sterically hindered than **162**. That more sterically congested titanium catalysts exhibit higher activity has been previously observed for a series of bis(amidato) alkyne hydroamination precatalysts.¹¹⁰ These opposing trends could be due to differing mechanistic pathways accessed by the two metal centers. It is well established that titanium catalysts proceed *via* an imido-mediated, [2+2] cycloaddition as the key C–N bond forming step.²²² On the other hand, zirconium precatalysts **156-158** are proposed to operate *via* an alternate, σ -bond insertion pathway.^{240,241} In the former case, steric compression may accelerate the reaction, while in the latter, steric accessibility may be required for the olefin to approach the metal center.

Finally, it is also clear that precatalysts supported by tethered ligands are generally the most active. Here, **167** is the only precatalyst to take both reactions to completion in the time allotted. This effect is even more dramatic when examining the second set of screening experiments. As mentioned above, very few group 4 catalysts are able to use secondary amines as substrates for hydroamination.²³⁸⁻²⁴² In order to identify a system capable of this transformation, all of the precatalysts were tested for the cyclization of secondary aminoalkene **172** (Table 3.7). None of the non-tethered systems form **173** to

any detectable degree, leaving the aminoalkene unaffected; however, precatalysts with tethered ligands *are* able to effect this challenging transformation, with **167** as the most active system. Furthermore, **167** is the only ureate precatalyst to consistently outperform its amidate counterpart, in striking contrast to the data obtained for the other pairings. This can be partially attributed to the reduced electron donation exerted by the ureate ligand of **167**, proposed above based on spectroscopic and computational evidence; however, this effect may be only one of several responsible factors.

Table 3.7. Precatalyst screening for secondary aminoalkene hydroamination.^a

Reaction scheme: **172** (N-methyl-N-phenyl-2-allylamine) reacts with 10 mol% precatalyst in C₆D₆ at 100 °C for 4 h to form **173** (N-methyl-N-phenyl-2-phenylpropan-1-amine).

Entry	Urate precatalyst	Conv. (%) ^b	Amidate precatalyst	Conv. (%) ^b
1	89 (Ti)	<2	162 (Ti)	<2
2	159 (Zr)	<2	163 (Zr)	<2
3	160 (Ti)	<2	100 ^c (Ti)	<2
			139 (Ti)	<2
4	161 (Zr)	<2	164 ^c (Zr)	<2
			165 (Zr)	<2
5	166 (Ti)	<2	168 ^c (Ti)	19
6	167 (Zr)	>98 (92)	169 ^c (Zr)	57

^a[precatalyst] = 0.075 M, [substrate] = 0.750 M. ^bConversion determined by ¹H NMR spectroscopy, number in brackets is isolated yield. ^cPrecatalyst formed *in situ*.

The preceding investigation has established that ureate-supported hydroamination precatalysts are generally inferior to their amidate counterparts. This is likely due to the interrelated steric and electronic properties of these metal complexes. As observed previously, the most general catalysts incorporate sterically accessible zirconium centers

supported by multidentate ligands. In addition to developing a structure/activity relationship for group 4 hydroamination systems, these experiments have resulted in the discovery of a highly active catalyst in compound **167**.

3.2.5 Hydroamination Scope of Tethered Precatalyst

Based on the catalytic performance of **167** in screening experiments, its applicability for challenging hydroamination reactions was explored. The precatalysts pictured in Figure 3.7 are capable of the cyclization of secondary aminoalkene **172**;²³⁸⁻²⁴² however, no group 4 catalysts are reported for the intermolecular hydroamination of alkynes with secondary amines. As shown in Figure 3.17, **167** can effectively mediate these transformations for a range of amine and alkyne substrates. The resulting enamine products were either reduced to the amine and isolated (**174-179**), or quantified using 1,3,5-trimethoxybenzene as an internal NMR standard (**180-184**). This latter protocol was used for hydroamination reactions that did not proceed to completion (formation of **180-182**), or resulted in regioisomer mixtures (formation of **183** and **184**).

The hydroamination scope outlined below is very impressive for a zirconium catalyst. With the exception of the formation of **184**, these transformations are unprecedented for group 4 systems.¹⁸³ Second, **167** efficiently promotes the synthesis of various products, including those containing potentially coordinating heteroatoms (**176**, **178**, **179**, and **180-183**), protected amines and ketones (**178** and **179**), and a Lewis-acid sensitive group (**179**). Third, **167** is able to hydroaminate internal (as for **180** and **181**) and functionalized (**182**) alkynes, albeit with diminished yield. Finally, as the preparation of **184** indicates, **167** is effective with both primary and secondary amines. These

hydroamination reactions represent fundamentally useful transformations from a synthetic standpoint. The enamines initially formed can be utilized in a variety of subsequent reactions, including alkylation²⁴⁹ and cycloaddition.²⁵⁰ Also, masked functional groups, such as in **178** and **179**, provide handles for further synthetic elaboration

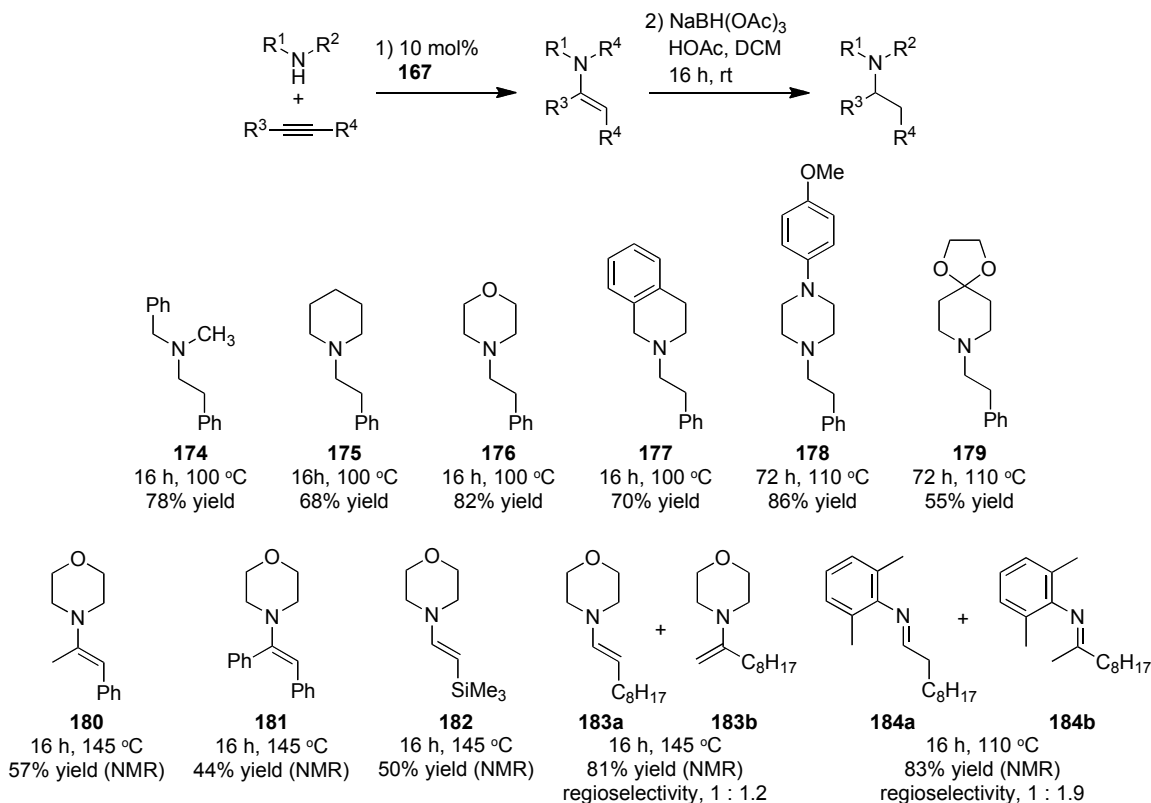


Figure 3.17. Hydroamination of alkynes using precatalyst **167**.

Certainly, the use of **167** does have limitations. As can be clearly observed for the synthesis of **183** and **184**, the use of sterically unhindered alkyl-substituted alkynes leads to regioisomeric mixtures with poor selectivity, slightly favouring the Markovnikov product. This low regioselectivity can be attributed to the sterically open nature of the zirconium center. Further, hydroamination scope with primary amine substrates is limited; the reactions often result in the formation of multiple products. This facet of the

reactivity of **167** will be revisited and expanded in Chapter Five, in the context of new reaction development. Finally, the use of *N,N*-arylalkyl amines (for example, *N*-methylaniline), leads to no conversion. This latter drawback is common to all reported d^0 -metal catalysts, and may originate from limitations imposed by the operative mechanism.¹⁸³

Given the broad reactivity exhibited by precatalyst **167** for alkyne hydroamination, it was tested for challenging aminoalkene cyclization reactions (Figure 3.18). Unless otherwise noted, all products were isolated as the neutral amine. As previously indicated in the introduction, unactivated 1,2-disubstituted alkenes are extremely difficult to hydroaminate; however, **167** mediates these transformations well, forming pyrrolidines **185** and **186** in good yield with high diastereoselectivity (**186**). The *gem*-disubstituent effect is not required for effective cyclization, as shown by the preparation of **187** and **188**. Furthermore, **167** is effective for the formation of five-, six-, and seven-membered heterocycles, including benzoazepane **193**. This ability is unprecedented for a group 4 catalyst,²³³ until now, only rare-earth catalysts have been able to mediate the formation of azepanes with any efficiency.¹⁸³ When presented with the aminoalkene substrates used to form **151** and **190-193**, other group 4 systems promote C–C bond formation as a major, if not the sole reaction pathway (Table 3.4). These hydroaminoalkylation products are not observed in any amount when using precatalyst **167**. This complete chemoselectivity renders this catalyst system particularly well suited to *N*-heterocycle synthesis.

In addition to the ability of **167** to catalyze the formation of **173** (Table 3.7), a series of secondary aminoalkenes are also effective substrates. Impressively, a sterically bulky cyclohexyl substituent on nitrogen does not prevent cyclization to **194**. This is the first

time a secondary alkyl group on a secondary amine has been accommodated by a hydroamination catalyst. As observed for the alkyne reactions, the bis(ureato) catalyst tolerates the presence of heteroatoms. Here, a piperonyl unit (**195**) and an *N*-benzyl pyrrole (**196**) are carried through cyclization as protected functional groups, with potential for further manipulation.

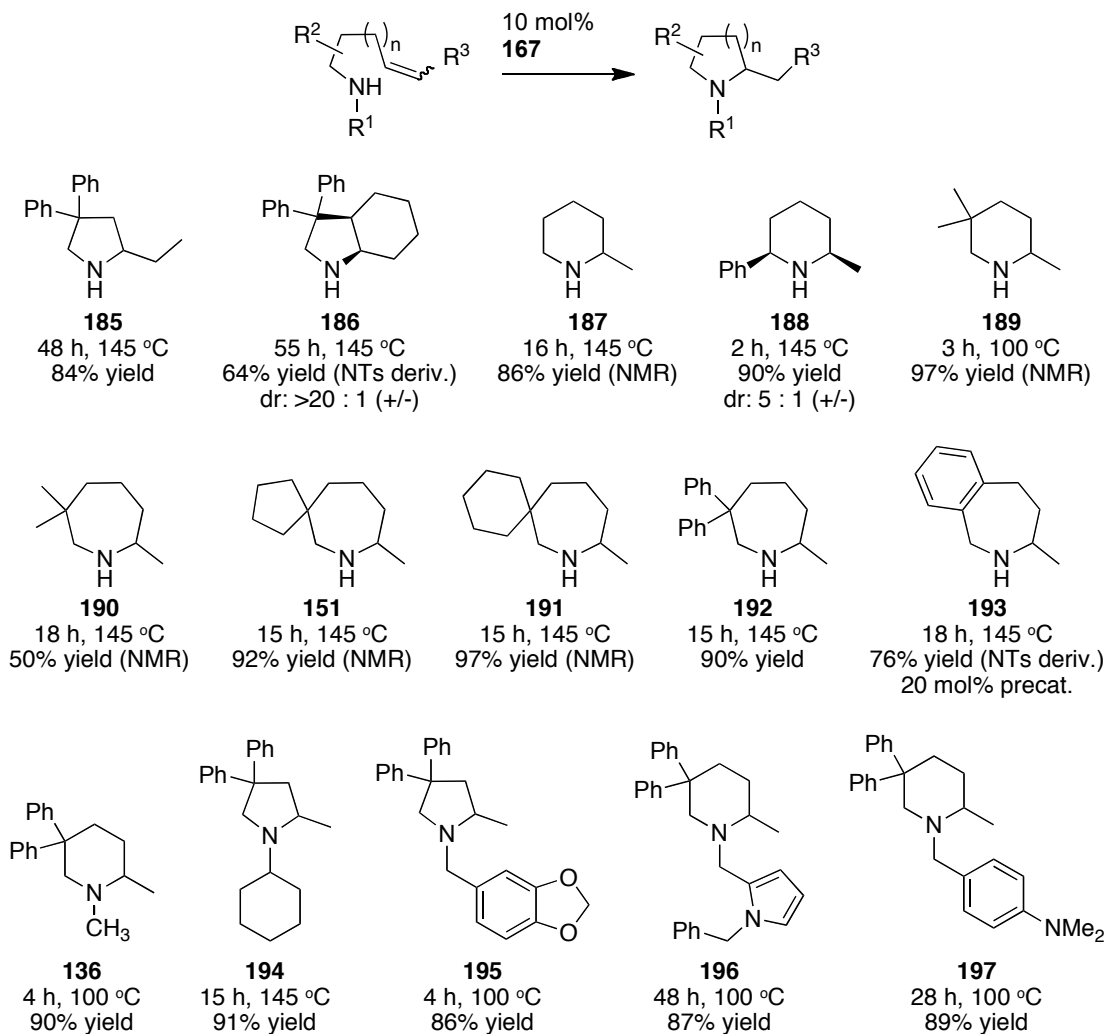


Figure 3.18. Cyclization of aminoalkenes using pre-catalyst **167**.

As before, limitations to the applicability of **167** are apparent. Attempted cyclizations of substrates containing unsaturated functional groups, such as esters or amides, were

unsuccessful, likely due to catalyst decomposition. Furthermore, several reactions require temperatures upward of 145 °C. Maintaining a solution of pure **167** at this temperature results in slow decomposition, as observed by ¹H NMR spectroscopy. This thermal instability is likely responsible for the lower yield of azepane **190**. Finally, all attempts at promoting intermolecular alkene hydroamination, using a variety of conditions and substrate combinations, have been unsuccessful.

Certainly, the generality exhibited by **167** in both inter- and intramolecular hydroamination reactions makes it a powerful addition to the rapidly growing arsenal of catalysts for these transformations. Furthermore, the functional group tolerance and selectivity of **167** mean that it is well suited to effect challenging and unprecedented hydroaminations. The scope outlined above, while impressive, is definitely not exhaustive. New applications for this simple and easy to use catalyst system are no doubt forthcoming.

3.3 Conclusions

Exploiting the steric and electronic characteristics of supporting ligands is the prevailing paradigm in homogeneous catalyst design. However, the relationship between ligand identity and catalyst behaviour is rarely ever obvious, or simple. The preceding investigation sought to establish such a relationship for a series of bis(amidato) and bis(ureato) group 4 compounds. Through a combination of solution-phase spectroscopy, X-ray crystallography, and collaborative DFT calculations, key differences between the amidate and ureate ligand sets have been identified. While seemingly sterically analogous, the electron-rich nature of the ureate results in stronger metal–ligand bonding. This brings the ligand closer to the metal, affecting both the electronic *and* steric environment about the metal center. Rather than strengthening the ureate–metal bonds in a covalent sense, computational investigations instead suggest that electron donation by the distal nitrogen increases the overall negative charge of the donor atoms, which likely results in a stronger electrostatic interaction between anion and cation.

These steric and electronic properties have a profound effect on reactivity. In nearly every case, the ureate-supported hydroamination precatalysts are inferior to their amidate counterparts. This indicates that the combination of an electron-rich supporting ligand and diminished metal steric accessibility negatively impacts catalytic reactivity for these transformations. In striking contrast to every other amidate/ureate pairing, sterically open tethered bis(ureato) zirconium complex **167** is *more* effective than its amidate partner. Use of this ureate precatalyst leads to unprecedented hydroamination catalytic reactivity for a group 4 system. An exploration of mechanistic possibilities that account for this unique behaviour is the focus of the following, penultimate chapter.

CHAPTER 4. Catalytic Hydroamination, Part II: Mechanistic Elucidation

4.1 Introduction

4.1.1 General Hydroamination Catalytic Cycles

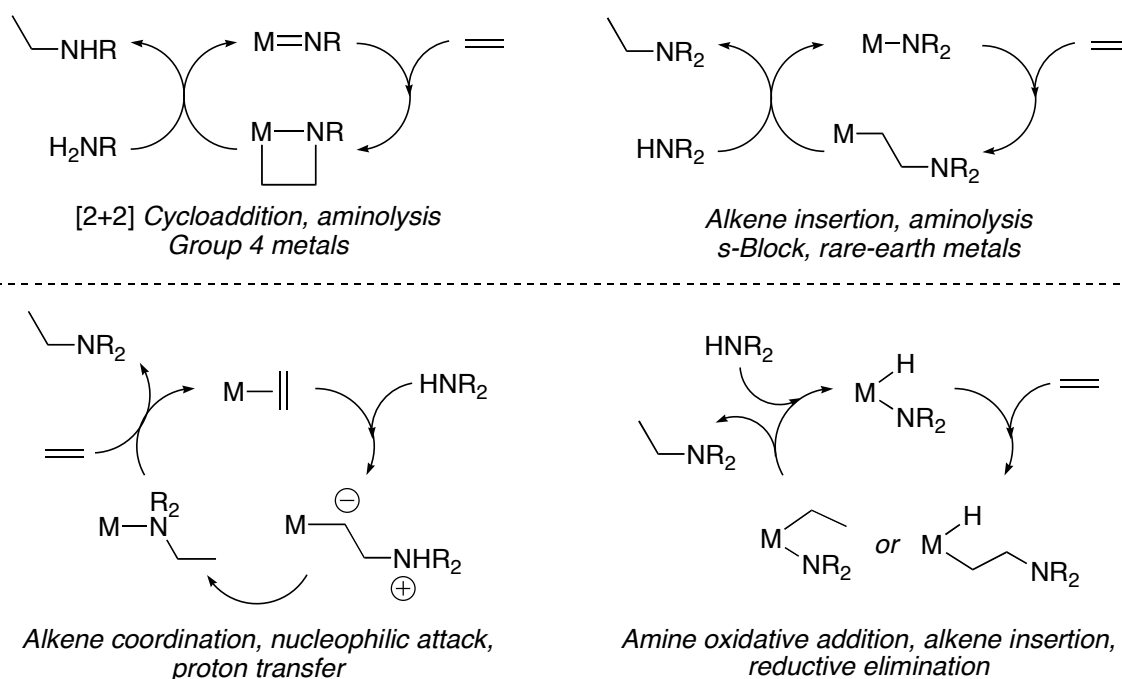
As established in the introduction to the previous Chapter, hydroamination reactions can be catalyzed by a diverse range of organometallic compounds containing metals from nearly all parts of the periodic table.¹⁸³ The mechanistic pathways accessed by these widely varied systems are equally diverse, and highly dependent upon catalyst identity. In a general sense, hydroamination mechanisms can be grouped into four major categories (Scheme 4.1).¹⁸³ The two catalytic cycles at the bottom of Scheme 4.1 are often proposed for late transition metal systems. On the left is a simplified cycle wherein C–N bond formation occurs *via* nucleophilic attack by an amine substrate onto a coordinated alkene (or alkyne). Subsequent proton transfer, rearrangement, and amine decoordination can release the product. On the right is a mechanism that proceeds *via* oxidative addition of the amine substrate to a low oxidation state metal center, generating an amido-hydrido complex. The alkene (or alkyne) can then insert into either the M–N or M–H bond. Reductive elimination forms the hydroamination product, and enables the metal center to undergo another oxidative addition. A plethora of mechanistic work has been performed to elucidate the specific details of these proposed pathways.^{89,218,251-267}

For catalysts based on metal ions with a d^0 -electronic configuration, such as Zr(IV), the bottom two catalytic cycles in Scheme 4.1 can be ruled out as plausible mechanistic possibilities. Alkene or alkyne complexes of d^0 -metals are rare, due to the absence of

metal-to-ligand synergistic bonding stabilization.¹³⁴⁻¹³⁶ Furthermore, the binding affinity of these hard metal centers would be much higher for an amine donor relative to an alkene,⁴⁴ reducing the possibility of an outer-sphere nucleophilic attack. Reductive elimination from a tetravalent group 4 metal center is also extremely rare, requiring redox-active supporting ligands.^{268,269}

Instead, catalysts containing metals from the *s*-block, *f*-block, and groups 3 and 4 must operate through alternate pathways, illustrated at the top of Scheme 4.1. By far the most common mechanism proposed for group 4 catalysts involves C–N bond formation *via* [2+2] cycloaddition between a metal–imido species and the C–C unsaturation.^{222,270} For *s*-block and rare-earth metals, a catalytic cycle based on alkene (or alkyne) insertion into a metal–amido bond is often proposed.^{187,201,271,272} The details of these two catalytic cycles will be reviewed below.

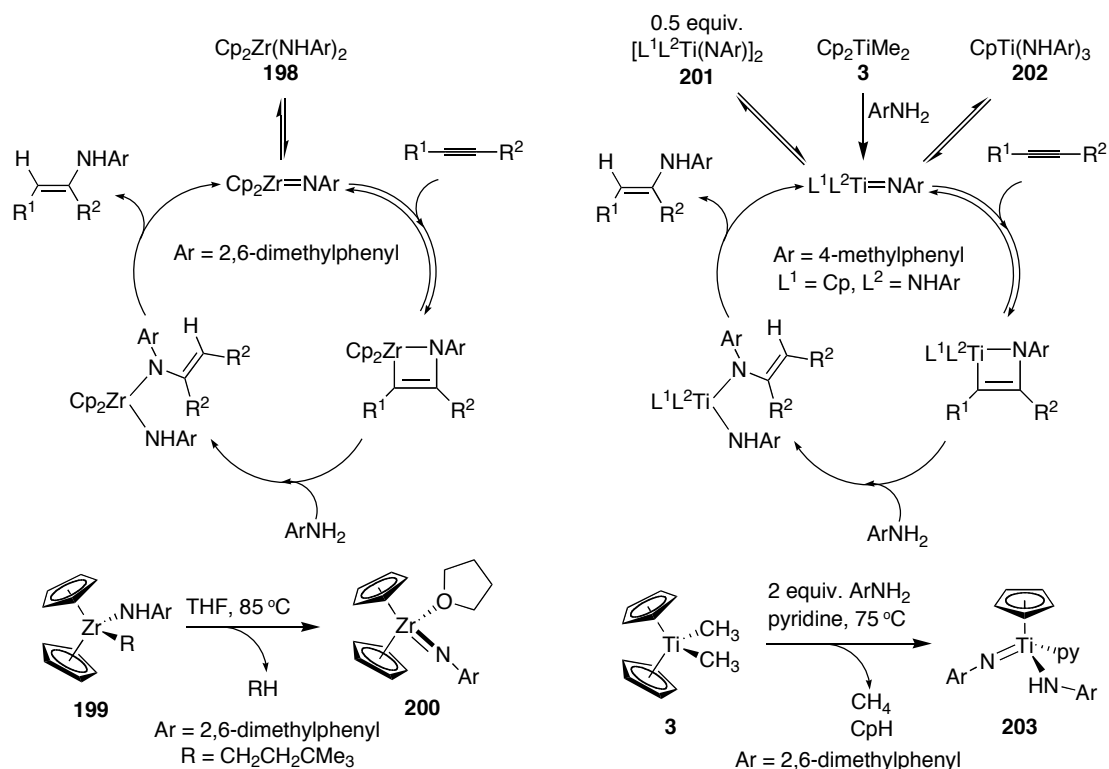
Scheme 4.1. Simplified pathways for metal-catalyzed hydroamination; top two routes common for early transition metals, bottom two for late transition metals.



4.1.2 Hydroamination *via* Imido Intermediates

As part of their seminal work on the first group 4 compounds capable of catalytic hydroamination, Bergman and co-workers proposed an imido-mediated catalytic cycle (Scheme 4.2, left).^{222,273} This proposal was based on precedent from stoichiometric reactivity,²⁷⁴ and a kinetic analysis of the catalytic reaction. The active catalyst, a zirconium imido species, is formed by amine elimination from a bis(amido) precatalyst (**198**). In the presence of an alkyne substrate, a formal, reversible [2+2] cycloaddition can occur, generating an azametallacyclobutene intermediate. Turnover-limiting protonolysis of the M–C bond by an incoming amine substrate then forms a mixed amido-enamido complex. Finally, intramolecular proton abstraction by the enamido group liberates the hydroamination product and regenerates the imido active species.

Scheme 4.2. Proposed mechanisms for the hydroamination of alkynes with zirconocene (**198**, left) and titanocene (**3**, right) precatalysts; formation of imido species.



In 2001, kinetic work by Pohlki and Doye using a titanocene precatalyst (**3**) led these researchers to similar conclusions (Scheme 4.2, right).²⁷⁰ All of the “on-cycle” features of their mechanistic proposal are completely analogous to those put forward by Bergman and co-workers a decade prior.²²² However, this later work provides insight into precatalyst activation and “off-cycle” deactivation pathways. In particular, hydroamination reactions involving **3** undergo a short induction period. The authors propose that during this time, **3** is converted into the active catalyst. Parallel work by Johnson and Bergman demonstrated that in the presence of excess 2,6-dimethylaniline and pyridine, **3** is transformed into the mono(cyclopentadienyl) imido complex **203** (Scheme 4.2).²⁷⁵ This new compound is more catalytically active than **3**; it is therefore likely that the active species is similar in structure to **203**. Pohlki and Doye also observed a non-linear relationship between reaction rate and precatalyst concentration. At concentrations of **3** greater than 0.02 M, the rate increases minimally with increased catalyst loading. The authors attribute this to catalyst deactivation *via* a reversible dimerization of the active species to **201**. Facile dimerization has been observed for many other group 4 imido complexes.^{274,276-281}

In addition to kinetic analyses that support an imido-mediated mechanism, there is also extensive synthetic evidence in favour of such a catalytic cycle. The formation of group 4 imido complexes through α -proton abstraction is well established,^{22,282} one relevant example is the synthesis of the trapped imido species **200** from the zirconocene complex **199** (Scheme 4.2).²⁷⁴ Furthermore, there are close to sixty characterized examples of isolated azametallacycles resulting from [2+2] cycloadditions of group 4 imido complexes with alkynes (**204-242**, Figure 4.1), allenes (**243-257**), and alkenes

(258-261).^{22,222,273,274,280,283-304} Finally, several of these azametallacycles have been treated with an excess of amine to release an enamine, and regenerate a bis(amido) compound.^{222,273,296,299} Thus, each step of the proposed catalytic cycle has been observed through stoichiometric reactions. Imido-mediated catalysis has also been supported by computational studies.³⁰⁵⁻³⁰⁸

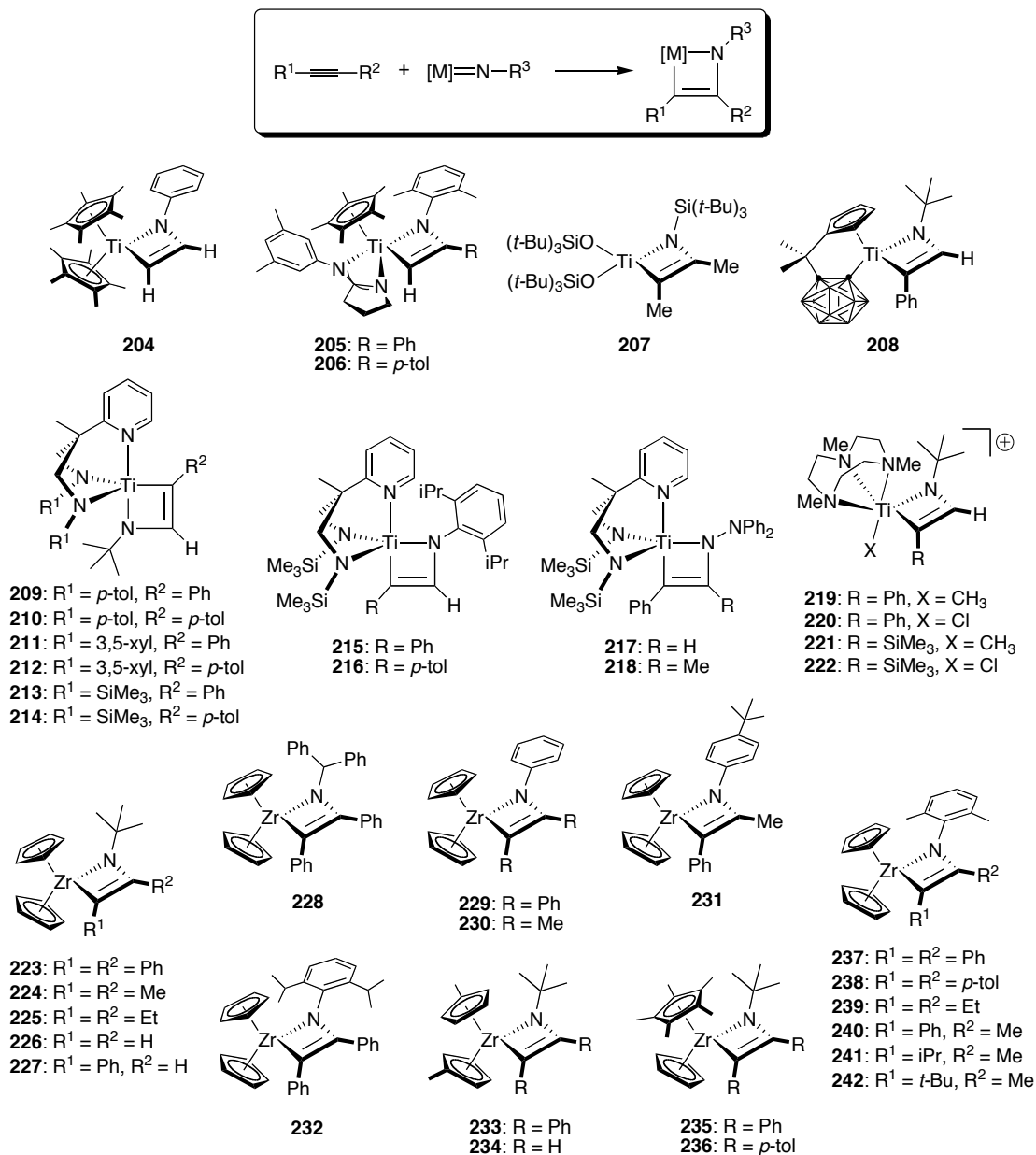


Figure 4.1. Azametallacyclobutenes of the group 4 metals formed by formal [2+2] cycloaddition between metal–imido bonds and alkynes.

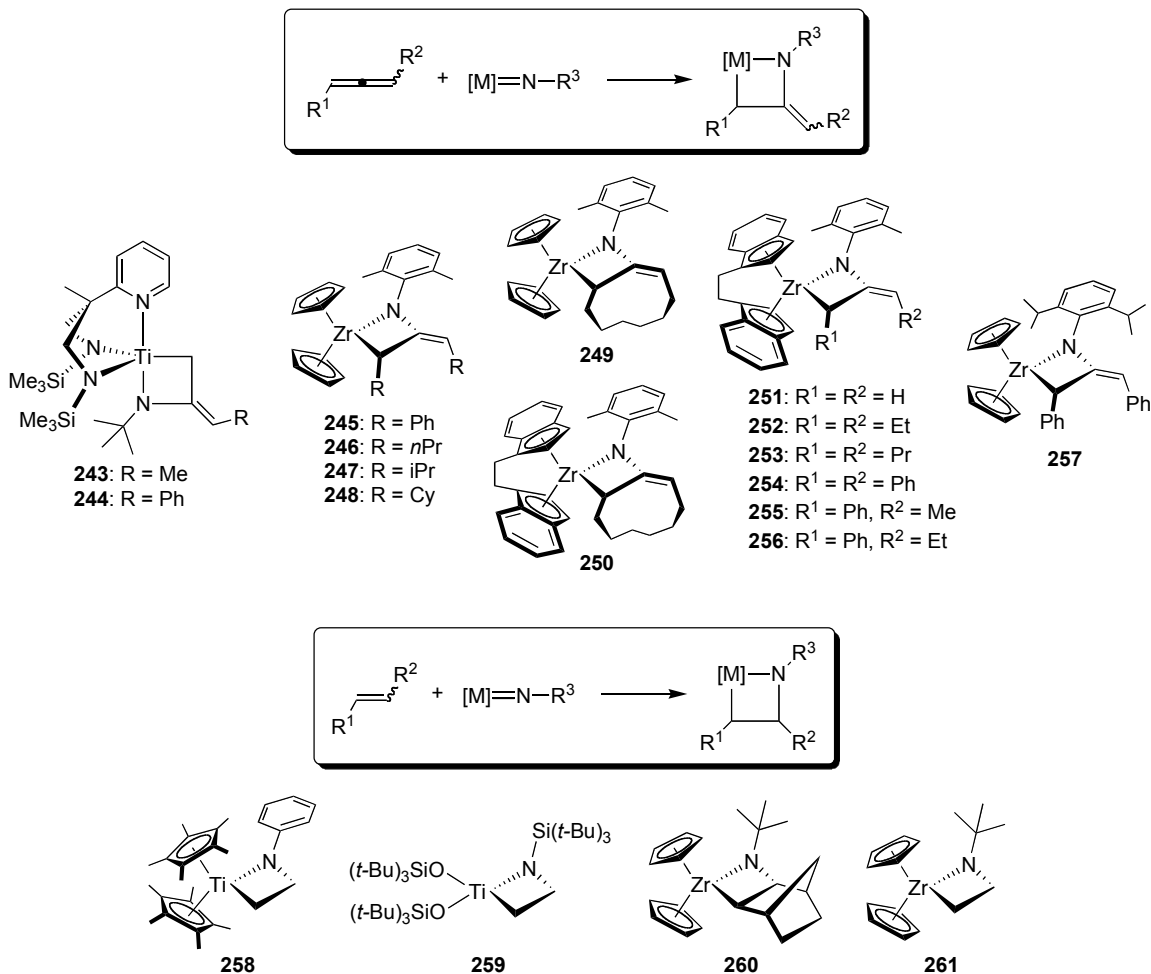


Figure 4.2. Azametallacyclobutanes of the group 4 metals formed by formal [2+2] cycloaddition between metal-imido bonds and allenes (top) or alkenes (bottom).

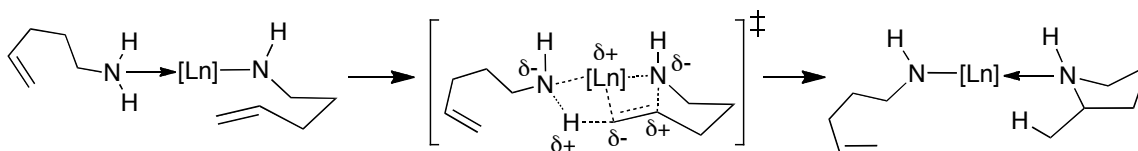
In the face of overwhelming evidence for the catalytic cycles in Scheme 4.2, nearly all group 4 catalysts have been proposed to operate *via* similar pathways;¹⁸³ however, in most cases these proposals are made by analogy. One often cited piece of evidence in favour of an imido-mediated mechanism is a lack of catalytic activity with secondary amine substrates. Clearly, a primary amine is required to generate the imido active species; however, forming a mechanistic conclusion based on a single experimental observation is far from definitive, especially considering recent experimental support for a feasible alternative mechanism involving alkene insertion into a Zr–N bond.²⁴⁰

4.1.3 Hydroamination *via* Insertion

Until recently, the Bergman cycloaddition mechanism was the only catalytic cycle proposed for neutral group 4 catalysts. In contrast, *s*-block and rare-earth systems have long been established to operate *via* pathways that form new C–N bonds through turnover-limiting σ -bond insertion of an alkene (or alkyne) into a metal–amido linkage (Scheme 4.1, top right).^{183,199,271,272} Gagné and Marks first proposed this mechanism in 1989;¹⁹⁸ shortly thereafter, in-depth kinetic work was reported that strongly supported this catalytic cycle for lanthanocene precatalysts.²⁰¹ There have since been myriad mechanistic investigations supporting this insertion pathway.^{187,188,203,207,272,309-312}

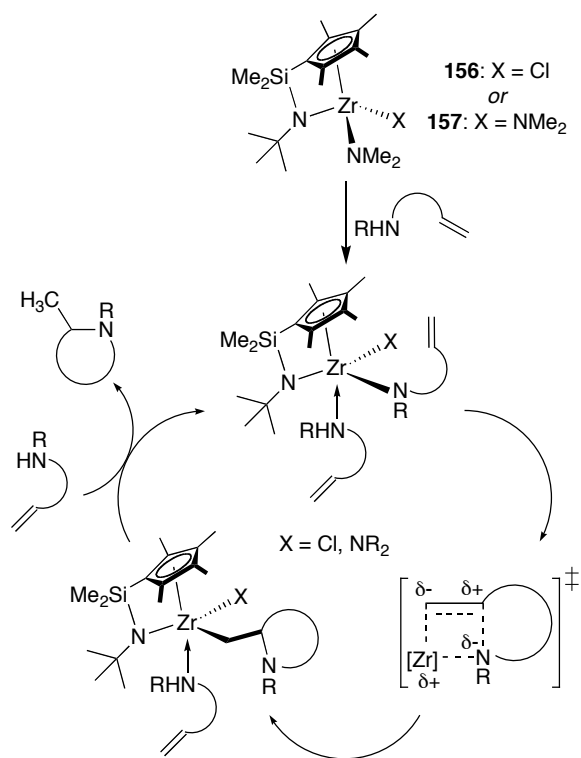
One intriguing aspect of the kinetic investigations carried out by Marks and co-workers,²⁰¹ and later Hultsch and co-workers,¹⁸⁷ is that use of *N*-deuterated aminoalkene substrates results in observation of a primary kinetic isotope effect (KIE). This indicates that the turnover-limiting step must involve cleavage of an N–H/D bond, and/or formation of a C–H/D bond; however, alkene insertion into the Ln–N bond is proposed as turnover-limiting. In order to explain this apparent inconsistency, Marks and co-workers suggested in 1992 that the turnover-limiting step may be concerted insertion/protonolysis (Scheme 4.3).²⁰¹ A discussion of this mechanistic model is conspicuously absent from subsequent kinetic or theoretical studies. Rather, this primary KIE is explained as arising from amine coordination to the metal center during insertion.^{187,309}

Scheme 4.3. Originally proposed concerted insertion/protonolysis transition-state, accounting for primary KIE in lanthanide-catalyzed aminoalkene hydroamination.



In 2007, Stubbert and Marks disclosed the first hard evidence that neutral group 4 systems could also operate *via* an insertion-based mechanism (Scheme 4.4).²⁴⁰ Sterically accessible constrained-geometry zirconium precatalysts **156** and **157** were shown to be operative with both primary and secondary aminoalkene substrates, as related in the previous chapter. This simple observation, along with in-depth kinetic and synthetic work, led the authors to propose the catalytic cycle shown in Scheme 4.4. Notably, a KIE for these zirconium systems was not reported.

Scheme 4.4. Proposed σ -bond insertion mechanism for the hydroamination of primary or secondary aminoalkenes for constrained geometry zirconium precatalysts **156** and **157**.

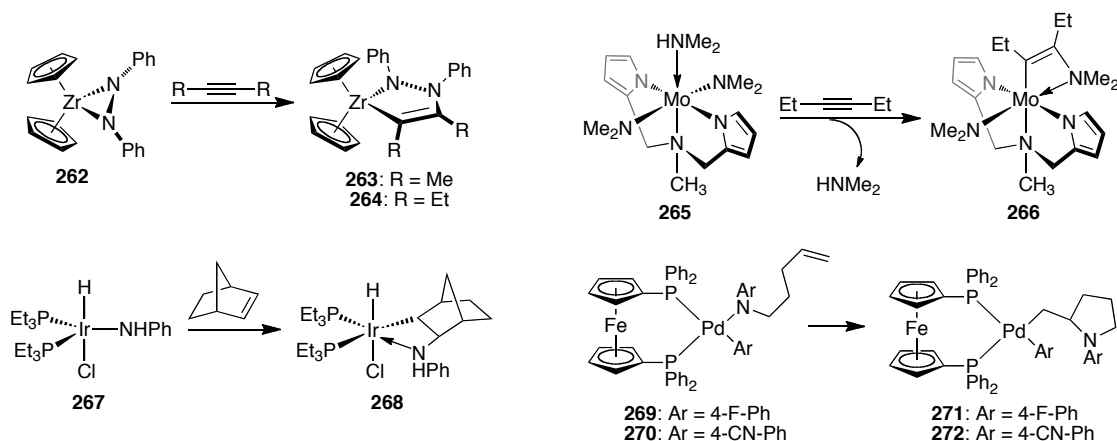


As described previously, there are a few other examples of neutral group 4 catalysts that can perform hydroamination with secondary amines,^{241,242} however, no other mechanistic work has been reported to support an insertion mechanism. Computational modeling has provided evidence for the feasibility of such catalytic cycles;^{306,308} although

these theoretical investigations indicate that hypothetical cycloaddition and insertion mechanisms have similar activation barriers.

While authentic examples of [2+2] cycloaddition reactions between M=N bonds and C=C unsaturations are ubiquitous (Figures 4.1 and 4.2), there is a paucity of characterized compounds resulting from non-polar C=C multiple bond insertion into M=N bonds (Scheme 4.5). The sole examples of non-polar alkyne insertion into d^0 -metal–nitrogen bonds, reported by Bergman and co-workers in 1990, involves a strained azametallacycle (**262**).³¹³ There are only three further examples if all transition metals are considered. Casalnuovo and co-workers observed the insertion of norbornene into an Ir–N bond of an active hydroamination catalyst (**267**);³¹⁴ Odom and co-workers characterized the product of 3-hexyne insertion (**266**) into a Mo–N bond;³¹⁵ and Wolfe and co-workers recently used ¹³C NMR spectroscopy to observe alkene insertion into Pd–N bonds.³¹⁶

Scheme 4.5. Characterized alkyne (top) and alkene (bottom) insertion products.



Due to its ability to perform hydroamination with secondary amines, the tethered bis(ureato)zirconium precatalyst from the previous chapter (**167**) must be able to access some permutation of the insertion-based mechanism. For hydroamination reactions with primary amine substrates, however, either pathway is possible. Mechanistic work is

therefore required to differentiate between these two catalytic cycles. One other noteworthy feature of precatalyst **167** is that no hydroaminoalkylation side-reactivity is observed, even with substrates that are biased toward this alternate reaction. Possible reasons for this chemoselectivity will be discussed below in the context of the stoichiometric reactivity of **167**. Establishing a rationale for the observed selectivity is also fundamentally important, since it would influence further catalyst design for *both* reactions.

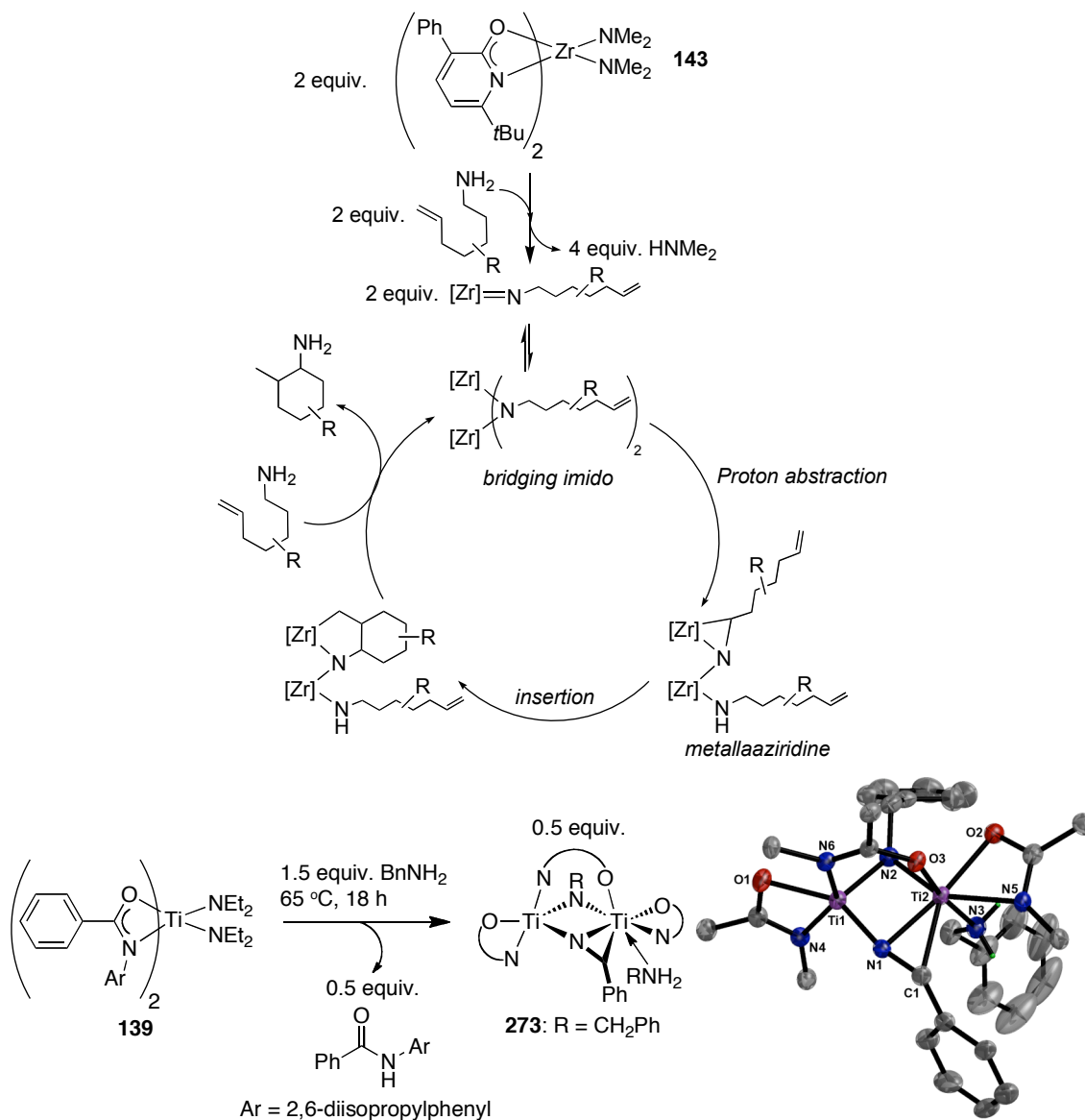
4.1.4 Proposed Hydroaminoalkylation Mechanism

In order to rationalize the chemoselectivity of **167** for hydroamination over hydroaminoalkylation, an understanding of the mechanistic details for this latter reaction is needed. Recent work from our research group using the zirconium precatalyst **143** suggests that C–C bond formation is mediated by dinuclear metallaaziridines (Scheme 4.6).²³³ Under catalytic conditions, the precatalyst can first be converted into an imido complex, which can subsequently dimerize. Proton abstraction from the carbon adjacent to nitrogen by a basic ligand would generate a dinuclear metallaaziridine. Then, insertion of the alkene into the metal–carbon bond would result in cyclization. Finally, protonolysis of the Zr–C and Zr–N bonds would release the product.

The dinuclear nature of the active species is suggested by two observations. First, as the concentration of precatalyst is increased, the selectivity for hydroaminoalkylation over hydroamination similarly increases. Second, a catalytically active, dinuclear titanaaziridine complex (**273**) can be generated by treating the bis(amidato)bis(amido)-titanium compound **139** with 1.5 equivalents of benzylamine (Scheme 4.6, bottom). One

striking aspect of this reaction is that half an equivalent of amide proligand is formed concurrently. This suggests that one of the amidate ancillary ligands is responsible for the proton abstraction to generate the initial metallaaziridine intermediate. Notably, secondary aminoalkenes are not effective substrates for this reaction, further supporting the intermediacy of a zirconium imido species.

Scheme 4.6. Proposed mechanism for the hydroaminoalkylation of primary aminoalkenes by zirconium precatalyst **143**; synthesis and solid-state molecular structure of dinuclear titanaaziridine **273**.



The field of hydroamination has benefited greatly from the mechanistic work carried out to elucidate the catalytic cycles depicted in Scheme 4.1. For catalysts based on d^0 -metals, it is generally accepted that hydroamination occurs *via* two general pathways, involving either cycloaddition between a metal–imido bond and the alkene/alkyne, or alkene/alkyne insertion into a metal–amido bond.¹⁸³ The remainder of this chapter will detail the results of a comprehensive mechanistic investigation regarding hydroamination reactions with precatalyst **167**. A major goal of this work is to elucidate the details of the catalytic cycle or cycles that are accessed by this system. In particular, discerning between an imido-mediated mechanism (Scheme 4.2) and an insertion-based mechanism (Scheme 4.4) for hydroamination with primary amines is paramount to understanding the source of the unique catalytic activity observed for **167**.

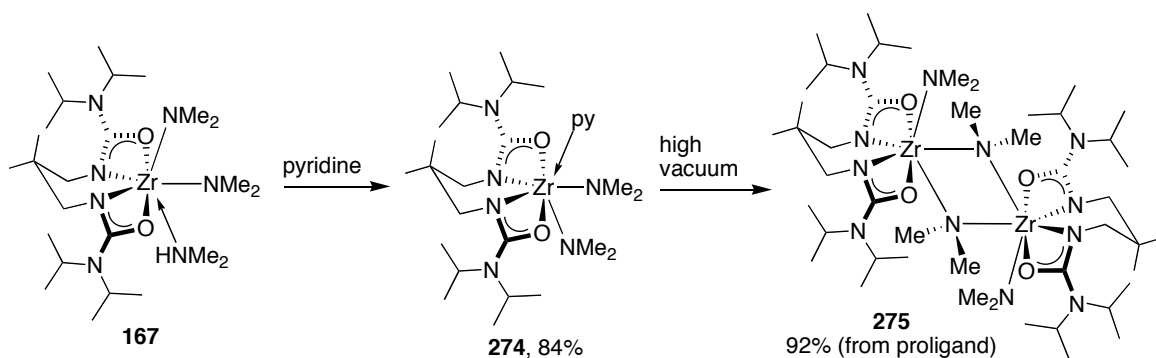
A two-fold approach has been executed to probe the operative catalytic cycles. First, the reactivity of **167** has been explored in a stoichiometric sense. These investigations allowed the isolation of several model compounds, enabling an evaluation of the thermodynamic feasibility of certain catalytic processes. Second, a kinetic analysis on the cyclization of aminoalkenes has been performed to gain insight into the catalytic reaction itself. Through the determination of an empirical rate law, inhibition kinetics, substituent effects on rate, and activation parameters, a possible reaction mechanism that accounts for all observations can be envisioned. The data suggest a concerted insertion/protonolysis event is operative, akin to the proposed transition state in Scheme 4.3. Furthermore, the ureate-supported catalyst system is not susceptible to common deactivation pathways, such as reversible dimerization/aggregation at high catalyst loading, or competitive inhibition by the hydroamination product.

4.2 Results and Discussion

4.2.1 Precatalyst Reactivity I: Effect of Neutral Donors

Initial stoichiometric experiments using precatalyst **167** focused on the effects of neutral donors to the solution-phase and solid-state coordination sphere of zirconium. The molecular structure of **167** was discussed previously; the structural formula is provided for reference in Scheme 4.7. Following the synthetic protocol established in Chapter Three, **167** is isolated as the dimethylamine adduct. Dissociation of this extra donor would generate a coordinatively unsaturated species, which could be a model for catalytically relevant intermediates. Therefore, the lability of the dimethylamine ligand was evaluated by treating **167** with a slight excess of pyridine (Scheme 4.7). Upon addition of 1.1 equivalents of pyridine to a solution of **167**, an immediate colour change from colourless to yellow is observed. Clarification of the suspension by heating and subsequent crystallization afforded the pyridine adduct (**274**) in 84% yield as yellow crystals. The NMR spectra of **274** are nearly identical to that of **167**, except for aromatic signals corresponding to the pyridine ligand, and an NMe₂ signal that integrates to twelve rather than eighteen. X-ray crystallography reveals that the structure of **274** is closely related to **167**; the solid-state molecular structure of **274** is shown in Figure 4.3.

Scheme 4.7. Replacement and removal of neutral donors from complex **167**.



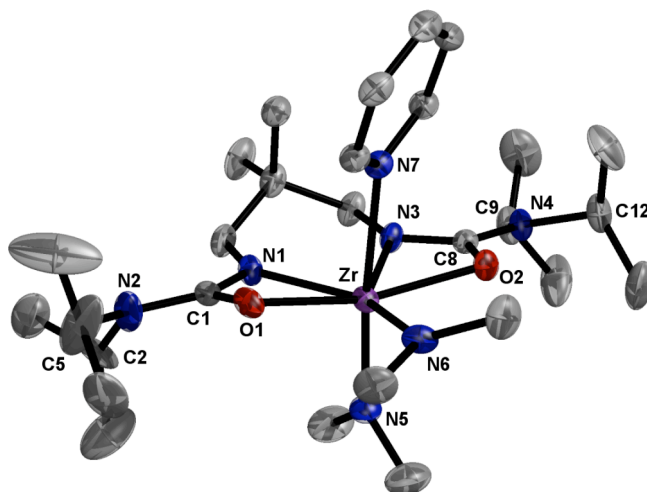


Figure 4.3. ORTEP representation of the molecular structure of **274** (ellipsoids plotted at 50% probability, hydrogens omitted) with selected bond lengths (Å), bond and torsion angles (°): Zr–N1, 2.224(3); Zr–O1, 2.248(3); Zr–N5, 2.067(3); Zr–N6, 2.097(3); Zr–N7, 2.508(3); C1–N1, 1.299(5); C1–O1, 1.288(4); C1–N2, 1.362(5); N1–Zr–O1, 57.7(1); N5–Zr–N7, 173.8(1); N3–C8–N4–C9: 24.0(6).

The lability of the dimethylamine ligand of complex **167** is in stark contrast to analogous dichloride compounds **92** and **93**, which were discussed in Chapter Two. This is likely due to the increased electron donation afforded by the amido ligands, which may help to stabilize a proposed six-coordinate intermediate. Synthesis of such a six-coordinate species was attempted by subjecting solid **274** to high vacuum for 48 hours (Scheme 4.7). Compound **274** was chosen for this reaction because the disappearance of pyridine can be easily monitored by NMR spectroscopy; however, similar treatment of **167** gives the same result. The resulting colourless solid has low solubility in common organic solvents, indicating possible aggregation. The NMR spectra of this new compound are nearly identical to those of both **167** and **274**, and consistent with a base-free formulation; however, electron-impact mass spectrometry provides evidence for a dimeric structure (**275**).

Compound **275** could be recrystallized from toluene for an X-ray crystallographic study (Figure 4.4), which confirms the structure as an amido dimer. The two halves of the complex are related by an inversion center, giving overall C_{2h} -symmetry. Each zirconium is seven-coordinate, as in the mononuclear parent complexes. Two amido ligands are bound exclusively to one zirconium, with the remaining two bridging between the metal centers. This results in much longer Zr–N bonds for these bridging amido groups (2.323(1) Å) relative to the terminal amido ligands (2.108(1) Å).

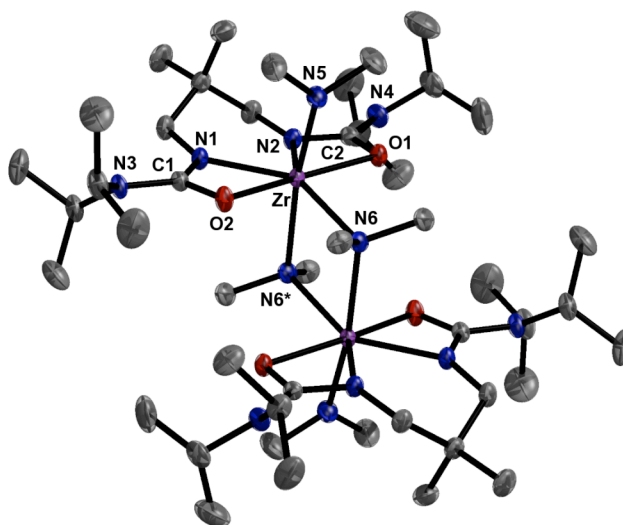


Figure 4.4. ORTEP representation of the molecular structure of **275** (ellipsoids plotted at 50% probability, hydrogens omitted) with selected bond lengths (Å), bond and torsion angles (°): Zr–N1, 2.241(1); Zr–O1, 2.226(1); Zr–N5, 2.108(1); Zr–N6, 2.323(1); Zr–N6*, 2.374(1); C1–N1, 1.312(2); C1–O2, 1.296(2); C1–N3, 1.373(2); N1–Zr–O2, 58.37(4); N1–Zr–N2, 74.43(4); N5–Zr–N6, 93.69(4); N5–Zr–N6*, 170.01(4); N6–Zr–N6*, 76.34(4); Zr–N6–Zr*, 103.66(4); N1–C1–N3–C8, 44.1(2).

Attempts to observe a solution-phase equilibrium between **275** and a putative six-coordinate complex by NMR spectroscopy were unsuccessful; however, the treatment of **275** with excess pyridine immediately regenerates **274**, as judged by ^1H NMR spectroscopy. These results suggest that in the presence of neutral donors, as during catalysis, a neutral ligand stabilized, seven-coordinate species is thermodynamically favoured. Therefore, this dimerization is not likely to be catalytically relevant.

4.2.2 Precatalyst Reactivity II: Thermal Stability

Another aspect of precatalyst reactivity relevant to catalysis is the possibility of thermally induced supporting ligand disproportionation. Many zirconium hydroamination precatalysts with tethered, tetradentate ligands (**147**, **276-279**) have been observed to undergo disproportionation reactions to form homoleptic complexes (**280-284**, Figure 4.5).^{228,317} This is a significant concern with regard to catalyst lifetime, especially during reactions that require high temperatures. Furthermore, the $\text{Zr}(\text{NMe}_2)_4$ that would be generated by ligand disproportionation can catalyze unwanted side-reactions, such as the previously described hydroaminoalkylation reaction. The thermal sensitivity of precatalyst **167** was previously mentioned in Chapter Three. Given the structural similarities between complexes **147**, **276-279** and the ureate precatalyst **167**, the possibility of this deactivation pathway has been examined.

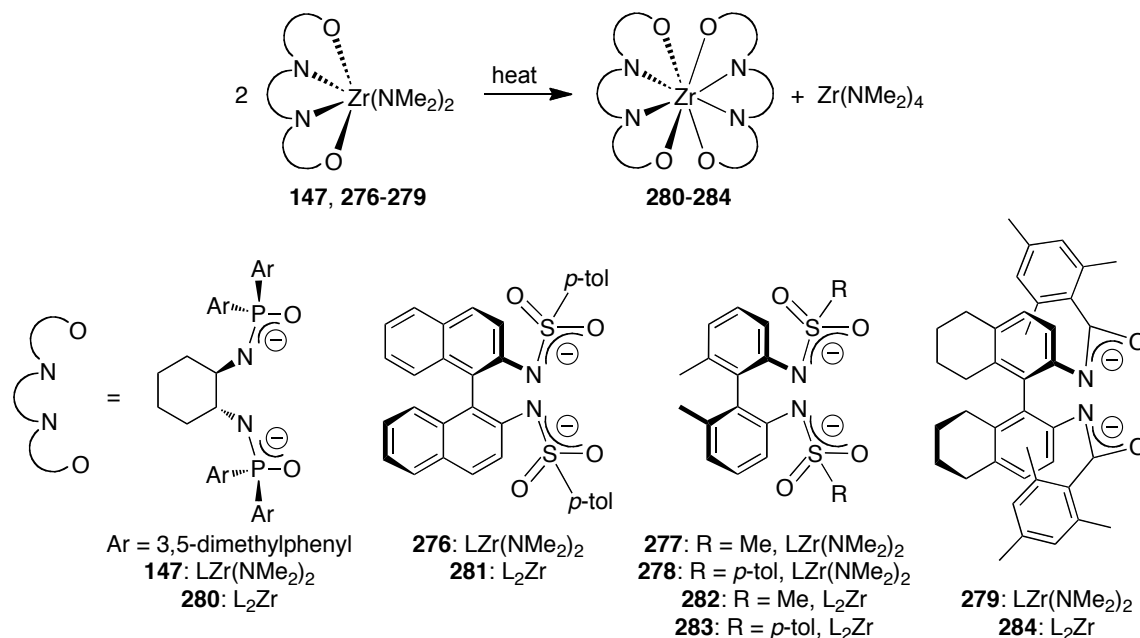


Figure 4.5. Thermally induced ligand disproportionation of zirconium hydroamination precatalysts supported by tethered ligands.

Heating a solution of **167** in *d*₈-toluene to 145 °C results in slow decomposition, as indicated by ¹H NMR spectroscopy. The sharp, well resolved ligand signals become broadened over a period of several hours; however, the concomitant formation of Zr(NMe₂)₄ is not observed. An attempt has also been made to prepare the tetrakis(ureato) compound independently by treating Zr(NMe₂)₄ with two equivalents of the bis(urea) proligand **87**. ¹H NMR spectroscopy of the reaction mixture revealed a full equivalent of unreacted proligand. After heating to 65 °C, and recrystallization of the crude material from hexanes, a white crystalline solid can be obtained; however, this has been identified as the unreacted proligand (**87**). This indicates that a tetrakis(ureato)zirconium complex is not easily formed.

Given the apparent difficulty in generating the homoleptic ureate compound even when using appropriate reaction stoichiometry, the failure to observe Zr(NMe₂)₄ formation while heating **167**, and the ability of **167** to effectively catalyze chemoselective hydroamination reactions at high temperatures, deactivation by ligand disproportionation does not appear to be a significant problem for this catalyst. This may be due to stronger metal–ligand interactions enabled by the electron-rich ureate relative to those ligands in Figure 4.6, resulting in a robust, well-defined catalyst system. Another possible reason is that the tetradentate ligand of **167** forms a stable six-membered chelate ring with zirconium, as opposed to the more strained five- and seven-membered chelates of **147** and **276-279**. Finally, the geometry of the 2,2-dimethyl-propyl tether enables a nearly perfect planar arrangement of the ureate chelates, which likely imparts further stability. Therefore, gradual thermal decomposition of this catalyst may be due to alternate, as yet uncharacterized pathways.

4.2.3 Precatalyst Reactivity III: Synthesis of Imido Compounds

As described in the introduction to this chapter, the most common mechanism invoked for group 4 catalyzed hydroamination involves catalytically active imido complexes.¹⁸³ This is also the case for the hydroaminoalkylation reaction, in which dinuclear imidos are proposed to play a key role.²³³ It is therefore critical to prepare and characterize ureate-supported imido complexes as models for potential catalytic intermediates. In this manner, one can assess the feasibility of imido formation *via* aminolysis of precatalyst **167**, a model reaction for the catalyst activation step in the imido-mediated hydroamination mechanism. Furthermore, a structural analysis of these complexes may give insight into their suitability as hydroamination intermediates. In addition to affording potential insight into hydroamination catalysis, the preparation of group 4 imido compounds is important from a purely fundamental perspective. These species exhibit remarkable stoichiometric reactivity, including hydrocarbon C–H activation,^{274,293,318–326} and are implicated in a number of other catalytic processes, including imine metathesis,^{283,286,287} guanidine transamination,³²⁷ and carboamination.²⁹¹

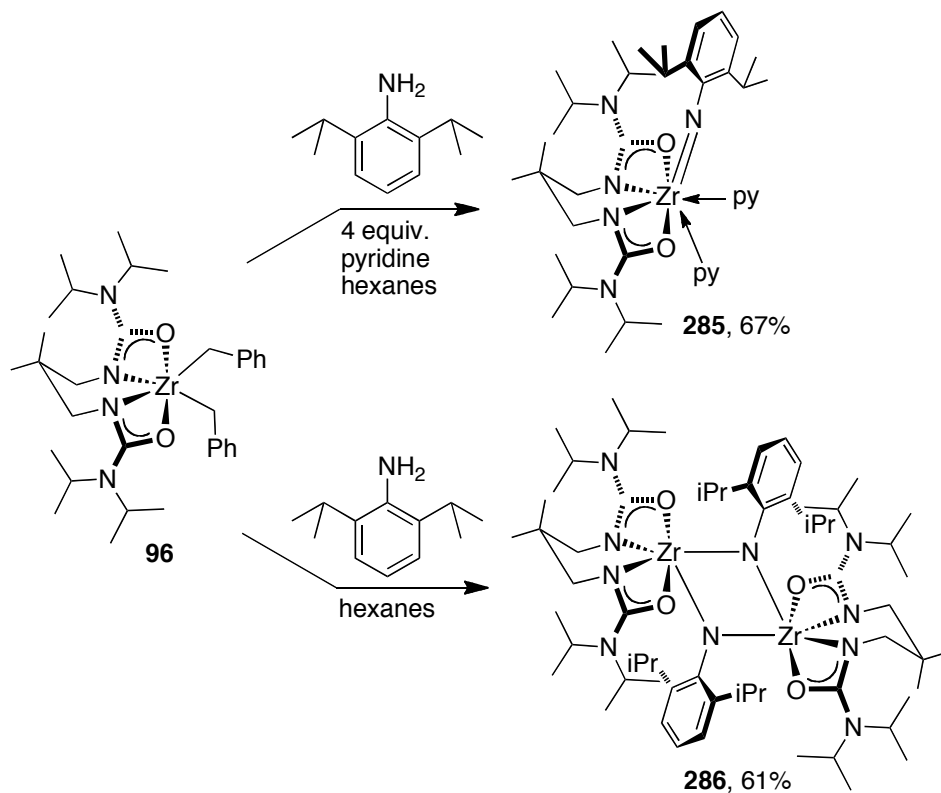
Several synthetic routes have been applied to the synthesis of these species, most involving salt metathesis reactions.^{22,282} Mountford and co-workers have developed titanium and zirconium starting materials of the form $M(NR)Cl_2py_2$ ($M = Ti, Zr$), which provide a convenient source of the metal–imido fragment.^{279,328,329} By treating these starting materials with alkali-metal salts of a variety of ancillary ligands, many group 4 imido complexes have been successfully prepared.^{282,330–332} Another common synthetic route involves a two-step process, in which an amido species of the form $L_nM(NHR)(R')$ is generated by salt metathesis, followed by thermally induced α -proton abstraction to

give $L_nM(NR)$ and $R'H$.^{22,274,293,318-326} However, neither of these methods is representative of hydroamination catalyst activation; therefore, a direct aminolysis reaction between **167** and one equivalent of primary amine has been examined. This route has been used previously to prepare several titanium and zirconium imidos from $L_2M(NMe_2)_2$ precursors,^{246,333-336} including amidate-supported derivatives.^{81,113,116}

Several attempts have been made to prepare imido species directly from the bis(amido) **167**. Treatment of **167** with one equivalent of 2,6-diisopropylaniline in the presence or absence of pyridine repeatedly gives mixtures resulting from incomplete protonolysis, even with elevated reaction temperatures. The presence of dimethylamine liberated during protonolysis is a possible cause for this inability to isolate pure imido compounds. Therefore, the dialkyl compound **96** was chosen as an alternate starting material (Scheme 4.8) due to the higher basicity of alkyl ligands, and the inert nature of the toluene byproduct.

Previously reported amidate-supported imido complexes have been stabilized by the presence of neutral donors in order to facilitate isolation and characterization.^{81,113,116} Given the observed propensity of complexes supported by the tethered bis(ureato) ligand from **167** to adopt seven-coordinate geometries, a similar strategy was employed for the preparation of compound **285**. Thus, reacting **96** with 2,6-diisopropylaniline and four equivalents of pyridine at room temperature results in a red suspension that can be clarified by gentle heating. On standing overnight at room temperature, an orange crystalline product, **285**, is deposited from this solution in 64% yield.

Scheme 4.8. Synthesis of mononuclear (**285**) and dimeric (**286**) imido complexes through aminolysis of dibenzyl compound **96**.



The solid-state molecular structure of **285** is shown in Figure 4.6, confirming the structure as a seven-coordinate, mononuclear imido complex. As for all other tethered bis(ureato) complexes, the ureate ligand adopts a planar arrangement. The two pyridine donors are *cis*-disposed, one in an equatorial position and the other axial. The imido ligand is axial, *trans* to one of the pyridine donors. The Zr–N1 distance of 1.891(3) Å, and Zr–N1–C1 angle of 177.6(3)° are consistent with a formal zirconium–nitrogen triple bond, characteristic of a zirconium–imido linkage. The axial pyridine is weakly bound (Zr–N6, 2.579(3) Å), likely due to the strong *trans*-influence of the imido ligand.

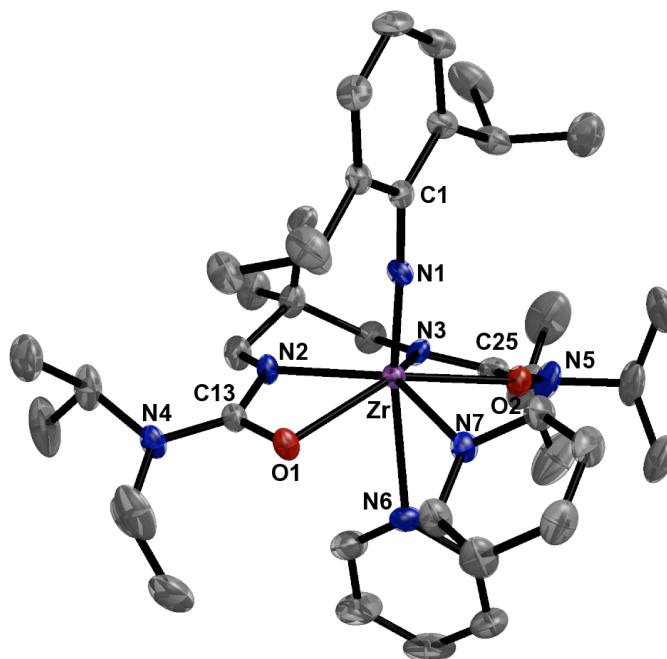


Figure 4.6. ORTEP representation of the molecular structure of **285** (ellipsoids plotted at 50% probability, hydrogens omitted) with selected bond lengths (Å), bond and torsion angles (°): Zr–N1, 1.891(3); Zr–N2, 2.245(3), Zr–O1, 2.244(2); Zr–N6, 2.579(3); Zr–N7, 2.375(3); C13–N2, 1.322(4); C13–O1, 1.290(4); C13–N4, 1.369(4); N2–Zr–O1, 58.44(9); Zr–N1–C1, 177.6(3); O1–C13–N4–C14, 20.2(5).

Combustion analysis of the crystalline material confirms the empirical formula and purity of compound **285**; however, solution-phase NMR spectroscopy reveals a more complicated situation. The ^1H NMR spectrum of a solution of crystalline **285** indicates the presence of two compounds in a 1:1 ratio; in addition, two broad pyridine *ortho*-proton signals are observed, assigned to exchanging bound and free pyridine. The addition of excess pyridine (10 equivalents) to this solution increases the ratio of components to 2:1. Upon heating to 65 °C for one hour followed by cooling to room temperature, only one organometallic compound is observed by NMR spectroscopy, assigned as the mononuclear imido **285**. The ^1H NMR spectral features of this compound after the above treatment are sharp and consistent with the proposed structure. The

methyl groups on the alkyl-tether are inequivalent, and the methylene protons diastereotopic, indicating different magnetic environments above and below the plane of the ligand. In addition, the isopropyl methine proton signals from the ureate ligand are split into two resonances, as are the signals for the corresponding methyl groups. This represents the only case of hindered rotation about the (*i*-Pr)₂N–C bond for this ligand, possibly due to steric compression by the large diisopropylphenyl group attached to the imido nitrogen.

The solution-phase behaviour of compound **285** suggests that, while stable in the solid-state, in solution **285** is in equilibrium with a base-free, dimeric imido species **286**, even in the presence of neutral donors. This tendency to dimerize may come as a result of the weak bond between the zirconium center and the pyridine *trans* to the imido, and the sterically accessible nature of the bis(ureato) ligand. Considering the size of the substituent on the imido nitrogen, favourable dimer formation is remarkable; only three examples of group 4 dimeric imidos with this bulky aryl group have been reported.^{276,279} In order to confirm this dimerization hypothesis, **286** was independently synthesized by treating compound **96** with only 2,6-diisopropylaniline (Scheme 4.8). Analytically pure crystals of **286** were isolated in 61% yield. On the basis of electron-impact mass spectrometry and X-ray crystallography (Figure 4.7), it has been confirmed that **286** is indeed a dimeric, base-free imido complex. Additionally, ¹H NMR spectroscopy of **286** confirms its identity as the second component in solution with the untreated compound **285**. Consistent with the anticipated reactivity of this dimeric species, treatment of **286** with an excess of pyridine and heat forms the mononuclear imido **285** in solution phase.

The molecular structure of **286** reveals that each zirconium center is six-coordinate. Adopting the convention that each ureate occupies *one* coordination site, previously used for complexes **95-97** from Chapter Two, each zirconium is best described as distorted tetrahedral. One striking structural feature is unique to this complex: the bis(ureato) ligand distorts itself to accommodate the bulky aryl group on the imido nitrogens. Rather than adopting a planar conformation, as observed for every other titanium or zirconium complex supported by this ligand, the two ureate chelates bend upward, away from the 2,6-diisopropylphenyl group, while maintaining a tetradentate binding mode.

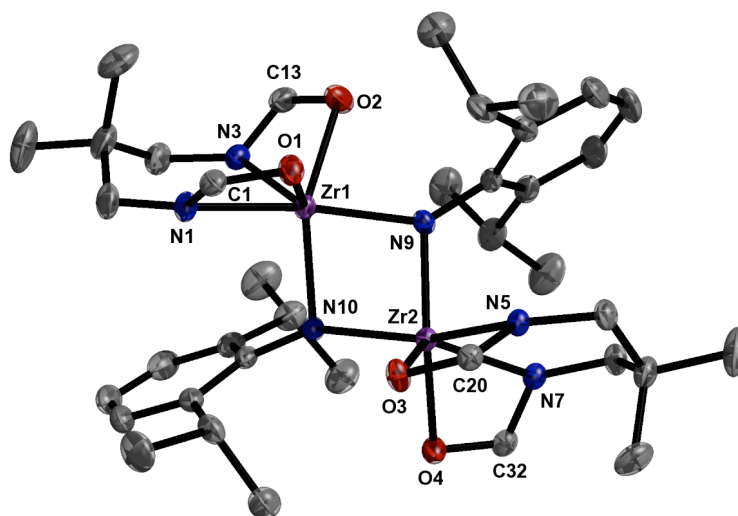
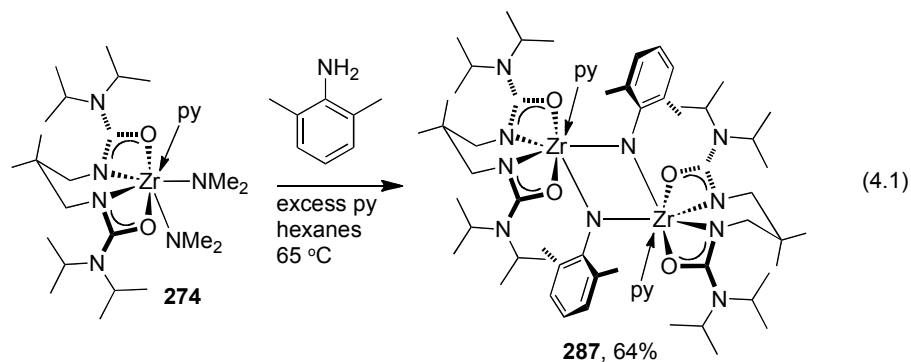


Figure 4.7. ORTEP representation of the molecular structure of **286** (ellipsoids plotted at 50% probability, hydrogens and N(*i*-Pr)₂ groups omitted) with selected bond lengths (Å), bond and torsion angles (°): Zr1–N1, 2.279(1); Zr1–N3, 2.243(1), Zr1–O1, 2.147(1); Zr1–O2, 2.192(1); Zr1–N9, 2.073(1); Zr2–N9, 2.125(1); Zr1–N10, 2.080(1); Zr2–N10, 2.089(1); C1–N1, 1.312(2); C1–O1, 1.314(2); C1–N2, 1.360(2); N1–Zr1–O1, 59.25(5); N1–Zr1–N3, 78.46(5); C1–Zr1–C13, 105.31(5); C1–Zr1–N9, 122.89(5); C1–Zr1–N10, 107.50(5); N9–Zr1–N10, 80.36(5); Zr1–N9–Zr2, 97.97(6).

Due to the observed propensity of imido complex **286** to dimerize, despite the size of the imido substituent and the presence of neutral ligands, the feasibility of mononuclear imido formation using less bulky primary amines was examined. By using

2,6-dimethylaniline, efficient aminolysis of the pyridine stabilized bis(amido) compound **274** occurs, in contrast to the situation described above for the synthesis of **285** and **286**. This is likely due to the reduced steric hindrance in this system, resulting in more facile α -proton abstraction by a dimethylamido ligand. A reaction between **274**, the aniline, and excess pyridine at 65 °C yielded a poorly soluble, pale yellow compound in 64% yield (eqn. 4.1). NMR spectroscopy reveals a ratio of ancillary ligand to 2,6-dimethylphenyl to pyridine of 1:1:1, consistent with an imido compound; however, the presence of only one equivalent of pyridine suggests that the complex is a dimer (**287**), as the more sterically protected mononuclear imido complex **285** contains two stabilizing neutral ligands. Electron-impact mass spectrometry and X-ray crystallography confirm this formulation (Figure 4.8).



The dimeric structure of **287** is very similar to that described above for the dinuclear amido complex **275**. Each half of the C_{2h} -symmetric molecule is similarly related by an inversion center. The weakly bound pyridine ligands (Zr–N6: 2.557(1) Å) are in axial positions at the seven-coordinate zirconium centers. The ureate ligands deviate slightly from planarity, but to a much lesser degree than for the 2,6-diisopropylphenyl substituted dimer **286**. In contrast to the reactivity observed for **286**, heating a mixture of **287** and excess pyridine to 65 °C does not result in any change to the spectral features. This

indicates that even in the presence of excess neutral ligands, **287** remains dimeric, or the equilibrium heavily favours the dimer.

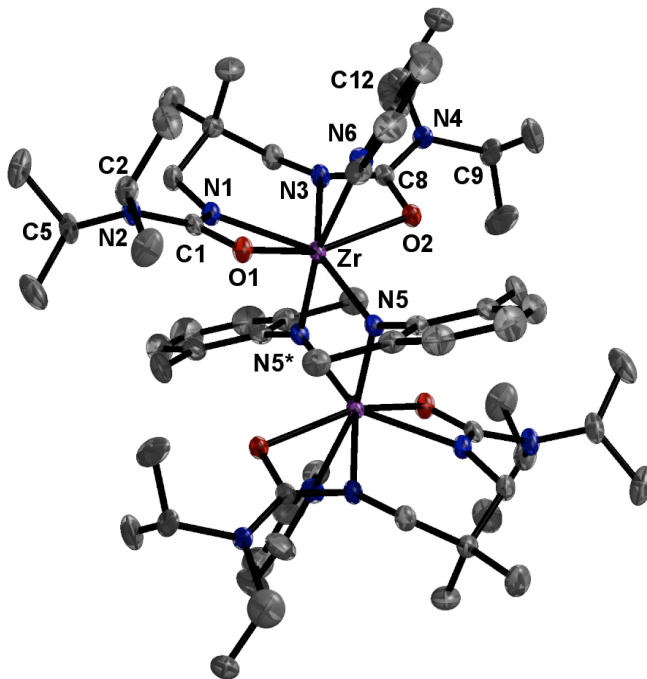
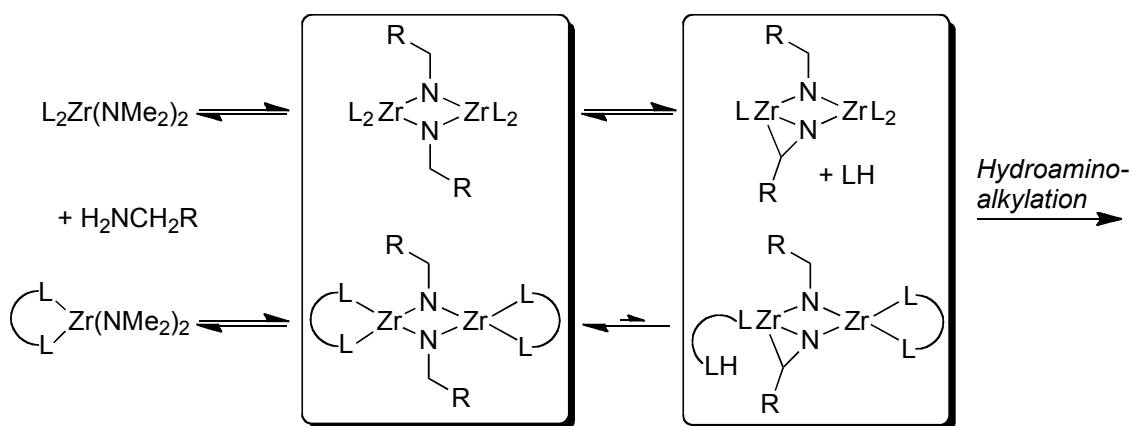


Figure 4.8. ORTEP representation of the molecular structure of **287** (ellipsoids plotted at 50% probability, hydrogens omitted) with selected bond lengths (Å), bond and torsion angles (°): Zr–N1, 2.2455(9); Zr–O1, 2.2373(8); Zr–N5, 2.1653(9); Zr–N5*, 2.0338(9); Zr–N6, 2.557(1); C1–N1, 1.321(1); C1–O1, 1.291(1); C1–N2, 1.361(1); N1–Zr–O1, 57.91(3); N1–Zr–N3, 74.21(4); N5–Zr–N6, 87.17(4); N5–Zr–N6*, 166.70(4); N5–Zr–N5*, 79.84(4); Zr–N6–Zr*, 100.16(4); N1–C1–N2–C5, 15.2(2); N3–C8–N4–C12, 42.6(2).

The dimerization of imido complexes supported by this tethered bis(ureato) is not surprising, considering the sterically accessible nature of the zirconium center. However, given that imido dimers are proposed as key catalytic intermediates for hydroaminoalkylation (Scheme 4.6),²³³ it is interesting that precatalyst **167** is not susceptible to this alternate catalytic pathway. A consideration of ligand structure provides a possible rationale (Scheme 4.9). The postulated hydroaminoalkylation

mechanism proceeds first *via* imido dimerization, then by an intramolecular β -proton abstraction and loss of proligand to generate a dinuclear metallaaziridine. The titanium model compound for this proposed intermediate (**273**, Scheme 4.6) is formed through C–H proton abstraction by one of the ancillary amidate ligands. Once this complex is formed, hydroaminoalkylation can occur *via* alkene insertion into the M–C bond. Using a cheating tetradentate ligand should therefore inhibit this process. The proton abstraction step is reversible;³³⁷ thus, the tethered urea moiety resulting from proton abstraction would effect intramolecular Zr–C bond protonolysis much faster than alkene insertion, preventing catalytic turnover. Accordingly, any group 4 precatalyst with a tethered ligand should not catalyze hydroaminoalkylation. At a fundamental level, this hypothesis has important consequences for future hydroamination and hydroaminoalkylation catalyst design.

Scheme 4.9. Chelate effect rationale for hydroamination chemoselectivity by tethered precatalyst **167**.



In terms of hydroamination catalysis, imido dimerization is often proposed as a reversible deactivation pathway for group 4 catalysts.¹⁸³ This deactivation has been observed to increase with higher catalyst loading; Pohlki and Doye observed significant

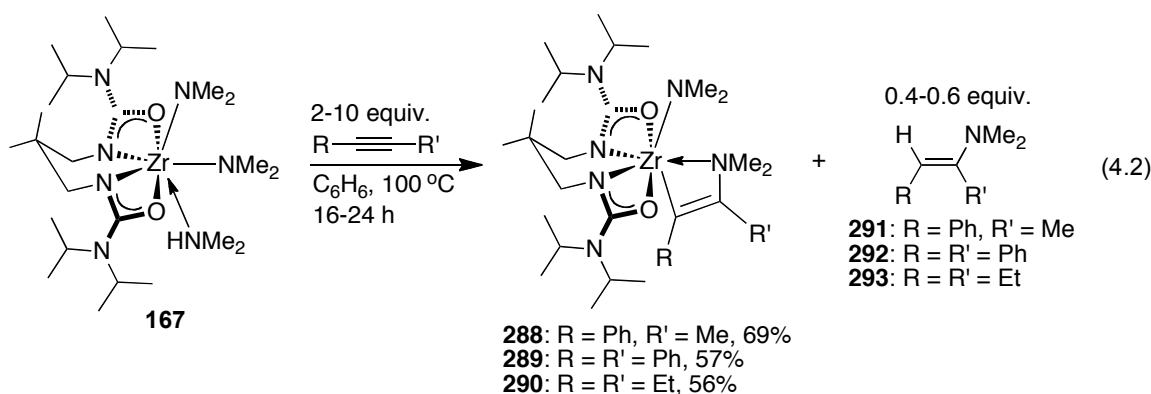
deactivation at precatalyst concentrations above 0.02 M.²⁷⁰ Given the facile dimerization exhibited by the imido complexes discussed above, this concentration-dependent deactivation should be a dominant feature of hydroamination reactions catalyzed by **167** if an imido-mediated pathway is operative. However, the concentration of **167** used for the hydroamination reactions described in the previous Chapter is remarkably high (0.075 M). Kinetic evidence presented below will demonstrate that no rate saturation occurs at high precatalyst concentration, suggesting that deactivation by imido dimerization pathways are not problematic for this system.

In addition to the structural insights gained through characterization of monomeric and dimeric imido complexes supported by the ureate ligand, one can model cycloaddition reactivity of these imido species in stoichiometric reactions with alkynes or alkenes. However, all attempts to effect a [2+2] cycloaddition between the above imido species and a number of alkynes have been unsuccessful. Heating a mixture of either **285** or **287** to 100 °C in the presence of excess terminal or internal alkynes results in no reaction, even after several days. While the failure to observe such cycloaddition reactivity does not completely rule out an imido-based mechanism, it suggests consideration of an insertion-based pathway for primary amine hydroamination.

4.2.4 Precatalyst Reactivity IV: Insertion of Alkynes

In the same way that the inability to observe cycloaddition reactivity provides evidence against an imido-based mechanism, effecting a successful stoichiometric insertion of a C–C unsaturation into a zirconium–amido bond of complex **167** would demonstrate the feasibility of an insertion-based mechanism. As described above, there

is only one previous report of stoichiometric non-polar alkyne insertion into a Zr–N bond, requiring a strained three-membered zirconacycle (**262**, Scheme 4.5).³¹³ Further, this is the only characterized example of such an insertion at any d^0 -metal center, despite the prevalence of proposed insertion-based hydroamination mechanisms for the s -block and rare-earth metals.^{183,187,188,203,207,272,309-312} In order to assess the potential for these insertion reactions to occur at a zirconium center supported by a tethered bis(ureato) ligand, **167** has been treated with an excess of several alkynes. Internal alkynes react selectively, yielding the metallacyclic complexes **288-290**, along with approximately half an equivalent of enamines **291-293** (eqn. 4.2).



The resulting organometallic compounds are crystalline solids, and therefore easily isolated, purified, and characterized. The NMR spectral features of **288-290** are very similar to one another, consistent with the molecular formulation in equation 4.2. Upon conversion from **167**, the protons of the *gem*-dimethyl moiety of the ureate ligand become inequivalent, as do the adjacent methylene protons, which resonate as a diagnostic AB quartet in all three cases. This indicates that the magnetic environments above and below the ligand are inequivalent, similar to that observed previously for the mononuclear imido complex **285**. Two signals are observed for the methyl protons on the NMe_2 groups, one assigned to the axial dimethylamido ligand, and one to the new

vinyl(dimethylamino) ligand. Compound **288** is formed as a single isomer, with no indication of the presence of the other insertion regioisomer. The ^{13}C NMR spectra of **288-290** are devoid of any alkynyl carbon signals. In each case, a new resonance near δ 180 ppm is observed, assigned to the carbon directly attached to zirconium. This chemical shift is similar to that previously observed for other metallacyclic sp^2 -hybridized carbons attached to zirconium, as for the azametallacyclobutenes pictured in Figure 4.1.^{22,222,273,274,280,283-304} Electron impact mass spectrometry enables the observation of molecular ions, as well as diagnostic fragments (loss of NMe_2) for each compound. Finally, combustion analyses are consistent with the empirical formulae.

Single crystals of **288** and **299** have been subject to X-ray crystallography in order to confirm the structural assignment; the molecular structures are shown in Figures 4.9 and Figure 4.10 respectively. Both complexes are largely analogous, having undergone only minimal geometric reorganization from the parent zirconium species. The asymmetric unit of the structure of **288** consists of a single molecule, while that of **289** contains three chemically identical but crystallographically distinct molecules. The C20–C27 lengths (**288**: 1.326(2) Å; **289**: 1.332(3) Å) are consistent with double bonds, while the C27–N5 distances (**288**: 1.477(3) Å; **289**: 1.488(3) Å) indicate single bonds, suggesting no delocalization through the N–C=C framework. The long Zr–N5 distances (**288**: 2.443(1) Å; **289**: 2.440(2) Å) confirm that the dimethylamino group of the vinylamine ligand is bound to zirconium in a neutral fashion, differentiating these species from the previously discussed metallacycles arising from cycloaddition between an imido and an alkyne (Figure 4.1). The structure of **288** reveals the regioisomer that is formed,

consistent with the regioselectivity previously determined for the hydroamination of 1-phenyl-1-propyne with morpholine catalyzed by **167**.

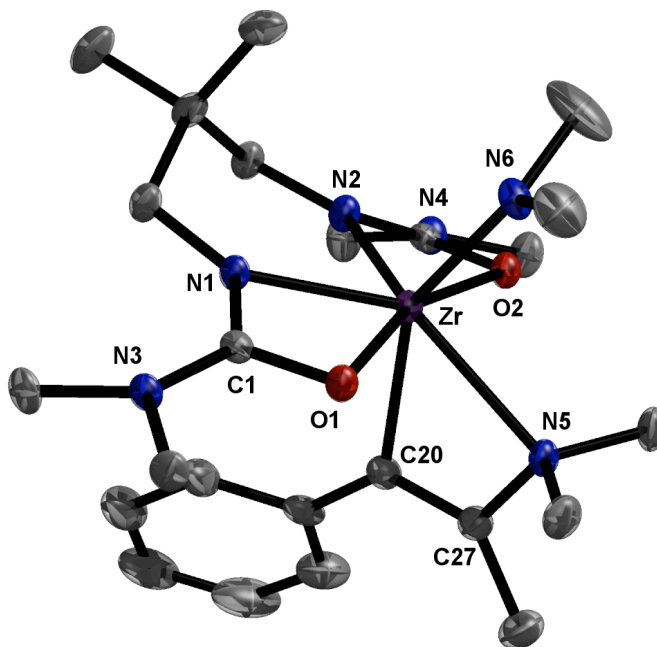


Figure 4.9. ORTEP representation of the molecular structure of **288** (ellipsoids plotted at 50% probability, hydrogens and methyls from isopropyl groups omitted) with selected bond lengths (Å), bond and torsion angles (°): Zr–N1, 2.208(1); Zr–N2, 2.188(2); Zr–N5, 2.443(1); Zr–N6, 2.087(2); Zr–C20, 2.324(2); Zr–O1, 2.200(1); Zr–O2, 2.227(1); C1–N1, 1.330(2); C1–O1, 1.296(2); C1–N3, 1.371(2); C20–C27, 1.326(2); C27–N5, 1.477(3); N1–Zr–O1, 59.28(5); N1–Zr–N2, 77.28(5); N5–Zr–C20, 58.25(6); N6–Zr–C20, 148.10(6); N1–C1–N3–C2, 20.4(3).

The observed geometric isomers of **288** and **289** suggest that alkynes insert preferentially into the equatorial amido ligand of **167** rather than the axial amido. Recall that in the solid-state molecular structure of **167**, this equatorial Zr–N bond distance was remarkably long (2.135(1) Å) relative to both the axial zirconium–amido length (2.092(2) Å) and to those of structurally similar complexes (range: 2.06–2.07 Å). The length of this equatorial amido bond cannot be rationalized in steric terms,³³⁸ nor can it be explained by electron-delocalization with an adjacent unsaturated organic group.²⁸⁷ Instead, it is possible that this elongation is due to reduced π -bonding character in the

equatorial Zr–NMe₂ linkage, arising from its coplanar orientation with the four donor atoms of the electron-rich ureate ligand. In contrast, the axial amido ligand is oriented to maximize π -orbital overlap with the vacant *d*-orbitals of the zirconium center. The strongly π -donating imido ligand from complex **285** similarly adopts an axial position.

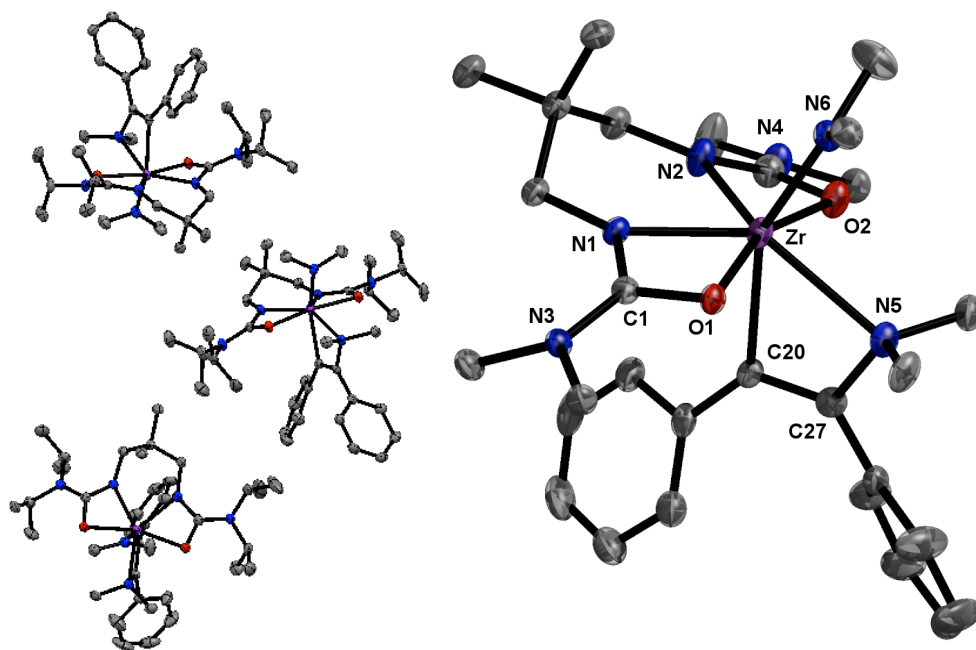


Figure 4.10. ORTEP representation of the asymmetric unit of **289** (left) and of one of three independent molecules (right) (ellipsoids plotted at 50% probability, hydrogens and methyls from isopropyl groups omitted) with selected bond lengths (Å), bond and torsion angles (°) averaged over three molecules: Zr–N1, 2.191(2); Zr–N2, 2.203(2); Zr–N5, 2.440(2); Zr–N6, 2.099(2); Zr–C20, 2.333(2); Zr–O1, 2.214(2); Zr–O2, 2.204(2); C1–N1, 1.327(3); C1–O1, 1.302(3); C1–N3, 1.352(3); C20–C27, 1.332(3); C27–N5, 1.488(3); N1–Zr–O1, 59.24(6); N1–Zr–N2, 77.69(7); N5–Zr–C20, 58.44(7); N6–Zr–C20, 149.00(8); N1–C1–N3–C2, 20.2(4).

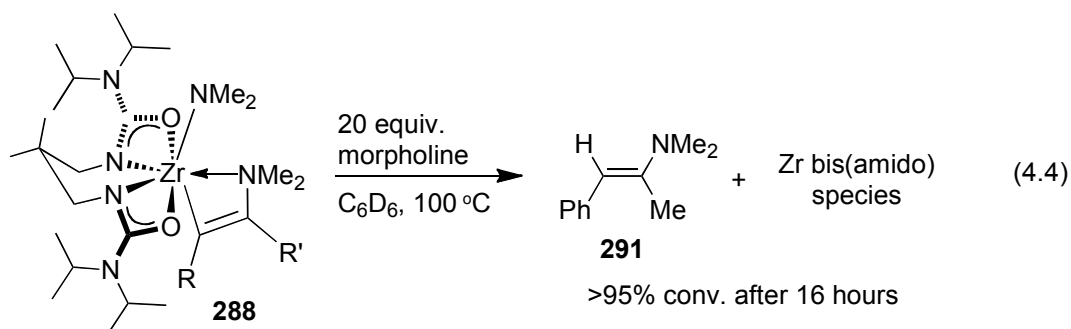
This proposed reduction of metal–ligand π -bonding of the equatorial amido would result in a more nucleophilic nitrogen atom *cis* to the axial site accessible for neutral ligand coordination. Ligand exchange between the dimethylamine and the incoming alkyne would position the substrate proximal to the reactive equatorial amido ligand, and activate it toward nucleophilic attack by lowering the energy of its π^* -LUMO.

294: R = Bn
295: R = Ph

296: R = Bn, >95% conv., 16 h
297: R = Ph, <2% conv., 4 d

138

phenylacetylene with morpholine to completion in sixteen hours at 100 °C. This activity is similar to that exhibited by precatalyst **167**.



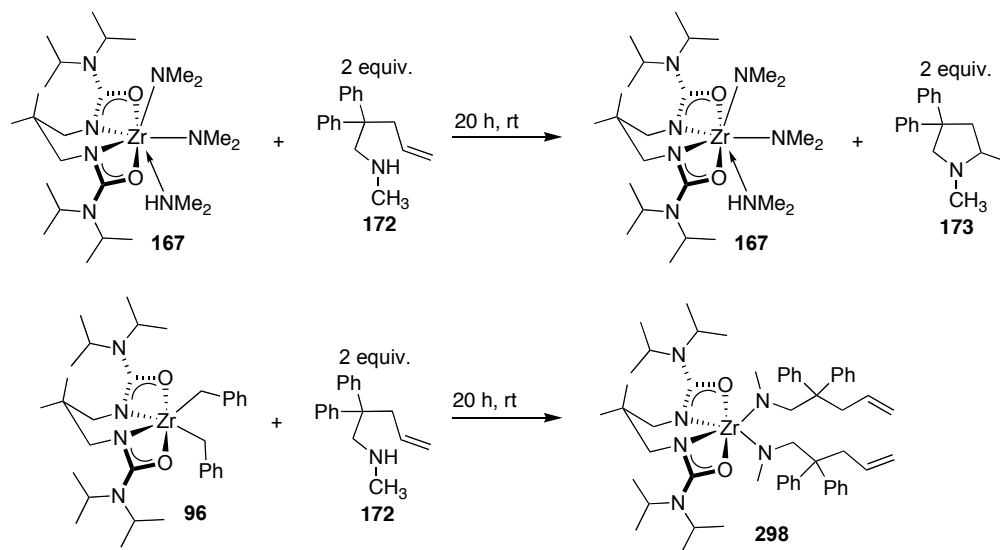
The stoichiometric chemistry described above represents the first time that the insertion process proposed for catalytic hydroamination with d^0 -metals has been directly observed. The ability of **167** to undergo such insertion reactions, and to stabilize the resulting products stems from the unique bonding environment imposed by the tethered bis(ureato) ligand. The seven-coordinate geometry adopted by these complexes places a nucleophilic amido ligand in close proximity to a labile neutral ligand, thus enabling facile σ -bond insertion of alkynes. The current hypothesis regarding catalytic activity is that it is precisely this structural facet that results in the high degree of hydroamination activity exhibited by precatalyst **167**.

4.2.5 Precatalyst Reactivity V: Insertion of Alkenes

Due to the favourable insertion reactivity observed between **167** and alkynes, several alkenes have been similarly tested. Unfortunately, all attempts at intermolecular alkene insertion into the Zr–N bonds of **167** have been unsuccessful, with negligible conversion observed. This is in accord with the inability of **167** to catalyze the intermolecular hydroamination of alkenes. Instead, analogous intramolecular insertions have been

investigated (Scheme 4.10). Treatment of **167** with two equivalents of the *N*-methylated aminoalkene **172** at room temperature for twenty hours does not give an insertion product, or even a substrate-derived bis(amido) complex. Rather, complete cyclization of **172** to **173** is observed, with no apparent change to the structure of the metal complex. This reaction mirrors the situation described above to account for the formation of enamine side-products during alkyne insertion. The dimethylamine liberated through aminolysis to form the initial zirconium–amido complex presumably reacts with any Zr–C bond that is formed to release **173**. Remarkably, this result reveals that **167** is able to catalyze intramolecular alkene hydroamination *at room temperature*. Only one other zirconium system is capable of such high catalytic activity (**145**).²³¹

Scheme 4.10. Attempted intramolecular alkene insertion reactions; evidence for proton-assisted insertion.



In order to prevent the generation of a proton source that initiates catalytic turnover to form **173**, the dialkyl complex **96** was used as an alternate starting material. The absence of protic byproducts from aminolysis of **96** would thus prevent the formation of **173**,

possibly enabling observation of the insertion product. However, subjecting **96** to identical reaction conditions leads exclusively to the bis(amido) species **298** as judged by NMR spectroscopy, with the alkene moieties intact. Upon treating **298** with two equivalents of morpholine and leaving the mixture to stand for twenty hours, complete conversion to **173** is again observed. These results suggest that *a proton source accelerates the insertion process*, which is entirely consistent with the proposed tandem insertion/protonation sequence for rare-earth catalysts pictured in Scheme 4.2. In order to further test this possibility, a detailed kinetic investigation of the cyclization of aminoalkenes has been executed.

4.2.6 Kinetic Analysis of Aminoalkene Cyclization

Up to this point, the mechanistic discussion has focused solely on stoichiometric reactivity involving precatalyst **167**. While such studies provide insight into the thermodynamic feasibility of model reactions, and the structures of model compounds, they are not necessarily representative of the processes or intermediates that occur under catalytic conditions. In order to accurately probe the catalytic cycle, a kinetic analysis is required. Therefore, the cyclization of aminoalkenes was chosen for this initial kinetic investigation. Figure 4.11 shows the results of monitoring the conversion of substrates **131** and **170** by ^1H NMR spectroscopy relative to an internal standard (1,3,5-trimethoxybenzene). All of the reactions described have an initial substrate concentration of 0.750 M, in accord with the conditions described previously for synthetic reactions (Chapter Three).

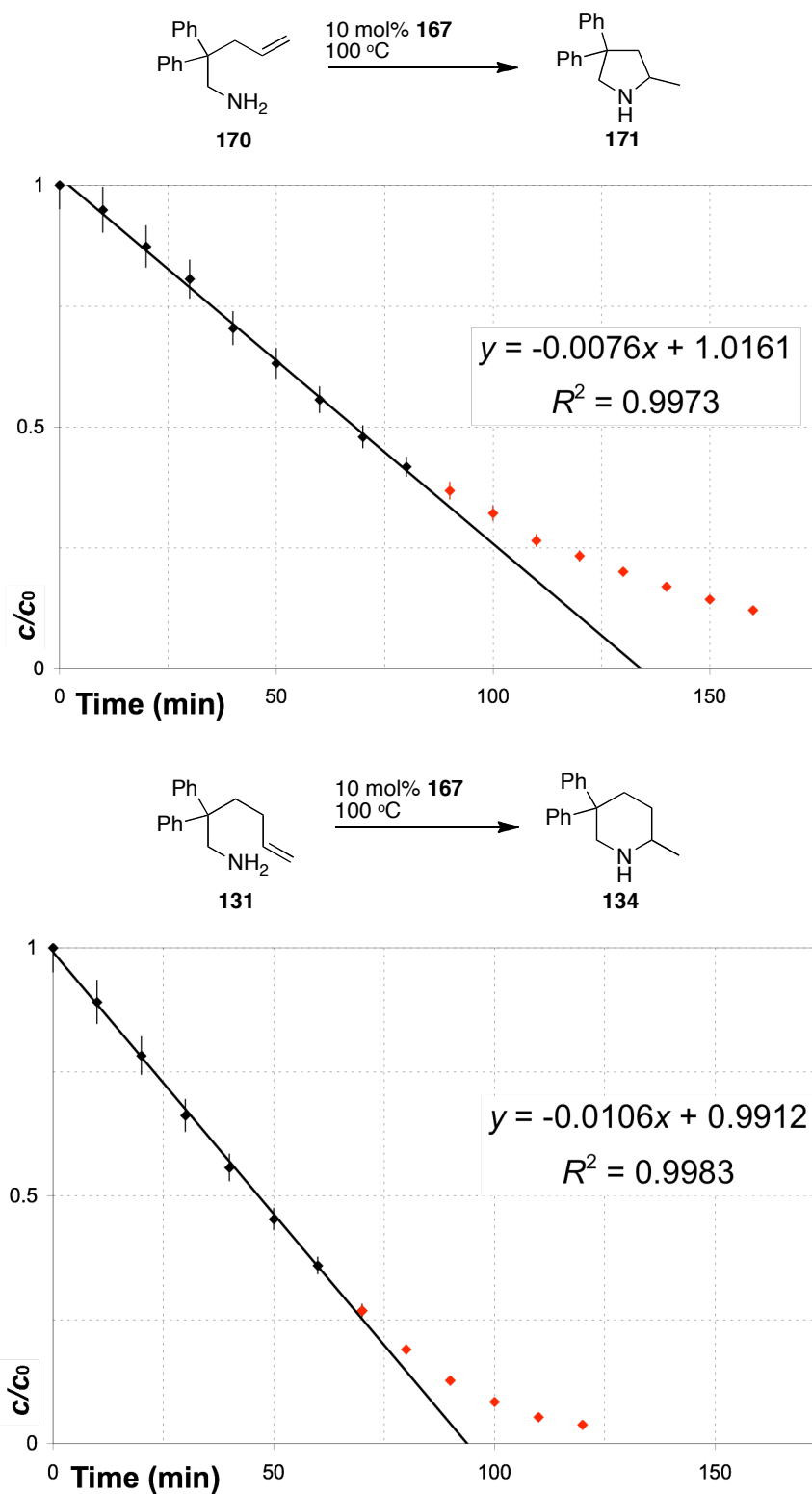


Figure 4.11. Plot of the consumption of aminoalkene substrates (c/c_0) versus time (min) through three (top) or five (bottom) half-lives. Red data points indicate exponential decay regime (not included in linear regression analysis). Error bars indicate $\pm 5\%$.

The plots in Figure 4.11 clearly show a linear decay of substrate during the initial stage of the reaction (up to 50-75% conversion, black points, best-fit line), indicative of zero-order dependence on aminoalkene concentration. This is identical to the situation often observed for lanthanide catalysts;²⁰¹ however, at high conversion the plot becomes non-linear, exhibiting exponential decay (red points). Kinetic profiles of this type could result from two scenarios. First, at high conversion the hydroamination product may competitively inhibit the catalytic process. Product inhibition kinetics have been observed previously with rare-earth,^{187,203,207,309,339} actinide,^{240,340} and group 4²⁴⁰ precatalysts, with analogous deviation from linearity at high substrate conversion.

In order to investigate the possibility of competitive product inhibition during hydroamination catalysis, a series of reactions were carried out with varying amounts of 2-methylpiperidine added. This specific “inhibitor” was chosen to mimic the structure of the hydroamination product **134**. Figure 4.12 illustrates the kinetic profiles of the conversion of **131** (105 °C) in the presence of one to six equivalents (0.750–4.50 M) of 2-methylpiperidine. Two striking features are observed for these reactions. First, the concentration dependence on substrate **131** changes from zero-order to first-order throughout the course of the reaction. With no added 2-methylpiperidine, this reaction is zero-order until ~70% conversion (Figure 4.12, grey line). Clearly, there is a change in turnover-limiting step induced by the addition of 2-methylpiperidine.

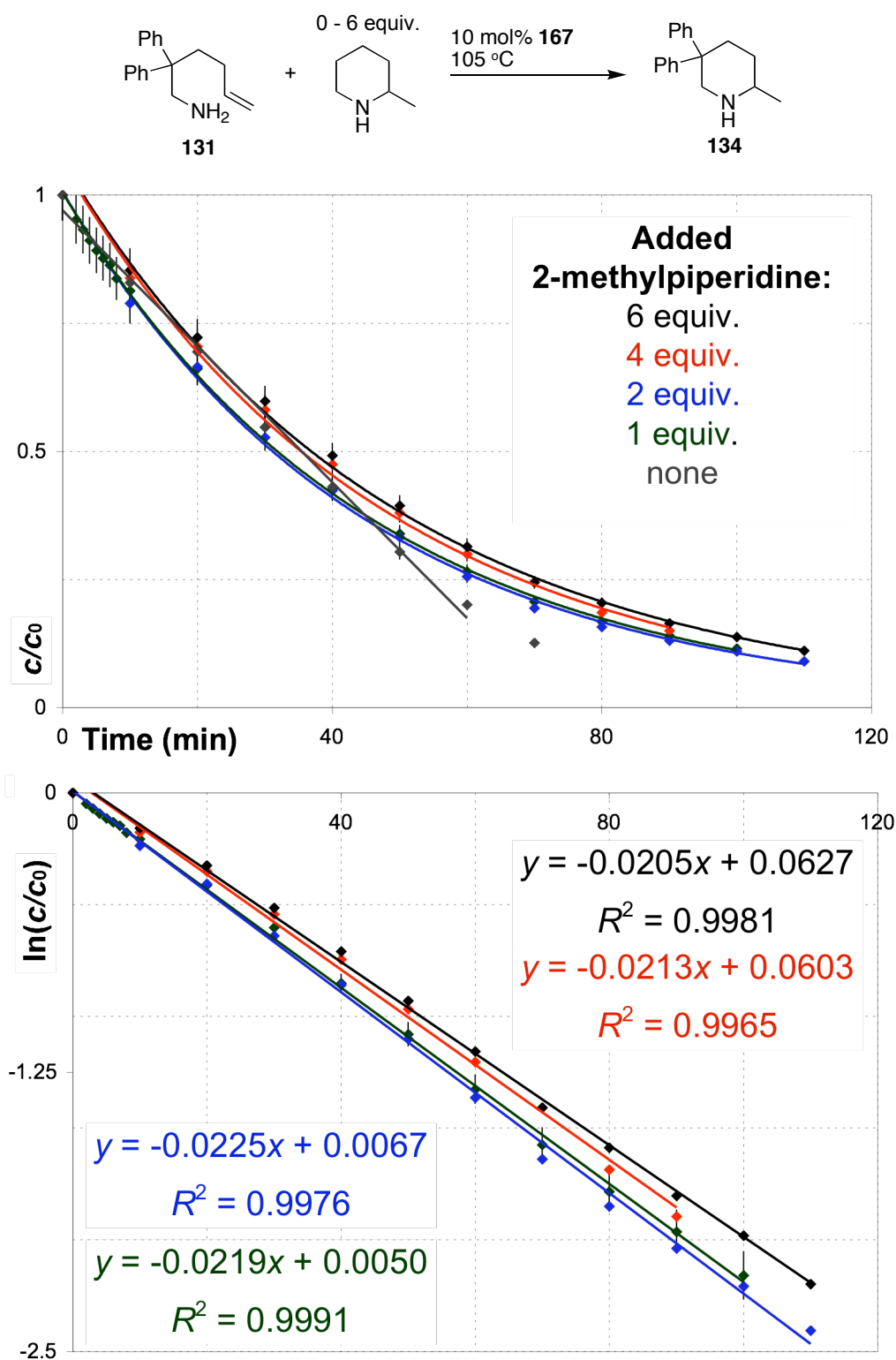
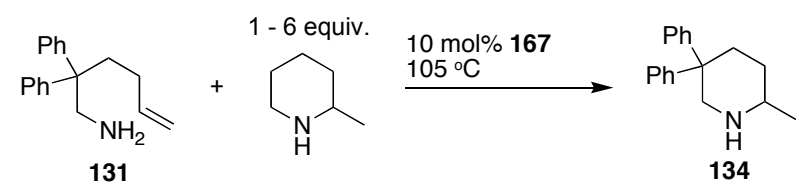


Figure 4.12. *Top:* Plot of the consumption of **131** (c/c_0) versus time (min) with added 2-methylpiperidine (0.750 to 4.50 M), error bars indicate $\pm 5\%$. *Bottom:* Plot of $\ln(c/c_0)$ versus time (min) for the same reactions.

Secondly, there is effectively no change in rate between these experiments, despite the large excess of “inhibitor” added to the latter reactions. Plotting k_{obs} versus the concentration of 2-methylpiperidine gives a linear correlation with a slightly negative slope; however, the difference in k_{obs} across this concentration range is less than 5% (Table 4.1, Figure 4.13). This indicates that the reaction has a nearly zero-order dependence on 2-methylpiperidine concentration, meaning that this product-mimic is not a competitive inhibitor. More importantly, these results rule out the possibility of competitive inhibition by product as a source of late-reaction non-linearity. Instead, the presence of high concentrations of the product (or analogue), and/or low concentrations of substrate, may change the turnover-limiting step of the reaction. In fact, it is remarkable that the catalytic efficiency of **167** is unaffected by the presence of a high concentration (4.50 M) of a potential inhibitor. For the remainder of this discussion, only the primary stage of the reaction will be considered for kinetic analysis.

Table 4.1. Effect of added 2-methylpiperidine on reaction rate.

		
Entry	[2-methylpiperidine] (M) ^a	k_{obs} (10 ⁻² M min ⁻¹) ^a
1	0.750	2.19 ± 0.02
2	1.50	2.25 ± 0.04
3	3.00	2.13 ± 0.04
4	4.50	2.05 ± 0.03

^aErrors estimated from regression analysis of individual data points.

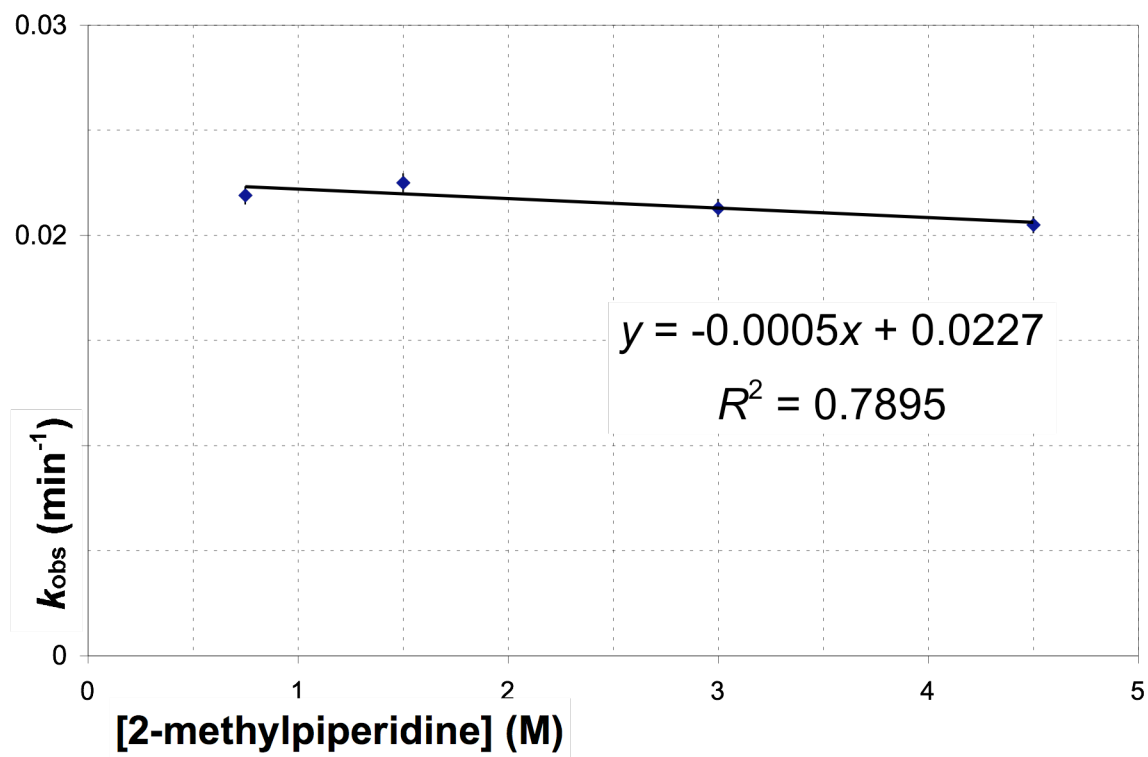


Figure 4.13. Plot of k_{obs} versus concentration of 2-methylpiperidine (M) showing zero-order dependence over a six-fold concentration range. Error bars represent standard errors from Table 4.1.

In order to gain further insight into the catalytic turnover-limiting step, the effects of *N*-substitution on reaction rate were probed by comparing the cyclization rates for substrates **131**, **133**, and *d*₂-**131** (Figure 4.14). The kinetic profiles and k_{obs} values for conversion of the primary aminoalkene **131** and the secondary aminoalkene **133** are statistically identical ($1.06 \times 10^{-2} \text{ min}^{-1}$ versus $1.05 \times 10^{-2} \text{ min}^{-1}$, $k_{\text{H}}/k_{\text{Me}} = 1.01$). Given that cyclization of **133** cannot proceed by a [2+2] cycloaddition mechanism, because the requisite imido intermediate cannot be formed, some type of insertion-based pathway must be operative. The fact that these two reactions have indistinguishable rates suggests that both primary and secondary aminoalkenes are cyclized by the same mechanism, which would have to be insertion-based.

As noted in the introduction to this chapter, primary KIEs have been observed for lanthanide-catalyzed hydroamination, despite the proposal of turnover-limiting σ -bond insertion (Scheme 4.4).^{187,201} In order to gauge the effect of *N*-deuteration on the reaction rate, the conversion of substrate *d*₂-**131** was followed. The cyclization of this aminoalkene is much slower than its *protio* counterpart **131**, leading to a $k_{\text{H}}/k_{\text{D}}$ of 5.6. This primary KIE is similar to the values obtained with lanthanide catalysts ($k_{\text{H}}/k_{\text{D}} = 2.7\text{--}5.2$).^{187,201} This large $k_{\text{H}}/k_{\text{D}}$ value means that N–H/D bond cleavage and/or C–H/D bond formation must be involved in the turnover-limiting transition state, which is in accord with the previously observed stoichiometric alkene insertion reaction using compound **274**. Recall that the presence of a proton source enables alkene insertion to occur, while the absence of a proton source results in no catalytic turnover (Scheme 4.10). Taken together, these results provide compelling evidence for a concerted insertion/protonolysis transition state,²⁰¹ as pictured in Scheme 4.3.

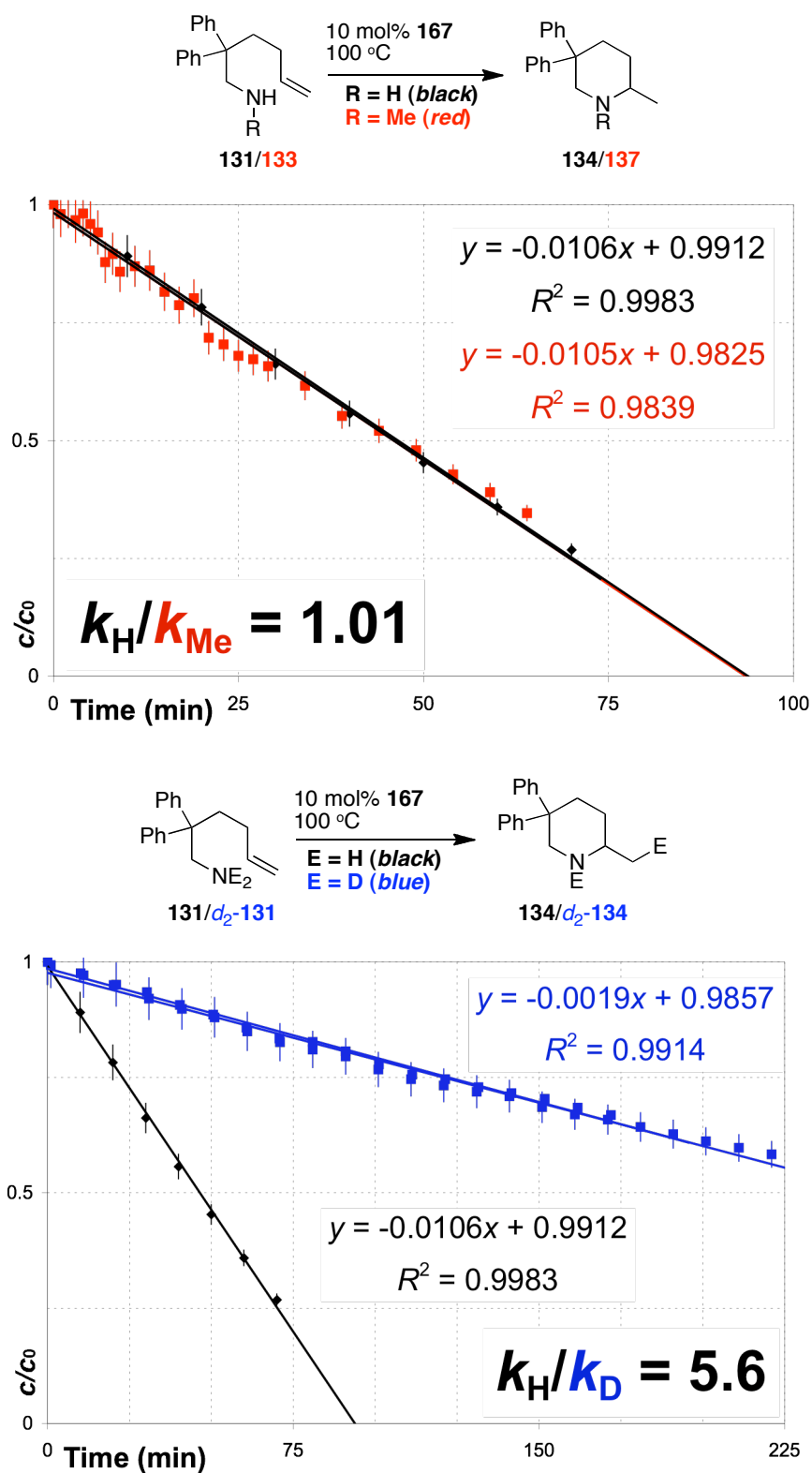


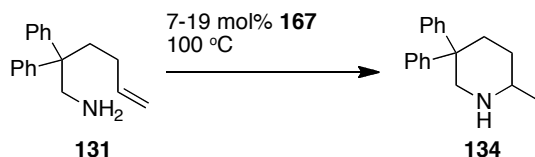
Figure 4.14. Effect of *N*-substitution on cyclization rate: statistically identical rates for primary and secondary aminoalkenes (top); primary kinetic isotope effect (bottom). Error bars indicate $\pm 5\%$.

The above results indicate that during the primary stage of the reaction, there is a zero-order dependence on substrate concentration for three different aminoalkenes. In order to establish empirical rate laws for this reaction, the rate of conversion of **131** was measured for a series of precatalyst concentrations (Table 4.2). A plot of the k_{obs} values obtained versus [**167**] shows a linear correlation in the range [**167**] = 0.05-0.15 M (Figure 4.15). Thus, there is a first-order dependence on catalyst concentration, giving the empirical rate law in equation 4.5 for the first stage of the hydroamination reaction. At high conversion, the empirical rate law in equation 4.6 is operative, with first-order dependence on both catalyst *and* substrate.

$$\text{Primary stage: } \text{Rate} = k[\text{substrate (131)}]^0[\text{catalyst (167)}]^1 \quad (4.5)$$

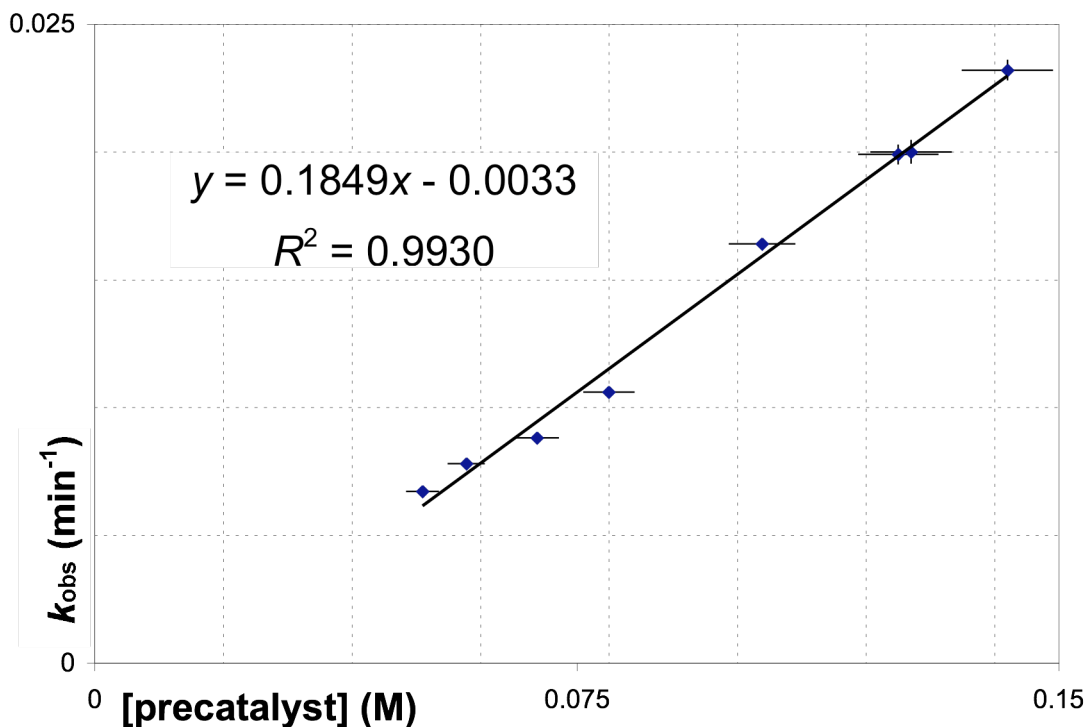
$$\text{Secondary stage: } \text{Rate} = k'[\text{substrate (131)}]^1[\text{catalyst (167)}]^1 \quad (4.6)$$

First-order catalyst dependence indicates that a well-defined, likely mononuclear catalytic species is present throughout the concentration range examined. Recall that hydroamination reactions using Cp_2TiMe_2 (**3**) have a non-linear catalyst dependence with [**3**] > 0.02 M, due to deactivation by reversible imido dimerization.²⁷⁰ The fact that there is first-order behaviour up to high concentrations of **167** is remarkable, especially given the steric accessibility of the zirconium center, and the facile imido dimerization discussed previously. This indicates that deactivation by dimerization or aggregation is not a factor for this catalyst system, further negating the possibility of imido intermediates. This is advantageous from a practical perspective, as it allows for minimal use of solvent while maintaining high catalytic efficiency. Finally, the onset of the secondary reaction stage appears to be largely independent of catalyst concentration.

Table 4.2. Aminoalkene cyclization at varying precatalyst concentrations.

Entry	[Precatalyst] (M) ^a (mol%)	k_{obs} ($10^{-3} \text{ M min}^{-1}$) ^b	Final Conv. (%) ^c
1	0.0510 (6.8)	6.72 ± 0.12	74
2	0.0578 (7.7)	7.81 ± 0.15	71
3	0.0688 (9.2)	8.82 ± 0.10	77
4	0.0800 (10.7)	10.6 ± 0.2	73
5	0.104 (13.9)	16.4 ± 0.2	74
6	0.125 (16.7)	19.9 ± 0.4	79
7	0.127 (16.9)	20.0 ± 0.5	78
8	0.142 (18.9)	23.2 ± 0.4	79

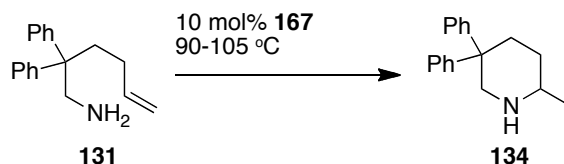
^aPrecatalyst concentration determined at start of reaction by ^1H NMR spectroscopy through relative integration to internal standard, $\pm 5\%$. ^bErrors estimated from regression analysis of individual data points. ^cConversion reached before exponential decay regime.

**Figure 4.15.** Plot of k_{obs} (min^{-1}) versus $[\text{precatalyst}]$ (M), showing first-order dependence up to ~ 0.15 M. Error bars from estimated errors tabulated in Table 4.2.

In addition to determining the effect of catalyst concentration on reaction rate, a series of experiments was carried out to establish the temperature dependence of the rate of cyclization of **131**. Table 4.3 contains the observed rate constants (s^{-1}) for reactions carried out at five degree intervals between 90 °C and 105 °C. The cyclizations show an expected rate increase as temperature is raised. A striking feature of these experiments is that the onset of exponential decay is also temperature dependent. At 90 °C, zero-order kinetics are observed up to 87% conversion, while at 105 °C exponential decay begins at 74% conversion. This effect is even more dramatic for reactions carried out at 110 °C, where exponential decay occurs after only 60% conversion. The observed temperature dependence governing the change in turnover-limiting step has important consequences for the overall catalytic cycle, which will be discussed in the following section.

In order to determine the activation parameters for the primary stage turnover-limiting step, an Eyring plot was generated from rate data obtained at 90-105 °C (Figure 4.16). This plot gives a linear correlation, from which activation parameters can be calculated. The ΔH^\ddagger value of 16.8 ± 1.0 kcal/mol and ΔS^\ddagger value of -32 ± 3 e.u. are similar to those determined for analogous reactions involving rare-earth catalysts,^{201,203,339} actinide catalysts,²⁴⁰ and zirconium precatalyst **157**.²⁴⁰ Notably, all of these systems are proposed to operate *via* σ -bond insertion; however, activation parameters alone cannot differentiate between cycloaddition-based and insertion-based mechanisms. The calculated ΔS^\ddagger is large, providing strong evidence for a highly ordered transition state. All of the synthetic and kinetic data described to this point is in accord with an insertion-based catalytic cycle. The following section will provide a detailed mechanistic proposal to account for all of the experimental observations detailed above.

Table 4.3. Observed rate constants for aminoalkene cyclization at varying reaction temperatures; parameters for Eyring analysis.



Entry	Temp. (K) ^a	k_{obs} (10^{-4} M s ⁻¹) ^b	$1/T$ (10^{-3} K ⁻¹)	$\ln(k_{\text{obs}}/T)$ ^b	Final Conv. (%) ^d
1	363.3	0.827 ± 0.003	2.752	-15.3 ± 0.0^c	87
2	368.4	1.19 ± 0.07	2.714	-15.0 ± 0.1	80
3	373.5	1.65 ± 0.25	2.677	-14.7 ± 0.2	77
4	378.1	2.14 ± 0.08	2.645	-14.4 ± 0.1	74

^aTemperature measured by NMR spectrometer, ± 0.1 K. ^bErrors estimated from multiple experiments at each temperature. ^cError is in the hundredths digit. ^dConversion reached before exponential decay regime.

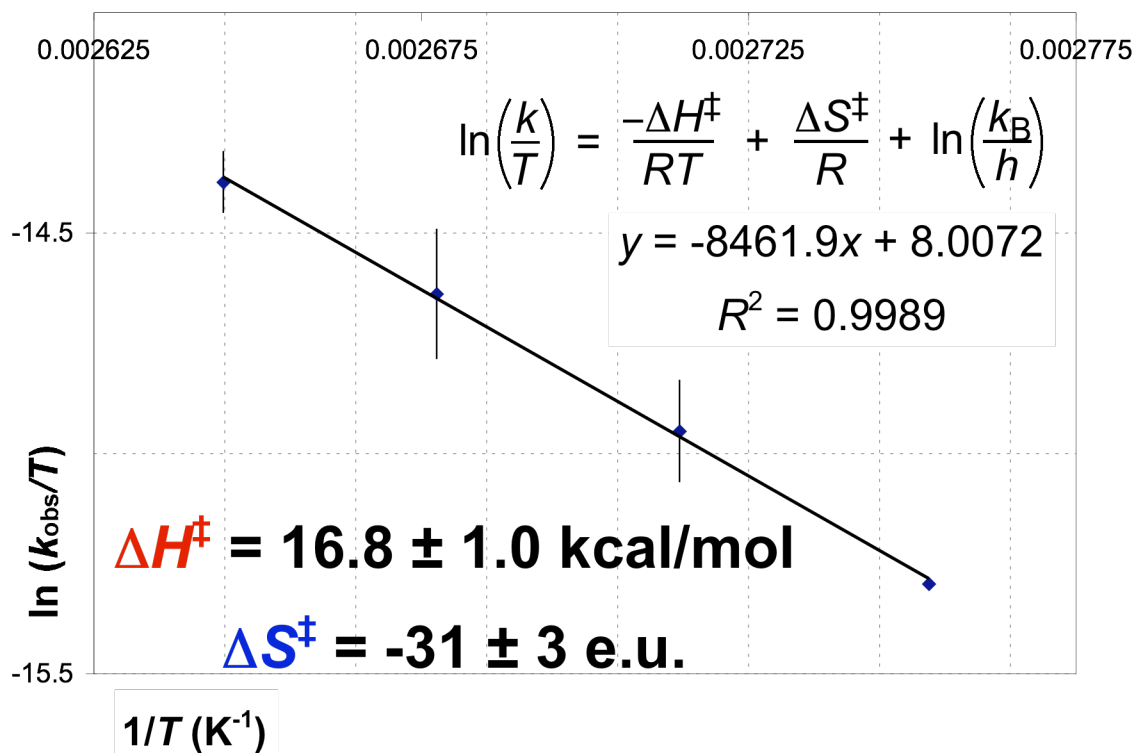


Figure 4.16. Eyring plot in the temperature range 90-105 °C; activation parameters as indicated. Error bars from estimated errors tabulated in Table 4.3; error on activation parameters estimated from regression analysis.

4.2.7 Summary of Pertinent Details and Mechanistic Proposal

Based on the large amount of data accumulated regarding both thermodynamic and kinetic factors underlying the reactivity of **167** and related compounds, a plausible catalytic cycle can be constructed. Before describing this proposed mechanism, a brief synopsis of the important points gleaned from the above investigations is required to provide context for the ensuing discussion.

In a thermodynamic sense, it has been established that in the presence of neutral donors, zirconium dichloro, dialkyl, and bis(amido) species supported by the tethered bis(ureato) ligand exist as mononuclear, seven-coordinate, base-stabilized complexes (Section 4.2.2). In contrast, zirconium imido fragments supported by this same ligand exhibit facile dimerization, even in the presence of pyridine; a mononuclear complex can only be accessed by using a large imido *N*-substituent and excess neutral donor. Furthermore, these imido compounds do not readily undergo [2+2] cycloaddition with alkynes to give metallacyclic products (Section 4.2.3). In contrast, the bis(amido) compound **167** *does* react with alkynes to generate isolable metallacycles *via* formal σ -bond insertion; concomitant formation of enamine side-products suggests this process is likely involved in hydroamination catalysis (Section 4.2.4). Aminolysis of these metallacycles similarly forms enamines, thus establishing the feasibility of an insertion/protonolysis sequence for a hydroamination catalytic cycle with zirconium. The results of attempted intramolecular insertions of an alkene into a Zr–N bond provide evidence that this insertion process is assisted by a proton source (Section 4.2.5).

Kinetically, the cyclization of aminoalkenes **131**, **133**, and **170** has a zero-order dependence on substrate concentration, with a switch to first-order dependence occurring

at high conversion, *or* with the addition of a product-analogue (2-methylpiperidine). The onset of this secondary reaction manifold is independent of catalyst concentration, but *is* dependent on temperature. The cyclization of **131** is first-order in catalyst up to [167] ~ 0.15 M, revealing that the catalytically active species is well-defined and not susceptible to deactivation at higher concentrations. Both primary (**131**) and secondary (**133**) aminoalkenes react with statistically identical rates, suggesting the same mechanistic pathway. As **133** cannot form an imido complex, this pathway must involve a formal σ -bond insertion. In addition, a primary KIE for the cyclization of *N*-deuterated substrate *d*₂-**131** indicates that N–H/D bond cleavage and/or C–H/D bond formation must be involved in the turnover-limiting step. Finally, the ΔS^\ddagger is large and negative, providing strong evidence for a highly ordered transition state.

A simplified proposed mechanism to account for all of these experimental observations is pictured below in Scheme 4.11. This catalytic cycle is illustrated for the conversion of **131** to **134**; however, it should be equally accurate for the cyclization of other primary and secondary aminoalkenes. Initial aminolysis of the precatalyst by excess substrate liberates dimethylamine to generate a structurally analogous bis(amido) species (**A**), which has a third substrate equivalent bound in an axial position. From this active state, intramolecular hydroamination takes place *via* concerted insertion/protonolysis (*k*₁) through a highly ordered transition state (**TS**).

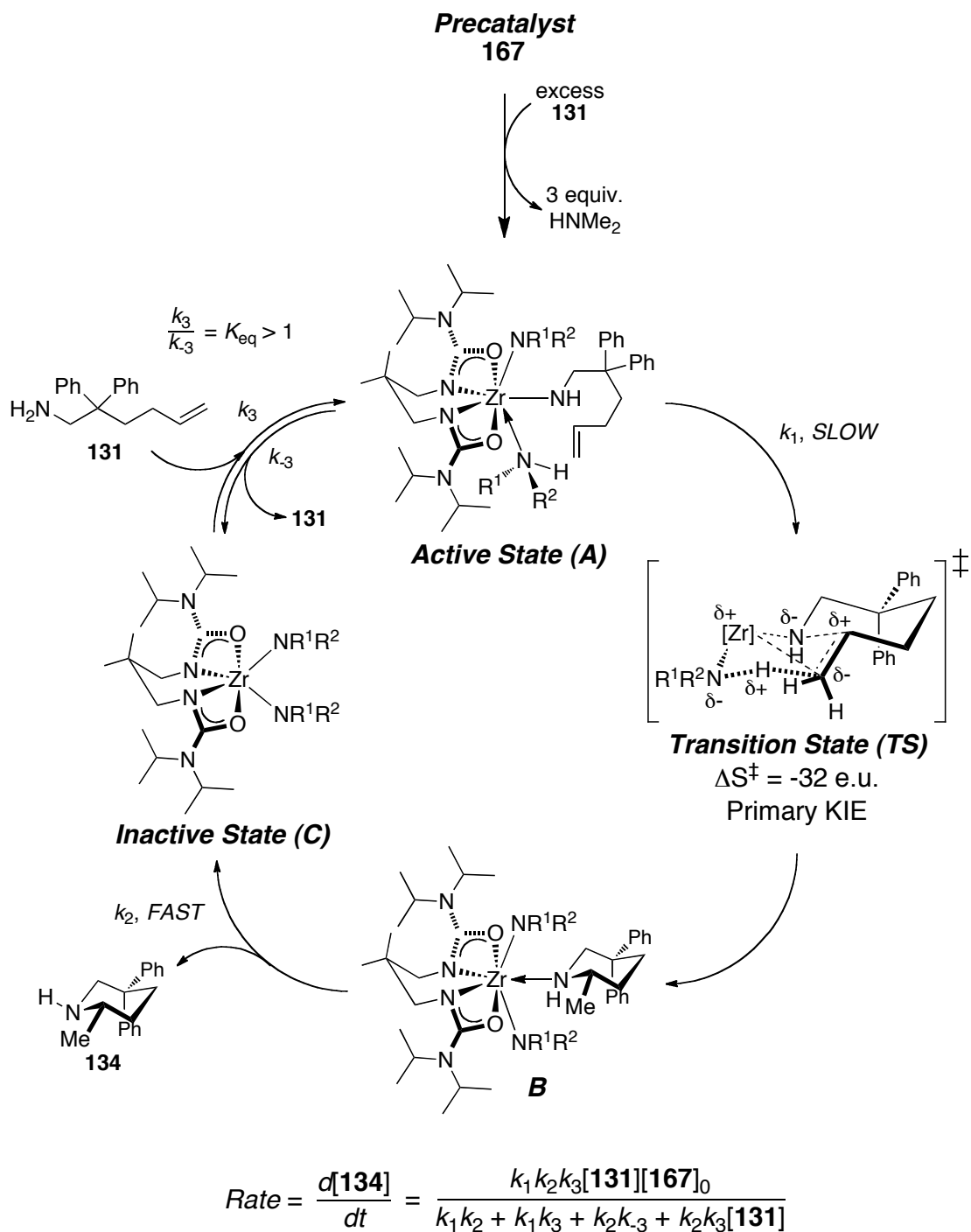
One interpretation of this concerted process is analogous to the transition state previously proposed for rare-earth catalysts (Scheme 4.3).²⁰¹ In this sense, σ -bond insertion can occur *via* a four-membered transition state, involving nucleophilic attack by equatorial amido ligand onto the alkene. Simultaneous protonation can also occur

through a four-membered transition state between the N–H bond of the axial neutral amine ligand and the partial Zr–C bond. Alternatively, this process can be viewed not as two connected four membered transition states, but as a single, chair-like six-membered transition state. In this alternate interpretation, there is minimal direct interaction between zirconium and the alkene. The actual transition state likely has features of both of these interpretations. As the nucleophilic substrate nitrogen attacks the alkene, both the zirconium center and an acidic N–H group are available to stabilize the buildup of negative charge on the terminal alkene carbon. Upon proton transfer to this carbon, the insertion process is completed without the need for a formal Zr–C bond. In either case, this concerted C–N, C–H bond formation accounts for the large negative ΔS^\ddagger , the primary KIE, and the observed proton-assisted insertion from Scheme 4.10.

Once cyclization has occurred, the piperidine **134** would be neutrally bound in an equatorial position, forcing an electronically disfavoured *trans* arrangement of two π -donating amido ligands (**B**). Rapid dissociation of **134** (k_2) would then generate a six-coordinate intermediate (**C**). This inactive state can bind another equivalent of substrate (k_3) to regenerate an active, seven-coordinate intermediate (**A**). This substrate binding is reversible (k_{-3}), leading to an equilibrium between active (**A**) and inactive (**C**) catalyst forms. Based on the neutral donor investigation described in Section 4.2.2, it can be deduced that this equilibrium favours the seven-coordinate species (i.e. $k_3 > k_{-3}$, or $K_{eq} > 1$). Applying the steady-state approximation for the concentrations of all catalytic intermediates, the differential rate law at the bottom of Scheme 4.11 can be derived. By making several reasonable assumptions regarding the relative magnitudes of the rate

constants, this complex rate law can be simplified into two regimes that account for the kinetic behaviour described previously.

Scheme 4.11. Simplified proposed catalytic cycle for intramolecular alkene hydroamination using **167**, with derived differential rate law (steady-state approximation for **[A]**, **[B]**, and **[C]**).



The first situation is valid for the primary stage of the reaction. Based on the fact that neutral ligand association/dissociation is facile, the rate constants k_2 , k_3 , and k_{-3} are likely much larger than k_1 . In other words, the concerted insertion/protonolysis (k_1) is the slow step in the catalytic sequence. Because $k_1 \ll k_2$, k_3 , and k_{-3} , all of the denominator terms containing k_1 can be negated. Furthermore, given the observed thermodynamic preference for seven-coordinate species (type **A**) over coordinatively unsaturated six-coordinate species (type **C**), the forward direction of the equilibrium between **C** and **A** is favoured. This means that $k_3 > k_{-3}$, or $K_{eq} > 1$. Finally, during the initial stage of the reaction, the concentration of substrate is high; therefore, $k_2k_3[\mathbf{131}] \gg k_2k_{-3}$. Applying these assumptions gives the simplified rate law in equation 4.7, which is zero-order in $[\mathbf{131}]$ and first-order in $[\mathbf{167}]$. Furthermore, the only rate constant that contributes to the overall rate is k_1 , which corresponds to the concerted insertion/protonolysis step. This same rate law can be derived in an intuitive fashion by assuming $k_1 \ll k_2$, k_3 , and k_{-3} , and $[\mathbf{B}] + [\mathbf{C}] \ll [\mathbf{A}] \approx [\mathbf{167}]_0$. In this sense, catalytic turnover is dependent only on the concentration of the active species **A**, which is much higher than that of **B** or **C**, and the rate constant of the insertion/protonolysis (k_1).

$$Rate = \frac{d[\mathbf{134}]}{dt} = \frac{k_1k_2k_3[\mathbf{131}][\mathbf{167}]_0}{\cancel{k_1k_2} + \cancel{k_1k_3} + \cancel{k_2k_{-3}} + k_2k_3[\mathbf{131}]} = \frac{\cancel{k_1k_2k_3[\mathbf{131}]}[\mathbf{167}]_0}{\cancel{k_2k_3[\mathbf{131}]}} = k_1[\mathbf{167}]_0 = k_{obs} \quad (4.7)$$

As the reaction progresses, there are multiple active (**A**) and inactive (**C**) catalytic intermediates that are possible, depending on the identity of the amido and amine ligands attached to zirconium (Figure 4.17). Initially, species **299** and **303** would predominate; but as product concentration increases, other intermediates will be formed (**A**: **300-302**, **C**: **304-305**). All of the active states have a substrate amido ligand bound in the

equatorial position, with the two axial ligands derived from either substrate (**131**) or product (**134**). Similarly, the inactive states can have amido ligands derived from **131** or **134**. Because there are many different possible catalytic intermediates, the K_{eq} governing the equilibrium between *C* and *A* is not static, and can change throughout the course of the reaction. In other words, k_3 and k_{-3} will be different depending on the specific pairing of *C* and *A*.

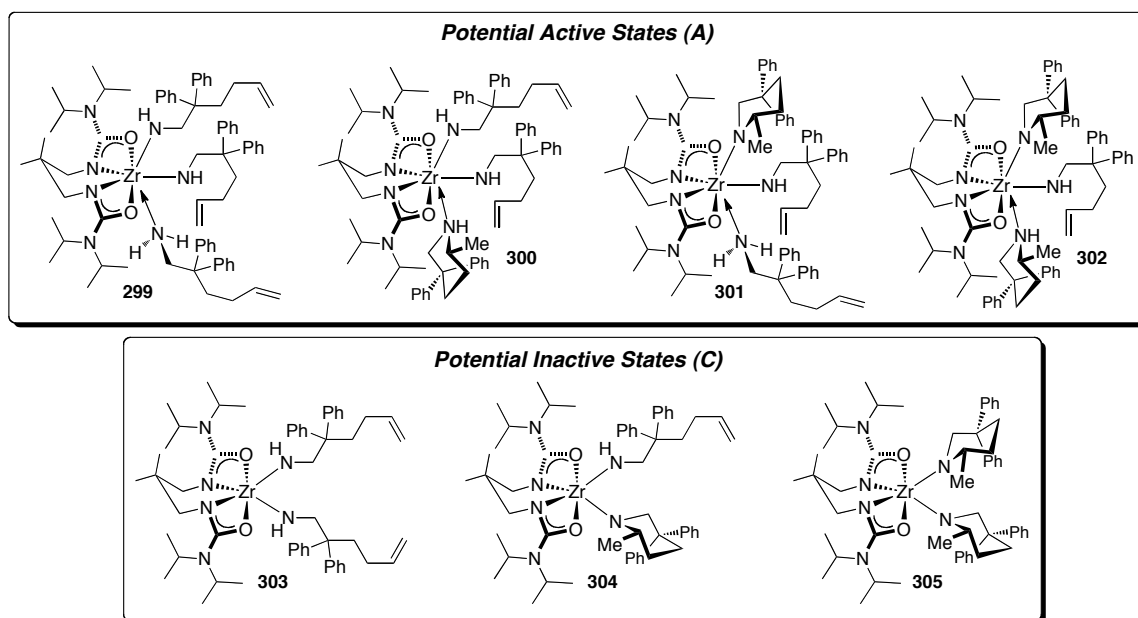


Figure 4.17. Possible active (*A*) and inactive (*C*) catalytic intermediates in the cyclization of **131**.

The secondary stage of hydroamination catalysis, which exhibits first-order dependence on [**131**], occurs at high product concentration. Therefore, the active (*A*) and inactive (*C*) species will be assigned as complexes **302** and **305** respectively. This pairing contains the most number of product-derived ligands, as would be expected for high [**134**]. In order to simplify the rate law from Scheme 4.11 to account for the kinetic behaviour at high conversion, the following assumptions can be made. First, k_1 is still much smaller than the other rate constants, so the denominator terms containing k_1 can be

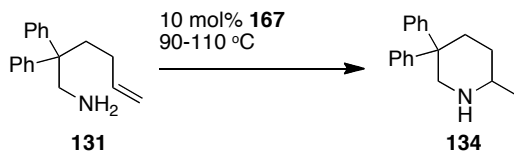
excluded in the same fashion as for equation 4.7. Second, at high conversion of **131**, the substrate concentration will be low. Finally, the values for k_3 and k_{-3} will not be the same as in the initial stage of the reaction. In this case, the inactive species (**305**) contains two sterically encumbering amido ligands derived from **134**. These large secondary amido groups will help to stabilize a six-coordinate species more than the less bulky substrate-derived amidos from intermediate **303**. Also, the active seven-coordinate intermediate **302** would be more sterically crowded than **299**, enabling more facile neutral ligand dissociation. Both of these factors will decrease the value of k_3 while increasing k_{-3} . In other words, K_{eq} will decrease.

Taking the above three assumptions into account, the rate law can be simplified as shown in equation 4.8. In this case, $k_2k_{-3} \gg k_2k_3[131]$, due to the low value of $[131]$, and the changes to k_3 and k_{-3} brought about by the predominance of **302** and **305** as catalytic intermediates. This has the effect of changing the turnover-limiting step to include both the equilibrium between **A** and **C** (K_{eq}), and the insertion/protonolysis step (k_1). Importantly, this rate law accounts for both the observed first-order dependence on $[131]$, and the observed *zero-order* dependence on added 2-methylpiperidine. Because of the structural similarity between 2-methylpiperidine and the hydroamination product **134**, one can infer that the reaction should also be zero-order in $[134]$. In other words, the product is not involved in the equilibrium that precedes the insertion/protonolysis step. If **134** were acting in such a capacity, as in a competitive inhibition process, the reaction should be inverse-order in product (or added 2-methylpiperidine).

$$Rate = \frac{d[134]}{dt} = \frac{k_1k_2k_3[131][167]_0}{\cancel{k_1k_2} + \cancel{k_1k_3} + k_2k_{-3} + \cancel{k_2k_3[131]}} = \frac{k_1\cancel{k_2}k_3[131][167]_0}{\cancel{k_2}k_{-3}} = k_1K_{eq}[131][167]_0 = k_{obs}'[131] \quad (4.8)$$

Comparing the simplified rate laws from equations 4.7 and 4.8 reveals another important relationship between the two reaction regimes. Because $k_{\text{obs}} = k_1[\mathbf{167}]_0$ (from equation 4.7), and $k_{\text{obs}}' = k_1K_{\text{eq}}[\mathbf{167}]_0$ (from equation 4.8), it follows that $k_{\text{obs}}' / k_{\text{obs}} = K_{\text{eq}}$, *if* the value of k_1 is the same for the two kinetic regimes. Given that the addition of excess 2-methylpiperidine to enforce an exponential decay of substrate does not affect the initial reaction rate (Figure 4.12), it is reasonable to assume that the rate constant for the turnover-limiting, unimolecular insertion/protonolysis step should not be affected by a large concentration of product. Applying the above assumption therefore allows estimation of the equilibrium constant governing the second stage of the reaction. Taking the ratio of k_{obs}' and k_{obs} for the cyclizations of **170** and **131** at 100 °C (Figure 4.11) gives values for K_{eq} of 2.11 and 3.77 respectively. This nearly two-fold difference reveals that a slight alteration to catalytic intermediate structure can result in a large change to K_{eq} . Similarly, the K_{eq} values for the cyclization of **131** change by a factor of 2.5 over the temperature range 90-110 °C (Table 4.4). Based on the data in Table 4.4, a van't Hoff plot can be constructed to quantify ΔH° and ΔS° for this equilibrium (Figure 4.18).

Table 4.4. Temperature dependence of K_{eq} values for the cyclization of **131**; parameters for van't Hoff analysis.^a



Entry	Temp. (K) ^b	k_{obs}' (10^{-2} min^{-1}) ^c	k_{obs} ($10^{-2} \text{ M min}^{-1}$) ^c	K_{eq}	$\ln(K_{eq})$
1	363.3	2.90 ± 0.13	0.498 ± 0.005	5.82 ± 0.14	1.76 ± 0.02
2	368.4	3.10 ± 0.06	0.754 ± 0.01	4.11 ± 0.07	1.41 ± 0.02
3	373.5	3.99 ± 0.08	1.06 ± 0.02	3.77 ± 0.10	1.33 ± 0.03
4	383.0	8.56 ± 0.09	3.74 ± 0.08	2.29 ± 0.17	0.828 ± 0.077

^aData at 378.4 K not included due to lack of sufficient data points for k_{obs}' determination. ^bTemperature measured by NMR spectrometer, ± 0.1 K. ^cErrors estimated from regression analysis of individual data points.

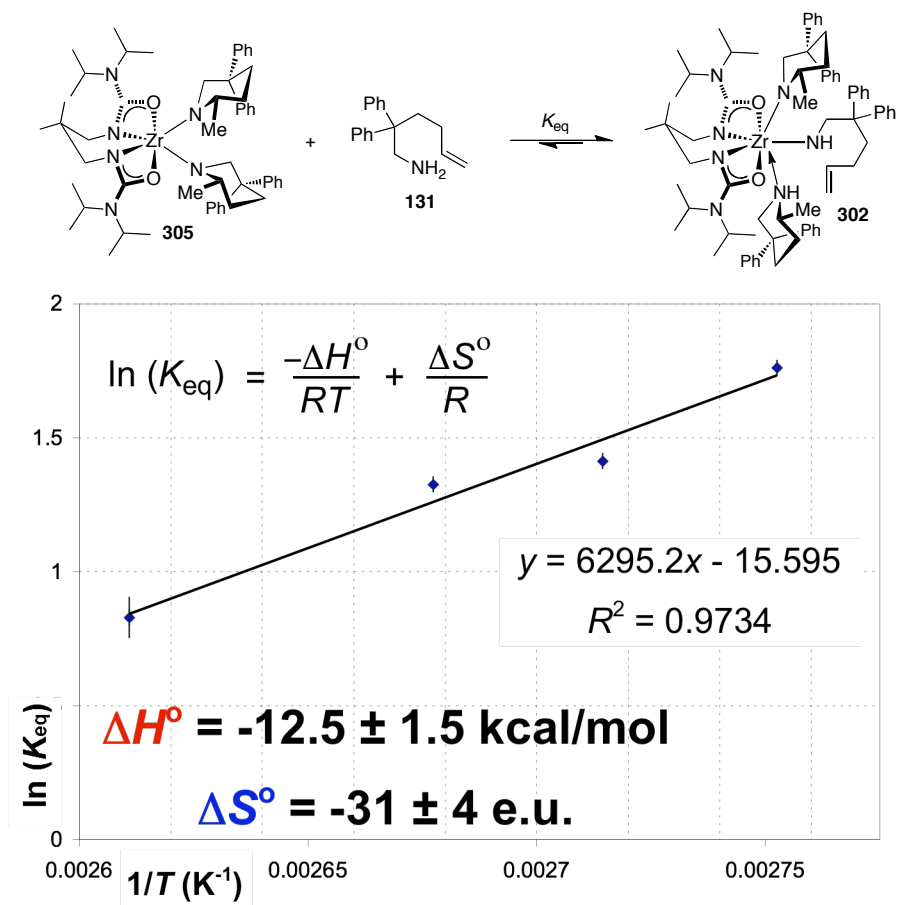
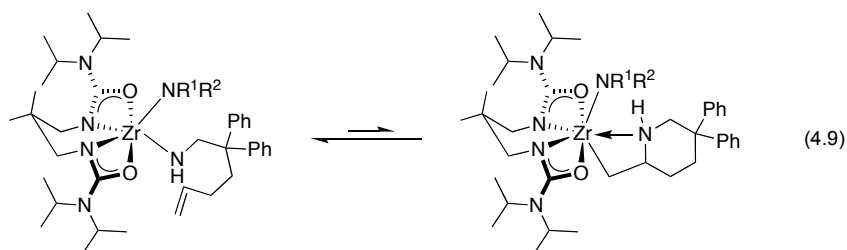


Figure 4.18. Determination of ΔH° and ΔS° values for the pictured equilibrium by van't Hoff analysis.

As proposed above, the equilibrium preceding the insertion/protonolysis step concerns the binding of a substrate (**131**) to an inactive intermediate **C** (here, **305**) to give an active intermediate **A** (here, **302**). Qualitatively speaking, the forward reaction should have a negative enthalpy change (new Zr–N bond formed), and a negative entropy change (two molecules into one). Calculating these parameters from the van't Hoff plot gives $\Delta H^\circ = -12.5 \pm 1.5$ kcal/mol and $\Delta S^\circ = -31 \pm 4$ e.u., which are in accord with the qualitative analysis. Changes in complex solvation on either side of the equilibrium may have an impact on these values. Nevertheless, all of the data presented above is consistent with a rapid pre-equilibrium between inactive (**C**) and active (**A**) catalyst states before insertion/protonolysis can occur. Thus, the mechanism shown in Scheme 4.11 is entirely plausible, and supported by multiple experimental observations.

There is an alternate mechanistic pathway that is consistent with the data presented here. Rather than a concerted turnover-limiting step as proposed above, the catalyst could operate through a stepwise mechanism involving rapid *reversible* alkene insertion into the Zr–N bond (equation 4.9) followed by a slow, intramolecular proton transfer from a coordinated amine. This alternate mechanism would also explain the observed kinetic behaviour, specifically the primary KIE, and the apparent proton-accelerated insertion from Scheme 4.10. However, observation of the reverse of alkene insertion into a metal–nitrogen bond, a β -amide elimination process, has never been reported. Further experimental work is therefore required to investigate this other mechanistic possibility.



Conclusions

One of the truly powerful aspects of homogeneous catalysis is the ability to iteratively and rationally improve catalyst design concepts through a detailed understanding of the underlying reaction mechanisms. The field of hydroamination has seen a large number of in-depth mechanistic studies performed,¹⁸³ the findings of which have provided a framework for subsequent research efforts. Complementary to the structure/activity relationships established in the previous chapter, the mechanistic work presented in this chapter constitutes a fundamental contribution toward a deeper understanding of group 4 catalyzed hydroamination. Through a combination of elucidating stoichiometric reactivity patterns, and kinetic analyses of catalytic reactions, a stereoelectronic rationale for the unique activity of the zirconium precatalyst **167** has been established.

The ability of the catalytic species derived from **167** to use both primary and secondary amines in hydroamination reactions stems directly from the steric and electronic environment imposed by the ancillary ligand. Use of this tethered ligand provides steric accessibility to the metal center. This results in the favourable formation of seven-coordinate bis(amido) complexes that can undergo insertion reactions with internal alkynes. This reactivity constitutes the first time an insertion process relevant to hydroamination has been directly observed and characterized at a d^0 -metal center. The increased nucleophilicity of the equatorial amido ligand imparted by the electron-rich ureate ligand, and the proximity of the coordinated neutral amine, are responsible for this novel reactivity.

The kinetic profile of aminoalkene cyclization indicates that the reaction proceeds through a unimolecular, highly ordered transition state. Based on the observation of

proton-assisted alkene insertion in stoichiometric reactions, and a primary KIE for cyclization of an *N*-deuterated aminoalkene, this transition state is proposed to involve concerted C–N and C–H bond formation. This can either be viewed as simultaneous σ -bond insertion of the alkene into the Zr–N bond and protonolysis of the partially formed Zr–C bond, or as simultaneous nucleophilic attack by the amido ligand and protonation of the alkene. These two interpretations differ in the role that zirconium plays in the process; in the former, the metal is directly involved in the C–N and C–H bond formation, while in the latter it is only indirectly involved.

Another key aspect of hydroamination catalysis with **167** is that competitive product inhibition does not occur, contrary to reports involving other d^0 -metal catalyst systems. Instead, two different kinetic regimes can operate, depending on the relative concentration of substrate and product. This dual reaction manifold is due to an on-cycle pre-equilibrium between a coordinatively unsaturated inactive catalyst form, and an active species that can undergo concerted insertion/protonolysis. This type of behaviour is unique among catalysts that operate *via* insertion-based catalytic cycles.

The mechanistic insight gleaned as a result of this investigation goes beyond that of the thermodynamic feasibility of individual catalytic steps or an empirical rate law. Based on the mechanism presented in Scheme 4.11, specific steric and electronic requirements must be met in order for group 4 catalysts to perform hydroamination with secondary amine substrates. Now that a hypothesis for the unique reactivity exhibited by precatalyst **167** has been determined, future group 4 systems can be constructed that are even more efficient for these reactions. In short, this work will be instrumental in the design of next generation group 4 hydroamination systems.

CHAPTER 5. Synopsis, Future Directions

5.1 Conclusions Drawn

The comprehensive investigation reported in this thesis regarding bis(ureato)titanium and zirconium complexes constitutes the first study of ureates as supporting ligands in group 4 chemistry. By establishing reliable synthetic protocols, collecting extensive structural and reactivity data, and developing these compounds for catalytic hydroamination, this research has laid the foundation for future work in this area. The most important conclusion to be drawn is that ureate ligands are not simply an amidate surrogate. While similar in many respects, these two ligand classes differ in several important ways, with dramatic consequences for both metal complex structure and reactivity.

The source of this divergence is the electron-rich nature of ureates relative to their amidate analogues. The π -electron donating potential of the distal disubstituted amino group has been established through both solid-state and solution-phase characterization. Importantly, this donation occurs with variable magnitude depending on the specific structure of the metal complex. Thus, ureates are more effective than amidates as supports for electron-poor group 4 dichloride and dialkyl fragments. Many such amidate-supported complexes suffer from synthetic challenges and fluxional behaviour,^{106,107,119} while ureate ligands can be used to minimize or eliminate these problems. Specifically, efficient protonolysis routes to ureate-supported metal dichlorides have been developed, despite previous difficulties involving amidate ligands.¹⁰⁷ Furthermore, the facile

preparation of coordinatively unsaturated zirconium dialkyl species has not been achieved with amidate ligands.^{119,174} The use of ureates in this capacity leads to well-defined compounds that exhibit remarkable stability to ambient heat and light. While as yet unrealized, additional catalytic screening efforts could establish the viability of ureate-supported dichloro and dialkyl compounds as olefin polymerization precatalysts. The research described in Chapter Two will also enable further elucidation of the stoichiometric and catalytic chemistry of these bis(ureato) derivatives.

A direct comparison of amidate- and ureate-supported metal complexes in terms of structure and reactivity has been accomplished using the hydroamination reaction as a metric. Group 4 amidate compounds are known to be particularly effective hydroamination precatalysts, a fact that is often attributed to the electron-deficient nature of catalytic species supported by these ligands.⁸¹ The differing electronics of amidates and ureates provides a method to assess this hypothesis, and develop catalyst structure/activity relationships. By comparing precatalyst structural details, the metal-ligand interaction was examined, revealing that ureate ligands are closer to the titanium and zirconium centers. This indicates that in addition to being more electron-rich, ureate ligands also increase the steric protection of the metal center. It is a combination of these factors that leads to the generally diminished catalytic activity of ureate precatalysts relative to their amidate partners. This fact provides further support for the prevailing notion regarding the effectiveness of amidate-supported hydroamination precatalysts.

In addition to affording insight into the relationship between precatalyst structure and hydroamination catalysis, evaluating ureate-supported catalysts has resulted in the discovery of a highly effective group 4 system for this reaction. This anomalous case

involves a ureate ligand that imparts *greater* catalytic activity than its amidate counterpart, and a significantly expanded reaction scope. The transformations performed by this precatalyst are extremely challenging, and beyond the reach of many systems. These include reactions involving both primary and secondary amines, 1,2-disubstituted alkynes and alkenes, substrates containing Lewis basic and acid-sensitive function groups, and the formation of medium-sized ring systems. Thus, the ureate-supported catalyst system developed here represents the current forefront of group 4 hydroamination technology, comparing favourably with catalysts from across the periodic table.¹⁸³

In order to establish the source of this reactivity, stoichiometric model reactions and catalytic kinetics have been examined. These studies reveal that a combination of steric and electronic factors are responsible, stemming from the unique bonding environment imposed by the tethered bis(ureato) ligand. While nearly every group 4 hydroamination catalyst is proposed to operate *via* an imido-mediated catalytic cycle based on [2+2] cycloaddition as the key bond forming step,^{183,222,270} the tethered bis(ureato)zirconium system is able to access an alternate, insertion-based mechanism. This has been established by demonstrating the viability of alkyne insertion into a zirconium–amido bond of the ureate precatalyst, representing the first time this reaction has been directly observed for a d^0 -metal center.³¹³

Model studies and kinetics both suggest that sequential alkene insertion and Zr–C protonolysis, commonly proposed for *s*-block and rare-earth systems,^{201,271} is not an accurate description of the catalytic process. The evidence collected instead points to a concerted pathway, involving simultaneous insertion and protonation. The mechanistic

model proposed to account for all experimental observations involves C–N bond formation between the C–C multiple bond and the equatorial amido ligand at the same time as proton transfer occurs from the axial neutral amine ligand to the C–C unsaturation. The precise role of the metal center in the highly ordered transition state is unclear; however, a direct M–C interaction need not be invoked, in contrast to every other mechanistic proposal involving d^0 -metal catalysts. Furthermore, many common catalyst deactivation pathways, including dimerization or aggregation at high catalyst concentration, and competitive inhibition by reaction products, are not a factor with the bis(ureato)zirconium precatalyst.

The wealth of group 4 ureate chemistry uncovered during this work is a remarkable feat for a supporting ligand that has been almost completely overlooked by the organometallic community. As a result, there are myriad opportunities for advancing this area of research. The following section describes the potential application of ureate complexes to other catalytic processes. Some of this discussion involves preliminary results in these areas. Much of this work was done collaboratively, with many of these projects being explored currently by other members of the Schafer group.

5.2 Further Research Avenues

5.2.1 Mechanistic Elucidation

The lack of definitive precedent for the mechanistic model proposed in Chapter Four makes the assertion of a concerted insertion/protonolysis event controversial, despite experimental support. Extensive further work is therefore needed to fully elucidate the details of hydroamination catalysis using the tethered bis(ureato)zirconium precatalyst.

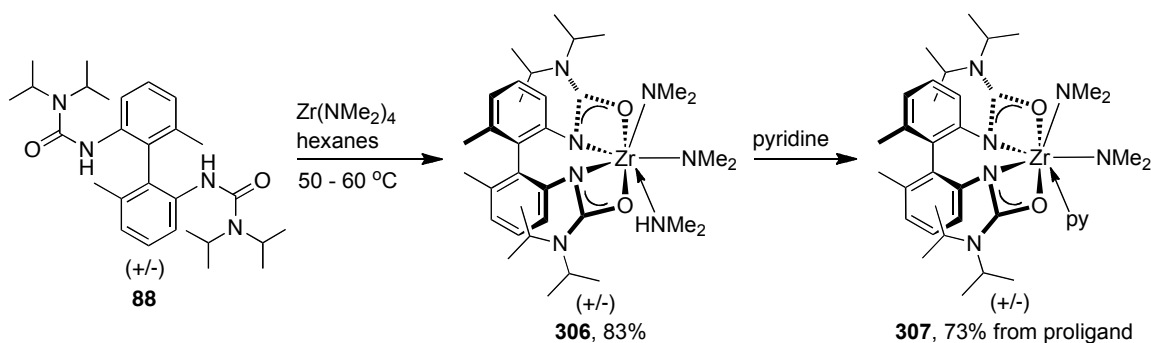
Of primary importance is an expansion of the kinetic studies reported here to include the intermolecular reaction between amines and alkynes. In addition to determining the catalytic pathway for this complementary process, greater insight can be gleaned by determining reaction orders for amine and alkyne separately. This is a significant advantage to analyzing an intermolecular reaction as opposed to an intramolecular version. A kinetic analysis of intermolecular alkyne hydroamination is particularly relevant given the isolation of discrete species resulting from σ -bond insertions (288-290). Clearly, a proton source is not a requirement for alkyne insertion, although it may still promote the process in catalytic reactions. Determining the nature of the turnover-limiting step for this catalytic process may reveal a similar concerted insertion/protonolysis pathway, or that alkyne hydroamination proceeds stepwise.

The ability to isolate pure insertion products also affords the opportunity to determine rate data for individual insertion and protonolysis steps. A comparison of this data with catalytic kinetics would allow one to probe whether or not a concerted insertion/protonolysis is operative for alkyne hydroamination catalyzed by **167**, and to calculate the magnitudes of individual rate constants. However, the question of metal center involvement in the transition state can only truly be answered by theoretical modeling. As described previously, no computational precedent for a concerted insertion/protonolysis reaction has been produced. Such an investigation may provide valuable insight that cannot be obtained through exclusively experimental means.

5.2.2 Enantioselective Hydroamination

A major limitation of the precatalyst developed for this thesis is that it cannot perform alkene hydroamination in an enantioselective manner. Given that dialkyl complex **98**•py, which is supported by the biaryl tethered ligand derived from **88**, adopts a similar coordination geometry to precatalyst **167**, bis(amido) compounds with this chiral ligand have been prepared (Scheme 5.1). The synthetic procedure is identical to that used for **167**. Both the dimethylamine adduct (**306**) and the pyridine adduct (**307**) can be obtained in good yield.

Scheme 5.1. Synthesis of biaryl tethered hydroamination precatalysts.



The solid-state molecular structure of **307** is shown in Figure 5.1, confirming that the chiral bis(ureato) ligand imparts an analogous coordination geometry to **167**. If the stereoelectronic rationale proposed in the previous chapter is valid, then precatalyst **306** should also be capable of secondary amine hydroamination. Figure 3.2 summarizes preliminary results obtained regarding the substrate scope and enantioselectivity of this chiral catalyst system. For these reactions, a homochiral version of **306** was employed, synthesized using enantiopure **88** derived from (–)-2,2′-diamino-6,6′-dimethylbiphenyl.¹¹⁵

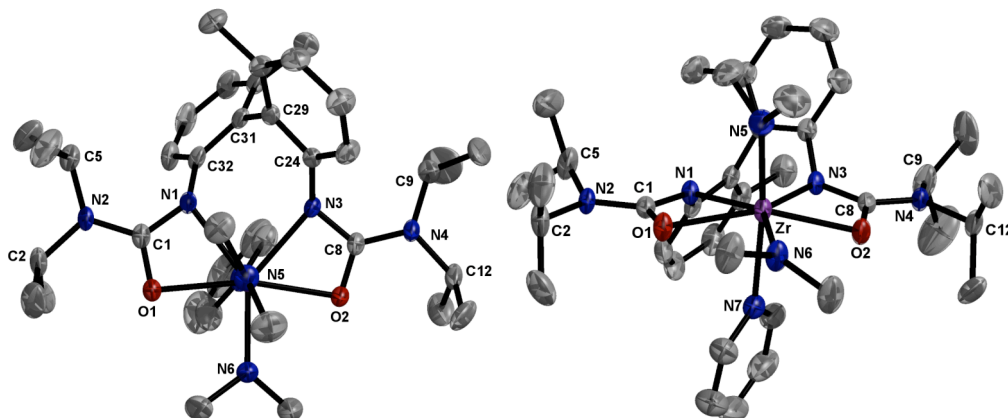


Figure 5.1. Two views of the ORTEP representation of the molecular structure of (±)-**307** (ellipsoids plotted at 50% probability, hydrogens omitted for clarity) with selected bond lengths (Å), bond and torsion angles (°): Zr–N1, 2.320(2); Zr–O1, 2.235(2); Zr–N5, 2.054(2); Zr–N7, 2.464(2); C1–N1, 1.336(3); C1–O1, 1.280(3); C1–N2, 1.346(3); N1–Zr–O1, 57.54(6); N1–Zr–N3, 77.71(6); N5–Zr–N7, 173.60(7); N1–C1–N2–C5, 15.9(3); C24–C29–C31–C32, 74.9(3).

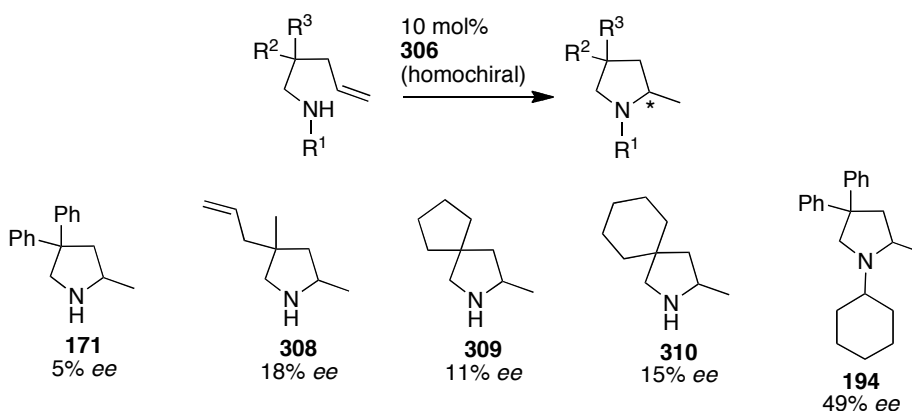


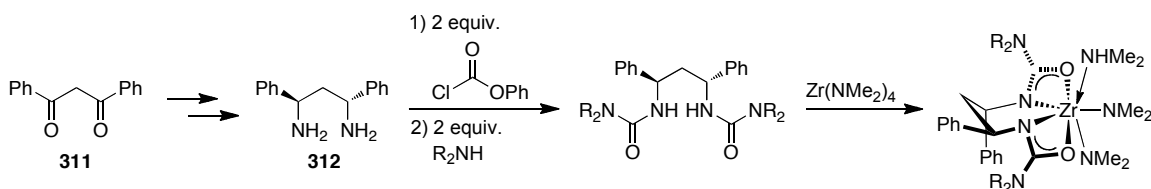
Figure 5.2. Enantioselective hydroamination with homochiral precatalyst **306** (derived from (-)-enantiomer of 2,2'-diamino-6,6'-dimethylbiphenyl).

Clearly, this catalyst system exhibits poor enantioselectivity in the cyclization of primary aminoalkenes, achieving a maximum *ee* of only 18%. One promising feature is that **306** is indeed able to work with a secondary amine substrate, and provides higher selectivity in this case. Notably, an analogous amidate precatalyst (**146**) is unreactive with secondary aminoalkenes.¹¹⁵ While the *ee* of **194** is a modest 49%, this result proves the feasibility of enantioselective secondary aminoalkene hydroamination using a neutral

group 4 catalyst.²³⁹ Furthermore, the modular nature of the ureate framework allows one to incorporate a wide variety of ligand substituents, which may help to increase the enantioselectivity of these systems. Further work on this project is currently ongoing in the group.

An alternate chiral ligand architecture can be envisioned that is more structurally similar to the bis(ureato) of **167**. Scheme 5.2 outlines a proposed short synthesis of chiral, C_2 -symmetric alkyl tethered ureas and the resulting hydroamination precatalysts. The chiral diamine required (**312**) is easily prepared as a single enantiomer in four steps using commercially available reagents (**311**).³⁴¹ This synthesis could be readily expanded to incorporate other substituents on the alkyl tether by starting with other β -diketones, enabling further control over catalyst structure.

Scheme 5.2. Proposed synthesis of chiral tethered hydroamination precatalysts.



The fact that very few group 4 systems are capable of highly enantioselective hydroamination speaks to the difficulty of this reaction. To achieve this, a modular ligand framework is a valuable asset, as it allows one to rapidly screen multiple precatalysts bearing a variety of substitution patterns. Another method to impart enantioselectivity would be to use chiral secondary amines in the proligand synthesis (**313-315**, Figure 5.3). This could be used in tandem with a chiral tether to expand the number of potential structures, increasing the likelihood that a highly selective system will be discovered. It must be stressed that the precatalyst structures proposed herein

represent only a small fraction of the design possibilities with ureate ligands. This will no doubt prove a fruitful area of further hydroamination catalyst development.

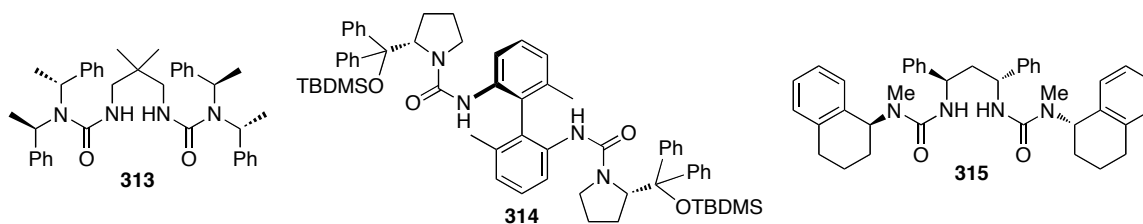


Figure 5.3. Potential urea proligands incorporating chirality in secondary amino group.

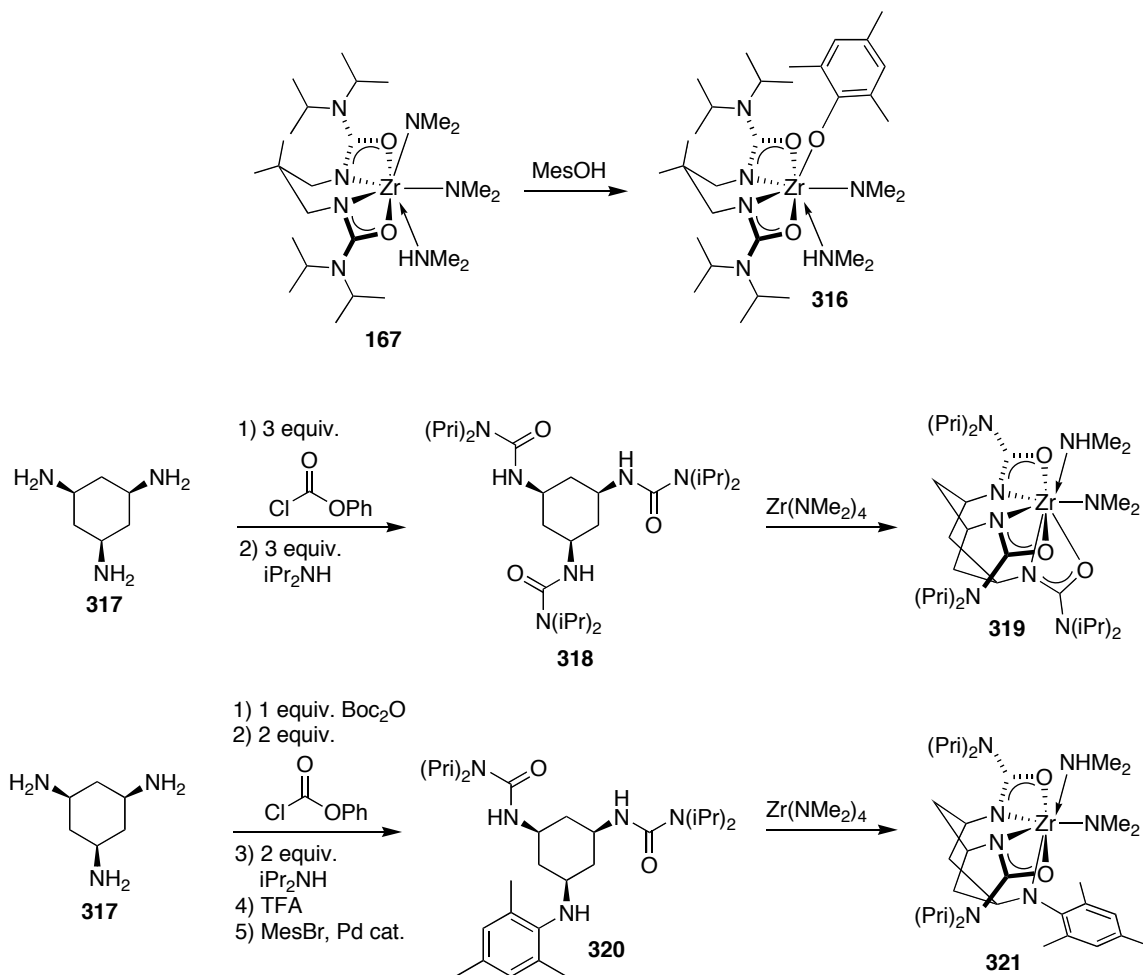
5.2.3 Toward Intermolecular Alkene Hydroamination

One of the consequences of the hydroamination mechanism proposed in the previous chapter is that only one reactive amido ligand need be incorporated into the precatalyst structure. While the equatorial amido and axial amino groups undergo reaction, the axial amido acts in a spectator fashion. This axial site can instead be occupied by an alternate supporting ligand, providing greater catalyst development opportunities (Scheme 5.3). In order to ensure the axial position is substituted, and not the equatorial position, the third anionic ligand must be a stronger π -donor than an amido, or be constrained by a rigid tether.

The proposed catalyst designs shown in Scheme 5.3 are based on using either a strongly π -donating aryloxide ligand to selectively substitute the axial position of **167**, or rigid triamine tether **317** to prepare trianionic ligands. Due to the ease of preparing **316**, precatalysts of this type should be the initial “next-generation” targets. In addition to hopefully imparting higher catalytic activity, this would provide method of testing the stereoelectronic hypothesis from Chapter Four. Use of a variety of aryloxide ligands

would allow for further steric and electronic manipulation, enabling the collection of structure/activity data, and the discovery of more active catalysts.

Scheme 5.3. Proposed synthesis of axially substituted hydroamination precatalysts.



While structurally more complex, precatalysts **319** and **321** are still readily assembled. Tris(amido) ligands based on **317** have been used previously with group 4 metals, confirming that this rigid framework enforces multidentate binding.^{342,343} This design is potentially superior to the use of aryloxide supports, as the third ligand need not be a strong π -donor to adopt an axial position. Presumably, a stronger interaction between the axial neutral amine ligand and the zirconium center would increase the

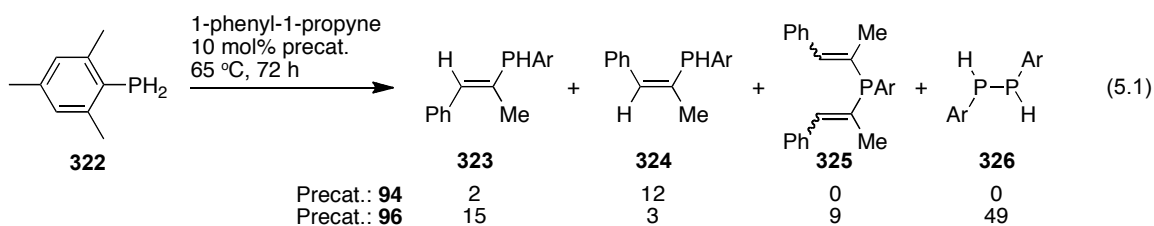
acidity of its N–H proton, enabling more facile alkene protonation. In this sense, use of a less electron donating axial ligand should strengthen neutral amine binding, increasing catalytic activity. Finally, the added chelating group should increase the thermal stability of the catalytic species.

The ultimate goal of these designs is to develop a catalyst system that is able to perform the intermolecular, anti-Markovnikov hydroamination of unactivated alkenes. Recall that this transformation was named one of the “Ten Challenges for Catalysis” more than fifteen years ago.¹⁸⁵ Given the established catalytic abilities of precatalyst **167**, and the breadth of design modifications available, this could be achievable in the near future using group 4 systems.

5.2.4 Hydrophosphination, Dehydrocoupling of Phosphines

The catalytic potential of group 4 ureate compounds is not limited to hydroamination. The feasibility of a closely related hydrofunctionalization reaction, hydrophosphination,³⁴⁴ has been established through preliminary experiments. Equation 5.1 outlines the results of a representative reaction between mesityl phosphine (**322**) and 1-phenyl-1-propyne using dialkyl compounds **94** and **96** as precatalysts. Monitoring these reactions by ³¹P NMR spectroscopy allows the identification of products by reference to known spectroscopic data, and by observation of P–H coupling. While the conversion of **322** is low when using **94**, the reaction proceeds much closer to completion with **96**, which has the same tethered ligand as hydroamination precatalyst **167**. Unfortunately, a mixture of compounds is produced in this latter reaction, including both

di- (**323**, **324**) and trisubstituted (**325**) phosphines. This latter product is formed through hydrophosphination of 1-phenyl-1-propyne by either **323** or **324**.

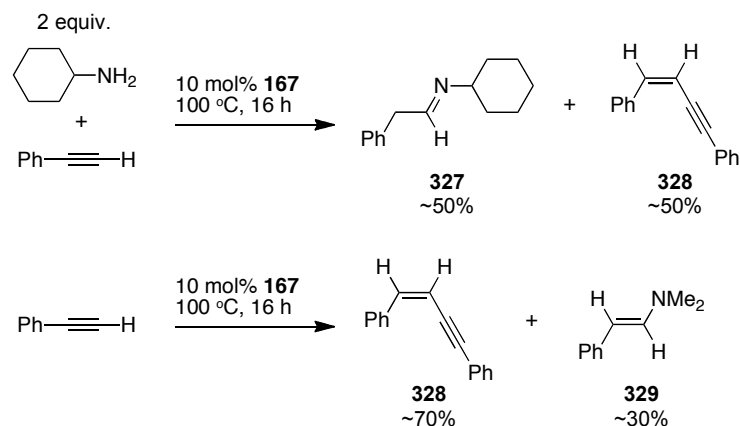


The major product formed in this case does not result from hydrophosphination, but rather from dehydrocoupling of **322** to form **326**. Phosphine dehydrocoupling, a useful reaction in its own right, can be promoted by a select number of group 4 catalysts.³⁴⁵ Surprisingly, attempted dehydrocoupling of **322** in the absence of alkyne was unsuccessful. This result indicates that a transfer hydrogenation process may be operative when alkyne is present, generating an alkene in tandem with **326**. Presumably, a zirconium hydride intermediate is formed at some stage of the dehydrocoupling process,³⁴⁶ which may rapidly decompose in the absence of an alkyne. Further catalyst design should endeavor to address this possibility, perhaps by using trianionic ligands, akin to those described in the previous section, to stabilize a potential hydride species.³⁴⁷ At this stage, the catalytic utility of ureate-supported precatalysts for both hydrophosphination and phosphine dehydrocoupling is extremely limited; however, these preliminary results are encouraging, especially considering the ease with which new catalyst architectures can be constructed.

5.2.5 Alkyne Coupling

Recall from Chapter Three that primary amine substrates are considerably less amenable to intermolecular alkyne hydroamination than secondary amines. Only one successful example was presented, due to a side product formed when using several other primary amine substrates. An examination of the mixture resulting from a reaction between phenylacetylene and cyclohexylamine led to the identification of this second product (**328**), which is formed in a 1:1 ratio with the expected imine (**327**, Scheme 5.4).

Scheme 5.4. Observation of phenylacetylene homocoupling with precatalyst **167**.



The side product **328** results from the addition of the C–H bond of one phenylacetylene molecule across the C≡C bond of a second phenylacetylene. This reaction is reminiscent of hydroamination, except that the C–H addition occurs in an exclusively *anti*-fashion, rather than the *syn*-addition observed for alkyne hydroamination. Treating phenylacetylene with **167** in the absence of external amine similarly results in the formation of **328**. In this case, the enyne product (**328**) is contaminated with ~30% of the enamine **329**, formed by hydroamination of phenylacetylene by the dimethylamine liberated from the precatalyst. While this type of

alkyne coupling is known, very few catalytic systems are capable mediating this transformation in a selective manner.³⁴⁸

Using analogous dialkyl compound **96** as a precatalyst for this reaction surprisingly results in no conversion to enyne **328**. It seems that an amine co-catalyst must be present for this alkyne coupling reaction to occur. The amine may act as a simple neutral donor to activate the catalytic species, or as a proton source. This latter possibility would be similar to the proton-assisted insertion process described in Chapter Four. Further reaction optimization carried out by another member of the Schafer group has determined that a 1:1 ratio of **96** and aniline is a highly effective catalyst composition for alkyne homocoupling. This formulation limits the formation of hydroamination byproducts, and enables the synthesis of several enyne products through alkyne coupling. Further catalyst development and reaction optimization is still needed to enable heterocoupling reactions. This reaction has the potential to generate versatile and biologically relevant³⁴⁹ enyne compounds in a stereoselective and atom-economic fashion.

The fact that group 4 complexes supported by ureate ligands have catalytic potential beyond the hydroamination reaction speaks to the versatile reactivity of these compounds. Developing complementary catalytic processes based on easily prepared and structurally similar precatalysts will hopefully allow future researchers to attain the goal of “one catalyst, many reactions,” and not be limited to the typical situation of “one catalyst, one reaction.” Already, two atom-economic carbon–element bond forming reactions, hydroamination and alkyne coupling, have been developed using nearly identical ureate-supported catalyst systems. These and related compounds will likely be applied to many more reactions in the future.

5.3 Concluding Statements

In analyzing the relationship between two very closely related ligand sets, this work truly highlights the subtlety inherent to organometallic chemistry, and the chemical discipline in general. A seemingly innocuous alteration to a chemical compound or process, be it in the form of changing a ligand substituent, using a different metal from the same group, or adjusting reaction temperature or reactant concentration, can manifest itself in significant and sometimes unexpected ways. On paper, amidates and ureates appear so similar as to be almost the same. But the subtle distinction between the two results in a rich and complementary relationship that can be exploited to great effect. There is no doubt that both of these supporting ligands deserve more attention from the synthetic community at large. Through the action of fundamental research, of which this thesis is only one part, the true potential of amidate and ureate chemistry will be realized.

*“I thought of another moral, more down to earth and concrete,
and I believe that every militant chemist can confirm it:
that one must distrust the almost-the-same, the practically identical,
the approximate, the or-even, all surrogates, and all patchwork.
The differences can be small, but they can lead to radically different consequences,
like a railroad’s switch points;
the chemist’s trade consists in good part in being aware of these differences,
knowing them close up, and forseeing their effects.
And not only the chemist’s trade.”*

-Primo Levi

The Periodic Table

REFERENCES

1. Kealy, T. J.; Pauson, P. L. *Nature* **1951**, *168*, 1039.
2. Miller, S. A.; Tebboth, J. A.; Tremaine, J. F. *J. Chem. Soc.* **1952**, 632.
3. Wilkinson, G.; Rosenblum, M.; Whiting, M. C.; Woodward, R. B. *J. Am. Chem. Soc.* **1952**, *74*, 2125.
4. Fischer, E. O.; Pfab, W. Z. *Naturforsch. B* **1952**, *7*, 377.
5. Laszlo, P.; Hoffmann, R. *Angew. Chem. Int. Ed.* **2000**, *39*, 123.
6. *Comprehensive Organometallic Chemistry III*; Crabtree, R. H.; Mingos, D. M. P., Eds. Elsevier: New York, 2007, Vol. 1-12.
7. Wilkinson, G.; Pauson, P. L.; Birmingham, J. M.; Cotton, F. A. *J. Am. Chem. Soc.* **1953**, *75*, 1011.
8. Wilkinson, G.; Birmingham, J. M. *J. Am. Chem. Soc.* **1954**, *76*, 4281.
9. Piper, T. S.; Wilkinson, G. *J. Inorg. Nucl. Chem.* **1956**, *3*, 104.
10. Kautzner, B.; Wailes, P. C.; Weigold, H. *Chem. Commun.* **1969**, 1105.
11. Tebbe, F. N.; Parshall, G. W.; Reddy, G. S. *J. Am. Chem. Soc.* **1978**, *100*, 3611.
12. Burlakov, V. V.; Rosenthal, U.; Petrovskii, P. V.; Shur, V. B.; Vol'pin, M. E. *Metalloorg. Khim.* **1988**, *1*, 953.
13. Chirik, P. *Organometallics* **2010**, *29*, 1500.
14. Wailes, P. C.; Weigold, H.; Bell, A. P. *J. Organomet. Chem.* **1971**, *27*, 373.
15. Schwartz, J.; Labinger, J. A. *Angew. Chem. Int. Ed.* **1976**, *15*, 333.
16. Wipf, P.; Kendall, C. *Top. Organomet. Chem.* **2004**, *8*, 1.
17. *Titanium and Zirconium in Organic Synthesis*; Marek, I., Ed.; Wiley-VCH: Weinheim, 2002.
18. Negishi, E.-I.; Tan, Z. *Top. Organomet. Chem.* **2004**, *8*, 139.

19. Petasis, N. A.; Bzowej, E. I. *J. Am. Chem. Soc.* **1990**, *112*, 6392.
20. Rosenthal, U.; Burlakov, V. V.; Arndt, P.; Baumann, W.; Spannenberg, A. *Organometallics* **2003**, *22*, 884.
21. Alt, H. G.; Koppl, A. *Chem. Rev.* **2000**, *100*, 1205.
22. Duncan, A. P.; Bergman R. G., *Chem. Rec.* **2002**, *2*, 431.
23. Arndt, S.; Okuda, J. *Chem. Rev.* **2002**, *102*, 1953.
24. Gibson, V. C.; Spitzmesser, S. K. *Chem. Rev.* **2003**, *103*, 283.
25. Britovsek, G. J. P.; Gibson, V. C.; Wass, D. F. *Angew. Chem., Int. Ed.* **1999**, *38*, 428.
26. Takeuchi, D. *Dalton Trans.* **2010**, *39*, 311.
27. Kempe, R. *Angew. Chem. Int. Ed.* **2000**, *39*, 468.
28. Yamamoto, A.; Kambura, S. *J. Am. Chem. Soc.* **1957**, *79*, 4344.
29. Dolgov, B. N.; Orlov, N. F. *Russ. Chem. Bull.* **1957**, *6*, 1414.
30. Shepard, A. F.; Dannels, B. F. US Patent Number 3,418,348. **1968**.
31. Lubben, T. V.; Wolczanski, P. T.; VanDuyne, G. D. *Organometallics* **1984**, *3*, 977.
32. Bradley, D. C.; Thomas, I. M. *J. Chem. Soc.* **1960**, 3857.
33. Taube, R. *Z. fuer Chem.* **1963**, *3*, 194.
34. Chandra, G.; Jenkins, A. D.; Lappert, M. F. *J. Chem. Soc. (A)* **1970**, 2250.
35. Gambarotta, S.; Strologo, S.; Floriani, C.; Chiesi-Villa, A.; Guastini, C. *J. Am. Chem. Soc.* **1985**, *107*, 6278.
36. Latham, I. A.; Leigh, G. J. *J. Chem. Soc. Dalton. Trans.* **1986**, 377.
37. Hitchcock, P. B.; Lappert, M. F.; Liu, D.-S. *J. Chem. Soc. Chem. Commun.* **1994**, 2637.
38. Dias, H. V. R.; Jin, W.; Wang, Z. *Inorg. Chem.* **1996**, *35*, 6074.
39. Macarovici, C. G.; Perte, E.; Motiu, E. *Rev. Roum. Chim.* **1966**, *11*, 59.
40. Bradley, D. C.; Hursthouse, M. B.; Rendall, I. F. *Chem. Commun.* **1969**, 672.

41. Klei, E.; Telgen, J. H.; Teuben, J. H. *J. Organomet. Chem.* **1981**, 209, 297.
42. Asslani, S.; Rahbarnoohi, R.; Wilson, B. L. *Inorg. Nucl. Chem. Lett.* **1979**, 15, 59.
43. Bazan, G. C.; Rodriguez, G. *J. Am. Chem. Soc.* **1996**, 118, 2291.
44. Pearson, R. G. *J. Am. Chem. Soc.* **1963**, 85, 3533.
45. Guillard, R.; Lecomte, C. *Coord. Chem. Rev.* **1985**, 65, 87.
46. Gade, L. H. *Chem. Commun.* **2000**, 173.
47. Gade, L. H.; Mountford, P. *Coord. Chem. Rev.* **2001**, 216-217, 65.
48. Gade, L. H. *Acc. Chem. Res.* **2002**, 35, 575.
49. Gade, L. H. *J. Organomet. Chem.* **2002**, 661, 85.
50. Radius, U. *Z. Anorg. Allg. Chem.* **2004**, 630, 957.
51. Matsuo, T.; Kawaguchi, H. *Chem. Lett.* **2004**, 33, 640.
52. Kawaguchi, H.; Matsuo, T. *J. Organomet. Chem.* **2004**, 689, 4228.
53. Odom, A. L. *Dalton Trans.* **2005**, 225.
54. Liang, L.-C. *Coord. Chem. Rev.* **2006**, 250, 1152.
55. Edelmann, F. T. *Adv. Organomet. Chem.* **2008**, 57, 183.
56. Ballmann, J.; Munha, R. F.; Fryzuk, M. D. *Chem. Commun.* **2010**, 46, 1013.
57. Bolton, P. D.; Mountford, P. *Adv. Synth. Catal.* **2005**, 347, 355.
58. Mindiola, D. J. *Acc. Chem. Res.* **2006**, 39, 813.
59. Zi, G. *Dalton Trans.* **2009**, 9101.
60. Braunschweig, H.; Breitling, F. M. *Coord. Chem. Rev.* **2006**, 250, 2691.
61. Fryzuk, M. D.; Love, J. B.; Rettig, S. J.; Young, V. G. *Science* **1997**, 275, 1445.
62. Bailey, B. C.; Fan, H.; Baum, E. W.; Huffman, J. C.; Baik, M.-H.; Mindiola, D. J. *J. Am. Chem. Soc.* **2005**, 127, 16016.
63. Fout, A. R.; Bailey, B. C.; Tomaszewski, J.; Mindiola, D. J. *J. Am. Chem. Soc.* **2007**, 129, 12640.
64. Matsuo, T.; Kawaguchi, H. *J. Am. Chem. Soc.* **2006**, 128, 12362.

65. Stanciu, C.; Jones, M. E.; Fanwick, P. E.; Abu-Omar, M. M. *J. Am. Chem. Soc.* **2007**, *129*, 12400.
66. Nugent, W. A. *Coord. Chem. Rev.* **1980**, *31*, 123.
67. Trofimenko, S. *Chem. Rev.* **1993**, *93*, 943.
68. Edelmann, F. T. *Coord. Chem. Rev.* **1994**, *137*, 403.
69. Barker, J.; Kilner, M. *Coord. Chem. Rev.* **1994**, *133*, 219.
70. Wolczanski, P. T. *Polyhedron* **1995**, *14*, 3335.
71. Dehnicke, K.; Krieger, M.; Massa, W. *Coord. Chem. Rev.* **1999**, *182*, 19.
72. Fu, G. C. *Adv. Organomet. Chem.* **2000**, *47*, 101.
73. Roesky, P. W. *Chem. Soc. Rev.* **2000**, *29*, 335.
74. Meléndez, E. M. *Crit. Rev. Oncol. Hemat.* **2002**, *42*, 309.
75. Makio, H.; Kashiwa, N.; Fujita, T. *Adv. Synth. Catal.* **2002**, *344*, 477.
76. Bourget-Merle, L.; Lappert, M. F.; Severn, J. R. *Chem. Rev.* **2002**, *102*, 3031.
77. Hubert-Pfalzgraf, L. G. *J. Mater. Chem.* **2004**, *14*, 3113.
78. Stephan, D. W. *Adv. Organomet. Chem.* **2006**, *54*, 267.
79. Wolczanski, P. T. *Chem. Commun.* **2009**, 740.
80. Tshuva, E. Y.; Ashenurst, J. A. *Eur. J. Inorg. Chem.* **2009**, 2203.
81. Lee, A. V.; Schafer, L. L. *Eur. J. Inorg. Chem.* **2007**, 2243.
82. Wood, D.; Yap, G. P. A.; Richeson, D. S. *Inorg. Chem.* **1999**, *38*, 5788.
83. Duncan, A. P.; Mullins, S. M.; Arnold, J.; Bergman, R. G. *Organometallics* **2001**, *20*, 1808.
84. Lam, H.-W.; Wilkinson, G.; Hussain-Bates, B.; Hursthouse, M. B. *J. Chem. Soc. Dalton Trans.* **1993**, 781.
85. Leung, W.-H.; Wilkinson, G.; Hussain-Bates, B.; Hursthouse, M. B. *J. Chem. Soc. Dalton Trans.* **1991**, 2791.
86. Lavoie, N.; Ong, T.-G.; Gorelsky, S. I.; Korobkov, I.; Yap, G. P. A.; Richeson, D. S. *Organometallics* **2007**, *26*, 6586.

87. Hevia, E.; Pérez, J.; Riera, V.; Miguel, D. *Chem. Commun.* **2002**, 1814.
88. Hevia, E.; Pérez, J.; Riera, V.; Miguel, D. *Organometallics* **2003**, 22, 257.
89. Cowan, R. L.; Trogler, W. C. *J. Am. Chem. Soc.* **1989**, 111, 4750.
90. Chandra, G.; Jenkins, A. D.; Lappert, M. F.; Srivastava, R. C. *J. Chem. Soc. (A)* **1970**, 2550.
91. Lappert, M. F.; Sanger, A. R. *J. Chem. Soc. (A)* **1971**, 1314.
92. Wang, H.; Li, H.-W.; Xie, Z. *Organometallics* **2003**, 22, 4522.
93. Wang, H.; Chan, H.-S.; Okuda, J.; Xie, Z. *Organometallics* **2005**, 24, 3118.
94. Hsieh, K.-C.; Lee, W.-Y.; Lai, C.-L.; Hu, C.-H.; Lee, H. M.; Huang, J.-H.; Peng, S.-M.; Lee, G.-H. *J. Organomet. Chem.* **2004**, 689, 3362.
95. Pothiraja, R.; Milanov, A. P.; Barreca, D.; Gasparotto, A.; Becker, H.-W.; Winter, M.; Fischer, R. A.; Devi, A. *Chem. Commun.* **2009**, 1978.
96. Abel, E. W.; Dunster, M. O. *J. Chem. Soc. Dalton Trans.* **1973**, 98.
97. Borovik, A. S. *Acc. Chem. Res.* **2005**, 38, 54.
98. Shook, R. L.; Borovik, A. S. *Chem. Commun.* **2008**, 6095.
99. Shook, R. L.; Borovik, A. S. *Inorg. Chem.* **2010**, 49, 3646.
100. MacBeth, C. E.; Golombek, A. P.; Jr., V. G. Y.; Yang, C.; Kuczera, K.; Hendrich, M. P.; Borovik, A. S. *Science* **2000**, 289, 938.
101. Gupta, R.; Zhang, Z. H.; Powell, D.; Hendrich, M. P.; Borovik, A. S. *Inorg. Chem.* **2002**, 41, 5100.
102. MacBeth, C. E.; Larsen, P. L.; Sorrell, T. N.; Powell, D.; Borovik, A. S. *Inorg. Chim. Acta* **2002**, 341, 77.
103. Zart, M. K.; Sorrell, T. N.; Powell, D.; Borovik, A. S. *Dalton Trans.* **2003**, 1986.
104. Zinn, P. J.; Powell, D. R.; Day, V. W.; Hendrich, M. P.; Sorrell, T. N.; Borovik, A. S. *Inorg. Chem.* **2006**, 45, 3484.
105. Sun, Y.; Zhang, Z.; Wang, X.; Li, X.; Weng, L.; Zhou, X. *Organometallics* **2009**, 28, 6320.
106. Gott, A. L.; Clarke, A. J.; Clarkson, G. J.; Scott, P. *Organometallics* **2007**, 26, 1729.

107. Leitch, D. C.; Beard, J. D.; Thomson, R. K.; Wright, V. A.; Patrick, B. O.; Schafer, L. L. *Eur. J. Inorg. Chem.* **2009**, 2691.
108. Bochmann, M. *J. Chem. Soc. Dalton Trans.* **1996**, 255.
109. Li, C.; Thompson, R. K.; Gillon, B.; Patrick, B. O.; Schafer, L. L. *Chem. Commun.* **2003**, 2462.
110. Zhang, Z.; Schafer, L. L. *Org. Lett.* **2003**, 5, 4733.
111. Ayinla, R. O.; Schafer, L. L. *Inorg. Chim. Acta* **2006**, 359, 3097.
112. Lee, A. V.; Schafer, L. L. *Synlett* **2006**, 2973.
113. Thomson, R. K.; Bexrud, J. A.; Schafer, L. L. *Organometallics* **2006**, 25, 4069.
114. Bexrud, J. A.; Li, C.; Schafer, L. L. *Organometallics* **2007**, 26, 6366.
115. Wood, M. C.; Leitch, D. C.; Yeung, C. S.; Kozak, J. A.; Schafer, L. L. *Angew. Chem., Int. Ed.* **2007**, 46, 354.
116. Zhang, Z.; Leitch, D. C.; Lu, M.; Patrick, B. O.; Schafer, L. L. *Chem. Eur. J.* **2007**, 13, 2012.
117. Bexrud, J. A.; Schafer, L. L. *Dalton Trans.* **2009**, 39, 361.
118. Lee, A. V.; Sajitz, M.; Schafer, L. L. *Synthesis* **2009**, 97.
119. Thomson, R. K.; Schafer, L. L. *Can. J. Chem.* **2005**, 83, 1037.
120. Liu, S.; Sun, W.-H.; Zeng, Y.; Wang, D.; Zhang, W.; Li, Y. *Organometallics* **2010**, 29, DOI: 10.1021/om1000748.
121. Vyboishchikov, S. F.; Musaev, D. G.; Froese, R. D. J.; Morokuma, K. *Organometallics* **2001**, 20, 309.
122. Boor, J. *Ziegler-Natta Catalysts and Polymerizations*. Academic Press: New York, 1979.
123. *History of Polyolefins*; Seymour, R. B.; Cheng, T., Eds.; D. Reidel Publishing Company: Boston, 1986.
124. *Metal Catalysts in Olefin Polymerization*; Guan, Z., Ed.; Topics in Organometallic Chemistry Vol. 26; Springer: Berlin, 2009.
125. Ziegler, K.; Holzkamp, E.; Breil, H.; Martin, H. *Angew. Chem.* **1955**, 67, 541.
126. Natta, G. *Angew. Chem.* **1956**, 68, 393.

127. Resconi, L.; Cavallo, L.; Fait, A.; Piemontesi, F. *Chem. Rev.* **2000**, *1000*, 1253.
128. Arriola, D. J.; Camahan, E. M.; Hustad, P. D.; Kuhlman, R. L.; Wenzel, T. T. *Science* **2006**, *312*, 714.
129. Coates, G. W.; Waymouth, R. M. *Science* **1995**, *267*, 217.
130. Landis, C. R.; Christianson, M. D. *Proc. Nat. Acad. Sci.* **2006**, *103*, 15349.
131. Wei, J.; Zhang, W.; Sita, L. R. *Angew. Chem. Int. Ed.* **2010**, *49*, 1768.
132. Grubbs, R. H.; Coates, G. W. *Acc. Chem. Res.* **1996**, *29*, 85.
133. Liu, Z.; Somsook, E.; White, C. B.; Rosaaen, K. A.; Landis, C. R. *J. Am. Chem. Soc.* **2001**, *123*, 11193.
134. Stoeckenau, E. J.; Jordan, R. F. *J. Am. Chem. Soc.* **2006**, *128*, 8162.
135. Stoeckenau, E. J.; Jordan, R. F. *J. Am. Chem. Soc.* **2006**, *128*, 8638.
136. Stoeckenau, E. J.; Jordan, R. F. *Organometallics* **2006**, *25*, 3379.
137. Sydora, O. L.; Kilyanek, S. M.; Jordan, R. F. *J. Am. Chem. Soc.* **2007**, *129*, 12952.
138. Guo, Z.; Swenson, D. C.; Jordan, R. F. *Organometallics* **1994**, *13*, 1424.
139. Jordan, R. F. *Adv. Organomet. Chem.* **1991**, *32*, 325.
140. Yang, X.; Stern, C. L.; Marks, T. J. *J. Am. Chem. Soc.* **1994**, *116*, 10015.
141. Chen, E. Y. X.; Marks, T. J. *Chem. Rev.* **2000**, *100*, 1391.
142. Andresen, A.; Cordes, H.-G.; Herwig, J.; Kaminsky, W.; Merck, A.; Mottweiler, R.; Pein, J.; Sinn, H.; Vollmer, H.-J. *Angew. Chem. Int. Ed.* **1976**, *15*, 630.
143. Rappe, A. K.; Skiff, W. M.; Casewit, C. J. *Chem. Rev.* **2000**, *100*, 1435.
144. Breslow, D. S.; Newburg, N. R. *J. Am. Chem. Soc.* **1959**, *81*, 81.
145. Sinn, H.; Kaminsky, W. *Adv. Organomet. Chem.* **1980**, *18*, 99.
146. Sinn, H.; Kaminsky, W.; Vollmer, H.-J.; Woldt, R. *Angew. Chem. Int. Ed.* **1980**, *19*, 390.
147. Kaminsky, W. *J. Polym. Sci. A* **2004**, *42*, 3911.
148. Brintzinger, H. H.; Fischer, D.; Muhlhaupt, R.; Rieger, B.; Waymouth, R. *Angew. Chem., Int. Ed. Engl.* **1995**, *34*, 1143.

149. Boffa, L. S.; Novak, B. M. *Chem. Rev.* **2000**, *100*, 1479.
150. Scollard, J. D.; McConville, D. H. *J. Am. Chem. Soc.* **1996**, *118*, 10008.
151. Scollard, J. D.; McConville, D. H.; Payne, N. C.; Vittal, J. J. *Macromolecules* **1996**, *29*, 5241.
152. Gibson, V. C.; Maddox, P. J.; Newton, C.; Redshaw, C.; Solan, G. A.; White, A. J. P.; Williams, D. J. *Chem. Commun.* **1998**, 1651.
153. Mitani, M.; Saito, J.; Ishii, S.-I.; Nakayama, Y.; Makio, H.; Matsukawa, N.; Matsui, S.; Mohri, J.-I.; Furuyama, R.; Terao, H.; Bando, H.; Tanaka, H.; Fujita, T. *Chem. Rec.* **2004**, *4*, 137.
154. Makio, H.; Fujita, T. *Acc. Chem. Res.* **2009**, *42*, 1532.
155. Garrett, R. H.; Grisham, C. M. *Biochemistry*. Brooks/Cole: Boston, 2010.
156. Yu, S.-M.; Mecking, S. *J. Am. Chem. Soc.* **2008**, *130*, 13204.
157. Mason, A. F.; Coates, G. W. *J. Am. Chem. Soc.* **2004**, *126*, 16326.
158. Webster, O. W. *Science* **1991**, *251*, 887.
159. Ouchi, M.; Terashima, T.; Sawamoto, M. *Chem. Rev.* **2009**, *109*, 4963.
160. Herskovics-Korine, D.; Eisen, M. S. *J. Organomet. Chem.* **1995**, *503*, 307.
161. Flores, J. C.; Chien, J. C. W.; Rausch, M. D. *Organometallics* **1995**, *14*, 2106.
162. Littke, A.; Sleiman, N.; Bensimon, C.; Richeson, D. S. *Organometallics* **1998**, *17*, 446.
163. Walther, D.; Fischer, R.; Gorls, H.; Koch, J.; Schweder, B. *J. Organomet. Chem.* **1996**, *508*, 13.
164. Sita, L. R. *Angew. Chem. Int. Ed.* **2009**, *48*, 2464.
165. Gool, M. V.; Bartolome, J. M.; Macdonald, G. J. *Tetrahedron Lett.* **2008**, *49*, 7171.
166. Cotarca, L.; Delogu, P.; Nardelli, A.; Sunjic, V. *Synthesis* **1996**, 553.
167. Diaz, D. J.; Darko, A. K.; McElwee-White, L. *Eur. J. Org. Chem.* **2007**, 4453.
168. Majer, P.; Randad, R. S. *J. Org. Chem.* **1994**, *59*, 1937.
169. Thavonekham, B. *Synthesis* **1997**, 1189.

170. Benzing, E.; Kornicker, W. *Chem. Ber.* **1961**, *94*, 2263.
171. Warren, T. H.; Erker, G.; Frohlich, R.; Wibbeling, B. *Organometallics* **2000**, *19*, 127.
172. Braum, S.; Kalinowski, H.-O.; Berger, S. *100 and More Basic NMR Experiments*. VCH Publishers: New York, 1996.
173. Spek, A. L. *J. Appl. Crystallogr.* **2003**, *36*, 7.
174. Thomson, R. K.; Schafer, L. L. *Organometallics* **2010**, *29*, submitted.
175. Schrock, R. R. *Chem. Rev.* **2002**, *102*, 145.
176. Legzdins, P.; Phillips, E. C.; Trotter, J.; Yee, V. C.; Einstein, F. W. B.; Jones, R. H. *Organometallics* **1991**, *10*, 986.
177. Giesbrecht, G. R.; Whitener, G. D.; Arnold, J. *Organometallics* **2000**, *19*, 2809.
178. Horrillo-Martinez, P.; Leitch, D. C.; Thomson, R. K.; Beard, J. D.; Schafer, L. L. *Manuscript in Preparation*.
179. Padmanabhan, S.; Sarma, K. R.; Sharma, S. *Ind. Eng. Chem. Res.* **2009**, *48*, 4866.
180. Trost, B. M. *Angew. Chem. Int. Ed.* **1995**, *34*, 259.
181. *Catalytic Heterofunctionalization*. Togni, A.; Grützmacher, H. J., Eds.; Wiley-VCH: Weinheim, 2001.
182. Hartwig, J. F. *Nature* **2008**, *455*, 314.
183. Müller, T. E.; Hultsch, K. C.; Yus, M.; Foubelo, F.; Tada, M. *Chem. Rev.* **2008**, *108*, 3795.
184. Müller, T. E.; Beller, M. *Chem. Rev.* **1998**, *98*, 675.
185. Haggins, J. *Chem. Eng. News* **1993**, *71* (22), 23.
186. Jimenez, O.; Müller, T. E.; Sievers, C.; Spirk, A.; Lercher, J. A. *Chem. Commun.* **2006**, 2974.
187. Gribkov, D. V.; Hultsch, K. C.; Hampel, F. *J. Am. Chem. Soc.* **2006**, *128*, 3748.
188. Li, Y.; Marks, T. J. *Organometallics* **1996**, *15*, 3770.
189. Utsunomiya, M.; Hartwig, J. F. *J. Am. Chem. Soc.* **2004**, *126*, 2702.
190. Utsunomiya, M.; Hartwig, J. F. *J. Am. Chem. Soc.* **2003**, *125*, 14286.

191. Utsunomiya, M.; Kuwano, R.; Kawatsura, M.; Hartwig, J. F. *J. Am. Chem. Soc.* **2003**, *125*, 5608.
192. Zhou, J.; Hartwig, J. F. *J. Am. Chem. Soc.* **2008**, *130*, 12220.
193. Dorta, R.; Egli, P.; Zurcher, F.; Togni, A. *J. Am. Chem. Soc.* **1997**, *119*, 10857.
194. Aillaud, I.; Collin, J.; Hannedouche, J.; Schulz, E. *Dalton Trans.* **2007**, 5105, 5118.
195. Hultzs, K. C. *Org. Biomol. Chem.* **2005**, *3*, 1819.
196. Hultzs, K. C. *Adv. Synth. Catal.* **2005**, *347*, 367.
197. Roesky, P. W.; Müller, T. E. *Angew. Chem., Int. Ed.* **2003**, *42*, 2708.
198. Gagné, M. R.; Marks, T. J. *J. Am. Chem. Soc.* **1989**, *111*, 4108.
199. Hong, S.; Marks, T. J. *Acc. Chem. Res.* **2004**, *37*, 673.
200. Housecroft, C. E.; Sharpe, A. G. *Inorganic Chemistry*. Prentice Hall: Essex, 2001.
201. Gagné, M. R.; Stern, C. L.; Marks, T. J. *J. Am. Chem. Soc.* **1992**, *114*, 275.
202. Tian, S.; Arredondo, V. M.; Stern, C. L.; Marks, T. J. *Organometallics* **1999**, *18*, 2568.
203. Li, Y.; Marks, T. J. *J. Am. Chem. Soc.* **1996**, *118*, 9295.
204. Motta, A.; Fragala, I. L.; Marks, T. J. *Organometallics* **2006**, *25*, 5533.
205. Ryu, J. S.; Marks, T. J.; McDonald, F. E. *J. Org. Chem.* **2004**, *69*, 1038.
206. Hong, S.; Marks, T. J. *J. Am. Chem. Soc.* **2002**, *124*, 7886.
207. Ryu, J. S.; Li, G. Y.; Marks, T. J. *J. Am. Chem. Soc.* **2003**, *125*, 12584.
208. Ryu, J. S.; Marks, T. J.; McDonald, F. E. *Org. Lett.* **2001**, *3*, 3091.
209. Kim, J. Y.; Livinghouse, T. *Org. Lett.* **2005**, *7*, 4391.
210. Kim, Y. K.; Livinghouse, T.; Horino, Y. *J. Am. Chem. Soc.* **2003**, *125*, 9560.
211. Hultzs, K. C.; Hampel, F.; Wagner, T. *Organometallics* **2004**, *23*, 2601.
212. Corbet, J.-P.; Mignani, G. *Chem. Rev.* **2006**, *106*, 2651.
213. Jakel, C.; Paciello, R. *Chem. Rev.* **2006**, *106*, 2912.

214. Vougioukalakis, G. C.; Grubbs, R. H. *Chem. Rev.* **2010**, *110*, 1746.
215. Bender, C. F.; Widenhoefer, R. A. *J. Am. Chem. Soc.* **2005**, *127*, 1070.
216. Liu, Z.; Hartwig, J. F. *J. Am. Chem. Soc.* **2008**, *130*, 1570.
217. Ohmiya, H.; Moriya, T.; Sawamura, M. *Org. Lett.* **2009**, *11*, 2145.
218. Hesp, K. D.; Tobisch, S.; Stradiotto, M. *J. Am. Chem. Soc.* **2010**, *132*, 413.
219. Shen, X.; Buchwald, S. L. *Angew. Chem. Int. Ed.* **2010**, *49*, 564.
220. Fukumoto, Y.; Asai, H.; Shimizu, M.; Chatani, N. *J. Am. Chem. Soc.* **2007**, *129*, 13792.
221. Garrett, C. E.; Prasad, K. *Adv. Synth. Catal.* **2004**, *346*, 889.
222. Walsh, P. J.; Baranger, A. M.; Bergman, R. G. *J. Am. Chem. Soc.* **1992**, *114*, 1708.
223. McGrane, P. L.; Jensen, M.; Livinghouse, T. *J. Am. Chem. Soc.* **1992**, *114*, 5459.
224. McGrane, P. L.; Livinghouse, T. *J. Am. Chem. Soc.* **1993**, *115*, 11485.
225. Bexrud, J. A.; Beard, J. D.; Leitch, D. C.; Schafer, L. L. *Org. Lett.* **2005**, *7*, 1959.
226. Kim, H.; Lee, P. H.; Livinghouse, T. *Chem. Commun.* **2005**, 5205.
227. Müller, C.; Loos, C.; Schulenberg, N.; Doye, S. *Eur. J. Org. Chem.* **2006**, 2499.
228. Watson, D. A.; Chiu, M.; Bergman, R. G. *Organometallics* **2006**, *25*, 4731.
229. Bexrud, J. A.; Schafer, L. L. *Dalton Trans.* **2010**, *39*, 361.
230. Janssen, T.; Severin, R.; Diekmann, M.; Friedemann, M.; Haase, D.; Saak, W.; Doye, S.; Beckhaus, R. *Organometallics* **2010**, *29*, 1806.
231. Manna, K.; Ellern, A.; Sadow, A. D. *Chem. Commun.* **2010**, *46*, 339.
232. Reznichenko, A. L.; Hultsch, K. C. *Organometallics* **2010**, *29*, 24.
233. Bexrud, J. A.; Eisenberger, P.; Leitch, D. C.; Payne, P. R.; Schafer, L. L. *J. Am. Chem. Soc.* **2009**, *131*, 2116.
234. Kubiak, R.; Prochnow, I.; Doye, S. *Angew. Chem., Int. Ed.* **2009**, *48*, 1153.
235. Prochnow, I.; Kubiak, R.; Frey, O. N.; Beckhaus, R.; Doye, S. *ChemCatChem* **2009**, *1*, 162.

236. Kubiak, R.; Prochnow, I.; Doye, S. *Angew. Chem., Int. Ed.* **2010**, *49* (14), 2626.
237. Roesky, P. W. *Angew. Chem. Int. Ed.* **2009**, *48*, 4892.
238. Gribkov, D. V.; Hultsch, K. C. *Angew. Chem., Int. Ed.* **2004**, *43*, 5542.
239. Knight, P. D.; Munslow, I.; O'Shaughnessy, P. N.; Scott, P. *Chem. Commun.* **2004**, 894.
240. Stubbert, B. D.; Marks, T. J. *J. Am. Chem. Soc.* **2007**, *129*, 6149.
241. Majumder, S.; Odom, A. L. *Organometallics* **2008**, *27*, 1174.
242. Müller, C.; Saak, W.; Doye, S. *Eur. J. Org. Chem.* **2008**, 2731.
243. Thomson, R. K. Amidate Complexes of the Group 4 Metals: Synthesis, Reactivity, and Hydroamination Catalysis. Ph. D. Thesis, University of British Columbia, Vancouver, BC, Canada, January 2008.
244. Turner, C. S.; Schafer, L. L. *Unpublished results*.
245. Horrillo-Martinez, P.; Schafer, L. L. *Unpublished results*.
246. Ackermann, L.; Bergman, R. G.; Loy, R. N. *J. Am. Chem. Soc.* **2003**, *125*, 11956.
247. Thomson, R. K.; Zahariev, F. E.; Zhang, Z.; Patrick, B. O.; Wang, Y. A.; Schafer, L. L. *Inorg. Chem.* **2005**, *44*, 8680.
248. Lauzon, J. M. P.; Schafer, L. L. *Unpublished results*.
249. Whitesell, J. K.; Whitesell, M. A. *Synthesis* **1983**, 517.
250. *Enamines*, 2nd edition; Cook, A. G., Ed.; Marcel Dekker: New York, 1988.
251. Müller, T. E.; Grosche, M.; Herdtweck, E.; Pleier, A. K.; Walter, E.; Yan, Y. K. *Organometallics* **2000**, *1*, 170.
252. Li, X.; Chianese, A. R.; Vogel, T.; Crabtree, R. H. *Org. Lett.* **2005**, *7*, 5437.
253. Karshtedt, D.; Bell, A. T.; Tilley, T. D. *J. Am. Chem. Soc.* **2005**, *127*, 12640.
254. Brunet, J. J.; Cadena, M.; Chu, N. C.; Diallo, O.; Jacob, K.; Mothes, E. *Organometallics* **2004**, *23*, 1264.
255. Penzien, J.; Haessner, C.; Jentys, A.; Kohler, K.; Müller, T. E.; Lercher, J. A. *J. Catal.* **2004**, *221*, 302.
256. Müller, T. E.; Berger, M.; Grosche, M.; Herdtweck, E.; Schmidtchen, F. P. *Organometallics* **2001**, *20*, 4384.

257. Kawatsura, M.; Hartwig, J. F. *J. Am. Chem. Soc.* **2000**, *122*, 9546.
258. Zhang, Z.; Liu, C.; Kinder, R. E.; Han, X.; Qian, H.; Widenhoefer, R. A. *J. Am. Chem. Soc.* **2006**, *128*, 9066.
259. Su, R. Q.; Nguyen, V. N.; Müller, T. E. *Top. Catal.* **2003**, *22*, 23.
260. Su, R. Q.; Müller, T. E. *Tetrahedron* **2001**, *57*, 6027.
261. Klein, D. P.; Ellern, A.; Angelici, R. J. *Organometallics* **2004**, *23*, 5662.
262. Beller, M.; Trauthwein, H.; Eichberger, M.; Breindl, C.; Müller, T. E. *Eur. J. Inorg. Chem.* **1999**, 1121.
263. Beller, M.; Trauthwein, H.; Eichberger, M.; Breindl, C.; Herwig, J.; Müller, T. E.; Thiel, O. R. *Chem. Eur. J.* **1999**, *5*, 1306.
264. Beller, M.; Eichberger, M.; Trauthwein, H. *Angew. Chem., Int. Ed. Engl.* **1997**, *36*, 2225.
265. Zhao, J.; Goldman, A. S.; Hartwig, J. F. *Science* **2005**, *307*, 1080.
266. Tsipis, C. A.; Kefalidis, C. E. *Organometallics* **2006**, *25*, 1696.
267. Cowan, R.; Trogler, W. C. *Organometallics* **1987**, *6*, 2451.
268. Haneline, M. R.; Heyduk, A. F. *J. Am. Chem. Soc.* **2006**, *128*, 8410.
269. Hayashi, Y.; Osawa, M.; Kobayashi, K.; Wakatsuki, Y. *Chem. Commun.* **1996**, 1617.
270. Pohlki, F.; Doye, S. *Angew. Chem., Int. Ed.* **2001**, *40*, 2305.
271. Crimmin, M. R.; Casely, I. J.; Hill, M. S. *J. Am. Chem. Soc.* **2005**, *127*, 2042.
272. Crimmin, M. R.; Arrowsmith, M.; Barrett, A. G. M.; Casely, I. J.; Hill, M. S.; Procopiou, P. A. *J. Am. Chem. Soc.* **2009**, *131*, 9670.
273. Baranger, A. M.; Walsh, P. J.; Bergman, R. G. *J. Am. Chem. Soc.* **1993**, *115*, 2753.
274. Walsh, P. J.; Hollander, F. J.; Bergman, R. G. *J. Am. Chem. Soc.* **1988**, *110*, 8729.
275. Johnson, J. S.; Bergman, R. G. *J. Am. Chem. Soc.* **2001**, *123*, 2923.
276. Arney, D. J.; Bruck, M. A.; Huber, S. R.; Wigley, D. E. *Inorg. Chem.* **1992**, *31*, 3749.

277. Dunn, S. C.; Hazari, N.; Jones, N. M.; Moody, A. G.; Blake, A. J.; Cowley, A. R.; Green, J. C.; Mountford, P. *Chem. Eur. J.* **2005**, *11*, 2111.
278. Owen, C. T.; Bolton, P. D.; Cowley, A. R.; Mountford, P. *Organometallics* **2007**, *26*, 83.
279. Dubberley, S. R.; Evans, S.; Boyd, C. L.; Mountford, P. *Dalton Trans.* **2005**, 1448.
280. Walsh, P. J.; Hollander, F. J.; Bergman, R. G. *Organometallics* **1993**, *12*, 3705.
281. Nikonov, G. I.; Blake, A. J.; Mountford, P. *Inorg. Chem.* **1997**, *36*, 1107.
282. Hazari, N.; Mountford, P. *Acc. Chem. Res.* **2005**, *38*, 839.
283. Meyer, K. E.; Walsh, P. J.; Bergman, R. G. *J. Am. Chem. Soc.* **1994**, *116*, 2669.
284. Lee, S. Y.; Bergman, R. G. *Tetrahedron* **1995**, *51*, 4255.
285. Polse, J. L.; Andersen, R. A.; Bergman, R. G. *J. Am. Chem. Soc.* **1998**, *120*, 13405.
286. Krska, S. W.; Zuckerman, R. L.; Bergman, R. G. *J. Am. Chem. Soc.* **1998**, *120*, 11828.
287. Zuckerman, R. L.; Krska, S. W.; Bergman, R. G. *J. Am. Chem. Soc.* **2000**, *122*, 751.
288. Sweeney, Z. K.; Salsman, J. L.; Andersen, R. A.; Bergman, R. G. *Angew. Chem., Int. Ed.* **2000**, *39*, 2339.
289. Zuckerman, R. L.; Bergman, R. G. *Organometallics* **2001**, *20*, 1792.
290. Michael, F. E.; Duncan, A. P.; Sweeney, Z. K.; Bergman, R. G. *J. Am. Chem. Soc.* **2003**, *125*, 7184.
291. Ruck, R. T.; Zuckerman, R. L.; Krska, S. W.; Bergman, R. G. *Angew. Chem. Int. Ed.* **2004**, *43*, 5372.
292. Michael, F. E.; Duncan, A. P.; Sweeney, Z. K.; Bergman, R. G. *J. Am. Chem. Soc.* **2005**, *127*, 1752.
293. Hoyt, H. M.; Bergman, R. G. *Angew. Chem. Int. Ed.* **2007**, *46*, 5580.
294. Bashall, A.; Collier, P. E.; Gade, L. H.; McPartlin, M.; Mountford, P.; Trosch, D. J. M. *Chem. Commun.* **1998**, 2555.
295. Trosch, D. J. M.; Collier, P. E.; Bashall, A.; Gade, L. H.; McPartlin, M.; Mountford, P.; Radojevic, S. *Organometallics* **2001**, *20*, 3308.

296. Ward, B. D.; Maisse-Francois, A.; Gade, L. H.; Mountford, P. *Chem. Commun.* **2004**, 704.
297. Vujkovic, N.; Ward, B. D.; Maisse-Francois, A.; Wadepohl, H.; Mountford, P.; Gade, L. H. *Organometallics* **2007**, 26, 5522.
298. Vujkovic, N.; Fillol, J. L.; Ward, B. D.; Wadepohl, H.; Mountford, P.; Gade, L. H. *Organometallics* **2008**, 27, 2518.
299. Weitershaus, K.; Ward, B. D.; Kubiak, R.; Müller, C.; Wadepohl, H.; Doye, S.; Gade, L. H. *Dalton Trans.* **2009**, 4586.
300. Bolton, P. D.; Feliz, M.; Cowley, A. R.; Clot, E.; Mountford, P. *Organometallics* **2008**, 27, 6069.
301. Harlan, C. J.; Hascall, T.; Fujita, E.; Norton, J. R. *J. Am. Chem. Soc.* **1999**, 121, 7274.
302. Harlan, C. J.; Tunge, J. A.; Bridgewater, B. M.; Norton, J. R. *Organometallics* **2000**, 19, 2365.
303. Bennett, J. L.; Wolczanski, P. T. *J. Am. Chem. Soc.* **1994**, 116, 2179.
304. Wang, H.; Chan, H. S.; Xie, Z. *Organometallics* **2005**, 25, 3772.
305. Straub, B. F.; Bergman, R. G. *Angew. Chem., Int. Ed.* **2001**, 40, 4632.
306. Tobisch, S., *Chem. Eur. J.* **2008**, 14, 8590.
307. Tobisch, S., *Chem. Eur. J.* **2007**, 13, 4884.
308. Müller, C.; Koch, R.; Doye, S., *Chem. Eur. J.* **2008**, 14, 10430.
309. Giardello, M. A.; Conticello, V. P.; Brard, L.; Gagné, M. R.; Marks, T. J., *J. Am. Chem. Soc.* **1994**, 116, 10241.
310. Li, Y.; Marks, T. J. *J. Am. Chem. Soc.* **1998**, 120, 1757.
311. Arredondo, V. M.; McDonald, F. E.; Marks, T. J. *Organometallics* **1999**, 18, 1949.
312. Hong, S.; Tian, S.; Metz, M. V.; Marks, T. J. *J. Am. Chem. Soc.* **2003**, 125, 14768.
313. Walsh, P. J.; Hollander, F. J.; Bergman, R. G. *J. Am. Chem. Soc.* **1990**, 112, 894.
314. Casalnuovo, A. L.; Calabrese, J. C.; Milstein, D. *J. Am. Chem. Soc.* **1988**, 110, 6738.

315. Katayev, E.; Li, Y.; Odom, A. L. *Chem. Commun.* **2002**, 838.
316. Neukom, J. D.; Perch, N. S.; Wolfe, J. P. *J. Am. Chem. Soc.* **2010**, *132*, 6276.
317. Zi, G.; Zhang, F.; Xiang, L.; Chen, Y.; Fang, W.; Song, H. *Dalton Trans.* **2010**, *39*, 4048.
318. Cummins, C. C.; Baxter, S. M.; Wolczanski, P. T. *J. Am. Chem. Soc.* **1988**, *110*, 8731.
319. Cummins, C. C.; Schaller, C. P.; Duyne, G. D. V.; Wolczanski, P. T.; Chan, A. W. C.; Hoffman, R. *J. Am. Chem. Soc.* **1991**, *113*, 2985.
320. Bennet, J. L.; Wolczanski, P. T. *J. Am. Chem. Soc.* **1994**, *116*, 2179.
321. Schaller, C. P.; Cummins, C. C.; Wolczanski, P. T. *J. Am. Chem. Soc.* **1996**, *118*, 591.
322. Bennet, J. L.; Wolczanski, P. T. *J. Am. Chem. Soc.* **1997**, *119*, 10696.
323. Bashall, A.; Collier, P. E.; L. H. Gade; McPartlin, M.; Mountford, P.; Trösch, D. J. M. *Chem. Commun.* **1998**, 2555.
324. Bennet, J. L.; Vaid, T. P.; Wolczanski, P. T. *Inorg. Chim. Acta.* **1998**, *270*, 414.
325. Cundari, T. R.; Klickman, T. R.; Wolczanski, P. T. *J. Am. Chem. Soc.* **2002**, *122*, 7953.
326. Hoyt, H. M.; Michael, F. E.; Bergman, R. G. *J. Am. Chem. Soc.* **2004**, *126*, 1018.
327. Ong, T.-G.; Yap, G. P. A.; Richeson, D. S. *J. Am. Chem. Soc.* **2003**, *125*, 8100.
328. Blake, A. J.; Collier, P. E.; Dunn, S. C.; Li, W.-S.; Mountford, P.; Shishkin, O. V. *J. Chem. Soc. Dalton Trans.* **1997**, 1549.
329. Dunn, S. C.; Batsanov, A. S.; Mountford, P. *J. Chem. Soc. Chem. Commun.* **1994**, 2007.
330. Li, Y.; Banerjee, S.; Odom, A. L. *Organometallics* **2005**, *24*, 3272.
331. Beck, J. F.; Baiz, T. I.; Neshat, A.; Schmidt, J. A. R. *Dalton Trans.* **2009**, 5001.
332. Lian, B.; Spaniol, T. P.; Horrillo-Martínez, P.; Hultsch, K. C.; Okuda, J. *Eur. J. Inorg. Chem.* **2009**, 429.
333. Clark, K. M.; Ziller, J. W.; Heyduk, A. F. *Inorg. Chem.* **2010**, *49*, 2222.
334. Hermann, H.; Fillol, J. L.; Wadepohl, H.; Gade, L. H. *Organometallics* **2008**, *27*, 172.

335. Ketterer, N. A.; Ziller, J. W.; Rheingold, A. L.; Heyduk, A. F. *Organometallics* **2007**, *26*, 5330.
336. Li, Y.; Shi, Y.; Odom, A. L. *J. Am. Chem. Soc.* **2004**, *126*, 1794.
337. Bexrud, J. A.; Schafer, L. L. *Unpublished work*.
338. Rupert, B. L.; Arnold, J.; Karjete, A. *Acta. Cryst.* **2006**, *E62*, m950.
339. Hong, S.; Kawaoka, A. M.; Marks, T. J. *J. Am. Chem. Soc.* **2003**, *125*, 15878.
340. Stubbert, B. D.; Marks, T. J. *J. Am. Chem. Soc.* **2007**, *129* (14), 4253.
341. Grasa, G. A.; Zanotti-Gerosa, A.; Hems, W. P. *J. Organomet. Chem.* **2006**, *691*, 2332.
342. Turculet, L.; Tilley, T. D. *Organometallics* **2002**, *21*, 3961.
343. Turculet, L.; Tilley, T. D. *Organometallics* **2004**, *23*, 1542.
344. Delacroix, O.; Gaumont, A. C. *Curr. Org. Chem.* **2005**, *9*, 1851.
345. Waterman, R. *Curr. Org. Chem.* **2008**, *12*, 1322.
346. Waterman, R. *Dalton Trans.* **2009**, 18.
347. Roering, A. J.; Maddox, A. F.; Elrod, L. T.; Chan, S. M.; Ghebream, M. B.; Donovan, K. L.; Davidson, J. J.; Hughes, R. P.; Shalumova, T.; MacMillan, S. N.; Tanski, J. M.; Waterman, R. *Organometallics* **2009**, *28*, 573.
348. Nishiura, M.; Hou, Z.; Wakatsuki, Y.; Yamaki, T.; Miyamoto, T. *J. Am. Chem. Soc.* **2003**, *125*, 1184.
349. Nicolau, K. C.; Dai, W.-M.; Tsay, S.-C.; Estevez, V. A.; Wrasidlo, W. *Science* **1992**, *256*, 1172.

APPENDIX A. Experimental Details

A.1 General Considerations

All reactions were performed under an atmosphere of dry, oxygen free dinitrogen using a glovebox or standard Schlenk techniques unless otherwise noted. Solvents were prepared for moisture-sensitive reactions as follows: dichloromethane was distilled from calcium hydride under an atmosphere of dinitrogen; tetrahydrofuran, diethyl ether, benzene, toluene, hexanes and pentane were purified and dried by passage through a column of activated alumina and sparged with dinitrogen; d_1 -chloroform was dried over activated 4 Å molecular sieves and stored under ambient atmosphere; d_6 -benzene and d_8 -toluene were degassed by several freeze-pump-thaw cycles and dried over activated 4 Å molecular sieves for at least 24 hours before use. Solvents for non-moisture sensitive operations were used as received. ^1H and ^{13}C NMR spectra were recorded on Bruker 300 MHz, 400 MHz or 600 MHz Avance spectrometers; chemical shifts are given relative to residual *protio* solvent at 298 K unless otherwise noted. Mass spectra were recorded on either a Kratos MS-50 spectrometer using an electron impact (70 eV) source by Mr. Marshall Lapawa, or a Bruker Esquire~LC using an electrospray ionization source by Mr. David Wong. Elemental analyses were recorded on a Carlo Erba Elemental Analyzer EA 1108 by Mr. David Wong. Single crystal X-ray structure determinations were performed at the Department of Chemistry, University of British Columbia by Dr. Brian O. Patrick, Mr. Robert K. Thomson, or Mr. Neal Yonson.

A.2 Materials

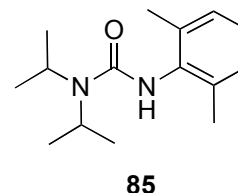
All common organic reagents, lithium metal, PhCH_2MgCl (1.0 M in diethyl ether), and $\text{Ti}(\text{NMe}_2)_4$ were purchased from Aldrich. Pyridine was distilled from sodium under dry, oxygen-free dinitrogen before use in air-sensitive reactions. Me_3SiCl was distilled under N_2 and degassed by three freeze-pump-thaw cycles. Amines, alkynes, and alkenes used in hydroamination reactions were distilled from calcium hydride before use. 1,3,5-Trimethoxybenzene was vacuum sublimed before use as an internal standard for NMR spectroscopic quantification of hydroamination products. All other reagents were used as received. $\text{Zr}(\text{NMe}_2)_4$, ZrCl_4 , $\text{Al}(i\text{-Bu})_3$, $\text{B}(\text{C}_6\text{F}_5)_3$, and $[\text{Ph}_3\text{C}][\text{B}(\text{C}_6\text{F}_5)_4]$ were purchased from Strem and used as received. Ethylene was purchased from Praxair and dried by passage through a column of anhydrous calcium chloride. Methylaluminoxane (MAO) was provided by Imperial Oil Ltd. as a 10% (w/w) solution in toluene. 2,2'-Diamino-6,6'-dimethylbiphenyl was synthesized and resolved as previously reported.¹ $\text{TiCl}_4(\text{THF})_2$,² $\text{ZrCl}_4(\text{THF})_2$,² $\text{Ti}(\text{NMe}_2)_2\text{Cl}_2$,³ $\text{Zr}(\text{CH}_2\text{Ph})_4$,⁴ and $\text{Zr}(\text{CH}_2\text{CMe}_3)_4$ ⁵ were prepared by previously reported methods.

$\text{Zr}(\text{NMe}_2)_2\text{Cl}_2(\text{DME})$: This compound was prepared using a different route to that previously published.⁶ $\text{Zr}(\text{NMe}_2)_4$ (1.00 g, 3.745 mmol) and $\text{ZrCl}_4(\text{THF})_2$ (1.41 g, 3.75 mmol) were dissolved in toluene (10 mL each) in separate flasks. The slurry of $\text{ZrCl}_4(\text{THF})_2$ was cooled to $-78\text{ }^\circ\text{C}$ prior to the addition of $\text{Zr}(\text{NMe}_2)_4$ *via* cannula. 1,2-Dimethoxyethane (1.00 mL) was subsequently added *via* syringe. The mixture was warmed to room temperature and then heated to $60\text{ }^\circ\text{C}$ for four hours. The solvent was removed *in vacuo*. The crude solid was suspended in pentane and filtered. The collected

solid was washed with several portions of pentane and subsequently dried *in vacuo* to give a pale yellow powder (2.19 g, 86% yield) that was used without further purification. ^1H NMR (C_6D_6 , 300 MHz): δ 3.14 (10H, br m, $\text{CH}_3\text{OCH}_2\text{CH}_2\text{OCH}_3$), 3.26 (12H, s, $-\text{N}(\text{CH}_3)_2$); ^{13}C NMR (C_6D_6 , 75 MHz): δ 44.8, 62.4, 72.0.

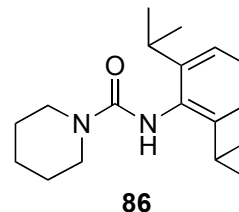
A.3 Synthesis of Urea Proligands

85: 2,6-Dimethylaniline (0.489 g, 0.500 mL, 4.03 mmol) was dissolved in dichloromethane (10 mL). The solution was cooled to 0 °C. Solid triphosgene (0.419 g, 1.41 mmol) was added in one portion and the solution stirred for 5 minutes. *N,N*-diisopropylethylamine (1.04 g, 1.40 mL, 8.06 mmol) was added and the cold bath removed. The mixture was stirred for 45 minutes. Diisopropylamine (0.407 g, 0.570 mL, 4.03 mmol) was slowly added, followed by another equivalent of *N,N*-diisopropylethylamine (0.520 g, 0.700 mL, 4.03 mmol). The mixture was stirred for an additional thirty minutes at room temperature. The solution was diluted with 1 M HCl (50 mL) and dichloromethane (30 mL). The organic phase was washed with 1 M HCl (3 \times 50 mL) and dried over MgSO_4 . Removal of the solvent gave the crude urea, which was purified by flash chromatography (1:1 hexanes/ethyl acetate) to give **85** as a white solid (0.90 g, 90% yield). Large-scale preparations were carried out in an analogous fashion, with purification by recrystallization from ethyl acetate. The compound was dried *in vacuo* for eighteen hours prior to use in protonolysis reactions. ^1H NMR (CDCl_3 , 300 MHz): δ 1.32 (12H, d, J = 6.9 Hz, $-\text{CH}(\text{CH}_3)_2$), 2.23 (3H, s, $-\text{CH}_3$), 4.02 (2H, m, J = 6.9 Hz, $-\text{CH}(\text{CH}_3)_2$), 5.57 (1H, br s, $-\text{NH}-$), 7.03 (3H, m, Ar- H); ^{13}C NMR (CDCl_3 , 75 MHz):



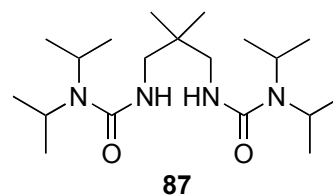
δ 19.9, 22.8, 46.7, 127.2, 129.2, 137.0, 137.6, 156.3; MS(ESI) m/z 249 ($M^+ + H$), 271 ($M^+ + Na$); HRMS m/z Calc'd for $C_{15}H_{25}N_2O$ ($M^+ + H$): 249.1967; Found: 249.1971; Anal. calcd. for $C_{15}H_{24}N_2O$: C, 72.54; H, 9.74; N, 11.28. Found: C, 72.69; H, 9.77; N, 11.47.

86: Prepared analogous to **85** using 2,6-diisopropylaniline (1.95 g, 2.08 mL, 11.0 mmol), triphosgene (1.309 g, 3.500 mmol), *N,N*-diisopropylethylamine (3.88 g, 5.25 mL, 30.0 mmol) and



piperidine (0.851 g, 0.99 mL, 10.0 mmol). White solid (2.85 g, 99% yield). 1H NMR ($CDCl_3$, 300 MHz) δ 1.19 (12H, d, $J = 6.9$ Hz, $2 \times -CH(CH_3)_2$), 1.54-1.65 (6H, m, $[-CH_2-]_3$), 3.11 (m, 2H, $J = 6.9$ Hz, $2 \times -CH(CH_3)_2$), 3.45 (4H, m, $2 \times CH_2N$), 5.70 (1H, br s, $-NH-$), 7.10-7.23 (3H, m, Ar- H); ^{13}C NMR ($CDCl_3$, 75 MHz) δ 23.8, 24.8, 26.1, 28.8, 45.9, 123.4, 127.6, 133.0, 146.6, 156.7; MS(ESI) m/z 289 ($M^+ + H$), 311 ($M^+ + Na$); HRMS m/z Calcd. for $C_{18}H_{29}N_2O$ ($M^+ + H$): 289.2280; Found: 289.2278; Anal. calcd. for $C_{18}H_{28}N_2O$: C, 74.96; H, 9.78; N, 9.71. Found: C, 75.01; H, 9.49; N, 10.00.

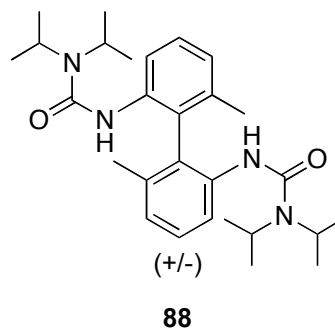
87: 2,2-Dimethyl-1,3-diaminopropane (5.00 g, 5.85 mL, 49.0 mmol) was dissolved in dichloromethane (150 mL). The solution was cooled to 0 °C prior to the addition of pyridine



(9.70 g, 9.90 mL, 122.5 mmol), followed by the addition of phenyl chloroformate (16.1 g, 12.95 mL, 103.0 mmol). The mixture was left to warm up to room temperature with stirring overnight. The reaction was quenched by the addition of 1 M HCl (100 mL).

The organic layer was separated and washed with a further portion of 1 M HCl (100 mL), brine (100 mL), and dried over MgSO₄. Removal of the solvent *in vacuo* gave a thick yellow oil, which solidified upon standing, in quantitative yield. The crude product was used in the next step without further purification. ¹H NMR (CDCl₃, 300 MHz) δ 0.97 (6H, s, 2 × -CH₃), 3.11 (4H, d, *J* = 6.9 Hz, 2 × -CH₂-), 5.95 (2H, br t, 2 × -NH), 7.15 (4H, d, *J* = 7.6 Hz, 4 × Ar-*H*_{ortho}), 7.23 (2H, t, *J* = 7.34 Hz, 2 × Ar-*H*_{para}) 7.39 (4H, m, 4 × Ar-*H*_{meta}); ¹³C NMR (CDCl₃, 75 MHz) δ 23.4, 36.8, 47.8, 121.7, 125.4, 129.4, 151.2, 156.0; MS(ESI) *m/z* 365 (M⁺ + Na). The next step was performed without the exclusion of water or air. The crude bis(phenylcarbamate) (1.11 g, 3.25 mmol) was dissolved in dimethylsulfoxide (10 mL). Diisopropylamine (0.657 g, 0.91 mL, 6.50 mmol) was added *via* syringe. The mixture was stirred overnight at room temperature, during which time a solid product precipitated. Dichloromethane (30 mL) was added to clarify the suspension. The organic phase was washed successively with water (2 × 50 mL), 1 M HCl (50 mL), water (50 mL), 1 M NaOH (50 mL), and brine (50 mL). The organic phase was dried over MgSO₄ and the solvent removed *in vacuo*. The crude product was purified by recrystallization from ethyl acetate to give **87** as white crystals (1.06 g, 92% yield). ¹H NMR (CDCl₃, 400 MHz) δ 0.83 (6H, s, -C(CH₃)₂), 1.23 (24H, d, *J* = 6.8 Hz, 4 × -CH(CH₃)₂), 2.99 (4H, d, *J* = 6.4 Hz, 2 × -CH₂-), 3.84 (4H, m, *J* = 6.8 Hz, 4 × -CH(CH₃)₂), 5.31 (2H, br t, 2 × -NH); ¹³C NMR (CDCl₃, 75 MHz) δ 22.4, 24.6, 37.6, 46.2, 47.6, 158.7; MS(ESI) *m/z* 379 (M⁺ + Na); Anal. calcd. for C₁₉H₄₀N₄O₂: C, 64.00; H, 11.31; N, 15.71. Found: C, 64.15; H, 11.29; N, 15.72.

88: Prepared analogous to **87** using 2,2'-diamino-6,6'-dimethylbiphenyl (4.20 g, 19.8 mmol), pyridine (3.91 g, 4.17 mL, 49.5 mmol), phenyl chloroformate (6.52 g, 5.24 mL, 41.6 mmol) in the first step. The bis(phenylcarbamate) was isolated as an off white solid (8.55 g, 4.78 mmol, 96% yield)

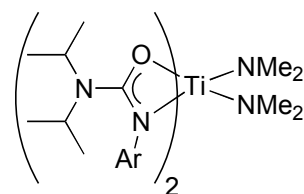


which was used in the next step without further purification. ^1H NMR (CDCl_3 , 300 MHz) δ 2.01 (6H, s, $2 \times -\text{CH}_3$), 6.48 (2H, s, $2 \times -\text{NH}-$), 7.09 (4H, d, $J = 7.8$ Hz, $4 \times \text{Ph}-\text{H}$), 7.15–7.41 (10H, m, $6 \times \text{Ph}-\text{H}$ and $4 \times \text{Ar}-\text{H}$), 8.14 (2H, d, $J = 8.17$ Hz, $2 \times \text{Ar}-\text{H}$); ^{13}C NMR (CDCl_3 , 100 MHz) δ 20.8, 118.8, 122.7, 126.8, 127.3, 130.4, 130.7, 136.7, 138.6, 151.5, 152.8; MS(ESI) m/z 475 ($\text{M}^+ + \text{Na}$). The second step was performed using bis(phenylcarbamate) (8.55 g, 18.9 mmol) and diisopropylamine (4.02 g, 5.58 mL, 39.7 mmol). The crude product was purified by recrystallization from a hexanes / ethyl acetate mixture to yield **88** as off-white crystals (7.58 g, 16.3 mmol, 86% yield). ^1H NMR (CDCl_3 , 300 MHz) δ 0.92 (12H, d, $J = 6.9$ Hz, $2 \times -\text{CH}(\text{CH}_3)_2$), 0.94 (12H, d, $J = 6.9$ Hz, $2 \times -\text{CH}(\text{CH}_3)_2$), 1.93 (6H, s, $2 \times -\text{CH}_3$), 3.75 (4H, m, $J = 6.9$ Hz, $4 \times -\text{CH}(\text{CH}_3)_2$), 6.01 (2H, s, $-\text{NH}-$), 6.95 (2H, d, $J = 7.5$ Hz, $2 \times \text{Ar}-\text{H}$), 7.24 (2H, t, $J = 7.9$ Hz, $2 \times \text{Ar}-\text{H}_{\text{meta}}$), 8.21 (2H, d, $J = 8.3$ Hz, $2 \times \text{Ar}-\text{H}$); ^{13}C NMR (CDCl_3 , 75 MHz) δ 19.9, 20.9, 21.0, 44.9, 117.8, 124.0, 129.3, 137.3, 138.4, 154.3 (one quaternary carbon not observed); MS(ESI) m/z 467 ($\text{M}^+ + \text{H}$); Anal. Calcd. for $\text{C}_{28}\text{H}_{42}\text{N}_4\text{O}_2$: C, 72.07; H, 9.07; N, 12.01. Found: C, 72.18; H, 9.00; N, 11.86.

A.4 Synthesis of Metal Complexes

A.4.1 Dichlorides (Chapter Two)

89: Urea **85** (0.400 g, 1.61 mmol) was dissolved in THF (15 mL). The resulting slurry was cooled to -78 °C. $\text{Ti}(\text{NMe}_2)_4$ (0.181 g, 0.806 mmol) in THF (5 mL) was added *via* cannula.

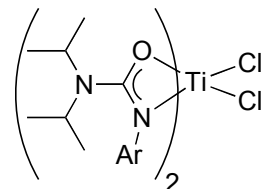


Ar = 2,6-dimethylphenyl

89

The solution was warmed to room temperature with stirring over a period of three hours. The solvent was removed *in vacuo* and the crude solid redissolved in hexanes. This solution was filtered through a bed of Celite and the solvent was removed. Recrystallization from pentane at -35 °C afforded **89** as yellow-orange crystals (0.467 g, 92% yield). ^1H NMR (C_6D_6 , 300 MHz) δ 0.62-1.67 (24H, br m, $4 \times -\text{CH}(\text{CH}_3)_2$), 2.52 (12H, s, $4 \times \text{Ar}-\text{CH}_3$), 3.10 (12H, s, $2 \times -\text{N}(\text{CH}_3)_2$), 3.46-3.74 (4H, br m, $4 \times -\text{CH}(\text{CH}_3)_2$), 6.92 (2H, t, $J = 7.3$ Hz, $2 \times \text{Ar}-\text{H}$), 7.09 (4H, d, $J = 7.4$ Hz, $4 \times \text{Ar}-\text{H}$); ^{13}C NMR (C_6D_6 , 100 MHz) δ 19.6, 20.9-23.9 (br), 46.1-47.1 (br), 47.9, 123.8, 133.6, 146.6, 166.1 (one aromatic carbon not observed); MS(EI) m/z 630 (M^+), 586 ($\text{M}^+ - \text{NMe}_2$); Anal. calcd. for $\text{C}_{34}\text{H}_{58}\text{N}_6\text{O}_2\text{Ti}$: C, 64.74; H, 9.27; N, 13.32. Found: C, 64.14; H, 9.50; N, 13.01; repeated attempts gave consistent low carbon analysis.

90: Route A: Urea **85** (0.500 g, 2.02 mmol) and $\text{Ti}(\text{NMe}_2)_2\text{Cl}_2$ were dissolved in THF (20 mL) at -78 °C. The solution was warmed to room temperature with stirring overnight.



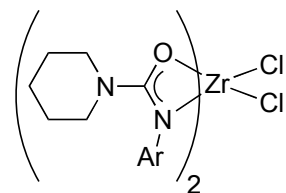
Ar = 2,6-dimethylphenyl

90

The solvent was removed *in vacuo* and the crude solid triturated with pentane. This slurry was filtered and the yellow solid collected. No further purification was required, giving **90** (0.471 g, 77% yield). Recrystallization from toluene

afforded yellow crystals used for X-ray diffraction. **Route B:** Titanium complex **89** (0.200 g, 0.317 mmol) was dissolved in THF (10 mL). The solution was cooled to -78 °C. Chlorotrimethylsilane (0.345 g, 0.400 mL, 3.17 mmol) was added *via* syringe. The cold bath was removed and the mixture stirred overnight at room temperature. The compound was isolated as described above (0.110 g, 57% yield). ^1H NMR (C_6D_6 , 300 MHz) δ 0.54 (12H, d, $J = 6.6$ Hz, $2 \times -\text{CH}(\text{CH}_3)_2$), 1.38 (12H, d, $J = 6.7$ Hz, $2 \times -\text{CH}(\text{CH}_3)_2$), 2.67 (12H, s, $4 \times \text{Ar}-\text{CH}_3$), 2.90 (2H, m, $J = 6.5$ Hz, $2 \times -\text{CH}(\text{CH}_3)_2$), 3.59 (2H, m, $J = 6.4$ Hz, $2 \times -\text{CH}(\text{CH}_3)_2$), 6.92 (2H, m, Ar- H), 7.02 (4H, m, Ar- H); ^{13}C NMR (C_6D_6 , 75 MHz) δ 18.5, 19.4, 19.8, 21.1, 21.5, 46.6, 47.2, 125.7, 128.1, 132.7, 145.9, 166.1; MS(EI) m/z 612 (M^+), 577 ($\text{M}^+ - \text{Cl}$); HRMS m/z Calcd. for $\text{C}_{30}\text{H}_{46}\text{N}_4\text{O}_2^{35}\text{Cl}_2^{48}\text{Ti}$ (M^+): 612.24773; Found: 612.24742; Anal. calcd. for $\text{C}_{30}\text{H}_{46}\text{N}_4\text{O}_2\text{Cl}_2\text{Ti}$: C, 58.73; H, 7.56; N, 9.13. Found: C, 59.22; H, 7.68; N, 9.53.

91: As above using route A from urea **86** (0.500 g, 1.74 mmol) and $\text{Zr}(\text{NMe}_2)_2\text{Cl}_2(\text{DME})$ (0.295 g, 0.868 mmol). The resulting product was **91**•THF as colourless crystals (0.499 g, 71% yield). These crystals were subject to high



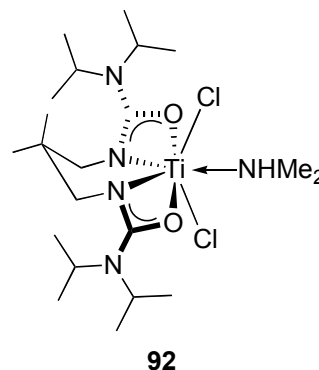
Ar = 2,6-diisopropylphenyl

91

vacuum for 48 hours to remove the THF ligand, giving **91** quantitatively. **91**•THF: ^1H NMR (C_6D_6 , 400 MHz, 345 K): δ 1.20 (12H, m), 1.21 (4H, m, H_{THF}), 1.36 (12H, d, $J = 6.8$ Hz, $\text{CH}(\text{CH}_3)_2$), 1.57 (12H, d, $J = 6.4$ Hz, $\text{CH}(\text{CH}_3)_2$), 2.55 (8H, m), 2.90 (8H, m, $\text{CH}(\text{CH}_3)_2$ and H_{THF}), 3.59 (2H, m, $J = 6.4$ Hz, $\text{CH}(\text{CH}_3)_2$), 6.92 (2H, m, Ar- H), 7.02 (4H, m, Ar- H); ^{13}C NMR (C_6D_6 , 100 MHz, 345 K) δ 24.7, 24.8, 25.9, 26.1, 26.6, 28.6, 41.5, 46.1, 124.5, 126.4, 141.8, 166.0. **91:** ^1H NMR (C_6D_6 , 300 MHz) δ 1.00-1.40 (12H,

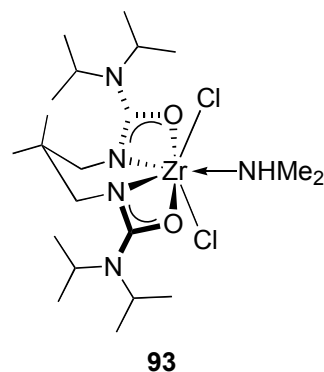
m, $2 \times (-CH_2-)_3$), 1.18 (12H, m, $2 \times CH(CH_3)_2$), 1.31 (3H, d, $J = 6.8$ Hz, $CH(CH_3)_2$), 1.37 (3H, d, $J = 7.2$ Hz, $CH(CH_3)_2$), 1.51 (3H, d, $J = 6.4$ Hz, $CH(CH_3)_2$), 1.67 (3H, d, $J = 6.4$ Hz, $CH(CH_3)_2$), 2.85 (2H, br m, $(-CH_2-)_2N-$), 2.93 (2H, br m, $(-CH_2-)_2N-$), 3.08 (4H, br m, $(-CH_2-)_2N-$), 3.43 (2H, m, $J = 6.4$ Hz, $2 \times -CH(CH_3)_2$), 4.24 (1H, m, $J = 6.8$ Hz, $-CH(CH_3)_2$), 4.34 (1H, m, $J = 6.8$ Hz, $-CH(CH_3)_2$), 6.94-7.13 (4H, m, Ar-H), 7.20-7.36 (2H, m, Ar-H); MS(EI) m/z 736 (M^+); Anal. calcd. for $C_{36}H_{54}N_4O_2Cl_2Zr$: C, 58.67; H, 7.36; N, 7.60. Found: C, 58.68; H, 7.76; N, 7.37.

92: Urea **87** (0.753 g, 2.12 mmol), and $Ti(NMe_2)_2Cl_2$ (0.437 g, 2.12 mmol) were dissolved in toluene (10 mL). The solution was heated to 65 °C with stirring for three hours. The solvent was removed and the crude solid subject to high vacuum at 65 °C overnight. The residue was recrystallized from



benzene to give **92** as yellow crystals (0.923 g, 84% yield). 1H NMR (C_6D_6 , 400 MHz) δ 1.17 (24H, d, $J = 6.8$ Hz, $4 \times -CH(CH_3)_2$), 1.28 (6H, s, $-C(CH_3)_2$), 2.91 (6H, d, $J = 6.4$ Hz, $HN(CH_3)_2$), 3.53 (4H, m, $J = 6.8$ Hz, $4 \times -CH(CH_3)_2$), 3.54 (4H, s, $2 \times -CH_2-$), 3.63 (1H, br m, $HN(CH_3)_2$); ^{13}C NMR (C_6D_6 , 100 MHz) δ 22.4, 26.9, 36.2, 42.7, 47.9, 59.3, 171.8; MS(EI) m/z 472 ($M^+ - HNMe_2$); Anal. calcd. for $C_{21}H_{45}N_5O_2Cl_2Ti$: C, 48.66; H, 8.75; N, 13.51. Found: C, 48.47; H, 8.63; N, 13.80.

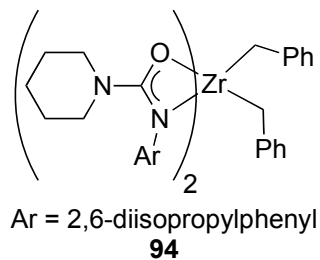
93: As above from **87** (1.00 g, 2.81 mmol), and $\text{Zr}(\text{NMe}_2)_2\text{Cl}_2(\text{DME})$ (0.955 g, 2.81 mmol). Colourless crystals (1.40 g, 89% yield). ^1H NMR (C_6D_6 , 400 MHz) δ 1.18 (24H, d, $J = 6.8$ Hz, $4 \times -\text{CH}(\text{CH}_3)_2$), 1.18 (6H, s, overlapping with previous, $-\text{C}(\text{CH}_3)_2$), 2.66 (6H, d, $J = 6.4$ Hz, $\text{HN}(\text{CH}_3)_2$), 2.97



(1H, br m, $\text{HN}(\text{CH}_3)_2$), 3.35 (4H, s, $2 \times -\text{CH}_2-$), 3.57 (4H, m, $J = 6.8$ Hz, $4 \times -\text{CH}(\text{CH}_3)_2$); ^{13}C NMR (C_6D_6 , 100 MHz) δ 22.4, 26.6, 37.0, 40.2, 47.5, 57.3, 170.1; MS(EI) m/z 516 ($\text{M}^+ - \text{HNMe}_2$); Anal. calcd. for $\text{C}_{21}\text{H}_{45}\text{N}_5\text{O}_2\text{Cl}_2\text{Zr}$: C, 44.90; H, 8.07; N, 12.47. Found: C, 45.14; H, 7.96; N, 12.49.

A.4.2 Dialkyls (Chapter Two)

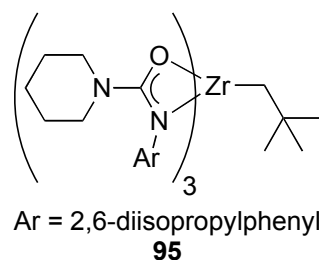
94: This reaction was performed with exclusion of ambient light. **86** (0.300 g, 1.042 mmol) and $\text{Zr}(\text{CH}_2\text{Ph})_4$ (0.237 g, 0.521 mmol) were dissolved in THF (10 mL) at -78 °C in a foil-wrapped Schlenk tube. The solution was



warmed to room temperature with stirring over a period of three hours. The solvent was removed *in vacuo* and the crude solid redissolved in hexanes. This solution was filtered through a bed of Celite and the solvent was removed. Recrystallization from pentane at -35 °C afforded **94** as colourless microcrystals (0.265 g 60% yield). ^1H NMR (C_6D_6 , 400 MHz) δ 1.02-1.48 (12H, m, $2 \times (-\text{CH}_2-)_3$), 1.11 (12H, d, $J = 7.2$ Hz, $2 \times \text{CH}(\text{CH}_3)_2$), 1.38 (12H, d, $J = 7.2$ Hz, $2 \times -\text{CH}(\text{CH}_3)_2$), 2.39 (4H, s, $\text{Zr}(\text{CH}_2\text{Ph})_2$), 2.93 (8H, br m, $2 \times (-\text{CH}_2-)_2\text{N}$), 3.16 (4H, m, $J = 6.8$ Hz, $4 \times \text{CH}(\text{CH}_3)_2$), 6.84 (2H, m, Ar-H), 7.05-7.22 (14H, m, Ar-H); ^{13}C NMR (C_6D_6 , 100 MHz) δ 24.7, 25.3, 25.8, 26.6, 28.4, 45.9, 75.4,

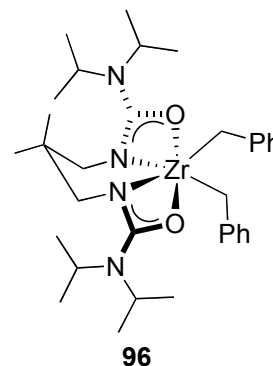
121.5, 124.6, 126.0, 128.7, 141.5, 143.9, 147.2, 166.8; MS(EI) m/z 755 ($M^+ - \text{CH}_2\text{Ph}$);
 Anal. Calcd. for $\text{C}_{50}\text{H}_{68}\text{N}_4\text{O}_2\text{Zr}$: C, 70.79; H, 8.08; N, 6.60. Found: C, 70.42; H, 8.12;
 N, 6.42.

95: This reaction was performed with exclusion of ambient
 light. **86** (0.288 g, 1.00 mmol) and $\text{Zr}(\text{CH}_2\text{CMe}_4)_4$ (0.188 g,
 0.500 mmol) were dissolved in THF (10 mL) at -78°C in a foil-
 wrapped Schlenk tube. The solution was warmed to room



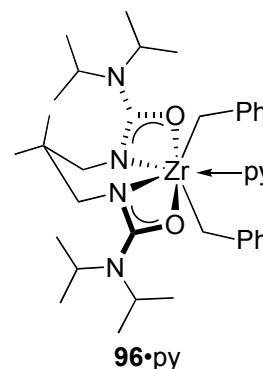
temperature with stirring over a period of three hours. The solvent was removed *in vacuo*
 and the crude solid redissolved in hexanes. This solution was filtered through a bed of
 Celite and the solvent was removed. Recrystallization from pentane at -35°C afforded a
 few colourless crystals of **95** (yield not determined). ^1H NMR (C_6D_6 , 400 MHz, 338 K)
 δ 0.93 (18H, br m, $3 \times (-\text{CH}_2-)_3$), 1.00 (27H, m, $3 \times -\text{CH}(\text{CH}_3)_2 + \text{C}(\text{CH}_3)_3$), 1.13 (18H,
 d, $J = 9.3$ Hz, $3 \times -\text{CH}(\text{CH}_3)_2$), 2.83 (12H, br m, $3 \times (-\text{CH}_2-)_2\text{N}$), 3.55 (6H, br m,
 $6 \times \text{CH}(\text{CH}_3)_2$), 7.12-7.17 (9H, m, Ar-H), neopentyl methylene protons not observed;
 ^{13}C NMR (C_6D_6 , 100 MHz, CH_2 and C determined from DEPT) δ 24.4 (CH_2), 25.1,
 25.9 (CH_2), 27.7, 34.5, 35.7 (C), 45.7 (CH_2), 81.7 (CH_2), 123.9, 124.6, 142.8 (C),
 143.6(C), 165.9(C); MS(EI) m/z 951 ($M^+ - \text{CH}_2\text{CMe}_3$); satisfactory elemental analysis
 could not be obtained due to difficulty obtaining pure material in sufficient quantity.

96: This reaction was performed with exclusion of ambient light. A foil-wrapped 20 mL scintillation vial was charged with $\text{Zr}(\text{CH}_2\text{Ph})_4$ (0.228 g, 0.500 mmol) and a Teflon-coated stir bar. A separate vial was charged with **87** (0.178 g, 0.500 mmol). Toluene was added to both vials (5 mL each) and both solutions were cooled



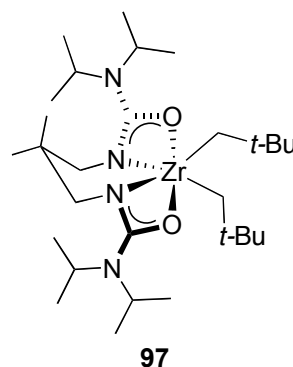
to $-35\text{ }^\circ\text{C}$. The proligand solution was added dropwise to the stirred solution of $\text{Zr}(\text{CH}_2\text{Ph})_4$. The resulting mixture was allowed to warm to room temperature with stirring overnight. The solvent was removed *in vacuo* and the crude solid redissolved in hexanes. The hexanes solution was filtered through Celite, concentrated, and cooled to $-35\text{ }^\circ\text{C}$ to give colourless microcrystals of **96** (0.245 g, 78% yield). ^1H NMR (C_6D_6 , 400 MHz) δ 0.85 (6H, s, $2 \times \text{CH}_3$), 1.27 (24H, d, $J = 6.7\text{ Hz}$, $4 \times \text{CH}(\text{CH}_3)_2$), 2.47 (4H, s, $\text{Zr}(\text{CH}_2\text{Ph})_2$), 2.94 (4H, s, $2 \times \text{CH}_2$), 3.49 (4H, sept, $J = 6.7\text{ Hz}$, $4 \times \text{CH}(\text{CH}_3)_2$), 7.05 (2H, t, $J = 7.2\text{ Hz}$, $2 \times \text{Ph-H}_{\text{para}}$), 7.39 (4H, t, $J = 8.0\text{ Hz}$, $4 \times \text{Ph-H}_{\text{meta}}$), 7.47 (4H, d, $J = 7.2\text{ Hz}$, $4 \times \text{Ph-H}_{\text{ortho}}$); ^{13}C NMR (C_6D_6 , 100 MHz, CH_2 and C determined from DEPT) δ 21.9, 24.7, 35.8 (C), 46.8, 57.1 (CH_2), 62.0 (CH_2), 121.0, 128.3, 129.0, 144.6 (C), 170.0 (C); MS(EI) m/z 535 ($\text{M}^+ - \text{CH}_2\text{Ph}$); Anal. Calcd. for $\text{C}_{33}\text{H}_{52}\text{N}_4\text{O}_2\text{Zr}$: C, 63.11; H, 8.35; N, 8.92. Found: C, 62.80; H, 8.43; N, 9.00.

96•py: This reaction was performed with exclusion of ambient light. A foil-wrapped Schlenk tube was charged with $\text{Zr}(\text{CH}_2\text{Ph})_4$ (0.639 g, 1.40 mmol) and a Teflon-coated stir bar. A separate tube was charged with **87** (0.500 g, 1.40 mmol) and pyridine (0.111 g,



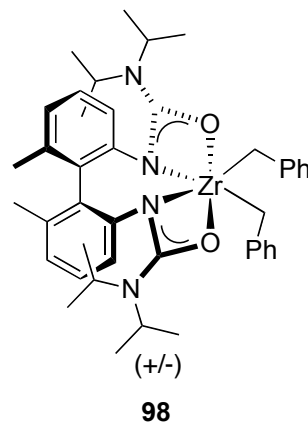
118.3 μL , 1.40 mmol). Toluene was added to both flasks (10 mL each) and the $\text{Zr}(\text{CH}_2\text{Ph})_4$ solution was cooled to $-78\text{ }^\circ\text{C}$. The proligand solution was cannula transferred to the stirred solution of $\text{Zr}(\text{CH}_2\text{Ph})_4$. The resulting mixture was allowed to warm to room temperature with stirring overnight. The solvent was removed *in vacuo* and the crude solid redissolved in hexanes. The hexanes solution was filtered through Celite, concentrated, and cooled to $-35\text{ }^\circ\text{C}$ to give orange crystals of **96**•py (0.687 g, 70% yield). ^1H NMR (C_6D_6 , 400 MHz) δ 1.08 (6H, s, $\text{C}(\text{CH}_3)_2$), 1.37 (24H, d, $J = 6.8\text{ Hz}$, $4 \times \text{CH}(\text{CH}_3)_2$), 2.14 (4H, s, $2 \times -\text{CH}_2\text{Ph}$), 3.02 (4H, s, $2 \times \text{CH}_2$), 3.73 (4H, br m, $4 \times \text{CH}(\text{CH}_3)_2$), 6.81 (2H, t, $J = 7.2\text{ Hz}$, $2 \times \text{Ph}-H_{\text{para}}$), 6.89 (2H, t, $J = 6.4\text{ Hz}$, $2 \times \text{Py}-H_{\text{meta}}$), 6.94 (4H, d, $J = 7.6\text{ Hz}$, $4 \times \text{Ph}-H_{\text{ortho}}$), 7.04 (1H, t, $J = 7.6\text{ Hz}$, $\text{Py}-H_{\text{para}}$), 7.18 (4H, t, $J = 7.6\text{ Hz}$, $4 \times \text{Ph}-H_{\text{meta}}$), 9.38 (2H, br m, $2 \times \text{Py}-H_{\text{ortho}}$); ^{13}C NMR (C_6D_6 , 100 MHz, CH_2 and C determined from DEPT) δ 22.1, 25.7, 36.1 (C), 46.7, 56.4 (CH_2), 58.3 (CH_2), 117.4, 123.7, 124.8, 127.4, 135.9, 147.9, 154.7 (C), 168.8 (C); MS(EI) m/z 535 ($\text{M}^+ - \text{py}$, CH_2Ph); Anal. Calcd. for $\text{C}_{38}\text{H}_{57}\text{N}_5\text{O}_2\text{Zr}$: C, 64.54; H, 8.12; N, 9.90. Found: C, 64.25; H, 8.28; N, 9.82.

97: This reaction was performed with exclusion of ambient light. A foil-wrapped 20 mL scintillation vial was charged with $\text{Zr}(\text{CH}_2\text{CMe}_3)_4$ (0.211 g, 0.562 mmol) and a Teflon-coated stir bar. A separate vial was charged with **87** (0.200 g, 0.562 mmol). Toluene was added to both vials (5 mL each) and both solutions were cooled to $-35\text{ }^\circ\text{C}$. The proligand solution was added dropwise to the stirred solution of $\text{Zr}(\text{CH}_2\text{CMe}_3)_4$. The resulting mixture was allowed to warm to room temperature with



stirring overnight. The solvent was removed *in vacuo* and the crude solid redissolved in pentane. The pentane solution was filtered through Celite, concentrated, and cooled to -35 °C to give colourless crystals of **97** (0.225 g, 69% yield). ¹H NMR (C₆D₆, 400 MHz) δ 0.88 (6H, 2 × CH₃), 1.23 (4H, s, Zr(CH₂CMe₃)₂), 1.36 (24H, d, *J* = 6.7 Hz, 4 × CH(CH₃)₂), 1.53 (18H, s, Zr(CH₂C(CH₃)₃), 3.12 (4H, s, 2 × CH₂N), 3.61 (4H, sept, *J* = 6.7 Hz 4 × CH(CH₃)₂); ¹³C NMR (C₆D₆, 100 MHz, CH₂ and C determined from DEPT) δ 22.1, 25.0, 34.9, 35.0 (C), 36.2 (C), 46.9, 57.5 (CH₂), 81.8 (CH₂), 170.4; MS(EI) gave no molecular ion or diagnostic fragments due to suspected instability to the ionization conditions; Anal. Calcd. for C₂₉H₆₀N₄O₂Zr: C, 59.23; H, 10.28; N, 9.53. Found: C, 59.61; H, 10.45; N, 9.52.

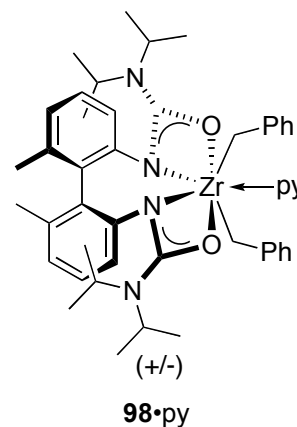
98: This reaction was performed with exclusion of ambient light. A foil-wrapped 20 mL scintillation vial was charged with Zr(CH₂Ph)₄ (0.195 g, 0.429 mmol) and a Teflon-coated stir bar. A separate vial was charged with **88** (0.200 g, 0.429 mmol). Toluene was added to both vials (5 mL each) and both solutions were cooled to -35 °C. The proligand solution was added



dropwise to the stirred solution of Zr(CH₂Ph)₄. The resulting mixture was allowed to warm to room temperature with stirring overnight. The solvent was removed *in vacuo* and the crude solid redissolved in hexanes. The hexanes solution was filtered through Celite, concentrated, and cooled to -35 °C to give pale yellow crystals of **98** (0.237 g, 75% yield). ¹H NMR (C₆D₆, 400 MHz) δ 0.67-0.85 (12H, br m, 2 × -CH(CH₃)₂), 1.30-1.52 (12H, br m, 2 × -CH(CH₃)₂), 2.13 (6H, s, 2 × Ar-CH₃), 2.41 (4H, AB q,

$J = 9.9$ Hz, $\text{Zr}(\text{CH}_2\text{Ph})_2$), 2.99 (2H, br m, $2 \times \text{CH}(\text{CH}_3)_2$), 3.97 (2H, br m, $2 \times -\text{CH}(\text{CH}_3)_2$), 6.65 (2H, d, $J = 7.7$ Hz, $2 \times \text{Ar}-\text{H}$), 7.00 (2H, d, $J = 7.4$ Hz, $2 \times \text{Ar}-\text{H}$), 7.06 (4H, d, $J = 7.5$ Hz, $4 \times \text{Ph}-H_{\text{ortho}}$), 7.21-7.34 (8H, m, $2 \times \text{Ar}-\text{H} + 4 \times \text{Ph}-H_{\text{meta}} + 2 \times \text{Ph}-H_{\text{para}}$); ^{13}C NMR (C_6D_6 , 100 MHz, CH_2 and C determined from DEPT) δ 19.7, 65.3 (CH_2), 119.9, 121.8, 124.6, 127.2, 128.7, 128.8, 132.1 (C), 137.0 (C), 143.9 (C), 145.3 (C), 168.3 (C), broad resonances (δ 15-50) for the isopropyl carbons are not assigned; MS(EI) gave no molecular ion or diagnostic fragments due to suspected instability to the ionization conditions; Anal. Calcd. for $\text{C}_{42}\text{H}_{54}\text{N}_4\text{O}_2\text{Zr}$: C, 68.34; H, 7.37; N, 7.59. Found: C, 68.56; H, 7.77; N, 7.36.

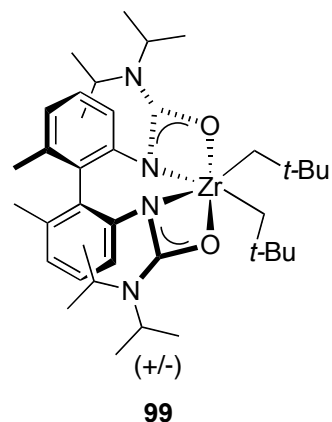
98•py: This reaction was performed with exclusion of ambient light. A foil-wrapped Schlenk tube was charged with $\text{Zr}(\text{CH}_2\text{Ph})_4$ (0.195 g, 0.429 mmol) and a Teflon-coated stir bar. A separate tube was charged with **88** (0.200 g, 0.429 mmol) and pyridine (0.039 g, 36.1 μL , 0.43 mmol). Toluene was added to both flasks (10 mL each) and the $\text{Zr}(\text{CH}_2\text{Ph})_4$ solution was cooled



to -78 $^{\circ}\text{C}$. The proligand solution was cannula transferred to the stirred solution of $\text{Zr}(\text{CH}_2\text{Ph})_4$. This resulting mixture was allowed to warm to room temperature with stirring overnight. The solvent was removed *in vacuo* and the crude solid redissolved in hexanes. The hexanes solution was filtered through Celite, concentrated, and cooled to -35 $^{\circ}\text{C}$ to give orange crystals of **98•py** (0.171 g, 49% yield). ^1H NMR (C_6D_6 , 400 MHz) δ 0.85-0.92 (12H, br m, $2 \times \text{CH}(\text{CH}_3)_2$), 1.47-1.55 (12H, br m, $2 \times \text{CH}(\text{CH}_3)_2$), 1.95 (2H, d, $J = 8.6$ Hz, $\text{Zr}-\text{CH}_2\text{Ph}$), 2.06 (2H, d, $J = 8.6$ Hz, $\text{Zr}-\text{CH}_2\text{Ph}$), 2.27 (6H, s,

2 × Ar-CH₃), 3.10 (2H, br m, 2 × CH(CH₃)₂), 4.23 (2H, br m, 2 × CH(CH₃)₂), 6.49 (4H, m, 4 × Ar-H), 6.77 (4H, m, 4 × Ar-H), 7.00 (7H, m, 7 × Ar-H), 7.07 (2H, d, *J* = 7.3 Hz, 2 × Ar-H), 7.16 (2H, t, *J* = 7.6 Hz, 2 × Ar-H), 8.94 (2H, br m, 2 × Py-H_{ortho}); ¹³C NMR (C₆D₆, 100 MHz, CH₂ and C determined from DEPT) δ 18.2, 20.0, 21.1, 21.6, 23.1, 45.6, 48.4, 61.9 (CH₂), 118.2, 119.1, 123.8, 124.5, 124.7, 127.2, 127.3, 132.1 (C), 137.1 (C), 146.4 (C), 168.8 (C), two pyridine carbons not observed; MS(EI) *m/z* 645 (M⁺ - py, CH₂Ph); Anal. Calcd. for C₄₇H₅₉N₅O₂Zr: C, 69.08; H, 7.28; N, 8.57. Found: C, 69.32; H, 7.31; N, 8.58.

99: This reaction was performed with exclusion of ambient light. A foil-wrapped 20 mL scintillation vial was charged with Zr(CH₂CMe₃)₄ (0.161 g, 0.429 mmol) and a Teflon-coated stir bar. A separate vial was charged with **88** (0.200 g, 0.429 mmol). Toluene was added to both vials (5 mL each) and both solutions were cooled to -35 °C. The

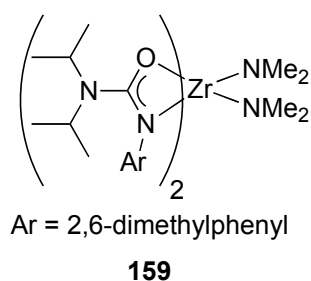


proligand solution was added dropwise to the stirred solution of Zr(CH₂CMe₃)₄. The resulting mixture was allowed to warm to room temperature with stirring overnight. The solvent was removed *in vacuo* and the crude solid redissolved in pentane. The pentane solution was filtered through Celite, concentrated, and cooled to -35 °C to give colourless leaf crystals of **99** (0.161 g, 54% yield); the crystal morphology was not conducive to X-ray diffraction analysis. ¹H NMR (C₆D₆, 400 MHz) δ 0.70-0.88 (12H, br m, 2 × CH(CH₃)₂), 1.42 (18H, s, Zr(CH₂C(CH₃)₃)₂), 1.45 (4H, AB q, *J* = 12.2 Hz, Zr(CH₂CMe₃)₂), 1.57-1.68 (12H, br m, 2 × -CH(CH₃)₂), 2.11 (6H, s, 2 × Ar-CH₃), 3.12

(2H, br m, $2 \times \text{CH}(\text{CH}_3)_2$), 4.06 (2H, br m, $2 \times -\text{CH}(\text{CH}_3)_2$), 6.96 (4H, m, $4 \times \text{Ar}-\text{H}$), 7.09 (2H, t, $J = 7.7$ Hz, $2 \times \text{Ar}-\text{H}$); ^{13}C NMR (C_6D_6 , 100 MHz) δ 18.3 (br), 19.7, 20.9 (br), 21.8 (br), 22.9 (br), 34.7, 35.1, 45.8 (br), 47.9 (br), 85.5, 119.8, 124.5, 126.9, 132.1, 137.0, 145.1, 168.0; MS(EI) m/z 625 ($\text{M}^+ - \text{CH}_2\text{CMe}_3$); Anal. Calcd. for $\text{C}_{38}\text{H}_{62}\text{N}_4\text{O}_2\text{Zr}$: C, 65.37; H, 8.95; N, 8.03. Found: C, 65.31; H, 9.19; N, 7.99.

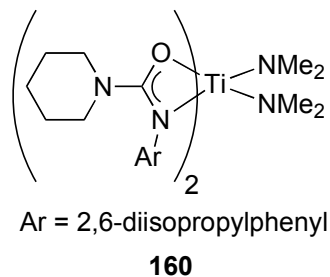
A.4.3 Bis(amido)s (Chapter Three, Chapter Five)

159: Urea **85** (0.400 g, 1.61 mmol) and $\text{Zr}(\text{NMe}_2)_4$ (0.215 g, 0.806 mmol) were dissolved in THF (15 mL) at -78°C . The solution was warmed to room temperature with stirring over a period of three hours. The solvent was removed *in vacuo* and



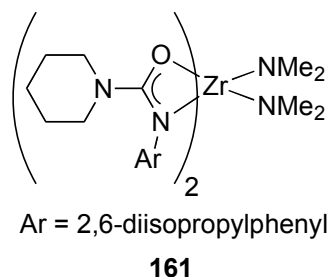
the crude solid redissolved in hexanes. This solution was filtered through a bed of Celite and the solvent was removed. Recrystallization from pentane at -35°C gave colourless crystals of **159** (0.505 g, 93% yield). ^1H NMR (C_6D_6 , 300 MHz) δ 0.52–0.81 (12H, br m, $2 \times -\text{CH}(\text{CH}_3)_2$), 1.31–1.62 (12H, br m, $2 \times -\text{CH}(\text{CH}_3)_2$), 2.50 (12H, s, $4 \times \text{Ar}-\text{CH}_3$), 2.94 (12H, s, $2 \times -\text{N}(\text{CH}_3)_2$), 3.60–3.80 (4H, br m, $4 \times -\text{CH}(\text{CH}_3)_2$), 6.91 (2H, t, $J = 6.9$ Hz, $\text{Ar}-\text{H}$), 7.06 (4H, d, $J = 7.8$ Hz, $\text{Ar}-\text{H}$); ^{13}C NMR (C_6D_6 , 75 MHz) δ 19.5, 21.2–22.6 (br), 43.3, 46.8 (br), 123.8, 128.5, 133.1, 145.7, 166.2; MS(EI) m/z 672 ($[\text{M}]^+$), 628 ($[\text{M} - \text{NMe}_2]^+$); Anal. calcd. for $\text{C}_{34}\text{H}_{58}\text{N}_6\text{O}_2\text{Zr}$: C, 60.58; H, 8.67; N, 12.47. Found: C, 60.28; H, 9.06; N, 12.37.

160: Urea **86** (2.078 g, 7.22 mmol) was dissolved in THF (15 mL). The resulting slurry was cooled to -78 °C. Ti(NMe₂)₄ (0.808 g, 3.61 mmol) in THF (5 mL) was added *via* cannula. The solution was warmed to room temperature



with stirring over a period of three hours. The solvent was removed *in vacuo* and the crude solid redissolved in hexanes. This solution was filtered through a bed of Celite and the solvent was removed. Recrystallization from pentane at -35°C afforded orange crystals of **160** (1.966 g, 77% yield). ¹H NMR (C₆D₆, 300 MHz) δ 1.15 (12H, d, *J* = 5.5 Hz, 2 × CH(CH₃)₂), 1.36 (12H, d, *J* = 5.2 Hz, 2 × CH(CH₃)₂), 1.39–1.46 (12H, m, 2 × (–CH₂–)₃), 2.98–3.06 (8H, m, 2 × (–CH₂–)₂N–), 3.21 (12H, s, 2 × N(CH₃)₂), 3.65–3.72 (4H, m, 4 × CH(CH₃)₂), 7.17–7.22 (6H, m, Ar–H); MS(EI) *m/z* 666 ([M – NMe₂]⁺), 622 ([M – 2 × NMe₂]⁺); HRMS *m/z* Calcd. for C₃₈H₆₀N₅O₂⁴⁸Ti ([M – NMe₂]⁺): 666.42265; Found: 666.42313; Anal. calcd. for C₄₀H₆₆N₆O₂Ti: C, 67.58; H, 9.36; N, 11.82. Found: C, 67.87; H, 9.73; N, 12.20.

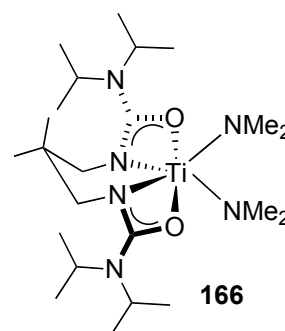
161: Urea **86** (1.000 g, 3.47 mmol) and Zr(NMe₂)₄ (0.464 g, 1.735 mmol) were dissolved in THF (15 mL) at -78 °C. The solution was warmed to room temperature with stirring over a period of three hours. The solvent was



removed *in vacuo* and the crude solid redissolved in hexanes. This solution was filtered through a bed of Celite and the solvent removed. The crude solid was recrystallized from pentane at -35 °C to give colourless crystals of **161** (0.940 g, 72% yield). ¹H NMR (C₆D₆, 300 MHz) δ 1.02–1.11 (12H, m, 2 × (–CH₂–)₃), 1.35 (12H, d, *J* = 6.9 Hz,

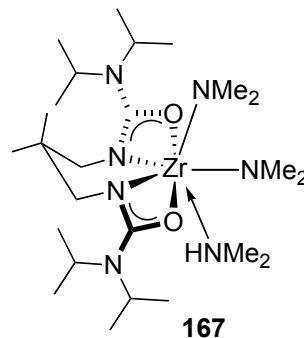
2 × CH(CH₃)₂), 1.48 (12H, d, *J* = 6.8 Hz, 2 × CH(CH₃)₂), 2.98 (12H, s, 2 × N(CH₃)₂), 3.04 (8H, m, 2 × (–CH₂–)₂N–), 3.72 (4H, m, *J* = 6.84 Hz, 4 × CH(CH₃)₂), 7.13–7.23 (6H, m, Ar–H); ¹³C NMR (C₆D₆, 75 MHz) δ 24.1, 24.4, 24.8, 25.7, 26.0, 27.5, 27.9, 42.7, 45.2, 123.5, 124.0, 124.5, 142.3, 142.8, 143.1, 165.5; MS(EI) *m/z* 752 ([M]⁺), 708 ([M – NMe₂]⁺), 664 ([M⁺ – 2 × NMe₂]⁺); Anal. calcd. for C₄₀H₆₆N₆O₂Zr: C, 63.70; H, 8.82; N, 11.14. Found: C, 63.31; H, 8.83; N, 10.93.

166: A 20 mL vial was charged with **87** (0.300 g, 0.843 mmol). This solid was suspended in ~2 mL of hexanes prior to the addition of and Ti(NMe₂)₄ (0.189 g, 0.843 mmol) in hexanes (~2 mL). The suspension was clarified with shaking and gentle heating. Once dissolution was complete, the sealed vial



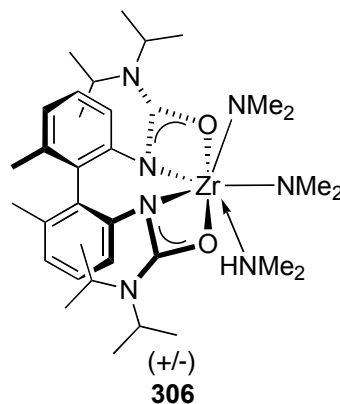
was left to stand at room temperature for several hours, during which time crystals formed. The solution was cooled to –35 °C overnight before decantation of the mother liquor. The red crystals were dried under vacuum to remove residual solvent to give **166** (0.349 g, 84%). ¹H NMR (C₆D₆, 400 MHz, 368 K) δ 0.90 (6H, s, –C(CH₃)₂), 1.26 (24H, br s, 4 × –CH(CH₃)₂), 3.08 (4H, s, 2 × CH₂), 3.39 (12H, br s, 2 × –N(CH₃)₂), 3.56 (4H, br m, 4 × –CH(CH₃)₂); ¹³C NMR (C₆D₆, 100 MHz) δ 22.2 (CH₃), 24.9 (CH₃), 36.3 (C), 46.7 (CH₃), 48.4 (CH), 58.1 (CH₂), 169.9 (CO). MS(EI) *m/z* 490 ([M]⁺), 446 ([M – NMe₂]⁺); Anal. calcd. for C₂₃H₅₀N₆O₂Ti: C, 56.31; H, 10.27; N, 17.13. Found: C, 56.66; H, 9.93; N, 16.84.

167: A 20 mL vial was charged with **87** (0.300 g, 0.843 mmol), and $\text{Zr}(\text{NMe}_2)_4$ (0.225 g, 0.843 mmol). These solids were dissolved in ~3 mL of hexanes with shaking and gentle heating, resulting in a colour change from colourless to light yellow. Once dissolution was complete, the sealed vial was



left to stand at room temperature for several hours, during which time crystals formed. The solution was cooled to $-35\text{ }^\circ\text{C}$ overnight before decantation of the mother liquor. The light yellow crystals were dried under slight vacuum to remove residual solvent to give **167** (0.625 g, 96% yield). ^1H NMR (C_6D_6 , 400 MHz) δ 0.94 (6H, s, $-\text{C}(\text{CH}_3)_2$), 1.25 (24H, d, $J = 6.80\text{ Hz}$, $4 \times -\text{CH}(\text{CH}_3)_2$), 3.01 (18H, br s, $2 \times -\text{N}(\text{CH}_3)_2$, $\text{HN}(\text{CH}_3)_2$), 3.12 (4H, s, $2 \times \text{CH}_2$), 3.52 (4H, m, $J = 6.80\text{ Hz}$, $4 \times -\text{CH}(\text{CH}_3)_2$); ^{13}C NMR (C_6D_6 , 75 MHz) δ 22.7 (CH_3), 25.7 (CH_3), 37.0 (C), 43.5 (br, $\text{N}(\text{CH}_3)_2$), 47.1 (CH), 57.8 (CH_2), 169.6 (CO). MS(EI) m/z 533 ($[\text{M} - \text{HNMe}_2]^+$), 488 ($[\text{M} - \text{HNMe}_2, \text{NMe}_2]^+$); Anal. calcd. for $\text{C}_{25}\text{H}_{57}\text{N}_7\text{O}_2\text{Zr}$: C, 51.86; H, 9.92; N, 16.93. Found: C, 51.83; H, 9.66; N, 16.73.

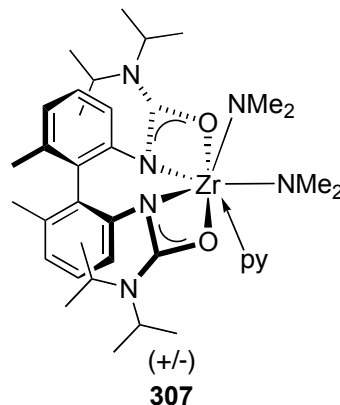
306: A small vial was charged with a Teflon-coated stir bar, **12** (1.00 g, 2.15 mmol), and $\text{Zr}(\text{NMe}_2)_4$ (0.573 g, 2.15 mmol). Hexanes (10 mL) was quickly added to the stirring solids, resulting in the release of a gas. The suspension was stirred with heating until all solids dissolved. The stir bar was then removed and the vial sealed and left to stand at room



temperature for several hours. The solvent was removed *in vacuo* to give an off-white powder (1.224 g, 83% yield) of **313**, which was used for catalytic experiments without

further purification. The compound was recrystallized from pentane to give an analytically pure sample. ^1H NMR (C_6D_6 , 400 MHz): δ 0.88 (6H, br m, $-\text{CH}(\text{CH}_3)_2$), 0.96 (6H, br m, $-\text{CH}(\text{CH}_3)_2$), 1.60 (12H, br m, $2 \times -\text{CH}(\text{CH}_3)_2$), 2.10 (6H, br s, $\text{HN}(\text{CH}_3)_2$), 2.16 (6H, s, $2 \times \text{Ar}-\text{CH}_3$), 3.13 (2H, br m, $2 \times -\text{CH}(\text{CH}_3)_2$), 3.36 (12H, br s, $2 \times \text{Zr}-\text{N}(\text{CH}_3)_2$), 4.26 (2H, br m, $2 \times -\text{CH}(\text{CH}_3)_2$), 6.79 (2H, d, $J = 7.6$ Hz, $2 \times \text{Ar}-\text{H}$), 6.93 (2H, d, $J = 7.6$ Hz, $2 \times \text{Ar}-\text{H}$), 7.15 (2H, t, $J = 7.6$ Hz, $2 \times \text{Ar}-\text{H}$); ^{13}C NMR (C_6D_6 , 100 MHz, C determined from DEPT) δ 18.4 (br), 20.0, 21.1 (br), 21.3 (br), 22.6 (br), 38.7 (br), 44.5, 45.2 (br), 48.2 (br), 117.9, 122.4, 126.7, 132.0 (C), 137.1 (C), 148.5 (C), 168.4 (C); MS(EI) m/z 642 ($\text{M}^+ - \text{HNMe}_2$); Anal. calcd. for $\text{C}_{34}\text{H}_{59}\text{N}_7\text{O}_2\text{Zr}$: C, 59.26; H, 8.63; N, 14.23. Found: C, 59.32; H, 8.32; N 14.05.

307: A small vial was charged with a Teflon-coated stir bar, 12 (0.250 g, 0.536 mmol), and $\text{Zr}(\text{NMe}_2)_4$ (0.143 g, 0.536 mmol). In a separate vial, pyridine (50.8 mg, 54.2 μL , 0.643 mmol) was dissolved in 3 mL of hexanes. This hexanes solution was quickly added to the stirring solids, resulting in the release of a gas and a colour change from colourless to

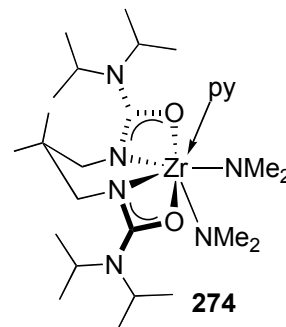


orange. The suspension was stirred with heating until all solids dissolved. The stir bar was then removed and the vial sealed and left to stand at room temperature for several hours, during which time crystals formed. The solution was cooled to -35°C overnight before decantation of the mother liquor. The yellow crystals were dried under slight vacuum to remove residual solvent to give 0.280 g (72 % yield) of the pyridine adduct. These crystals were subject to X-ray diffraction for structure determination. ^1H NMR

(C₆D₆, 300 MHz): δ 0.83 (6H, d, J = 6.2 Hz, $-\text{CH}(\text{CH}_3)_2$), 0.85 (6H, d, J = 6.3 Hz, $-\text{CH}(\text{CH}_3)_2$), 1.48 (6H, d, J = 6.8 Hz, $-\text{CH}(\text{CH}_3)_2$), 1.52 (6H, d, J = 6.7 Hz, $-\text{CH}(\text{CH}_3)_2$), 2.10 (6H, s, $2 \times \text{Ar}-\text{CH}_3$), 3.03 (2H, m, J = 6.0 Hz, $2 \times -\text{CH}(\text{CH}_3)_2$), 3.30 (12H, br s, $2 \times -\text{N}(\text{CH}_3)_2$), 4.21 (2H, m, J = 6.0 Hz, $2 \times -\text{CH}(\text{CH}_3)_2$), 6.45 (2H, br d, $2 \times \text{Ar}-\text{H}$), 6.64 (2H, m, $2 \times \text{py}-H_{\text{meta}}$), 6.82 (2H, d, J = 7.3 Hz, $2 \times \text{Ar}-\text{H}$), 6.94 (3H, m, $2 \times \text{Ar}-\text{H} + \text{py}-H_{\text{para}}$), 8.45 (2H, br d, $2 \times \text{py}-H_{\text{ortho}}$); ¹³C NMR (C₆D₆, 75 MHz) δ 18.3, 19.9, 21.0, 21.2, 22.5, 44.4, 45.0, 48.1, 117.8, 121.8, 123.2, 126.4, 131.9, 135.3, 136.7, 148.7, 149.9, 168.6. MS(EI) m/z 642 ($\text{M}^+ - \text{py}$); Satisfactory elemental analysis could not be obtained due to partial loss of the pyridine ligand during sample preparation.

A.4.4 Catalytic Model Compounds (Chapter Four)

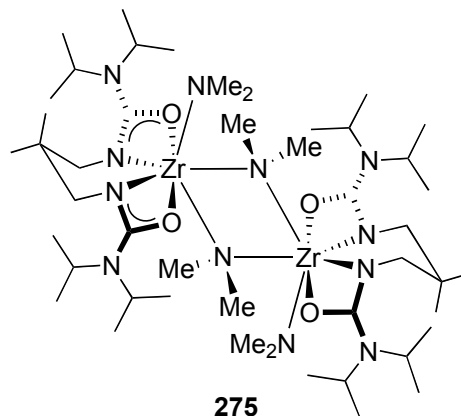
274: **167** (0.200 g, 0.346 mmol) was treated with pyridine (0.0301 g, 35.7 μL , 0.381 mmol) in ~2 mL of pentane. The solution was clarified with shaking and gentle heat, and then left to stand for several hours, during which time crystals formed. The solution was cooled to -35°C overnight before decantation of



the mother liquor, giving **274** (0.179 g, 84%). These crystals were subject to X-ray diffraction for structure determination, and to slight vacuum prior to combustion analysis. ¹H NMR (C₆D₆, 300 MHz): δ 0.94 (6H, s, $-\text{C}(\text{CH}_3)_2$), 1.28 (24H, d, J = 6.70 Hz, $4 \times -\text{CH}(\text{CH}_3)_2$), 3.00 (12H, br s, $2 \times -\text{N}(\text{CH}_3)_2$), 3.24 (4H, s, $2 \times -\text{CH}_2-$), 3.60 (4H, m, J = 6.70 Hz, $4 \times -\text{CH}(\text{CH}_3)_2$), 6.69 (2 H, m, $2 \times \text{Py}-H_{\text{meta}}$), 6.97 (1 H, m, $\text{Py}-H_{\text{para}}$), 8.61 (2 H, br d, $2 \times \text{Py}-H_{\text{ortho}}$); ¹³C NMR (C₆D₆, 75 MHz) δ 22.1 (CH₃), 25.3 (CH₃), 36.5 (C), 43.3 (br, N(CH₃)₂), 46.4 (CH), 57.2 (CH₂), 123.2, 135.3, 150.0, 168.3 (CO); MS(EI) m/z

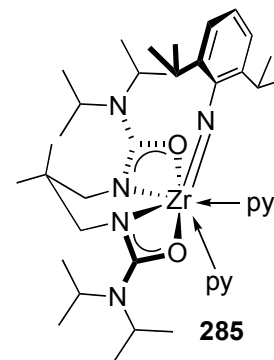
533 ($M^+ - \text{py}$), 488 ($M^+ - \text{NMe}_2$); Anal. calcd. for $\text{C}_{28}\text{H}_{55}\text{N}_7\text{O}_2\text{Zr}$: C, 54.86; H, 9.04; N, 15.99. Found: C, 54.54; H, 9.00; N, 15.72.

275: **274** was prepared as above using **87** (0.750 g, 2.107 mmol), $\text{Zr}(\text{NMe}_2)_4$ (0.563 g, 2.11 mmol) and pyridine (0.183 g, 2.32 mmol) in 5 mL of hexanes. After crystallization, **274** was subject to high vacuum for 48 hours to completely remove pyridine, giving **275** (1.033 g, 92%). This



compound was recrystallized from hot toluene for X-ray structure determination. ^1H NMR (C_6D_6 , 400 MHz) δ 0.93 (6H, s, $-\text{C}(\text{CH}_3)_2$), 1.25 (24H, d, $J = 6.80$ Hz, $4 \times -\text{CH}(\text{CH}_3)_2$), 3.04 (12H, br s, $2 \times -\text{N}(\text{CH}_3)_2$), 3.11 (4H, s, $2 \times -\text{CH}_2-$), 3.51 (4H, m, $J = 6.80$ Hz, $4 \times -\text{CH}(\text{CH}_3)_2$); ^{13}C NMR (C_6D_6 , 75 MHz) δ 22.6 (CH_3), 25.7 (CH_3), 37.1 (C), 43.7 (br, $\text{N}(\text{CH}_3)_2$), 47.0 (CH), 57.6 (CH_2), 169.4 (CO). MS(EI) m/z 488 ($[\text{LZrNMe}_2]^+$ or $[\text{LZrNMe}_2]_2^{2+}$); Anal. calcd. for $\text{C}_{46}\text{H}_{100}\text{N}_{12}\text{O}_4\text{Zr}$: C, 51.74; H, 9.44; N, 15.74. Found: C, 51.62; H, 9.28; N, 15.46.

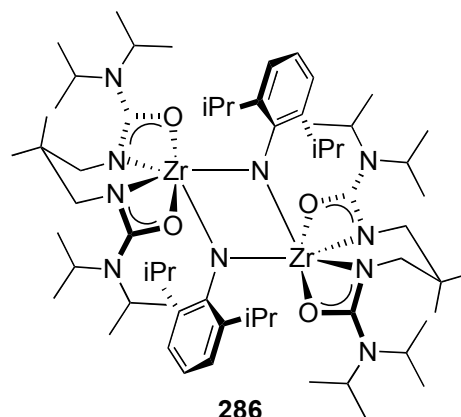
285: **96** (0.100 g, 0.159 mmol), 2,6-diisopropylaniline (0.0282 g, 30.1 μL , 0.159 mmol), and pyridine (0.0497 g, 53.0 μL , 0.637 mmol) were dissolved in hexanes with gentle heating. The solution was left to stand at room temperature overnight, during which time orange crystals of **10** formed. Yield: 0.079 g (64%).



^1H NMR (C_6D_6 , 400 MHz, excess pyridine added) δ 0.93 (3H, s, CH_3), 1.21 (12H, d,

$J = 6.6$ Hz, $2 \times \text{CH}(\text{CH}_3)_2$), 1.51 (12H, d, $J = 6.5$ Hz, $2 \times \text{CH}(\text{CH}_3)_2$), 1.57 (15H, d and obscured s, $J = 6.9$ Hz, $2 \times \text{CH}(\text{CH}_3)_2$ and CH_3), 3.43 (2H, d, $J = 11.6$ Hz, CH_2), 3.65 (2H, d, $J = 11.6$ Hz, CH_2), 3.82 (4H, sept, $J = 6.7$ Hz, $4 \times \text{CH}(\text{CH}_3)_2$), 4.74 (2H, sept, $J = 6.9$ Hz, $2 \times \text{CH}(\text{CH}_3)_2$), 6.79 (4H, m, $4 \times \text{Py-H}$), 6.83 (1H, t, $J = 7.4$ Hz, $\text{Ar-H}_{\text{para}}$), 7.11 (4H, br m, $4 \times \text{Py-H}$), 7.26 (2H, d, $J = 7.6$ Hz, $2 \times \text{Ar-H}_{\text{meta}}$), 8.60 (4H, br m, $4 \times \text{Py-H}_{\text{ortho}}$); ^{13}C NMR (C_6D_6 , 100 MHz, CH_2 and C assigned from DEPT, excess pyridine added): δ 22.4, 22.7, 25.7, 27.1, 27.4, 37.2 (C), 46.2, 57.7 (CH_2), 113.7, 121.4, 123.5, 135.5, 142.1 (C), 150.1, 154.7 (C), 164.2 (C); MS(EI) m/z 620 ($\text{M}^+ - 2 \text{ py}$); Anal. Calcd. for $\text{C}_{41}\text{H}_{65}\text{N}_7\text{O}_2\text{Zr}$: C, 63.20; H, 8.41; N, 12.58. Found: C, 62.97; H, 8.23; N, 12.65.

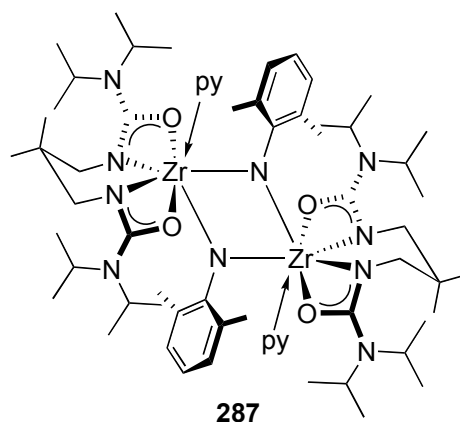
286: **96** (0.100 g, 0.159 mmol) and 2,6-diisopropylaniline (0.0282 g, 30.1 μL , 0.159 mmol) were dissolved in hexanes with gentle heating. The solution was left to stand at room temperature overnight, during which time colourless crystals of **286** formed. Yield: 0.060 g (61%).



^1H NMR (C_6D_6 , 400 MHz, 298 K) δ 0.67 (3H, s, CH_3), 0.78 (3H, s, CH_3), 1.05-1.45 (24H, br m, $4 \times \text{CH}(\text{CH}_3)_2$), 1.67 (12H, br m, $2 \times \text{CH}(\text{CH}_3)_2$), 2.80 (2H, br m, CH_2), 3.00 (2H, br d, $J = 12$ Hz, CH_2), 3.42 (4H, br m, $4 \times \text{CH}(\text{CH}_3)_2$), 4.38 (2H, br m, $2 \times \text{CH}(\text{CH}_3)_2$), 7.13 (1H, t, $J = 7.6$ Hz, $\text{Ar-H}_{\text{para}}$), 7.44 (2H, d, $J = 7.6$ Hz, $2 \times \text{Ar-H}_{\text{meta}}$); ^1H NMR (C_6D_6 , 400 MHz, 343 K) δ 0.72 (6H, br s, $2 \times \text{CH}_3$), 1.24 (24H, br m, $4 \times \text{CH}(\text{CH}_3)_2$), 1.61 (12H, d, $J = 6.8$ Hz, $2 \times \text{CH}(\text{CH}_3)_2$), 2.90 (4H, br m, $2 \times \text{CH}_2$), 3.49

(4H, sept, $J = 6.8$ Hz, $4 \times \text{CH}(\text{CH}_3)_2$), 4.34 (2H, sept, $J = 6.8$ Hz, $2 \times \text{CH}(\text{CH}_3)_2$), 7.04 (1H, t, $J = 7.6$ Hz, $\text{Ar}-H_{\text{para}}$), 7.37 (2H, d, $J = 7.6$ Hz, $2 \times \text{Ar}-H_{\text{meta}}$); ^{13}C NMR (C_6D_6 , 100 MHz, 298 K, CH_2 and C assigned from DEPT): δ 20.8 (br), 22.6 (br), 23.7 (br), 24.0, 26.0, 27.4 (br), 38.4 (C), 47.2 (br), 57.0 (br, CH_2), 118.4, 121.9, 153.1 (C), two quaternary carbons not observed; ^{13}C NMR (C_6D_6 , 100 MHz, 343 K): δ 21.0-22.8 (br), 24.1, 28.5 (br), 38.3, 47.2, 57.1, 118.4, 121.9, 138.1, 153.2, 170.0; MS(EI) m/z 1240 (M^+), 620 (LZrNAr^+); Anal. Calcd. for $\text{C}_{62}\text{H}_{110}\text{N}_{10}\text{O}_4\text{Zr}_2$: C, 59.95; H, 8.93; N, 11.28. Found: C, 60.08; H, 8.85; N, 11.22.

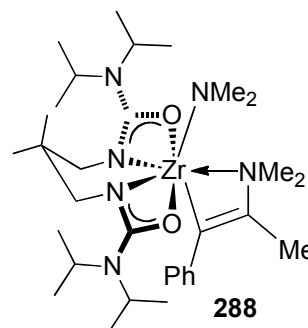
287: **274** was prepared as above in a Schlenk tube using **87** (0.400 g, 1.124 mmol), $\text{Zr}(\text{NMe}_2)_4$ (0.300 g, 1.124 mmol) and pyridine (0.089 g, 94.6 μL , 1.124 mmol) in 5 mL of hexanes. Once the solids had dissolved, 2,6-dimethylaniline (0.1360 g, 138.9 μL , 1.124 mmol) and pyridine (0.1776 g,



189.2 μL , 2.248 mmol) were added. The flask was sealed and the headspace evacuated. The solution was stirred at 65 °C for one hour prior to the removal of the solvent under vacuum. The residue was triturated with pentane and filtered to give an off-white solid. The filtrate was concentrated and filtered again to give 0.465 g (64%) of **287**. The product was recrystallized from hexanes / toluene for X-ray structure determination. ^1H NMR (C_6D_6 , 300 MHz) δ 0.71 (6H, s, $-\text{C}(\text{CH}_3)_2$), 1.19 (24H, d, $J = 6.19$ Hz, $4 \times -\text{CH}(\text{CH}_3)_2$), 2.88 (10H, s, $2 \times -\text{CH}_2-$ and $2 \times \text{Ar}-\text{CH}_3$), 3.42 (4H, m, $J = 6.17$ Hz, $4 \times -\text{CH}(\text{CH}_3)_2$), 6.62 (2H, t, $J = 5.78$ Hz, $2 \times \text{Py}-H_{\text{meta}}$), 6.81 (1H, t, $J = 7.25$ Hz,

Ar- H_{para}), 6.91 (1H, t, $J = 7.30$ Hz, Py- H_{para}), 7.29 (2H, d, $J = 7.13$ Hz, $2 \times$ Ar- H_{meta}), 8.51 (2H, br d, $2 \times$ Py- H_{ortho}); ^{13}C NMR (C_6D_6 , 150 MHz) δ 21.7, 22.6, 25.7, 38.1, 47.5, 56.6, 117.0, 123.4, 127.3, 128.9, 129.0, 136.3, 150.9, 156.9, 169.7; MS(EI) m/z 1128 ($\text{M}^+ - 2 \text{ py}$); Anal. calcd. for $\text{C}_{64}\text{H}_{104}\text{N}_{12}\text{O}_4\text{Zr}_2$: C, 59.68; H, 8.14; N, 13.05. Found: C, 59.35; H, 8.14; N, 12.96.

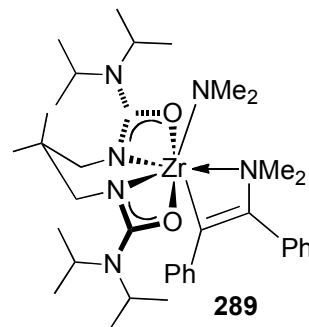
288: **167** (0.100 g, 0.173 mmol) and 1-phenyl-1-propyne (0.0401 g, 43.3 μL , 0.346 mmol) were dissolved in 1 mL of benzene. The solution was heated to 100 $^\circ\text{C}$ for sixteen hours prior to solvent removal under vacuum. The residue was recrystallized from pentane at -35 $^\circ\text{C}$ to give 0.078 g (69%) of



288. ^1H NMR (C_7D_8 , 400 MHz) δ 0.77 (3H, s, CH_3), 1.09 (3H, s, CH_3), 1.22 (12H, d, $J = 8.0$ Hz, $2 \times \text{CH}(\text{CH}_3)_2$), 1.24 (12H, d, $J = 8.0$ Hz, $2 \times \text{CH}(\text{CH}_3)_2$), 1.66 (3H, s, $[\text{Zr}]-\text{C}(\text{Ph})=\text{C}(\text{CH}_3)(\text{NMe}_2)$), 2.81 (6H, s, $\text{C}=\text{C}(\text{CH}_3)(\text{N}(\text{CH}_3)_2)$), 3.07 (4H, AB q, $J = 10.0$ Hz, $2 \times \text{Me}_2\text{C}(\text{CH}_2)\text{N}$), 3.29 (6H, s, $[\text{Zr}]-\text{N}(\text{CH}_3)_2$), 3.57 (4H, sept, $J = 8.0$ Hz, $4 \times -\text{CH}(\text{CH}_3)_2$), 6.93 (3H, m, $3 \times \text{Ph}-H$), 7.24 (2H, m, $2 \times \text{Ph}-H$); ^{13}C NMR (C_7D_8 , 100 MHz, CH_2 and C determined from DEPT) δ 6.5, 21.8, 22.1, 22.2, 27.0, 36.3 (C), 43.6, 45.4, 46.3, 57.3 (CH_2), 121.4, 124.8, 127.3, 145.6 (C), 149.8 (C), 168.5 (C), 182.2 (C); MS(EI) m/z 648 (M^+), 604 ($[\text{LZr}-\text{C}(\text{Ph})=\text{C}(\text{Me})(\text{NMe}_2)]^+$), 488 ($[\text{LZrNMe}_2]^+$); Anal. calcd. for $\text{C}_{32}\text{H}_{58}\text{N}_6\text{O}_2\text{Zr}$: C, 59.12; H, 8.99; N, 12.93. Found: C, 59.31; H, 8.91; N, 12.76.

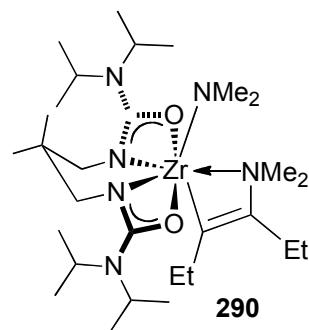
289: As above from **167** (0.100 g, 0.173 mmol) and diphenylacetylene (0.062 g, 0.35 mmol). Yield: 0.070 g, (57%).

^1H NMR (C_7D_8 , 400 MHz) δ 0.83 (3H, s, CH_3), 1.16 (3H, s, CH_3), 1.25 (12H, d, $J = 6.7$ Hz, $2 \times \text{CH}(\text{CH}_3)_2$), 1.28 (12H, d, $J = 6.7$ Hz, $2 \times \text{CH}(\text{CH}_3)_2$), 2.92 (6H, s, $\text{C}=\text{C}(\text{CH}_3)(\text{N}(\text{CH}_3)_2)$), 3.17 (4H, AB q, $J = 11.2$ Hz, $2 \times \text{Me}_2\text{C}(\text{CH}_2)\text{N}$), 3.32 (6H, s, $[\text{Zr}]-\text{N}(\text{CH}_3)_2$), 3.61 (4H, sept, $J = 6.7$ Hz, $4 \times -\text{CH}(\text{CH}_3)_2$), 6.75 (1H, t, $J = 7.3$ Hz, $1 \times \text{Ph}-\text{H}$), 6.90 (2H, d, $J = 7.9$ Hz, $2 \times \text{Ph}-\text{H}$), 6.96 (1H, t, $J = 7.3$ Hz, $1 \times \text{Ph}-\text{H}$), 7.02-7.09 (4H, m, $4 \times \text{Ph}-\text{H}$), 7.26 (2H, d, $J = 6.8$ Hz, $2 \times \text{Ph}-\text{H}$); ^{13}C NMR (C_7D_8 , 100 MHz, CH_2 and C determined from DEPT) δ 21.8, 21.9, 22.3, 27.2, 36.4 (C), 44.9, 45.3, 46.3, 57.5 (CH_2), 121.7, 125.7, 126.3, 127.0, 127.4, 130.8, 135.2 (C), 148.3 (C), 149.4 (C), 168.5 (C), 183.4 (br, C); MS(EI) m/z 710 (M^+), 666 ($[\text{LZr}-\text{C}(\text{Ph})=\text{C}(\text{Ph})(\text{NMe}_2)]^+$), 488 ($[\text{LZrNMe}_2]^+$); Anal. calcd. for $\text{C}_{37}\text{H}_{60}\text{N}_6\text{O}_2\text{Zr}$: C, 62.40; H, 8.49; N, 11.80. Found: C, 62.76; H, 8.52; N, 11.55.



290: **167** (0.100 g, 0.173 mmol) and 3-hexyne (0.142 g, 197 μL , 1.73 mmol) were dissolved in 0.8 mL of benzene. The solution was heated to 100 $^\circ\text{C}$ for 24 hours prior to solvent removal under vacuum. The residue was recrystallized from pentane at -35 $^\circ\text{C}$ to give 0.059 g (56%) of **290**. ^1H NMR

(C_6D_6 , 400 MHz) δ 1.01 (3H, s, CH_3), 1.27 (3H, t, $J = 7.6$ Hz, CH_2CH_3), 1.32 (24H, m, $4 \times \text{CH}(\text{CH}_3)_2$), 1.35 (3H, s, CH_3), 1.40 (3H, t, $J = 7.6$ Hz, CH_2CH_3), 2.24 (2H, q, $J = 7.6$ Hz, CH_2CH_3), 2.55 (2H, q, $J = 7.6$ Hz, CH_2CH_3), 2.87 (6H, s,



C=C(CH₃)(N(CH₃)₂)), 3.27 (2H, d, J = 11.2 Hz, Me₂C(CH₂)N), 3.42 (2H, d, J = 11.2 Hz, Me₂C(CH₂)N), 3.51 (6H, s, [Zr]–N(CH₃)₂), 3.67 (4H, sept, J = 6.8 Hz, 4 × –CH(CH₃)₂); ¹³C NMR (C₆D₆, 100 MHz, CH₂ and C determined from DEPT) δ 15.2 (CH₂), 16.3, 16.8, 21.9, 22.1, 22.6, 26.7, 27.6, 36.7 (C), 44.6, 45.8, 46.3, 57.9 (CH₂), 152.4 (C), 168.9 (C), 184.2 (C); MS(EI) m/z 614 (M⁺), 570 ([LZr–C(Et)=C(Et)(NMe₂)]⁺), 488 ([LZrNMe₂]⁺); Anal. calcd. for C₂₉H₆₀N₆O₂Zr: C, 56.54; H, 9.82; N, 13.64. Found: C, 56.20; H, 10.14; N, 13.85.

A.5 Procedure for Ethylene Polymerization Reactions (Chapter Two)

A.5.1 Dichloride Precatalysts (90, 91)

A 250 mL Schlenk flask was charged with toluene (50 mL), MAO (0.580 g, 10 % w/w in toluene, 10.0 mmol), and a Teflon-coated stirbar. The headspace was briefly evacuated and refilled with dry ethylene gas five times. Afterward, the flow of ethylene was maintained, with the stirring rate set at 750 rpm. A solution of the precatalyst in toluene (1.00 mL, 0.0100 M, 10.0 μmol) was added *via* syringe. The mixture was stirred for 20 minutes at either room temperature or 65 °C before the addition of 10 % HCl (v/v) in methanol (~100 mL). If a polymer precipitate appeared, the suspension was filtered. The residue was washed with methanol and dried *in vacuo* before weight determination.

A.5.2 Dibenzyl Precatalysts (94, 96, 98)

A 250 mL Schlenk flask was charged with toluene (50 mL), triisobutylaluminum (1.00 mL, 0.200 M, 200.0 μmol), and a Teflon-coated stirbar. The headspace was briefly evacuated and refilled with dry ethylene gas five times. Afterward, the flow of ethylene

was maintained, with the stirring rate set at 750 rpm. A solution of the precatalyst in toluene (1.00 mL, 0.0100 M, 10.0 μ mol) and a solution of the the co-catalyst activator, either $[\text{Ph}_3\text{C}][\text{B}(\text{C}_6\text{F}_5)_4]$ or $\text{B}(\text{C}_6\text{F}_5)_3$, in toluene (1.00 mL, 0.0100 M, 10.0 μ mol) were added *via* syringe. The mixture was stirred for 20 minutes at either room temperature or 65 °C before the addition of 10 % HCl (v/v) in methanol (~100 mL). If a polymer precipitate appeared, the suspension was filtered. The residue was washed with methanol and dried *in vacuo* before weight determination.

A.6 Procedure for Hydroamination Catalysis (Chapter Three)

A.6.1 Intramolecular Reactions

The precatalyst (0.0375 mmol) and the aminoalkene (0.375 mmol) were dissolved with gentle heating in 0.500 mL of either d_6 -benzene or d_8 -toluene in a small vial. Once dissolution was complete, the solution was transferred to a J. Young NMR tube. ^1H NMR spectroscopy revealed that no background reaction due to brief heating had occurred. The tube was heated to the appropriate temperature in an oil bath and monitored by ^1H NMR spectroscopy. For screening experiments, the conversion after four hours was estimated by ^1H NMR spectroscopy.

For substrate scope experiments (using precatalyst **167**), once >95% conversion was achieved, or the reaction was judged to have stopped due to prolonged inactivity, the yield was determined. For isolated compounds, the NMR tube was opened and the contents diluted with either dichloromethane or hexanes to quench the reaction. The amines were purified by flash chromatography on silica gel using a solvent system of dichloromethane/methanol/ammonium hydroxide (secondary amine products) or 0.5-2%

isopropylamine in hexanes (tertiary amine products). Those compounds isolated as the *p*-toluenesulfonamide were treated with 3.3 equivalents of tosyl chloride and 1.3 equivalents of triethylamine in dichloromethane prior to chromatography using a hexanes/ethyl acetate solvent system. For those products with NMR yields, an internal standard (1,3,5-trimethoxybenzene) was used to quantify the amine product by relative integration. The aromatic signal of the internal standard was used in all cases, as the methyl resonance often overlapped with product signals. In order to ensure accuracy, multiple product signals were compared where possible. All yields reported are the average of at least two experiments.

A.6.2 Intermolecular Reactions

Complex **167** (21.7 mg, 0.0375 mmol), the amine (0.750 mmol), the alkyne (0.375 mmol) and 1,3,5-trimethoxybenzene (0.500 M in C₆D₆, 125 μ L, 0.0625 mmol) were dissolved with gentle heating in 350 μ L of *d*₆-benzene. Once dissolution was largely complete, the slurry was transferred to a J. Young NMR tube. ¹H NMR spectroscopy revealed that no background reaction due to brief heating had occurred. The tube was heated to 100 °C, 110 °C, or 145 °C and monitored by ¹H NMR spectroscopy. NMR yields were determined as described above. For the synthesis of **178** and **179**, the ratio of amine to alkyne was reversed, (0.350 mmol amine to 0.750 mmol alkyne). This was observed to have a positive effect on reaction rate for these cases.

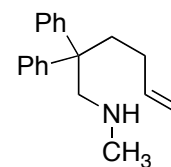
To obtain isolated yields of the products **174-179**, the following general procedure was applied. After completion of the hydroamination step, the reaction solution was diluted with dichloromethane to a volume of ~5 mL. Sodium triacetoxyborohydride

(160 mg, 0.75 mmol) and acetic acid (0.40 mL, 0.75 mmol) were added. The suspension was stirred overnight. The reaction was quenched by dilution with dichloromethane to a volume of ~15 mL and addition of 15 mL of 1 M NaOH. The phases were separated and the aqueous layer extracted with two further portions of dichloromethane. The combined organic phase was dried over MgSO₄ and filtered. After removal of the solvent, the resulting tertiary amine products were purified by column chromatography (0.5-2% isopropylamine in hexanes).

A.6.3 Aminoalkene Substrate Synthesis

The following compounds were prepared according to literature procedures: **131**,⁷ **170**,⁸ **172**,⁹ 2,2-diphenyl-hex-4-en-1-amine (*E/Z* mixture),⁷ 2-(cyclohex-2-enyl)-2,2-diphenylethanamine,¹⁰ hex-5-en-1-amine,¹¹ 1-phenylhex-5-en-1-amine,¹² 2,2-dimethyl-hex-5-en-1-amine,¹¹ 2,2-dimethyl-hept-6-en-1-amine,¹¹ **150**,¹³ [1-(pent-4-en-1-yl)cyclohexyl]methanamine,¹³ 2,2-diphenyl-hept-6-en-1-amine,¹⁴ [2-(but-3-en-1-yl)phenyl]methanamine,¹³ (2H-1,3-benzodioxol-5-ylmethyl)(2,2-diphenylpent-4-en-1-yl)amine,¹⁵ 4-methanamine-4-methyl-hepta-1,6-diene,¹⁶ [1-(prop-2-en-1-yl)cyclopentyl]-methanamine,¹⁷ and [1-(prop-2-en-1-yl)cyclohexyl]methanamine.¹⁸

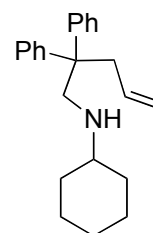
(2,2-Diphenylhex-5-en-1-yl)(methyl)amine: Prepared from 2,2-diphenyl-hex-5-en-1-amine (5.04 g, 20.1 mmol) by the method used previously to synthesize (2,2-diphenylpent-4-en-1-yl)(methyl)amine.⁹



Yield: 4.65 g (87%). ¹H NMR (CDCl₃, 300 MHz): δ 0.55 (1H, br s, NH), 1.84 (2H, m, -CH₂CH₂C(Ph)₂-), 2.34-2.40 (2H, m, =CHCH₂-), 2.42 (3H, s, -NH(CH₃)), 3.26 (2H, s,

–C(Ph)₂CH₂N–), 5.02 (2H, m, CH₂=CH–), 5.84 (1H, m, CH₂=CH–), 7.23-7.40 (10H, 10 × Ar–H); ¹³C NMR (CDCl₃, 75 MHz, CH₃, CH₂, CH, and C assigned from DEPT): δ 29.0 (CH₂), 36.8 (CH₂), 37.6 (CH₃), 50.5 (C), 59.3 (CH₂), 114.4 (CH₂), 126.2 (CH), 128.2 (CH), 139.2 (CH), 147.1 (C); MS(ESI): *m/z* 266 ([M + H]⁺); Anal. calcd. for C₁₉H₂₃N: C, 85.99; H, 8.74; N, 5.28. Found: C, 85.85; H, 8.78; N, 5.18.

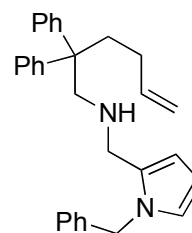
***N*-(2,2-diphenylpent-4-en-1-yl)cyclohexanamine:** 2,2-Diphenyl-pent-4-en-1-amine (1.00 g, 4.17 mmol) and cyclohexanone (0.41 g, 0.43 mL, 4.2 mmol) were dissolved in 10 mL of 1,2-dichloroethane. Sodium triacetoxyborohydride (1.77 g, 8.33 mmol) was added. The suspension was stirred for 5 minutes before the addition of acetic acid (0.25 g, 0.24 mL, 4.17 mmol). The solution was stirred overnight at 50 °C. The organic phase was poured into 50 mL of 1 M NaOH and stirred until the evolution of gas ceased. The aqueous phase was extracted with 3 × 50 mL of dichloromethane. The organic phase was dried over MgSO₄, and the solvent removed. The resulting solid was triturated with 10 mL of hexanes to give 0.82 g of the cyclohexylsubstituted amine. The hexanes wash was cooled to –30 °C for several days, during which time 0.29 g of the compound crystallized, giving a combined yield of 83%. The solid was dissolved in hexanes and dried over activated 4 Å molecular sieves before use in hydroamination experiments. ¹H NMR (CDCl₃, 300 MHz): δ 0.47 (1H, br s, N–H), 0.77-1.32 (6H, m, –CH₂CH₂CH₂–), 1.56-1.78 (4H, m, –CH₂CH(N)CH₂–), 2.30 (1H, m, –CH₂CH(N)CH₂–), 3.04 (2H, d, *J* = 7.0 Hz, =CHCH₂C(Ph)₂–), 3.21 (2H, s, –C(Ph)₂CH₂NH(Cy)), 5.00 (2H, m, CH₂=CH–), 5.40 (1H, m, CH₂=CH–), 7.18-7.32 (10H, m, 10 × Ar–H); ¹³C NMR (C₆D₆, 75 MHz, CH₂, CH, and



C assigned from DEPT): δ 25.2 (CH₂), 26.4 (CH₂), 33.8 (CH₂), 41.7 (CH₂), 50.1 (C), 53.4 (CH₂), 57.5 (CH), 117.7 (CH₂), 126.0 (CH), 128.0 (CH), 128.3 (CH), 135.2 (CH), 147.2 (C); HRMS calcd. for C₂₃H₃₀N ([M + H]⁺): 320.2378. Found: 320.2372.

[(1-Benzyl-1H-pyrrol-2-yl)methyl](2,2-diphenylhex-5-en-1-yl)amine:

2,2-diphenyl-hex-5-en-1-amine (0.323 g, 1.29 mmol) and 1-benzyl-pyrrole-2-carboxaldehyde (0.238 g, 1.29 mmol) were dissolved in 5 mL of dichloromethane. Sodium triacetoxyborohydride (0.547 g, 2.58 mmol) was added. The suspension was stirred for 5 minutes before the addition of acetic acid (0.077 g, 0.08 mL, 1.29 mmol). The solution was stirred overnight. The organic phase was poured into 25 mL of 1 M NaOH and stirred until the evolution of gas ceased. The aqueous phase was extracted with 3 × 25 mL of dichloromethane. The organic phase was dried over MgSO₄, and the solvent removed. The oil was purified by flash chromatography (96:2:2 DCM/MeOH/NH₄OH) to give 0.385 g (71%) of the secondary amine. The compound was dissolved in hexanes and dried over CaH₂ before use in hydroamination experiments. ¹H NMR (CDCl₃, 300 MHz): δ 0.70 (1H, br s, NH), 1.67 (2H, m, -CH₂CH₂C(Ph)₂-), 2.27 (2H, m, =CHCH₂-), 3.25 (2H, s, C(Ph)₂CH₂NH-), 3.60 (2H, s, -CH₂NHCH₂Ar), 4.93 (2H, m, CH₂=CH-), 5.14 (2H, s, -NCH₂Ph), 5.78 (1H, m, CH₂=CH-), 6.02 (1H, m, Ar-H), 6.10 (1H, m, Ar-H), 6.64 (1H, m, Ar-H), 6.97 (2H, m, Ph-H), 7.15-7.31 (13H, m, 13 × Ph-H); ¹³C NMR (CDCl₃, 75 MHz, CH₂ and C assigned from DEPT): δ 28.7 (CH₂), 36.3 (CH₂), 46.5 (CH₂), 50.3 (C), 50.4 (CH₂), 55.5 (CH₂), 106.9, 108.6, 114.2 (CH₂), 122.4, 126.1, 126.6, 127.3, 128.1, 128.2, 128.7, 131.2

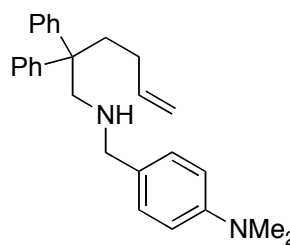


(C), 139.1 (C), 139.3, 147.3 (C); HRMS calcd. for $C_{30}H_{33}N_2$ ($[M + H]^+$): 421.2644.

Found: 421.2654.

4-[(2,2-diphenylhex-5-en-1-yl)amino]methyl}-N,N-dimethylaniline:

2,2-diphenyl-hex-5-en-1-amine (0.405 g, 1.61 mmol) and 4-dimethylaminobenzaldehyde (0.215 g, 1.61 mmol) were dissolved in 5 mL of dichloromethane. Sodium triacetoxyborohydride (0.682 g, 3.22 mmol) was added. The suspension was



stirred for 5 minutes before the addition of acetic acid (0.097 g, 0.09 mL, 1.61 mmol). The solution was stirred overnight. The organic phase was poured into 25 mL of 1 M NaOH and stirred until the evolution of gas ceased. The aqueous phase was extracted with 3×25 mL of dichloromethane. The organic phase was dried over $MgSO_4$, and the solvent removed. The oil was purified by flash chromatography (99:0.5:0.5 DCM/MeOH/ NH_4OH) to give 0.514 g (86%) of the secondary amine. The compound was dissolved in hexanes and dried over CaH_2 before use in hydroamination experiments.

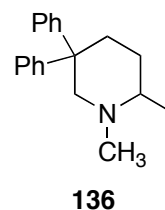
1H NMR ($CDCl_3$, 600 MHz): δ 0.78 (1H, br s, NH), 1.68 (2H, m, $-CH_2CH_2C(Ph)_2-$), 2.32 (2H, m, $=CHCH_2-$), 2.93 (6H, s, $-N(CH_3)_2$), 3.20 (2H, s, $-C(Ph)_2CH_2NH-$), 3.64 (2H, s, $-CH_2NHCH_2Ar$), 4.92 (2H, m, $CH_2=CH-$), 5.77 (1H, m, $CH_2=CH-$), 6.68 (2H, d, $J = 6.0$ Hz, $2 \times Ar-H_{ortho-to-NMe_2}$), 7.09 (2H, d, $J = 6.0$ Hz, $2 \times Ar-H_{meta-to-NMe_2}$), 7.18 (6H, m, $6 \times Ph-H$), 7.26 (4H, m, $4 \times Ph-H$); ^{13}C NMR (C_6D_6 , 150 MHz, CH_2 and C assigned from DEPT): δ 28.6 (CH_2), 36.3 (CH_2), 40.8, 50.2 (C), 53.5 (CH_2), 55.1 (CH_2), 112.6, 114.0 (CH_2), 125.8, 127.9, 128.1, 128.71, 139.3, 147.2 (C), 149.7 (C), one quaternary

carbon not observed; HRMS calcd. for $C_{27}H_{33}N_2$ ($[M + H]^+$): 385.2644. Found: 385.2636.

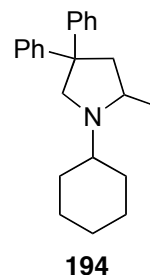
A.6.4 Product Characterization

The following hydroamination products are known compounds: **134**,⁸ **151**,¹³ **171**,¹⁹ **173**,⁹ **174**,²⁰ **175**,²⁰ **176**,²⁰ **177**,²⁰ **179**,²⁰ **180**,²¹ **181**,²¹ **185**,²² **186** (*N*-tosyl derivative),¹⁰ **187** (commercially available), **188** (*trans*-isomer,²³ *cis*-isomer²⁴), **189**,¹¹ **190**,¹¹ **192**,¹⁴ **193** (*N*-tosyl derivative),¹² **195**,¹⁵ **308**,¹⁶ **309**,¹⁷ and **310**.¹⁸ Confirmation of the identity of **183a**,²⁵ **183b**,²⁶ **184a**,²⁷ and **184b**,²⁸ was accomplished by NMR spectroscopic comparison with previously reported analogues containing two fewer carbons in the alkyl chain. The identity of **191** was similarly established by NMR spectroscopic comparison to known azepanes **151**,¹³ **190**,¹¹ and **192**.¹⁴

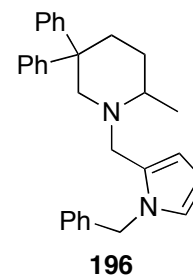
136: 1H NMR ($CDCl_3$, 400 MHz): δ 1.12 (3H, d, $J = 6.0$ Hz, $-CH_3$), 1.36 (1H, m, ring CH_2) 1.62 (1H, m, ring CH_2), 2.11 (1H, br m, ring CH_2), 2.24 (1H, td, $J = 12.0$ Hz, 6.0 Hz, ring CH_2), 2.37 (3H, s, NCH_3), 2.41 (1H, d, $J = 12.0$ Hz, ring CH_2), 2.52 (1H, m, ring CH_2), 3.58 (1H, m, ring CH), 7.20 (2H, t, $J = 6.0$ Hz, $2 \times Ph-H_{para}$), 7.29-7.36 (6H, m, $2 \times Ph-H_{ortho}$, $4 \times Ph-H_{meta}$) 7.52 (2H, d, $J = 6.0$ Hz $2 \times Ph-H_{ortho}$); ^{13}C NMR ($CDCl_3$, 100 MHz, CH_2 and C assigned from DEPT): δ 19.7, 31.0 (CH_2), 35.1 (CH_2), 43.2, 46.7 (C), 59.0, 66.0 (CH_2), 125.3, 125.8, 126.7, 127.7, 128.1, 128.8, 146.9 (C), 149.0 (C); HRMS calcd. for $C_{19}H_{24}N$ ($[M + H]^+$): 266.1909. Found: 266.1904.



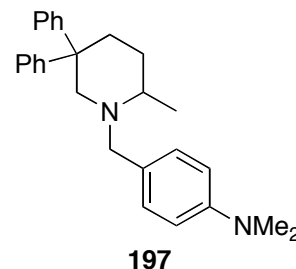
194: ^1H NMR (CDCl_3 , 400 MHz): δ 1.07 (3H, d, $J = 6.2$ Hz, $-\text{CH}_3$), 1.31-1.45 (5H, m, $-\text{CH}_2\text{CH}_2\text{CH}_2-$), 1.54 (1H, m, Cy- H), 1.75 (1H, br m, Cy- H), 1.91 (2H, br m, Cy- H), 2.02 (1H, br m, ring CH_2), 2.25 (1H, dd, $J = 12.5, 5.7$ Hz $-\text{C}(\text{Ph})_2\text{CH}_2\text{CH}(\text{CH}_3)-$), 2.66 (1H, m, $-\text{CH}_2\text{CH}(\text{N})\text{CH}_2-$), 2.92 (1H, dd, $J = 12.6, 8.2$ Hz, ring CH_2), 3.19 (1H, d, $J = 9.5$ Hz, $-\text{C}(\text{Ph})_2\text{CH}_2\text{N}(\text{Cy})-$), 3.27 (1H, m, $-\text{C}(\text{Ph})_2\text{CH}_2\text{CH}(\text{CH}_3)-$), 3.93 (1H, d, $J = 9.5$ Hz, $-\text{C}(\text{Ph})_2\text{CH}_2\text{N}(\text{Cy})-$), 7.23 (1H, m, Ph- H), 7.27 (1H, m, Ph- H), 7.32-7.41 (6H, m, $8 \times \text{Ph-}H$), 7.48 (2H, d, $J = 7.3$ Hz, $2 \times \text{Ph-}H_{\text{ortho}}$); ^{13}C NMR (CDCl_3 , 100 MHz, CH_2 and C assigned from DEPT): δ 21.1, 25.8 (CH_2), 26.3 (CH_2), 26.7 (CH_2), 27.1 (CH_2), 33.4 (CH_2), 47.2 (CH_2), 52.6 (C), 55.1, 58.5, 60.6 (CH_2), 125.6, 126.0, 127.4, 127.7, 128.1, 128.4, 149.3 (C), 150.2 (C); HRMS calcd. for $\text{C}_{23}\text{H}_{30}\text{N}$ ($[\text{M} + \text{H}]^+$): 320.2378. Found: 320.2377.



196: ^1H NMR (CDCl_3 , 400 MHz): δ 1.05 (3H, d, $J = 6.0$ Hz, $-\text{CH}_3$), 1.50 (1H, m, ring CH_2), 1.74 (1H, m, ring CH_2), 2.25 (1H, m, ring CH_2), 2.56 (3H, br m, ring CH_2), 3.06 (1H, d, $J = 12$ Hz, NCH_2Ar), 3.59 (1H, m, ring CH), 3.84 (1H, d, $J = 12.0$ Hz, NCH_2Ar), 4.99 (1H, d, $J = 12.0$ Hz, NCH_2Ph), 5.33 (1H, d, $J = 12.0$ Hz, NCH_2Ph), 6.20 (1H, m, Ar- H), 6.24 (1H, m, Ar- H), 6.81 (1H, m, Ar- H), 6.97 (2H, d, $J = 6.0$ Hz, $2 \times \text{Ph-}H$), 7.14- 7.25 (6H, m, $6 \times \text{Ph-}H$), 7.25-7.41 (6H, m, $6 \times \text{Ph-}H$); ^{13}C NMR (CDCl_3 , 100 MHz, CH_2 and C assigned from DEPT): δ 17.4 (br), 31.3 (CH_2), 33.9 (br, CH_2), 46.4 (C), 50.0 (CH_2), 50.3 (CH_2), 56.5 (br), 59.2 (br, CH_2), 107.1, 110.9, 122.5, 125.5, 125.8, 126.3, 127.2, 128.0, 128.2, 128.8, 129.2 (C), 139.3 (C), 147.1 (br, C), 148.3 (br, C); HRMS calcd. for $\text{C}_{30}\text{H}_{33}\text{N}_2$ ($[\text{M} + \text{H}]^+$): 421.2644. Found: 421.2633.



197: ^1H NMR (CDCl_3 , 400 MHz): δ 1.32 (3H, d, $J = 6.1$ Hz, $-\text{CH}_3$), 1.54 (1H, m, ring CH_2), 1.78 (1H, m, ring CH_2), 2.34 (1H, m, ring CH_2), 2.60 (3H, m, ring CH_2), 3.12 (6H, s, $-\text{N}(\text{CH}_3)_2$), 3.26 (1H, d, $J = 13.0$ Hz, NCH_2Ar), 3.56 (1H, m, ring CH), 4.15 (1H, d, $J = 13.0$ Hz, NCH_2Ar), 6.92 (2H, d, $J = 8.6$ Hz, $2 \times \text{Ar-H}$), 7.24-7.43 (12H, m, $10 \times \text{Ph-H}$, $2 \times \text{Ar-H}$); ^{13}C NMR (CDCl_3 , 100 MHz, CH_2 and C assigned from DEPT): δ 18.9 (br), 31.4 (CH_2), 34.6 (CH_2), 41.1, 46.9 (C), 56.2 (CH_2), 58.4 (CH_2), 60.9 (CH_2), 112.7, 125.5, 125.9, 127.3, 127.9, 128.2, 128.4, 128.9, 130.7, 147.3 (C), 149.1 (C), 150.1 (C); HRMS calcd. for $\text{C}_{27}\text{H}_{33}\text{N}_2$ ($[\text{M} + \text{H}]^+$): 385.2644. Found: 385.2647.



A.7 Procedure for Kinetics Experiments (Chapter Four)

Hydroamination reactions that were monitored for kinetic data were set up as follows. Aliquots of standard solutions of the aminoalkene substrate (**131**, ***d*₂-131**, **133**, or **170**, 1.50 M, 250 μL , 0.375 mmol) and 1,3,5-trimethoxybenzene (internal standard, 0.625 M, 100 μL , 0.0625 mmol) in d_6 -benzene were added to solid **167** (weighed for each experiment, 0.0255-0.0710 mmol). d_6 -Benzene was added (150 μL) to bring the total volume to 500 μL . The suspension was heated briefly and swirled to ensure complete dissolution of the precatalyst **167** before transferring to a J. Young NMR tube. The tube was inserted into a pre-heated NMR probe (300 MHz spectrometer). The temperature of the probe was calibrated using tabulated chemical shifts of ethylene glycol at five degree intervals by the NMR staff at the spectroscopic facility at the University of British Columbia. The tube and its contents were left to thermally equilibrate with the heated probe for five minutes before data acquisition was started. Each kinetic run was

performed using four-scan experiments (24 seconds total acquisition time) with pre-set delay times that allowed for automatic data acquisition. The substrate concentration was quantified by integration of the $\text{HC}=\text{CH}_2$ signal relative to the aromatic signal of the internal standard. To normalize the data collected between different runs, concentrations were plotted as c/c_0 (or $\ln(c/c_0)$). All errors on linear correlations were estimated from the standard error of the linear regression analysis performed using the Data Analysis Toolpack in Excel. This method underestimates the actual experimental error on the observed rate constants, which is mainly due to limitations on the detection technique (NMR integration) and the accuracy in weighing the precatalyst.

A.8 Derivation of the Catalytic Rate Law (Chapter Four)

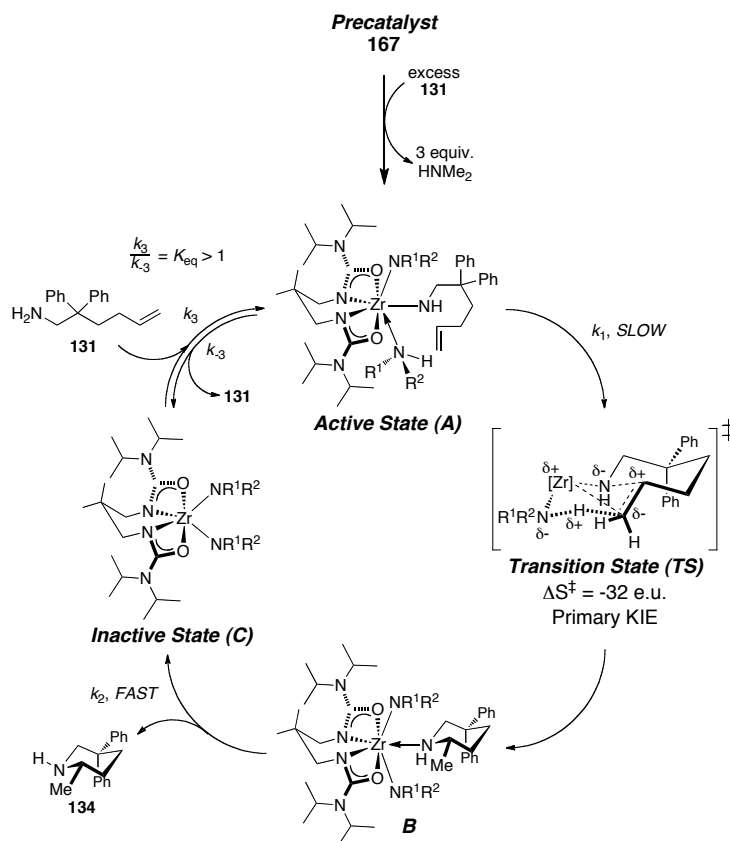


Figure A.1. Proposed catalytic cycle (reproduced from Scheme 4.11, Chapter Four).

The overall rate of the reaction can be written in terms of the production of **134**:

$$Rate = \frac{d[\mathbf{134}]}{dt} = k_2[\mathbf{B}] \quad (\text{A.1})$$

Applying the steady-state approximation to the concentrations of **A**, **B**, and **C**, and defining the concentration of catalytic intermediates in terms of the total catalyst concentration (i.e. the concentration of added precatalyst, assuming the concentrations of other species are negligible) gives the following relationships:

$$\frac{d[\mathbf{A}]}{dt} = -k_1[\mathbf{A}] + k_3[\mathbf{131}][\mathbf{C}] - k_{-3}[\mathbf{A}] = 0 \quad (\text{A.2})$$

$$\frac{d[\mathbf{B}]}{dt} = k_1[\mathbf{A}] - k_2[\mathbf{B}] = 0 \quad (\text{A.3})$$

$$\frac{d[\mathbf{C}]}{dt} = k_2[\mathbf{B}] - k_3[\mathbf{131}][\mathbf{C}] + k_{-3}[\mathbf{A}] = 0 \quad (\text{A.4})$$

$$[\mathbf{167}]_0 = [\mathbf{A}] + [\mathbf{B}] + [\mathbf{C}] \quad (\text{A.5})$$

Solving this set of simultaneous equations for **B** in terms of only **131**, **167**₀, and rate constants gives:

$$[\mathbf{B}] = \frac{k_1 k_3 [\mathbf{131}] [\mathbf{167}]_0}{k_1 k_2 + k_1 k_3 + k_2 k_{-3} + k_2 k_3 [\mathbf{131}]} \quad (\text{A.6})$$

Therefore, the overall rate can be written as:

$$Rate = \frac{d[\mathbf{134}]}{dt} = \frac{k_1 k_2 k_3 [\mathbf{131}] [\mathbf{167}]_0}{k_1 k_2 + k_1 k_3 + k_2 k_{-3} + k_2 k_3 [\mathbf{131}]} \quad (\text{A.7})$$

APPENDIX B. Tabulated Crystallographic Parameters

Table B.1. Crystallographic parameters for tethered proligand (Chapter Two).

87	
formula	$\text{C}_{19}\text{H}_{40}\text{N}_4\text{O}_2$
F_w	356.55
crystal size (mm)	$0.50 \times 0.40 \times 0.30$
colour, habit	colourless, prism
cell setting	orthorhombic
space group	$P\ b\ c\ a$
a (Å)	12.4945(5)
b (Å)	18.8284(6)
c (Å)	19.5149(6)
α (°)	90
β (°)	90
γ (°)	90
V (Å ³)	4590.9(3)
Z	8
ρ_{calcd} (g cm ⁻³)	1.032
radiation	$\text{MoK}\alpha$ ($\lambda = 0.71073$ Å)
$F(000)$	1584
μ (MoK α) (cm ⁻¹)	0.67
$2\theta_{\text{max}}$ (°)	44.96
total no. of reflns	11996
no. of unique reflns	2973 ($R_{\text{int}} = 0.0246$)
no. of reflns with $I = 2\sigma(I)$	2338
no. of variables	234
R_1 (F^2 , all data)	0.0694
wR_2 (F^2 , all data)	0.1377
R_1 (F , $I = 2\sigma(I)$)	0.0518
wR_2 (F , $I = 2\sigma(I)$)	0.1251
goodness of fit	1.030

Table B.2. Crystallographic parameters for dichloride compounds (Chapter Two).

	90	91•THF	92	93
formula	C ₃₀ H ₄₂ Cl ₂ N ₄ O ₂ Ti	C _{42.5} H ₆₇ Cl ₂ N ₄ O ₃ Zr	C ₂₇ H ₅₁ N ₅ O ₂ Ti	C ₂₁ H ₄₅ N ₅ O ₂ Zr
F_w	609.48	844.12	596.53	561.74
crystal size (mm)	0.25 × 0.15 × 0.10	0.25 × 0.10 × 0.10	0.80 × 0.50 × 0.20	0.35 × 0.15 × 0.10
colour, habit	yellow, plate	colourless, chip	yellow, prism	colourless, prism
cell setting	monoclinic	triclinic	triclinic	orthorhombic
space group	$C 2/c$	$P -1$	$P -1$	$C m c 21$
a (Å)	24.072(6)	10.532(2)	10.7519(6)	15.9460(8)
b (Å)	12.611(3)	12.162(3)	12.4824(7)	12.4515(6)
c (Å)	17.219(4)	17.907(4)	12.6443(7)	13.9449(6)
α (°)	90	81.666(10)	89.296(2)	90
β (°)	130.581(8)	76.329(10)	79.739(2)	90
γ (°)	90	82.263(10)	73.967(2)	90
V (Å ³)	3970.0(16)	2193.3(9)	1603.67(15)	2768.8(2)
Z	4	2	2	4
ρ_{calcd} (g cm ⁻³)	1.020	1.278	1.235	1.348
radiation	MoK α ($\lambda = 0.71073$ Å)			
$F(000)$	3312	1252	1560	836
μ (MoK α) (cm ⁻¹)	2.08	3.61	3.16	2.93
$2\theta_{\text{max}}$ (°)	50.04	55.00	60.22	55.82
total no. of reflns	99073	24563	45994	31903
no. of unique reflns	11533	7524	11674	9956
no. of reflns with $I = 2\sigma(I)$	($R_{\text{int}} = 0.0566$) 9273	($R_{\text{int}} = 0.0315$) 6040	($R_{\text{int}} = 0.0343$) 8888	($R_{\text{int}} = 0.0242$) 8848
no. of variables	638	357	452	462
R_1 (F^2 , all data)	0.0424	0.0423	0.0556	0.0426
wR_2 (F^2 , all data)	0.0792	0.0666	0.0890	0.0989
R_1 (F , $I = 2\sigma(I)$)	0.0310	0.0278	0.0340	0.0354
wR_2 (F , $I = 2\sigma(I)$)	0.0764	0.0619	0.0773	0.0933
goodness of fit	0.973	1.021	1.031	1.065

Table B.3. Crystallographic parameters for dialkyl compounds (Chapter Two).

	95	97	98	96•py	98•py
formula	C ₅₉ H ₉₂ N ₆ O ₃ Zr	C ₂₉ H ₆₀ N ₄ O ₂ Zr	C ₄₂ H ₅₄ N ₄ O ₂ Zr	C ₄₃ H ₆₉ N ₅ O ₂ Zr	C ₄₇ H ₅₉ N ₅ O ₂ Zr
F_w	1024.61	588.03	738.11	779.25	817.21
crystal size (mm)	1.00 × 0.80 × 0.50	0.50 × 0.50 × 0.30	0.80 × 0.50 × 0.40	0.25 × 0.20 × 0.10	0.20 × 0.20 × 0.10
colour, habit	colourless, prism	colourless, prism	yellow, prism	orange, irregular	orange, block
cell setting	trigonal	monoclinic	monoclinic	triclinic	orthorhombic
space group	P 63	P 21/c	P 21/c	P -1	C 2 2 21
a (Å)	24.5106(9)	13.7893(4)	11.7720(8)	12.6973(12)	15.151(2)
b (Å)	24.5106(9)	15.7596(4)	15.1692(13)	13.7484(12)	18.936(3)
c (Å)	18.9897(7)	15.9037(4)	22.6428(18)	14.2131(13)	15.576(3)
α (°)	90	90	90	69.300(4)	90
β (°)	90	107.1760(10)	101.173(3)	69.631(4)	90
γ (°)	120	90	90	78.194(4)	90
V (Å ³)	9879.7(2)	3301.96(15)	3966.7(5)	2166.4(3)	4468.8(12)
Z	6	4	4	2	4
ρ_{calcd} (g cm ⁻³)	1.033	1.173	1.236	1.195	1.215
radiation	MoK α (λ = 0.71073 Å)				
$F(000)$	3312	1252	1560	836	1728
μ (MoK α) (cm ⁻¹)	2.08	3.61	3.16	2.93	2.87
$2\theta_{\text{max}}$ (°)	50.04	55.00	60.22	55.82	70.72
total no. of reflns	99073	24563	45994	31903	16782
no. of unique reflns	11533	7524	11674	9956	7914
	(R_{int} = 0.0566)	(R_{int} = 0.0315)	(R_{int} = 0.0343)	(R_{int} = 0.0242)	(R_{int} = 0.0144)
no. of reflns with $I = 2\sigma(I)$	9273	6040	8888	8848	7172
no. of variables	638	357	452	462	255
R_1 (F^2 , all data)	0.0424	0.0423	0.0556	0.0426	0.0321
wR_2 (F^2 , all data)	0.0792	0.0666	0.0890	0.0989	0.0697
R_1 (F , $I = 2\sigma(I)$)	0.0310	0.0278	0.0340	0.0354	0.0257
wR_2 (F , $I = 2\sigma(I)$)	0.0764	0.0619	0.0773	0.0933	0.0645
goodness of fit	0.973	1.021	1.031	1.065	1.091

Table B.4. Crystallographic parameters for non-tethered bis(amido) compounds (Chapter Three).

	89	159	160	161
formula	C ₃₄ H ₅₈ N ₆ O ₂ Ti	C ₃₄ H ₅₈ N ₆ O ₂ Zr	C ₄₀ H ₆₆ N ₆ O ₂ Ti	C ₄₀ H ₆₆ N ₆ O ₂ Zr
F_w	630.76	674.08	710.89	754.21
crystal size (mm)	0.30 × 0.20 × 0.20	0.15 × 0.15 × 0.05	0.15 × 0.10 × 0.05	0.35 × 0.35 × 0.18
colour, habit	orange, prism	colourless, rod	orange, prism	colourless, tablet
cell setting	monoclinic	monoclinic	orthorhombic	orthorhombic
space group	<i>C</i> 2/c	<i>C</i> 2/c	<i>P</i> 21 21 21	<i>P</i> c a n
<i>a</i> (Å)	15.8053(6)	16.5035(11)	11.6861(5)	15.9379(8)
<i>b</i> (Å)	14.2179(5)	13.8792(9)	14.9220(7)	21.2422(9)
<i>c</i> (Å)	16.6842(5)	16.8961(12)	23.7688(12)	24.6910(11)
α (°)	90	90	90	90
β (°)	108-342(1)	110.108(3)	90	90
γ (°)	90	90	90	90
<i>V</i> (Å ³)	3558.7(3)	3634.2(4)	4144.82(34)	8359.3(7)
<i>Z</i>	4	4	4	8
ρ_{calcd} (g cm ⁻³)	1.177	1.232	1.139	1.199
radiation	MoK α (λ = 0.71073 Å)			
<i>F</i> (000)	1368	1440	1544	3232
μ (MoK α) (cm ⁻¹)	2.78	3.39	2.45	3.02
2 θ_{max} (°)	55.10	50.10	55.10	55.82
total no. of reflns	16277	17243	44298	62126
no. of unique reflns	4103	3220	8165	9989
no. of reflns with $I = 2\sigma(I)$	(<i>R</i> _{int} = 0.0289)	(<i>R</i> _{int} = 0.0371)	(<i>R</i> _{int} = 0.0492)	(<i>R</i> _{int} = 0.0838)
no. of variables	3291	2836	6494	6150
<i>R</i> ₁ (<i>F</i> ² , all data)	219	203	454	454
wR_2 (<i>F</i> ² , all data)	0.0672	0.0348	0.0468	0.0893
R_1 (<i>F</i> , $I = 2\sigma(I)$)	0.1334	0.0701	0.0657	0.1165
wR_2 (<i>F</i> , $I = 2\sigma(I)$)	0.0505	0.0279	0.0326	0.0440
goodness of fit	0.1231	0.0672	0.0632	0.0970
	1.205	1.072	0.926	1.008

Table B.5. Crystallographic parameters for tethered bis(amido) compounds (Chapter Three).

	166	167
formula	C ₂₃ H ₄₆ N ₆ O ₂ Ti	C ₂₅ H ₅₇ N ₇ O ₂ Zr
F_w	490.56	579.00
crystal size (mm)	0.50 × 0.30 × 0.20	1.00 × 0.30 × 0.30
colour, habit	red, prism	yellow, prism
cell setting	monoclinic	monoclinic
space group	<i>C</i> c	<i>P</i> 21/n
a (Å)	14.7425(5)	13.987(1)
b (Å)	13.9944(6)	16.192(1)
c (Å)	14.8228(6)	14.298(1)
α (°)	90	90
β (°)	112.176(2)	95.248(3)
γ (°)	90	90
V (Å ³)	2831.9(3)	3224.7(4)
Z	4	4
ρ_{calcd} (g cm ⁻³)	1.141	1.193
radiation	MoK α (λ = 0.71073 Å)	
$F(000)$	1056	1248
μ (MoK α) (cm ⁻¹)	3.30	3.72
$2\theta_{\text{max}}$ (°)	45.02	59.92
total no. of reflns	6390	34829
no. of unique reflns	3063 (R_{int} = 0.0289)	9324 (R_{int} = 0.0294)
no. of reflns with $I = 2\sigma(I)$	2888	7640
no. of variables	303	336
R_1 (F^2 , all data)	0.0410	0.0456
wR_2 (F^2 , all data)	0.0922	0.0943
R_1 (F , $I = 2\sigma(I)$)	0.0376	0.0334
wR_2 (F , $I = 2\sigma(I)$)	0.0904	0.0877
goodness of fit	1.032	1.033

Table B.6. Crystallographic parameters for catalytic model compounds (Chapter Four).

	274	275	285	286	287
formula	C ₂₈ H ₅₅ N ₇ O ₂ Zr	C ₄₆ H ₁₀₀ N ₁₂ O ₄ Zr ₂	C ₄₁ H ₆₅ N ₇ O ₂ Zr	C ₆₂ H ₁₁₀ N ₁₀ O ₄ Zr ₂	C ₆₄ H ₁₀₄ N ₁₂ O ₄ Zr ₂
F_w	613.01	1067.82	779.22	1242.04	1288.03
crystal size (mm)	0.30 × 0.25 × 0.20	0.50 × 0.30 × 0.30	0.40 × 0.40 × 0.20	1.00 × 0.70 × 0.20	0.15 × 0.10 × 0.08
colour, habit	orange, prism	colourless, prism	orange, prism	yellow, oval	yellow, prism
cell setting	monoclinic	monoclinic	monoclinic	monoclinic	triclinic
space group	$P 21/n$	$P 21/n$	$P 21/n$	$P 21/n$	$P -1$
a (Å)	13.319(3)	13.151(5)	13.7003(5)	12.8587(8)	12.3906(12)
b (Å)	16.010(2)	15.598(5)	20.8396(7)	29.109(2)	12.5842(13)
c (Å)	15.468(2)	13.856(5)	15.3980(5)	18.1209(13)	13.3974(14)
α (°)	90	90	90	90	63.414(4)
β (°)	99.281(7)	95.011(5)	94.5140(10)	91.361(3)	67.651(4)
γ (°)	90	90	90	90	65.864(4)
V (Å ³)	3255.1(9)	2831.4(17)	4382.6(4)	6780.8(8)	1654.3(3)
Z	4	2	4	4	1
ρ_{calcd} (g cm ⁻³)	1.251	1.252	1.181	1.217	1.293
radiation	MoK α ($\lambda = 0.71073$ Å)				
$F(000)$	1312	1144	1664	2656	684
μ (MoK α) (cm ⁻¹)	3.72	4.17	2.91	3.57	3.69
$2\theta_{\text{max}}$ (°)	50.50	60.16	49.98	54.98	68.02
total no. of reflns	21598	31129	24316	59909	31286
no. of unique reflns	5852	8291	7144	15448	10551
no. of reflns with $I = 2\sigma(I)$	($R_{\text{int}} = 0.0511$) 4347	($R_{\text{int}} = 0.0163$) 7278	($R_{\text{int}} = 0.1084$) 4741	($R_{\text{int}} = 0.0273$) 12859	($R_{\text{int}} = 0.0207$) 9833
no. of variables	357	303	474	731	382
R_1 (F^2 , all data)	0.0734	0.0302	0.1395	0.0433	0.0278
wR_2 (F^2 , all data)	0.1122	0.0803	0.1319	0.0768	0.0679
R_1 (F , $I = 2\sigma(I)$)	0.0483	0.0228	0.0364	0.0306	0.0246
wR_2 (F , $I = 2\sigma(I)$)	0.1008	0.0662	0.0919	0.0699	0.0649
goodness of fit	1.018	1.213	1.064	1.049	1.065

Table B.7. Crystallographic parameters for alkyne insertion products (Chapter Four).

	288	289
formula	$\text{C}_{32}\text{H}_{58}\text{N}_6\text{O}_2\text{Zr}$	$\text{C}_{37}\text{H}_{60}\text{N}_6\text{O}_2\text{Zr}$
F_w	650.06	712.13
crystal size (mm)	$0.40 \times 0.40 \times 0.40$	$0.50 \times 0.50 \times 0.20$
colour, habit	colourless, prism	yellow, prism
cell setting	triclinic	triclinic
space group	$P - 1$	$P - 1$
a (Å)	10.8995(4)	11.1851(6)
b (Å)	12.4986(5)	21.4755(10)
c (Å)	13.5670(5)	26.3317(14)
α (°)	79.016(2)	106.564(3)
β (°)	75.747(2)	98.567(3)
γ (°)	77.926(2)	102.450(3)
V (Å ³)	1732.74(11)	5768.4(5)
Z	2	6
ρ_{calcd} (g cm ⁻³)	1.246	1.230
radiation	MoK α ($\lambda = 0.71073$ Å)	
$F(000)$	696	2280
μ (MoK α) (cm ⁻¹)	3.53	3.24
$2\theta_{\text{max}}$ (°)	55.16	55.16
total no. of reflns	28698	95610
no. of unique reflns	7911 ($R_{\text{int}} = 0.0361$)	26313 ($R_{\text{int}} = 0.0423$)
no. of reflns with $I = 2\sigma(I)$	7107	19102
no. of variables	385	1285
R_1 (F^2 , all data)	0.0360	0.0686
wR_2 (F^2 , all data)	0.0799	0.0856
R_1 (F , $I = 2\sigma(I)$)	0.0308	0.0380
wR_2 (F , $I = 2\sigma(I)$)	0.0770	0.0751
goodness of fit	1.048	1.011

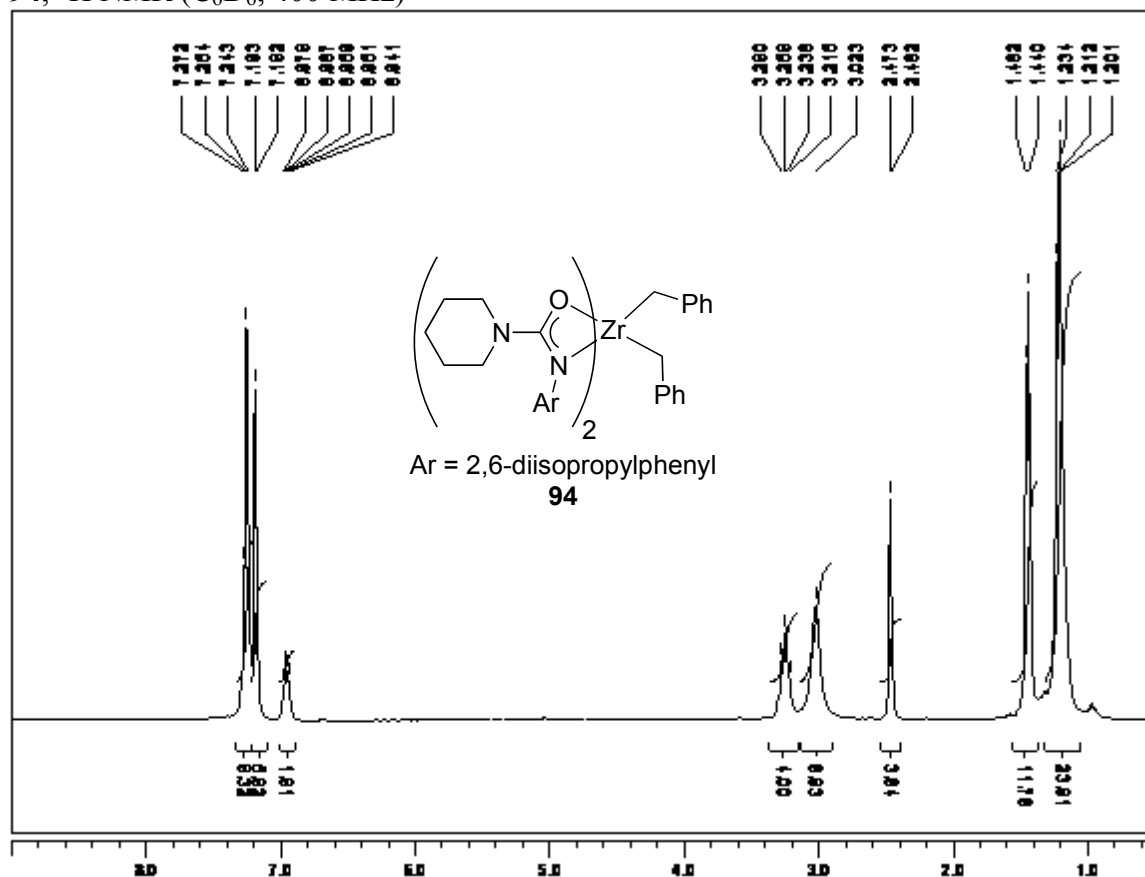
Table B.8. Crystallographic parameters for chiral bis(amido) complex (Chapter Five).

307	
formula	$\text{C}_{37}\text{H}_{57}\text{N}_7\text{O}_2\text{Zr}$
F_w	723.12
crystal size (mm)	$0.30 \times 0.20 \times 0.12$
colour, habit	yellow, irregular
cell setting	monoclinic
space group	$P 1 2_1/n 1$
a (Å)	10.8498(12)
b (Å)	18.367(2)
c (Å)	19.780(2)
α (°)	90
β (°)	98.201(5)
γ (°)	90
V (Å ³)	3901.6(8)
Z	4
ρ_{calcd} (g cm ⁻³)	1.231
radiation	$\text{MoK}\alpha$ ($\lambda = 0.71073$ Å)
$F(000)$	1536
μ (MoK α) (cm ⁻¹)	3.21
$2\theta_{\text{max}}$ (°)	50.38
total no. of reflns	49823
no. of unique reflns	6979 ($R_{\text{int}} = 0.0408$)
no. of reflns with $I = 2\sigma(I)$	5503
no. of variables	438
R_1 (F^2 , all data)	0.0486
wR_2 (F^2 , all data)	0.0824
R_1 (F , $I = 2\sigma(I)$)	0.0323
wR_2 (F , $I = 2\sigma(I)$)	0.0748
goodness of fit	1.043

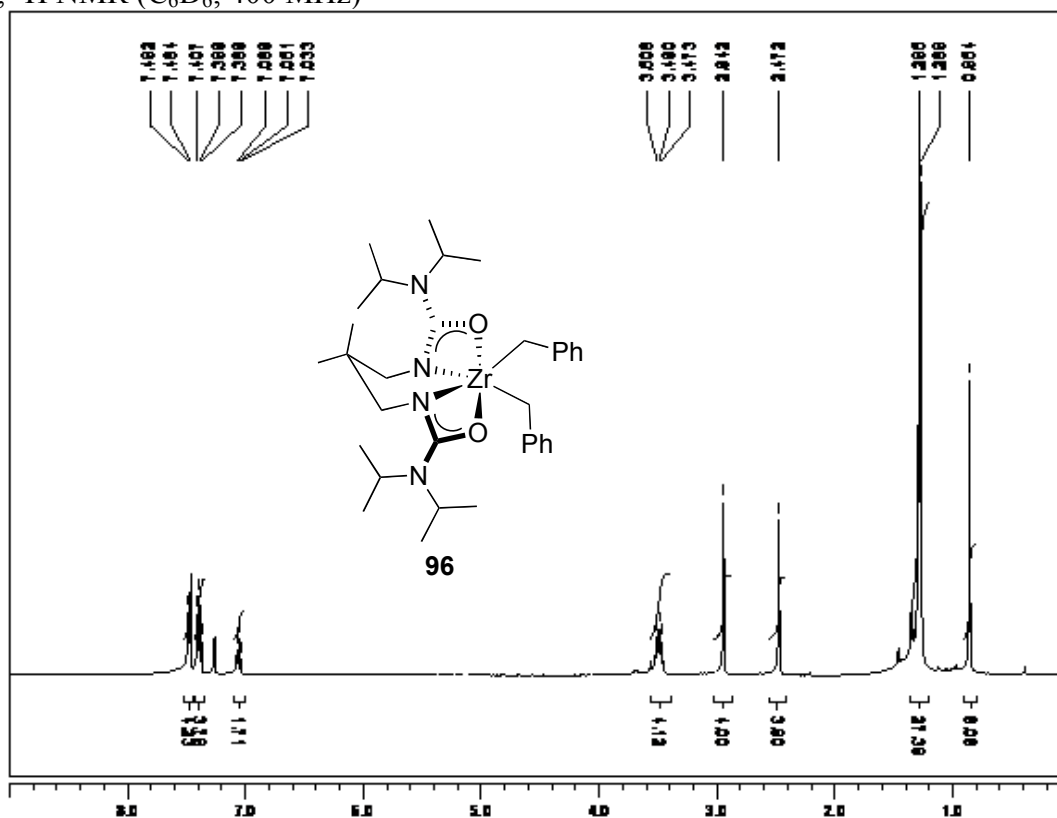
APPENDIX C. Selected NMR Spectra

Representative NMR spectra for select compounds are collected below. This section does not contain all spectra obtained. Unless otherwise noted, spectra were acquired at ambient temperature.

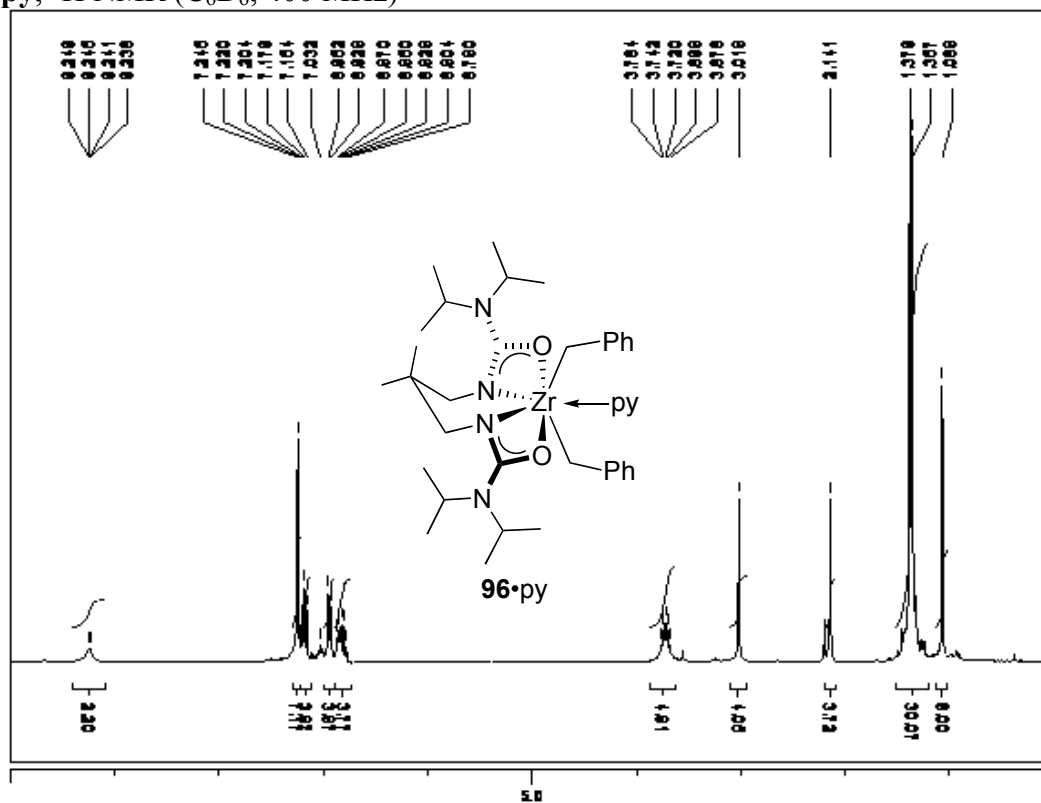
94, ^1H NMR (C_6D_6 , 400 MHz)



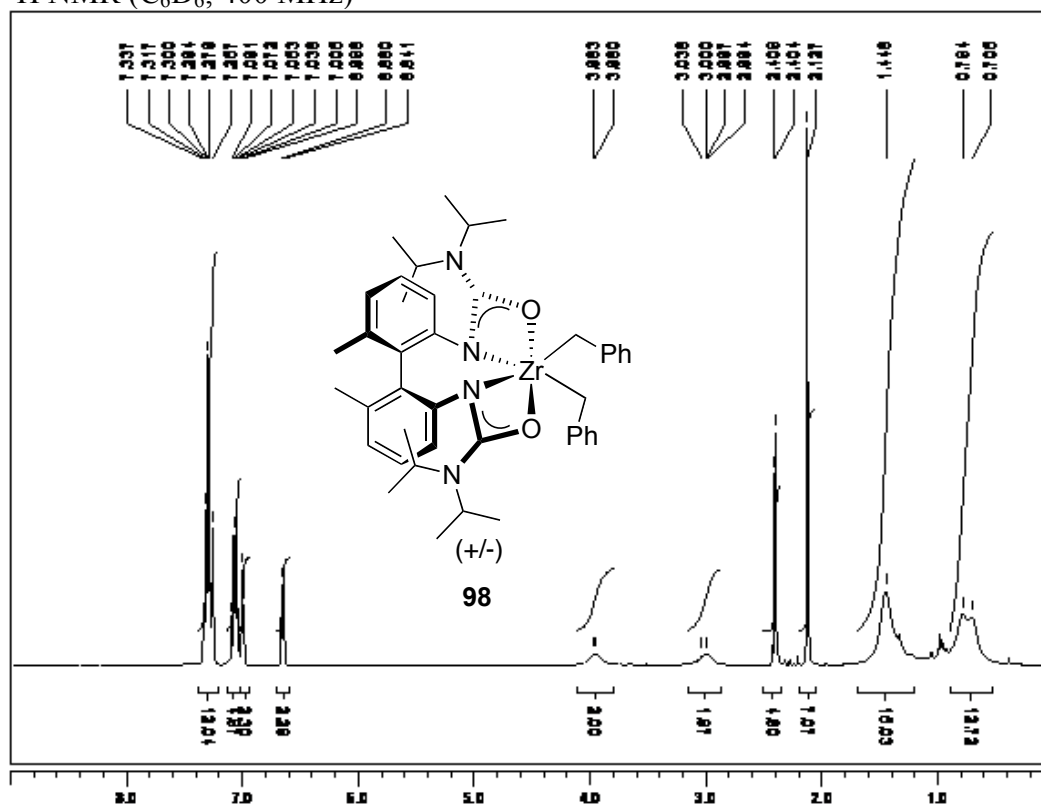
96, ^1H NMR (C_6D_6 , 400 MHz)



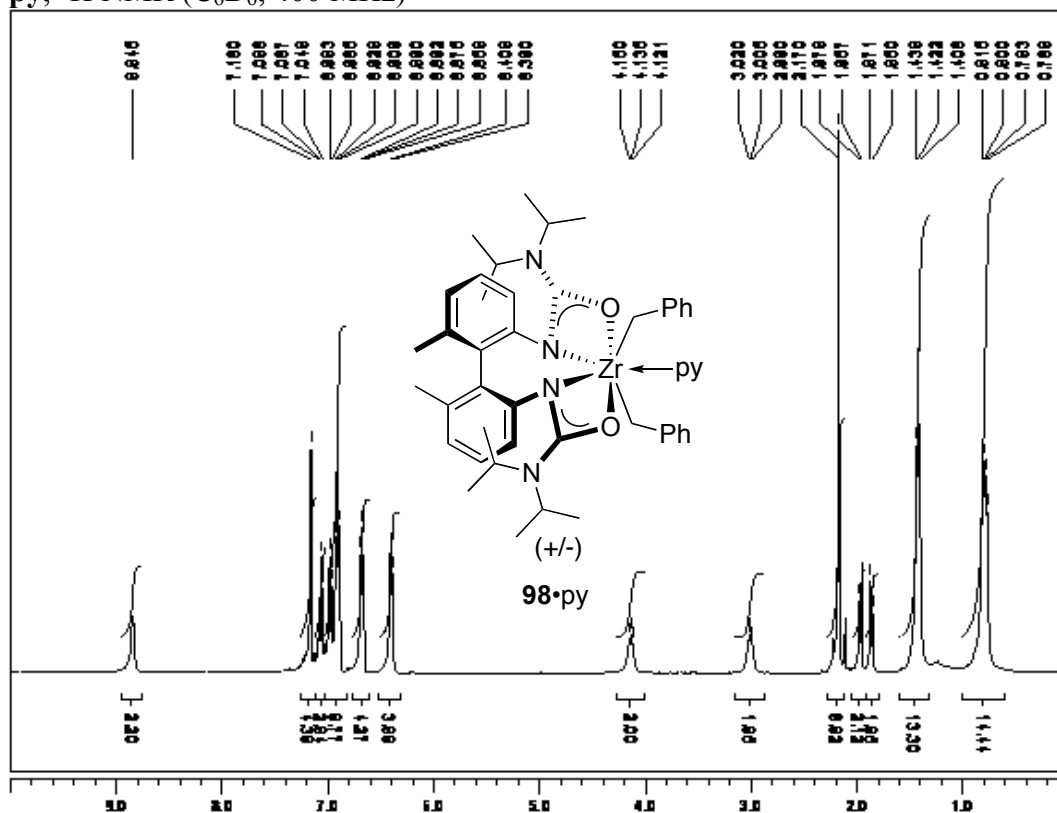
96•py, ^1H NMR (C_6D_6 , 400 MHz)



98, ^1H NMR (C_6D_6 , 400 MHz)

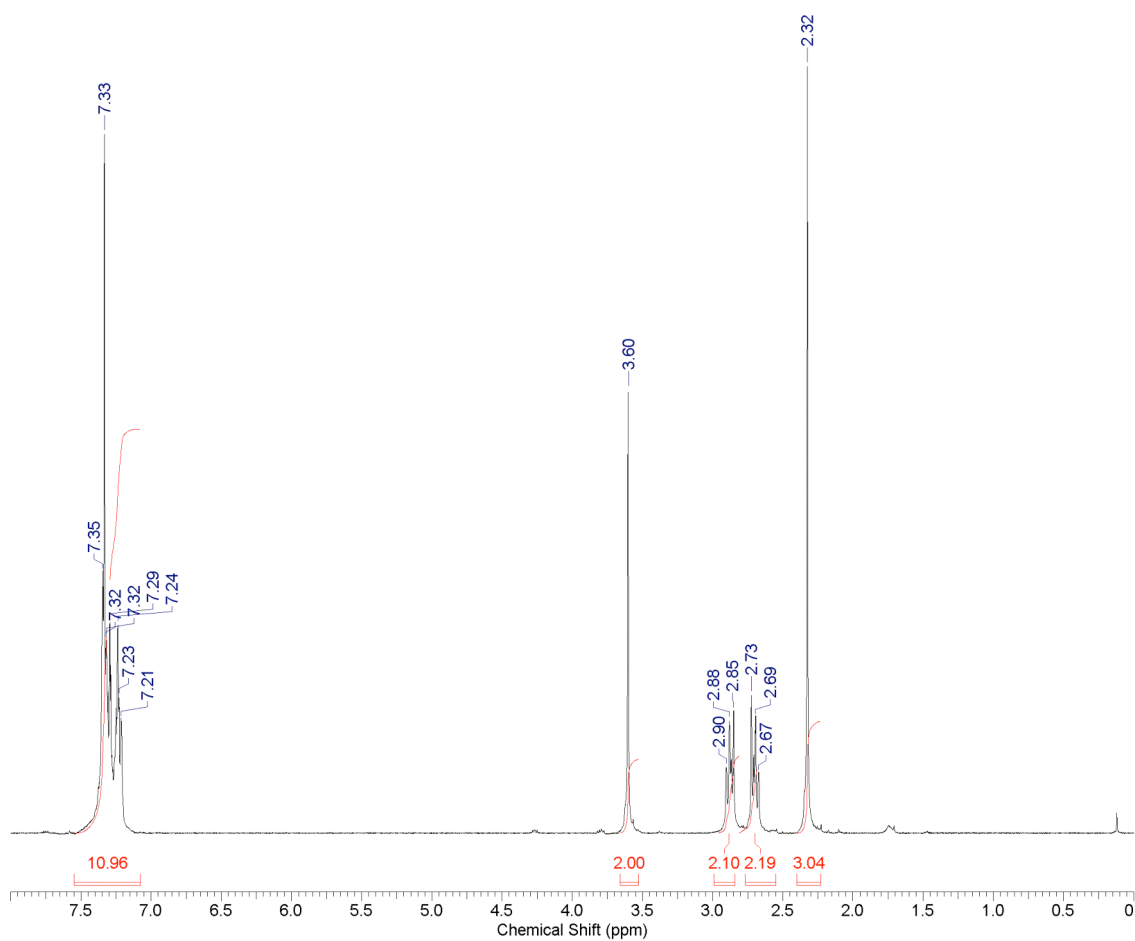
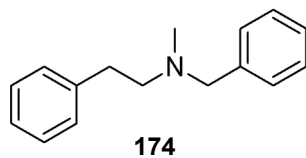


98•py, ^1H NMR (C_6D_6 , 400 MHz)



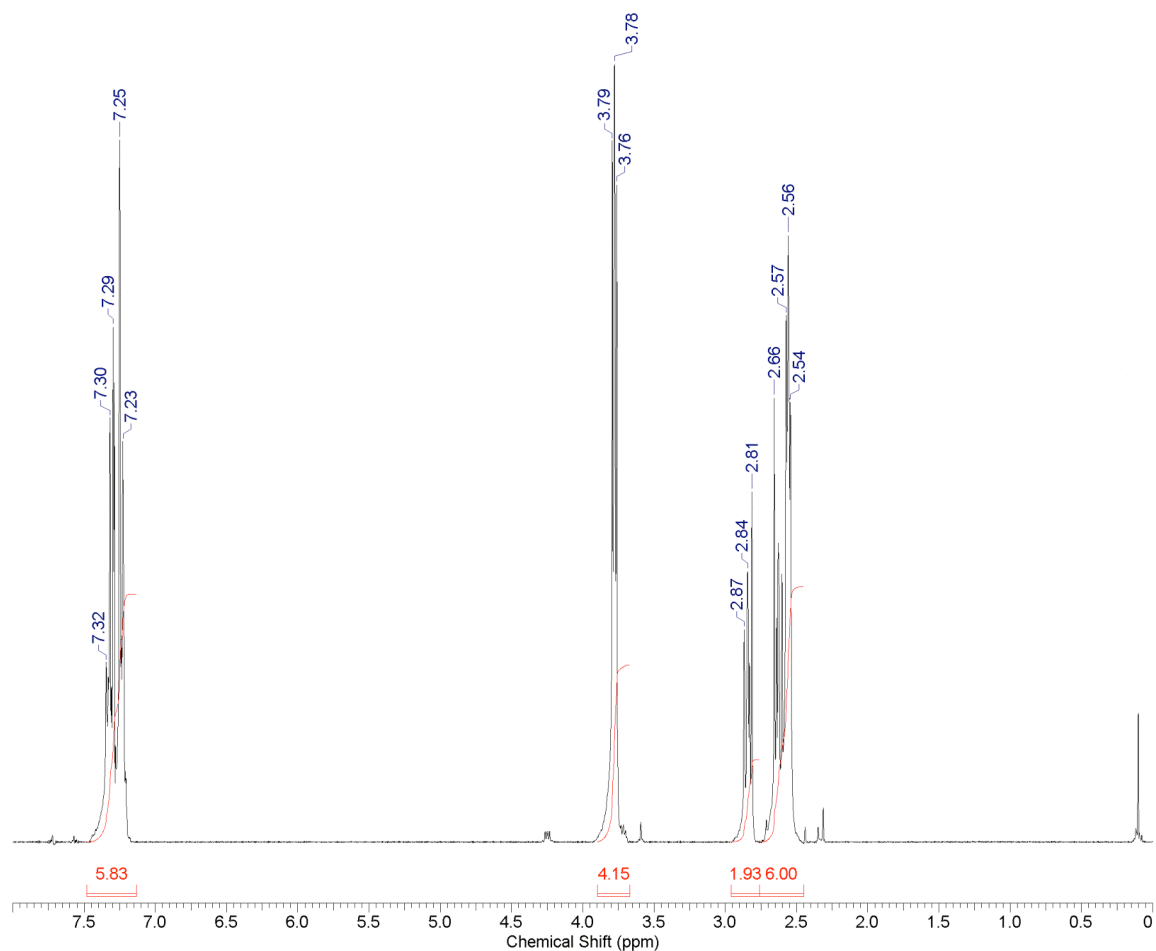
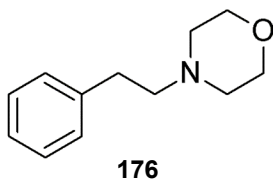
Acquisition Time (sec)	2.1999	Comment	DL-V-193 1H observe ref. to CDCl3 at 7.27 ppm	
Date	28 Oct 2009 02:46:24		Date Stamp	28 Oct 2009 02:46:24
File Name	F:\USB Documents\PhD Research\Papers\JACS Communication (Hydroamination)\SI Spectra\DL-V-193\DL-V-193_002000fid			
Frequency (MHz)	300.13	Nucleus	1H	Number of Transients 13
Origin	spect	Original Points Count	8233	Owner root
Points Count	16384	Pulse Sequence	zg30	Receiver Gain 203.20
SW(cyclical) (Hz)	3742.51	Solvent	CHLOROFORM-d	Spectrum Offset (Hz) 1793.8740
Sweep Width (Hz)	3742.29	Temperature (degree C)	25.160	

DL-V-193_002000fid



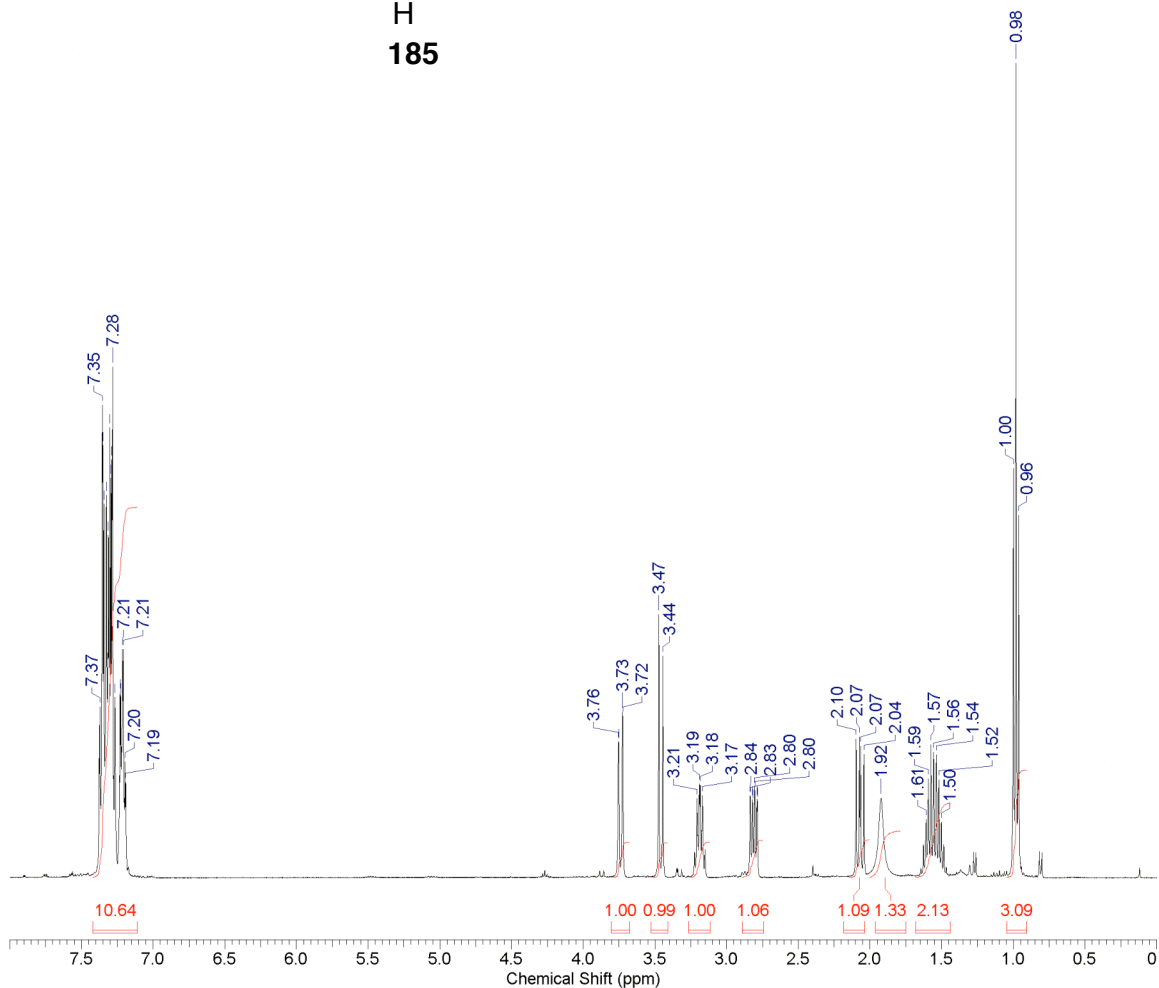
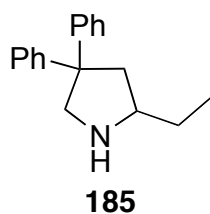
Acquisition Time (sec)	2.1999	Comment	DL-V-186 1H observe ref. to CDCl3 at 7.27 ppm	
Date	28 Oct 2009 02:42:08		Date Stamp	28 Oct 2009 02:42:08
File Name	F:\USB Documents\PhD Research\Papers\JACS Communication (Hydroamination)\SI Spectra\DL-V-186\DL-V-186_002000fid			
Frequency (MHz)	300.13	Nucleus	1H	Number of Transients 8
Origin	spect	Original Points Count	8233	Owner root
Points Count	16384	Pulse Sequence	zg30	Receiver Gain 406.40
SW(cyclical) (Hz)	3742.51	Solvent	CHLOROFORM-d	Spectrum Offset (Hz) 1793.8740
Sweep Width (Hz)	3742.29	Temperature (degree C)	25.160	

DL-V-186_002000fid



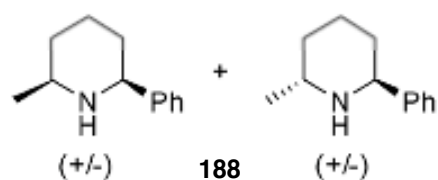
Acquisition Time (sec)	2.1998	Comment	DL-V-26 JOB NO: 1H spectrum ref. to CDCl3 at 7.27 ppm	
Date	07 Oct 2009 20:43:44	Date Stamp	07 Oct 2009 20:43:44	
File Name	F:\USB Documents\PhD Research\Papers\JACS Communication (Hydroamination)\SI Spectra\DL-V-26\DL-V-26_001000fid			
Frequency (MHz)	400.13	Nucleus	1H	Number of Transients 16
Origin	av400	Original Points Count	12303	Owner root
Points Count	16384	Pulse Sequence	zg30	Receiver Gain 143.70
SW(cyclical) (Hz)	5592.84	Solvent	CHLOROFORM-d	Spectrum Offset (Hz) 2395.7537
Sweep Width (Hz)	5592.50	Temperature (degree C)	25.160	

DL-V-26_001000fid

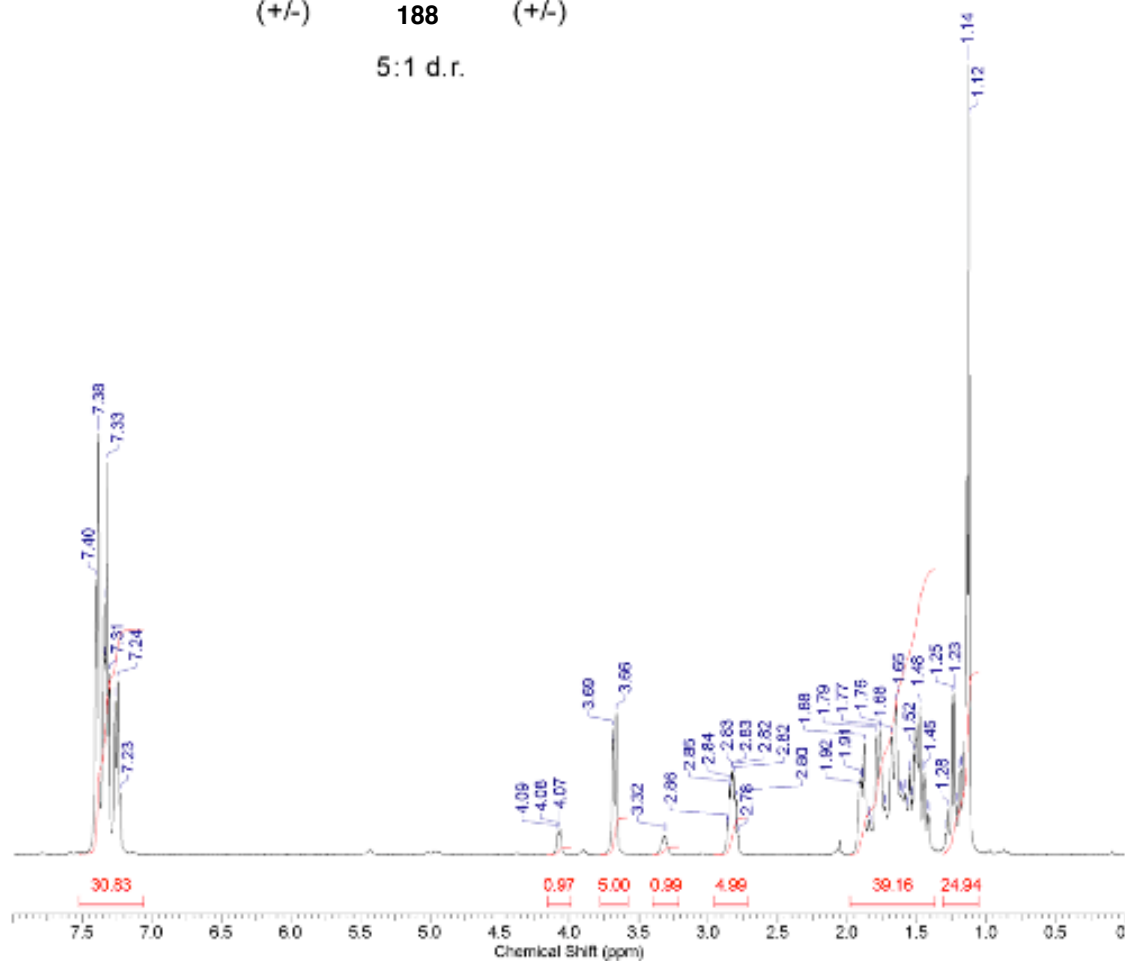


Acquisition Time (sec)	2.9295	Comment	1H UBC Bruker 400MHz BBO probe
Date	04 Nov 2009 17:12:32	Date Stamp	04 Nov 2009 17:12:32
File Name	C:\Documents and Settings\pippe\My Documents\PhD data\NMR\pp-01-6mem\pp-01-6mem_001000fid		
Frequency (MHz)	400.19	Nucleus	1H
Origin	spect	Original Points Count	16384
Points Count	16384	Pulse Sequence	zg30
SW(cyclical) (Hz)	5592.84	Solvent	CHLOROFORM-d
Spectrum Offset (Hz)	2590.5879	Sweep Width (Hz)	5592.50
		Temperature (degree C)	22.425

PP-01-6MEM 1H.ESP

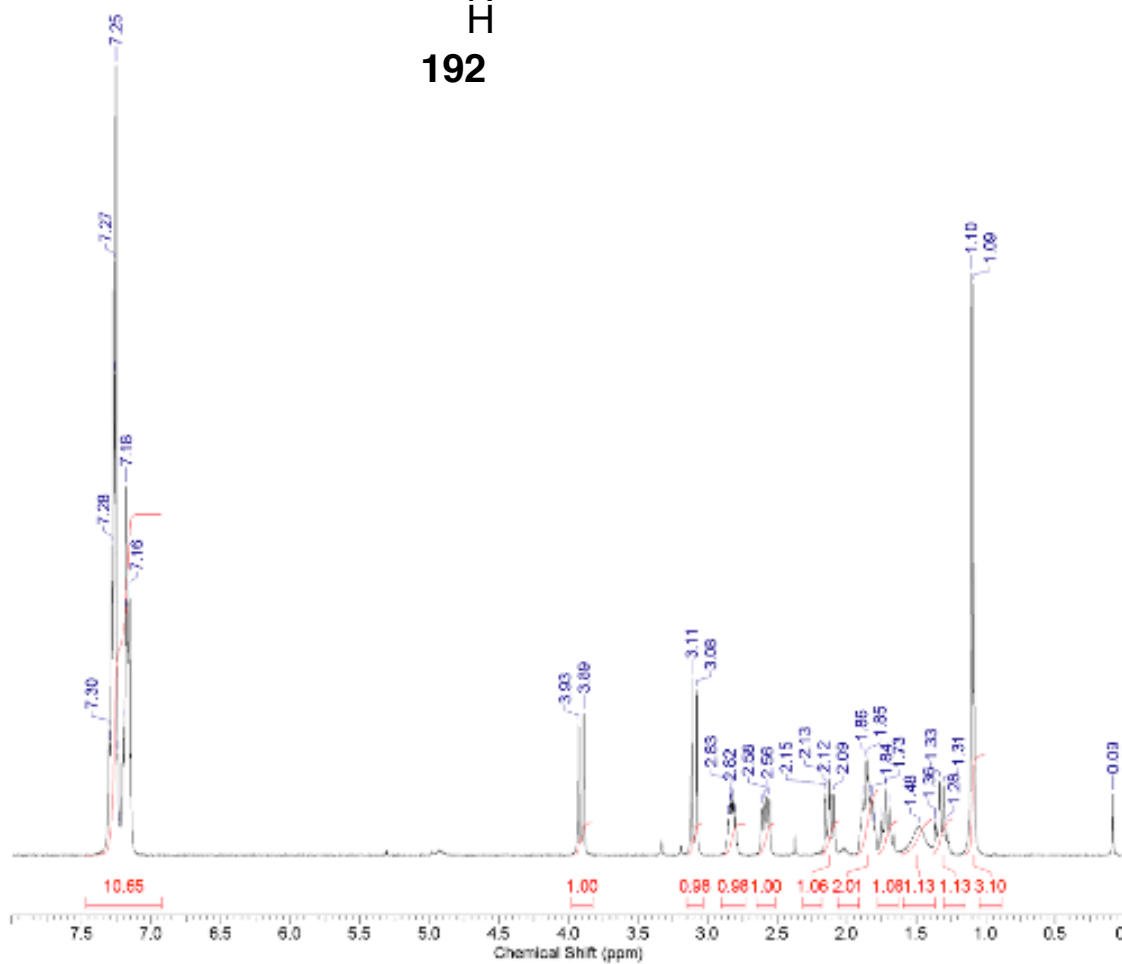
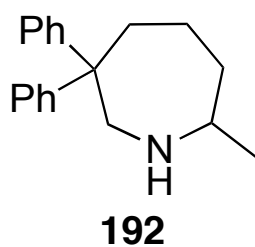


5:1 d.r.



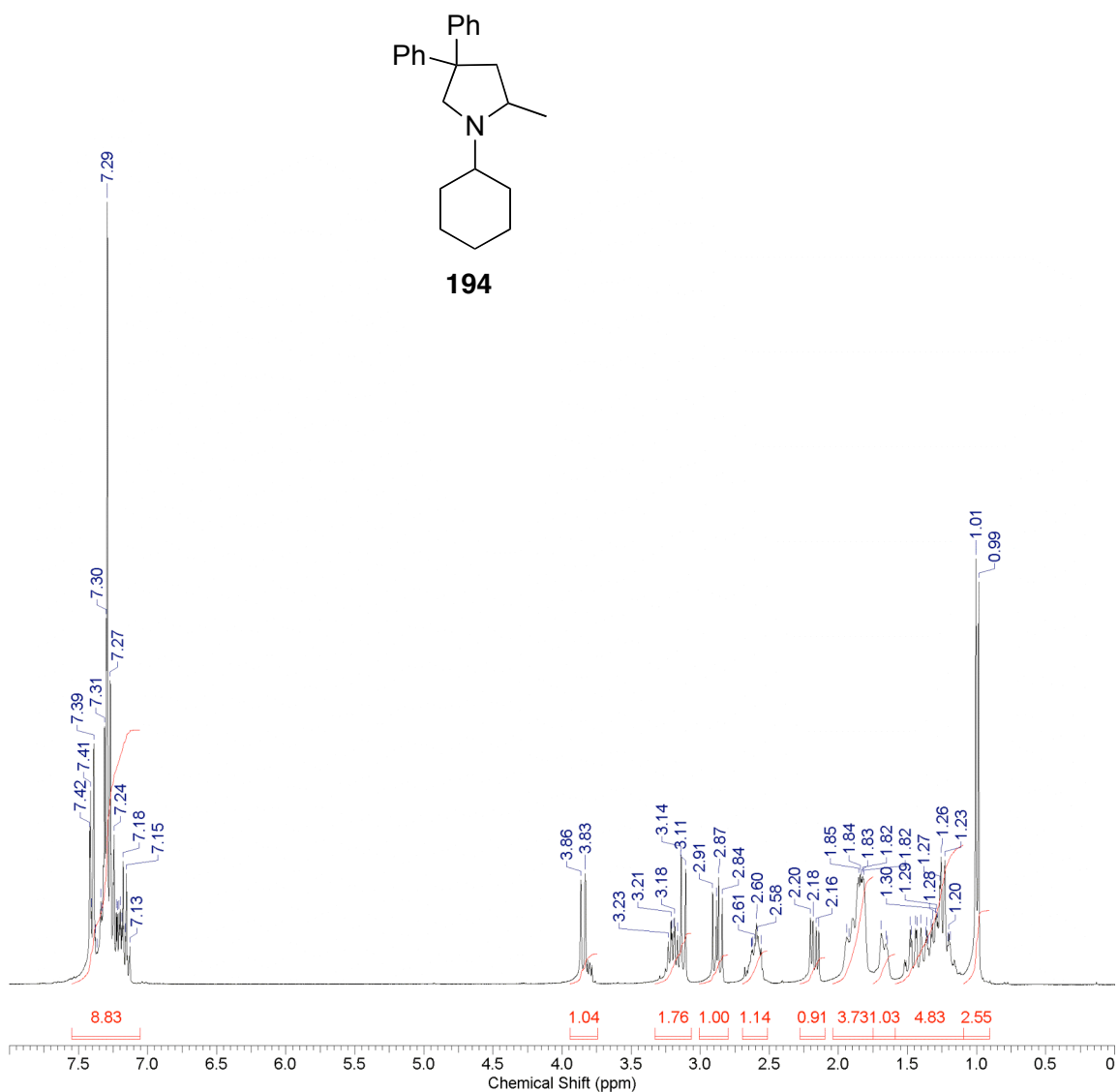
Acquisition Time (sec)	2.9295	Comment	1H A UBC Bruker 400MHz BBO probe		
Date	09 Nov 2009 11:56:48		Date Stamp	09 Nov 2009 11:56:48	
File Name	C:\Documents and Settings\pippe\My Documents\PhD data\NMR\pp-01-160\pp-01-160_001000f1d				
Frequency (MHz)	400.19	Nucleus	1H	Number of Transients	16
Origin	spect	Original Points Count	16384	Owner	root
Points Count	16384	Pulse Sequence	zg30	Receiver Gain	181.00
SW(cyclical) (Hz)	5592.84	Solvent	CHLOROFORM-d		
Spectrum Offset (Hz)	2590.5879	Sweep Width (Hz)	5592.50	Temperature (degree C)	23.394

PP-01-160 A 1H.ESP



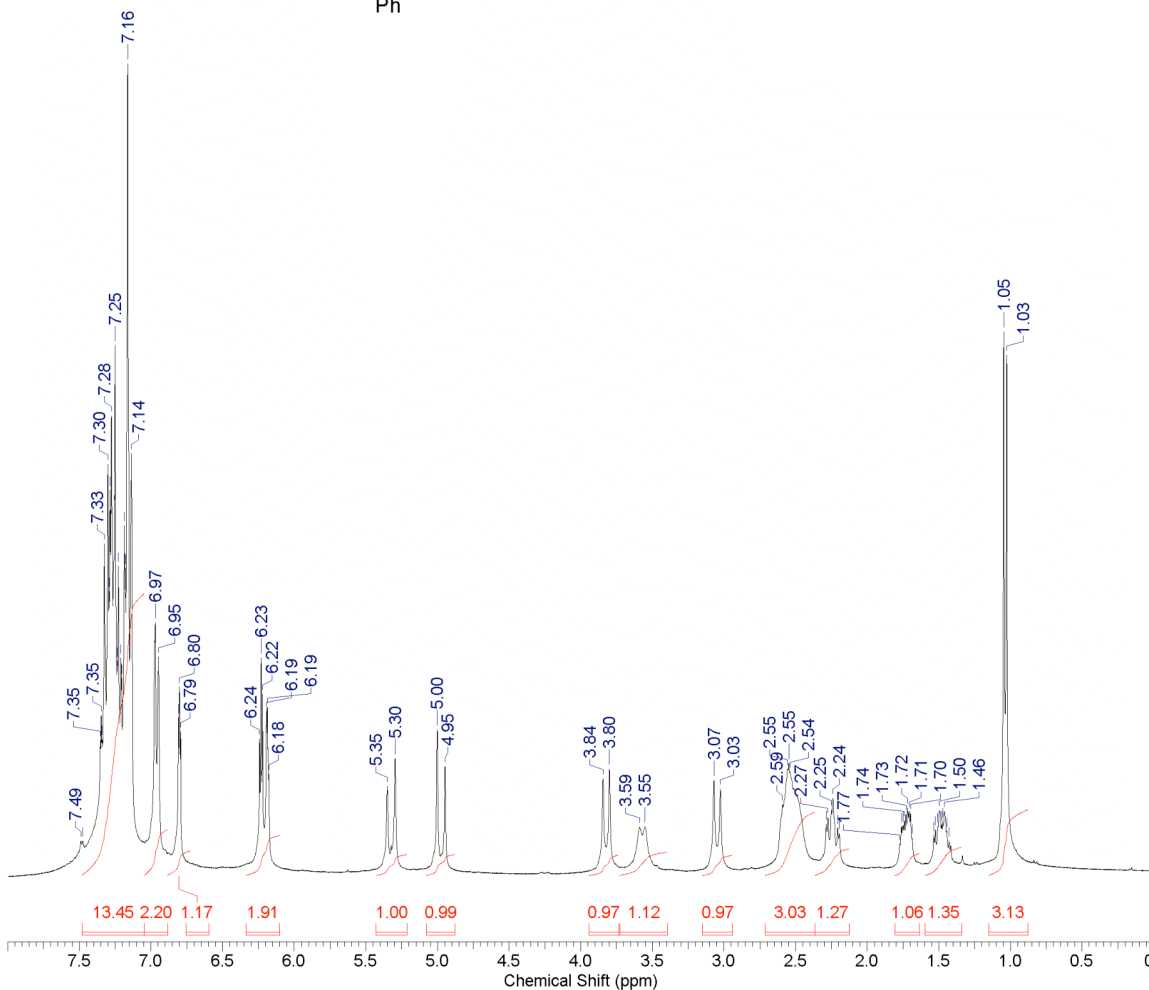
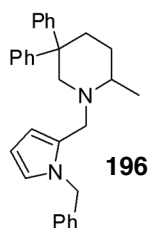
Acquisition Time (sec)	2.1999	Comment	DL-V-159 1H observe ref. to CDCl3 at 7.27 ppm	
Date	23 Oct 2009 04:05:20	Date Stamp	23 Oct 2009 04:05:20	
File Name	F:\USB Documents\PhD Research\Papers\JACS Communication (Hydroamination)\SI Spectra\DL-V-159\DL-V-159_001000fid			
Frequency (MHz)	300.13	Nucleus	1H	Number of Transients 32
Origin	spect	Original Points Count	8233	Owner root
Points Count	16384	Pulse Sequence	zg30	Receiver Gain 128.00
SW(cyclical) (Hz)	3742.51	Solvent	CHLOROFORM-d	Spectrum Offset (Hz) 1793.8740
Sweep Width (Hz)	3742.29	Temperature (degree C)	25.160	

DL-V-159_001000fid

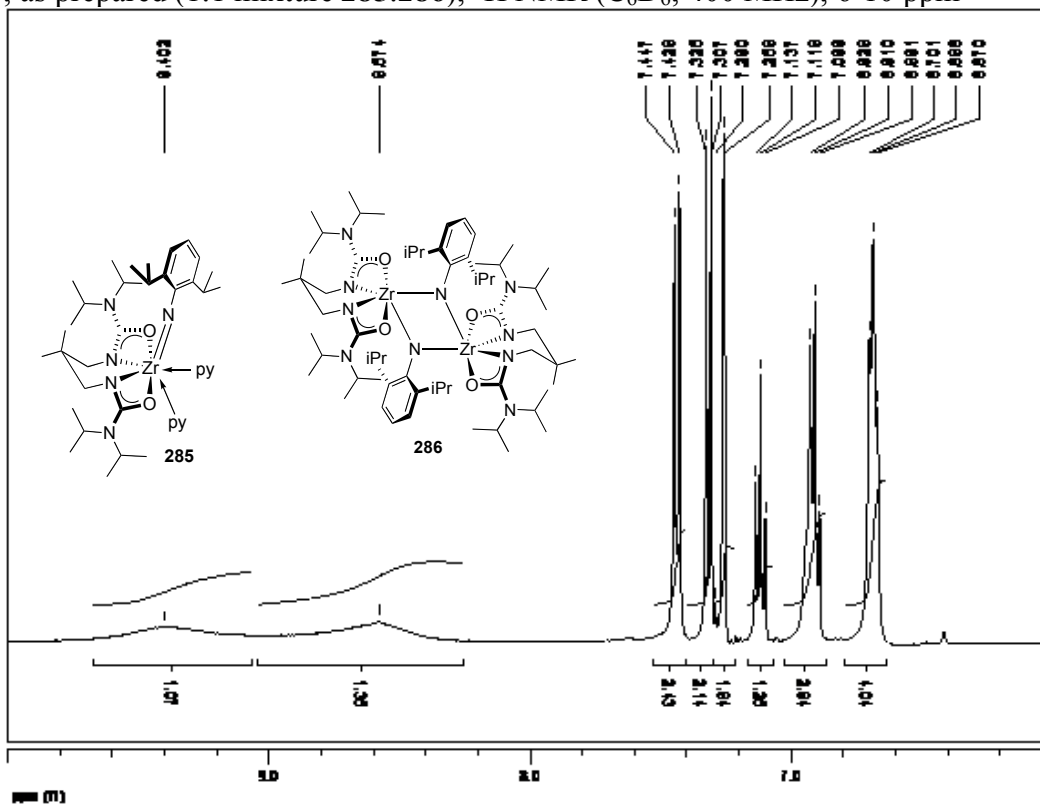


Acquisition Time (sec)	2.1999	Comment	DL-V-62 1H observe ref. to CDCl3 at 7.27 ppm
Date	09 Oct 2009 16:12:48	Date Stamp	09 Oct 2009 16:12:48
File Name	F:\USB Documents\PhD Research\Papers\JACS Communication (Hydroamination)\SI Spectra\DL-V-62\DL-V-62_005000fid		
Frequency (MHz)	300.13	Nucleus	¹ H
Origin	spect	Original Points Count	8233
Points Count	16384	Pulse Sequence	zg30
SW(cyclical) (Hz)	3742.51	Solvent	CHLOROFORM-d
Sweep Width (Hz)	3742.29	Temperature (degree C)	25.160
		Number of Transients	24
		Owner	root
		Receiver Gain	71.80
		Spectrum Offset (Hz)	1793.8740

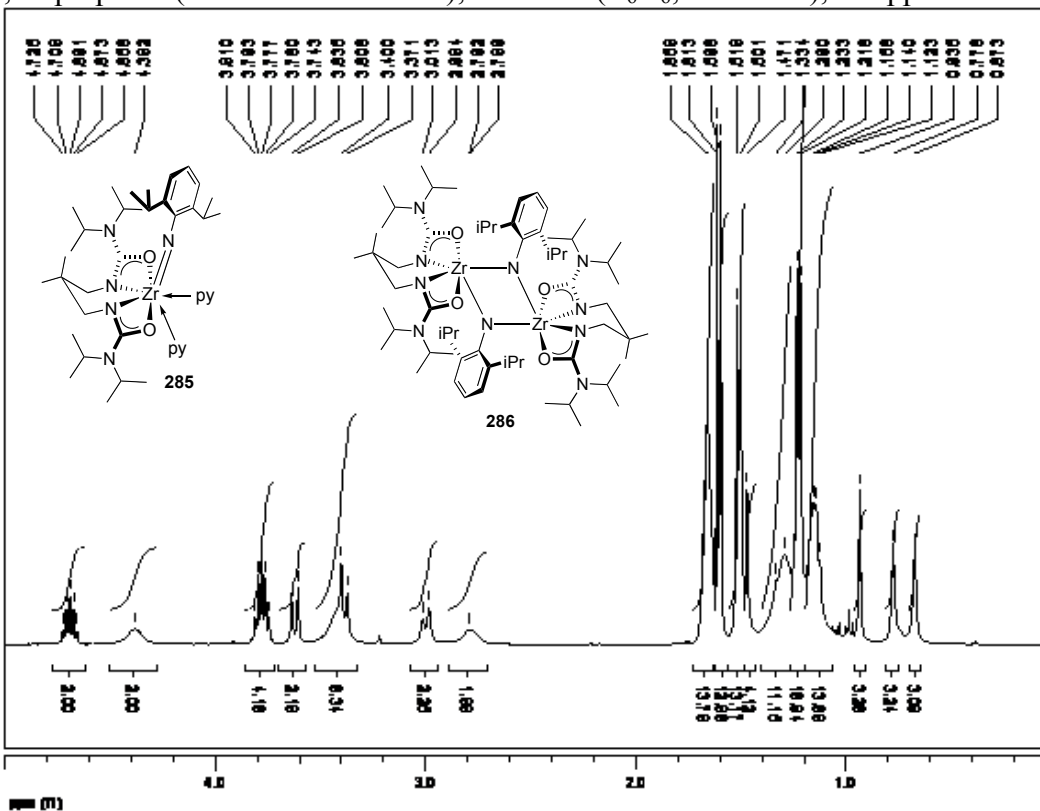
DL-V-62_005000fid



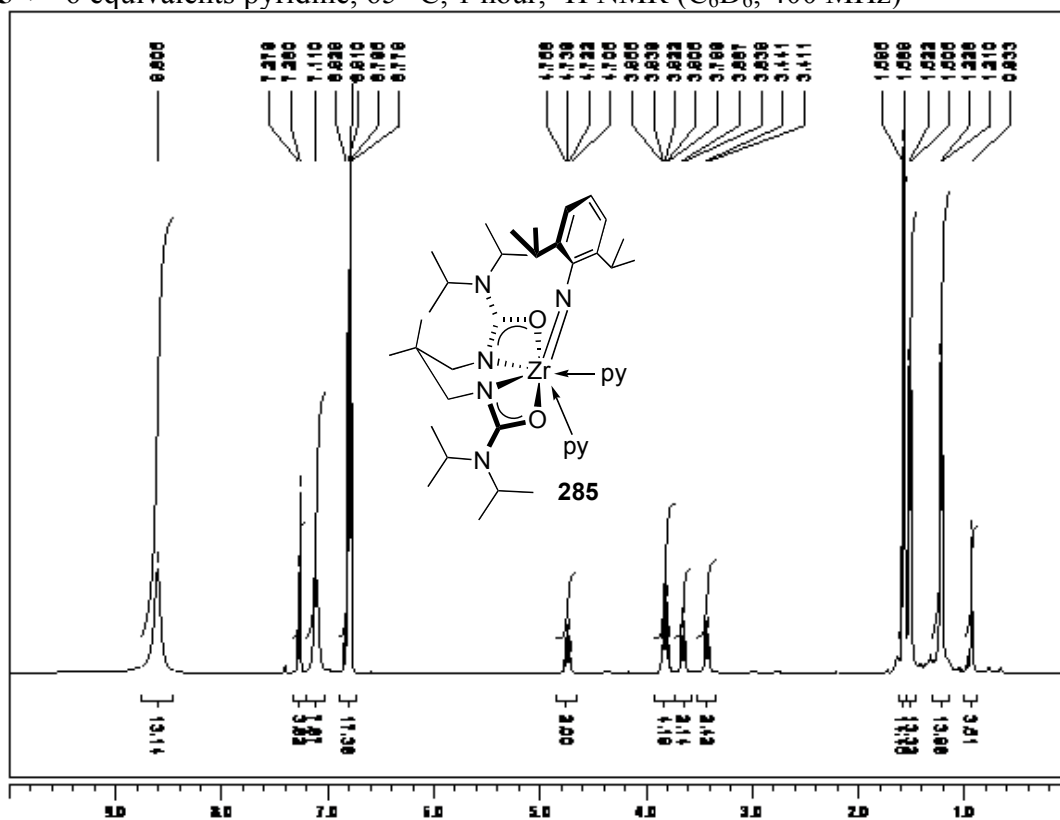
285, as prepared (1:1 mixture **285:286**), ¹H NMR (C₆D₆, 400 MHz), 6-10 ppm



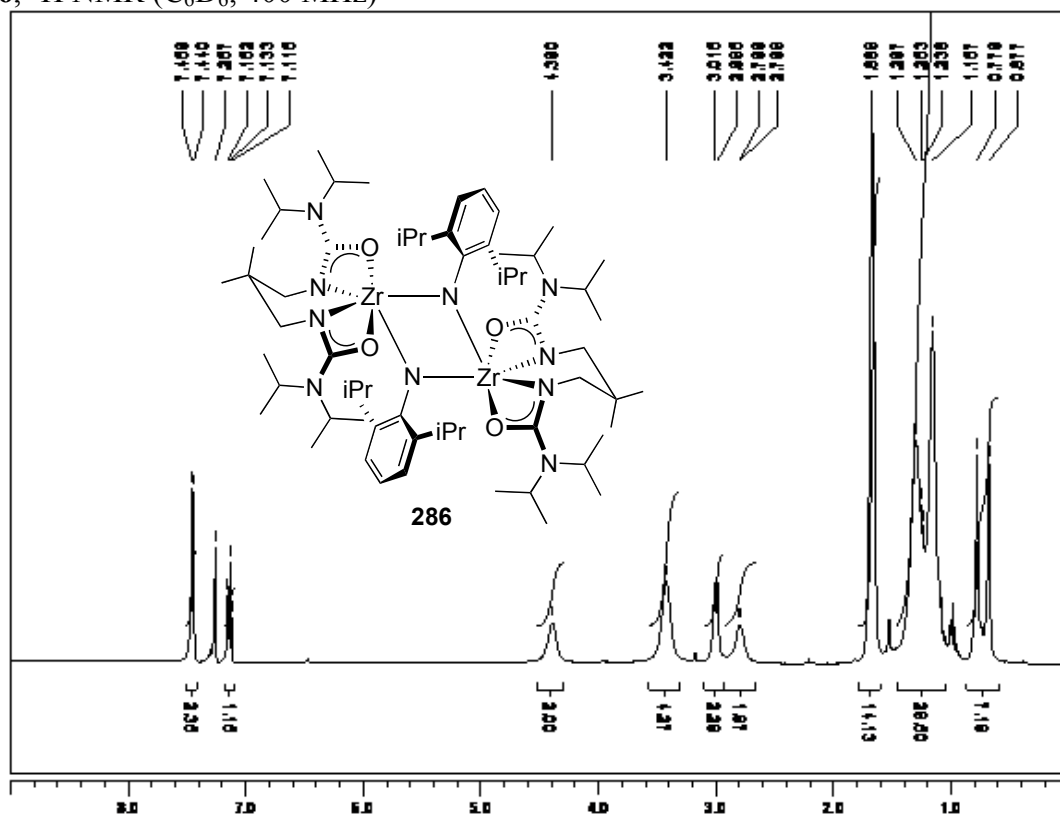
285, as prepared (1:1 mixture **285**:**286**), ¹H NMR (C₆D₆, 400 MHz), 0-5 ppm



285 + ~6 equivalents pyridine, 65 °C, 1 hour, ^1H NMR (C_6D_6 , 400 MHz)

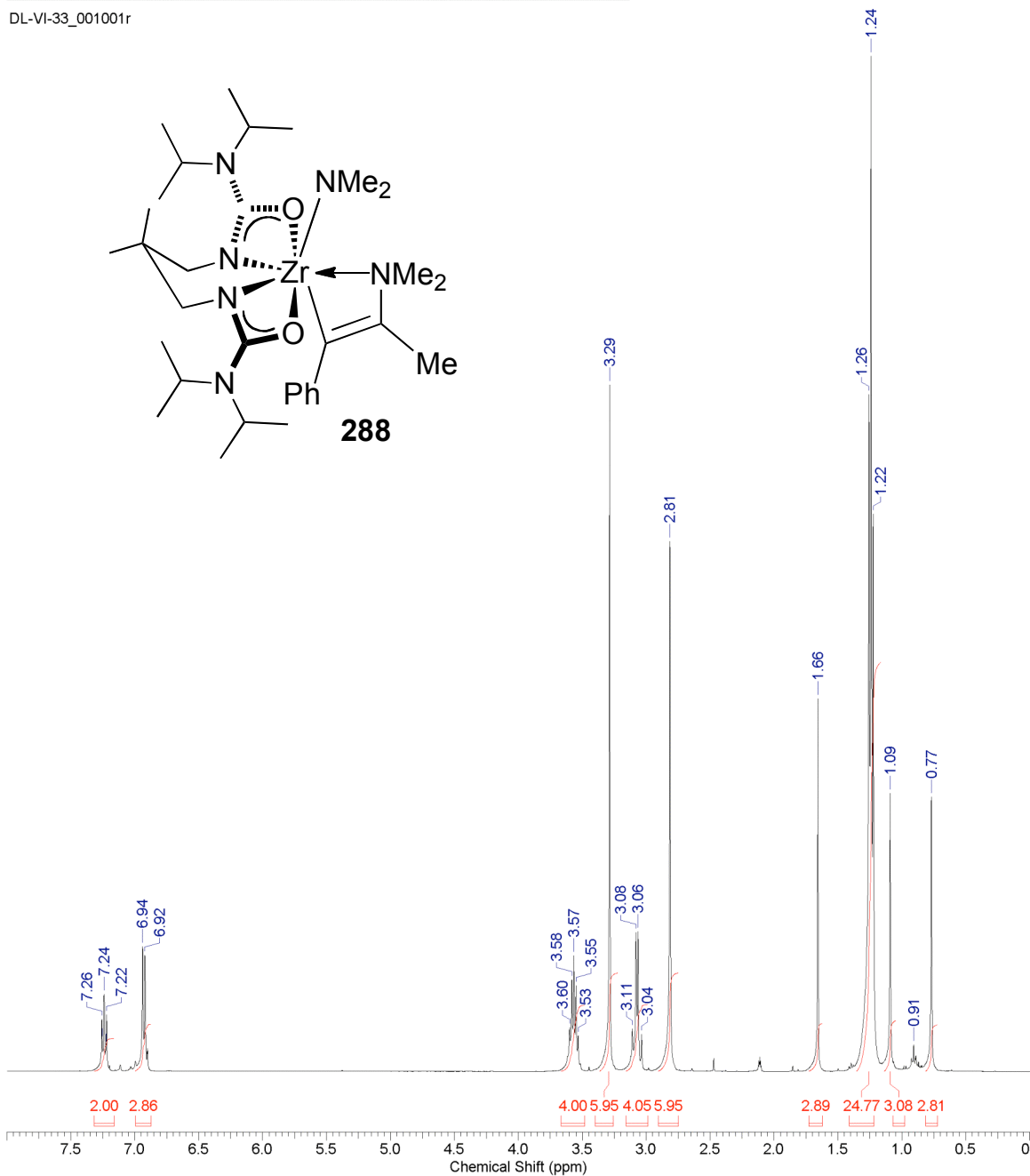


286, ^1H NMR (C_6D_6 , 400 MHz)



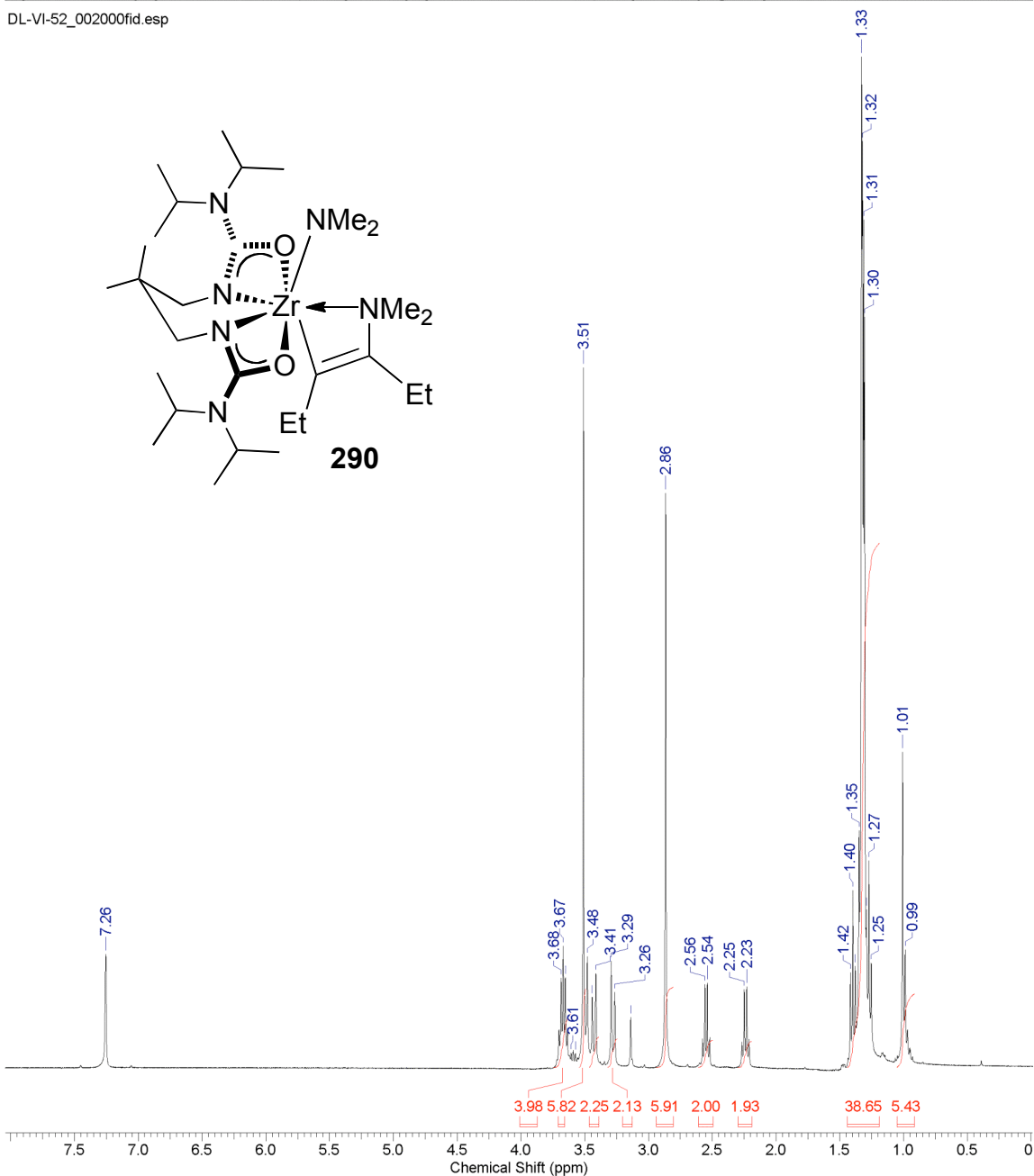
Acquisition Time (sec)	2.3622		
Comment	DL-VI-33 recrystallized, 69% yield JOB NO: 1H spectrum ref. to CDCl3 at 7.27 ppm		
Date	06 Dec 2009 01:42:24	Date Stamp	06 Dec 2009 01:42:24
File Name	C:\Documents and Settings\Dave\Desktop\DL-VI-33_001001r	Frequency (MHz)	400.13
Nucleus	1H	Number of Transients	40
Original Points Count	12303	Owner	root
Pulse Sequence	zg30	Receiver Gain	18.00
Solvent	CHLOROFORM-d	SW(cyclical) (Hz)	5208.33
Sweep Width (Hz)	5208.17	Temperature (degree C)	25.160
		Spectrum Offset (Hz)	2595.7866

DL-VI-33_001001r

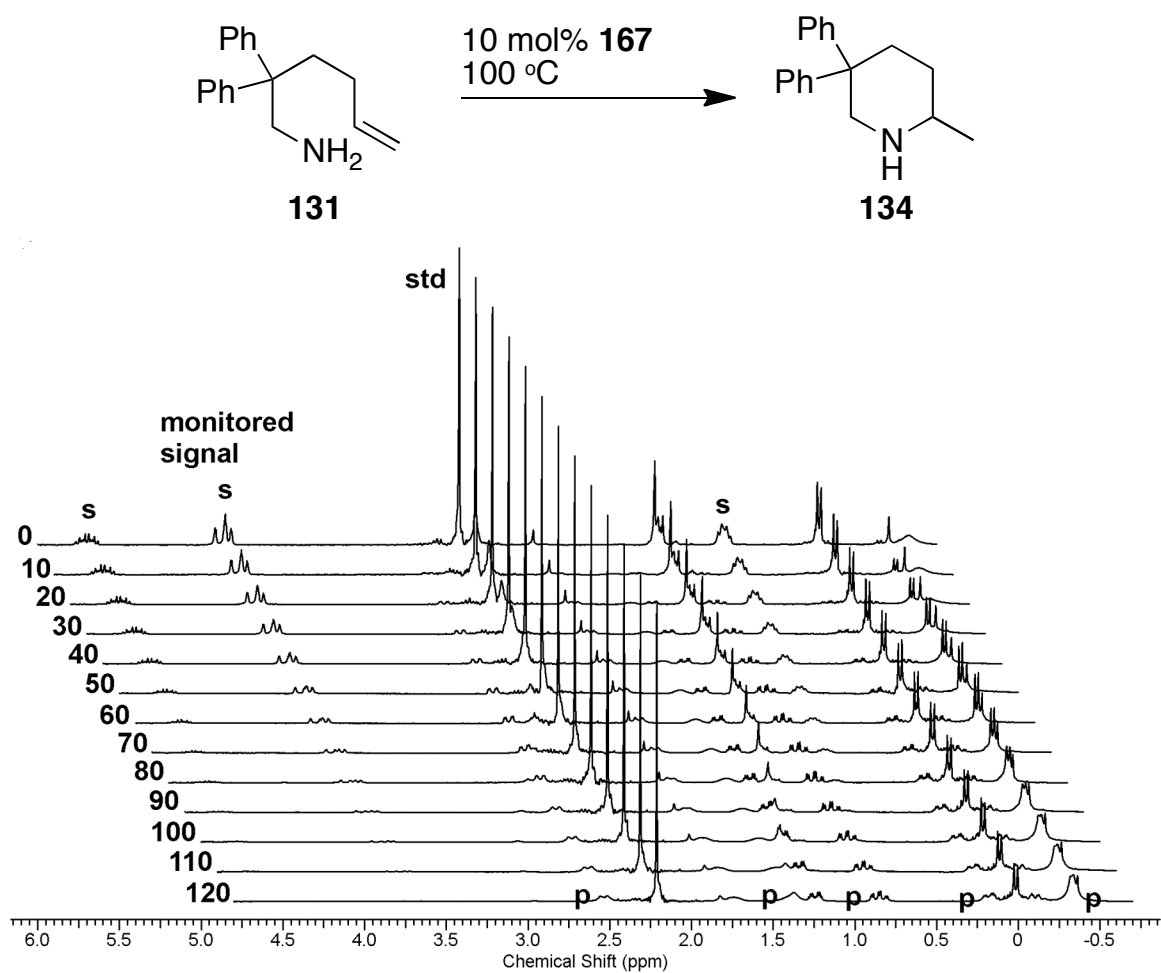


Acquisition Time (sec)	2.9295	Comment	DL-VI-52 recrystallized
Date	20 Dec 2009 22:15:28	Date Stamp	20 Dec 2009 22:15:28
File Name	C:\Documents and Settings\Courtney\Desktop\DL-VI-52\DL-VI-52_002000fid		
Frequency (MHz)	400.19	Nucleus	¹ H
Origin	spect	Original Points Count	16384
Points Count	16384	Pulse Sequence	zg30
SW(cyclical) (Hz)	5592.84	Solvent	CHLOROFORM-d
Spectrum Offset (Hz)	2590.5879	Sweep Width (Hz)	5592.50
		Temperature (degree C)	22.148

DL-VI-52_002000fid.esp



Stack-plot of a typical kinetics experiment for the conversion of **131** (s) to **134** (p). One spectrum acquired every ten minutes.



REFERENCES FOR APPENDICES

1. Wood, M. C.; Leitch, D. C.; Yeung, C. S.; Kozak, J. A.; Schafer, L. L. *Angew. Chem., Int. Ed.* **2007**, *46*, 354.
2. Manzer, L. E. *Inorg. Synth.* **1982**, *21*, 135.
3. Benzing, E.; Kornicker, W. *Chem. Ber.* **1961**, *94*, 2263.
4. Zucchini, U.; Albizzati, E.; Giannini, U. *J. Organomet. Chem.* **1971**, *26*, 357.
5. Mowat, W.; Wilkinson, G. *J. Chem. Soc. Dalton Trans.* **1973**, 1120.
6. Warren, T. H.; Erker, G.; Frohlich, R.; Wibbeling, B. *Organometallics* **2000**, *19*, 127.
7. Kondo, T.; Okada, T.; Mitsudo, T. *J. Am. Chem. Soc.* **2002**, *124*, 186.
8. Hong, S.; Tian, S.; Metz, M. V.; Marks, T. J. *J. Am. Chem. Soc.* **2003**, *125*, 14768.
9. O'Shaughnessy, P. N.; Knight, P. D.; Morton, C.; Gillespie, K. M.; Scott, P. *Chem. Commun.* **2003**, 1770.
10. Bexrud, J. A.; Schafer, L. L. *Dalton Trans.* **2010**, *39*, 361.
11. Gagné, M. R.; Stern, C. L.; Marks, T. J. *J. Am. Chem. Soc.* **1992**, *114*, 275.
12. Leitch, D. C.; Payne, P. R.; Dunbar, C. R.; Schafer, L. L. *J. Am. Chem. Soc.* **2009**, *131*, 18246.
13. Bexrud, J. A.; Eisenberger, P.; Leitch, D. C.; Payne, P. R.; Schafer, L. L. *J. Am. Chem. Soc.* **2009**, *131*, 2116.
14. Crimmin, M. R.; Arrowsmith, M.; Barrett, A. G. M.; Casely, I. J.; Hill, M. S.; Procopiou, P. A. *J. Am. Chem. Soc.* **2009**, *131*, 9670.
15. Bender, C. F.; Widenhoefer, R. A. *J. Am. Chem. Soc.* **2005**, *127*, 1070.
16. Gribkov, D. V.; Hultsch, K. C.; Hampel, F. *Chem. Eur. J.* **2003**, *9*, 4796.

17. Riegert, D.; Collin, J.; Meddour, A.; Schulz, E.; Trifonov, A. *J. Org. Chem.* **2006**, *71*, 2514.
18. Ates, A.; Quinet, C. *Eur. J. Org. Chem.* **2003**, 1623.
19. Lauterwasser, F.; Hayes, P. G.; Brase, S.; Piers, W. E.; Schafer, L. L. *Organometallics* **2004**, *23*, 2234.
20. Utsunomiya, M.; Hartwig, J. F. *J. Am. Chem. Soc.* **2004**, *126*, 2702.
21. Stradi, R.; Trimarco, P.; Vigevani, A. *J. Chem. Soc. Perkin. Trans. I* **1978**, 1.
22. Aillaud, I.; Collin, J.; Duhayon, C.; Guillot, R.; Lyubov, D.; Schulz, E.; Trifonov, A. *Chem. Eur. J.* **2008**, *14*, 2189.
23. Davis, F. A.; Xu, H.; Zhang, J. *J. Org. Chem.* **2007**, *72*, 2046.
24. Katritzsky, A. R.; Qiu, G.; Yang, B.; Steel, P. J. *J. Org. Chem.* **1998**, *63*, 6699.
25. Fukumoto, Y.; Asai, H.; Shimizu, M.; Chatani, N. *J. Am. Chem. Soc.* **2007**, *129*, 13792.
26. Barluenga, J.; Aznar, F.; Liz, R.; Rodes, R. *J. Chem. Soc. Perkin. Trans. I* **1983**, 1087.
27. Alonso-Moreno, C.; Carrillo-Hermosilla, F.; Romero-Fernandez, J.; Rodriguez, A. M.; Otero, A.; Antinolo, A. *Adv. Synth. Catal.* **2009**, *351*, 881.
28. Buil, M. L.; Esteruelas, M. A.; Lopez, A. M.; Mateo, C. A. *Organometallics* **2006**, *25*, 4079.